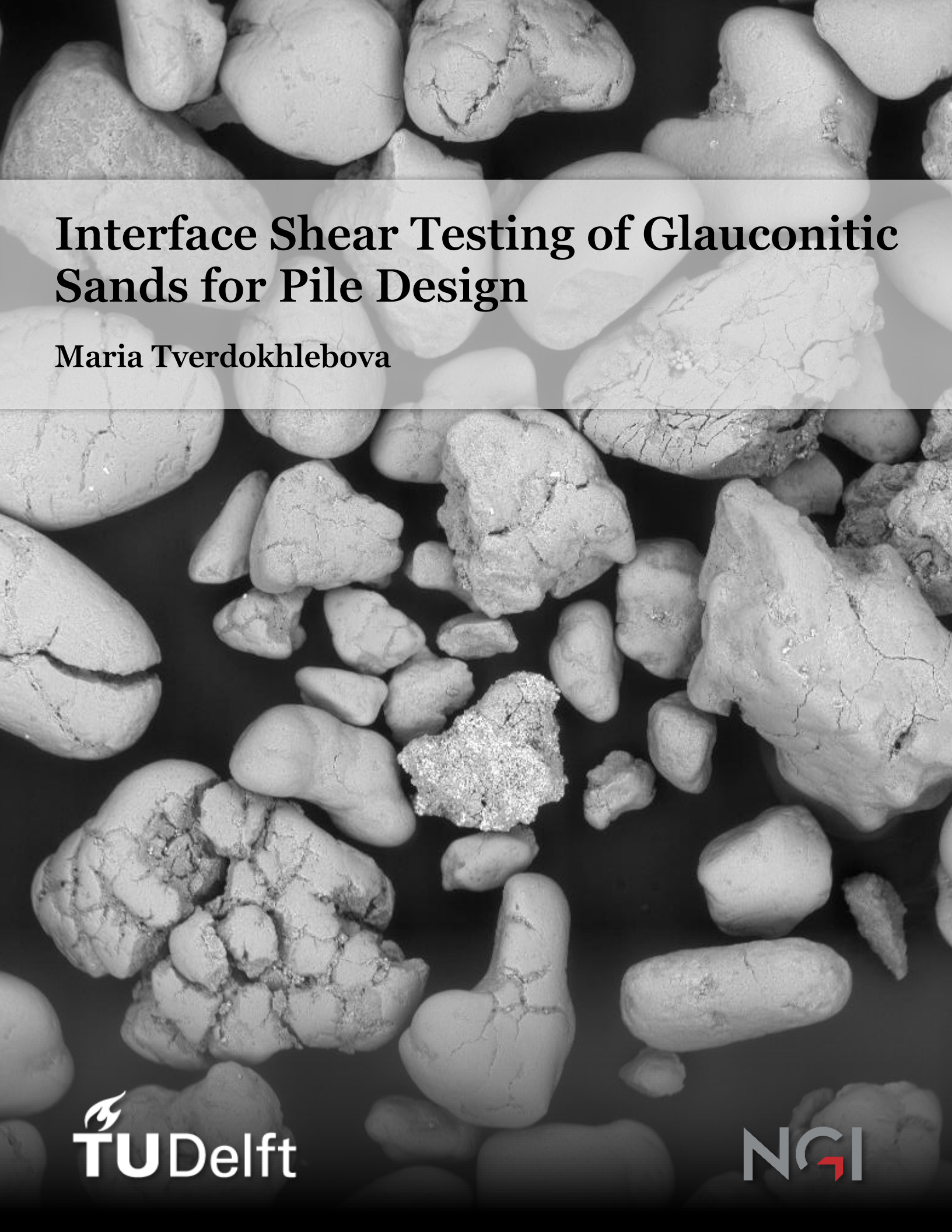

Interface Shear Testing of Glauconitic Sands for Pile Design

Maria Tverdokhlebova

TU Delft

NGI

Interface Shear Testing of Glauconitic Sands for Pile Design

Master Thesis

by

Maria Tverdokhlebova

to obtain the degree of Master of Science in Civil Engineering
at the Delft University of Technology,
to be defended publicly on Tuesday, November 26, 2024, at 11:00.

Student Number:	5838959	
Thesis Committee:	Prof. Dr. Kenneth Gavin,	TU Delft (Chair)
	Dr. Stefano Muraro,	TU Delft
	Dr. Luca Flessati,	TU Delft
	Dr. Tobias Schmiedel,	TU Delft
	Dr. Santiago Quinteros,	NGI

TU Delft

NGI

Abstract

With the continued growth of the offshore sector and plans for new wind farm developments, shallow marine environments are becoming key areas for the renewable energy projects. As a result, the likelihood of encountering glauconitic sands is growing, posing challenges to the offshore wind infrastructure. Glauconite, or glauconitic sand, also known as ‘greensand’, refers to a soil containing peloidal sand-sized grains primarily comprised of mineral glauconite, an iron- and potassium-rich 2:1 interlayer-deficient mica. The tendency of glauconite to transform from sand to fine-grained soil with shearing creates uncertainties in site characterization and negatively impacts pile drivability to targeted depths. This thesis examines shearing behavior of glauconitic sands at soil-pile interface using two samples of Belgian glauconitic sands. With the final goal being the derivation of reliable interface shear strength parameters, the study aims to develop test procedures capable of capturing the transition of glauconitic sands from their natural uncrushed state to a reworked degraded condition, simulating the effects of shear-induced particle breakage during pile installation. To achieve this, a systematic experimental program was completed in two phases. The first part focused on glauconitic sands in their natural state and the second aimed to assess the degraded soil. Comprehensive material characterization, including geotechnical index tests, mineralogical analyses, and soil-steel interface direct shear tests under various conditions, was carried out to support each phase. The findings link the interface shear behavior and strength of glauconitic sands to their intrinsic properties, identify limitations in current experimental procedures, and offer recommendations for future research. New insights are provided into the behavior of Belgian glauconitic sands with the relatively low glauconite content and varying crushability potential. Interface roughness, shear rate, and normal stress effects are considered.

Acknowledgments

I would like to start by thanking everyone who helped me throughout the experimental program. Special thanks to the laboratory support staff Cristina Cavero Panez, Karel Heller, and Jelle Kampf for their help with the direct shear test modifications and other tasks in the geotechnical laboratory.

I appreciate the assistance of the technicians from Stevinlab and Waterlab for introducing me to new equipment and guiding me through the testing process. I am also deeply grateful to Arjan Thijssen for dedicating his time to help me examine numerous samples under the ESEM.

Thank you to Bruno Stuyts from Ghent University for providing the primary Belgian sample for testing, as well as Alba Piedrabuena and Deltares for the opportunity to conduct tests unavailable at TU Delft and for supplying the second sample essential for this work.

Thank you to Qin Zhang for sharing her knowledge on glauconite and helping me proceed with the comprehensive assessment of glauconite pellets.

My sincere appreciation extends to the members of my graduation committee. I would like to thank Prof. Ken Gavin for helping me select such an exciting research topic and for granting me the freedom and support to make key decisions throughout the project.

I am especially grateful for the collaboration with NGI and would like to thank Santiago Quinteros for his guidance, availability for any questions, and shared enthusiasm for research. I have learned a lot in our meetings and appreciate this opportunity to look at geotechnical analyses from a different perspective.

Special thanks to Stefano Muraro for his unwavering support, exceptional advice, and many practical recommendations that allowed me to carry out this project.

Thank you to Luca Flessati for providing new insights, guiding me towards the unexplored directions, and offering valuable feedback throughout the research.

My deepest gratitude goes to Tobias Schmiedel for his impactful comments on scientific writing, fresh perspective, encouragement, and thoughtful advice.

Lastly, I would like to thank my long-time friends and all the wonderful people I was fortunate to meet during my time in the Netherlands for their encouragement and support. I am always and especially grateful to my loving family, my parents, and my husband for always being there for me, no matter how far away.

Nomenclature

Abbreviations

ASTM	American Society for Testing and Materials
CF	Clay Fraction
CL	Lean Clay
CNL	Constant Normal Load
COD	Crystallography Open Database
CPT	Cone Penetration Testing
CPTu	Cone Penetration Test with Pore Pressure Measurement
DS	Direct Shear
EDX	Energy-dispersive X-ray spectroscopy
ESEM	Environmental scanning electron microscopy
FC	Fines Content
GC	Glauconite Content
ICDD	International Centre for Diffraction Data
ICL	Imperial College London
ICP	Imperial College Pile
JIP	Joint Industry Project
LL	Liquid Limit
LOI	Loss of Ignition
ML	Silt
NC	Normally Consolidated
NGI	Norwegian Geotechnical Institute
NTNU	Norwegian University of Science and Technology
OC	Over-Consolidated
OCS	Outer Continental Shelf
PDF-5	Powder Diffraction File
PI	Plasticity Index
PL	Plastic Limit
PSD	Particle Size Distribution
SBTn	Normalized Soil Behavior Type
SC	Clayey Sand
SEM	Scanning electron microscopy
SM	Silty Sand
SP-SM	Poorly Graded Sand with Silt
USCS	Unified Soil Classification System
XRD	X-ray Diffraction
XRF	X-ray Fluorescence

Symbols

C_c	Coefficient of curvature
C_u	Coefficient of uniformity
D_{10}	Particle size corresponding to 10% finer by weight

D_{50}	Median particle size
D_r	Relative density
G_s	Specific gravity
R_{CLA}	Centerline average roughness
R_a	Average roughness
R_f	Friction ratio
R_{max}	Maximum roughness
R_n	Normalized roughness
R	Normalized roughness
c_{ap}	Peak adhesion
c_{ar}	Residual adhesion
f_s	Sleeve friction
q_t	Cone tip resistance
s_u	Undrained shear strength
δ	Interface friction angle
δ'	Effective interface friction angle
δ'_{20mm}	Interface friction angle at 20 mm horizontal displacement
δ_{cv}	Critical state (constant volume) interface friction angle
δ_p	Peak interface friction angle
δ_{peak}	Peak interface friction angle
δ_{res}	Residual interface friction angle
δ_{ult}	Ultimate interface friction angle
σ'_{rf}	Radial effective stress at failure
σ_n	Normal stress
σ_v	Vertical stress
σ'_{v0}	Initial vertical effective stress
τ_{av}	Average shear resistance
τ_f	Local shear resistance
ϕ_{cv}	Critical state angle of internal friction
ϕ_{res}	Residual angle of internal friction
e	Void ratio
w	Moisture content
α	Adhesion factor
γ	Unit weight
ρ	Density

Table of Contents

1 Introduction

Glauconite or glauconitic sand is a challenging material, limited understanding of which poses risk to both the offshore and onshore construction projects. Glauconitic sands have been associated with foundation installation and performance issues caused by their tendency to transform from coarse- to fine-grained material with continuous particle breakage occurring during pile advancement. The subsequent increase in shaft resistance leads to a higher risk of premature pile driving refusal that can result in significant added costs and serve as a major threat to project execution (NGI, 2024). Thus, with the focus shifting towards the offshore wind farms development, there is a growing demand for a better understanding of glauconite behavior and acquisition of reliable design parameters for piles installed in areas of glauconite formation.

1.1 Research Context

Glauconite has been extensively studied for years due to its significant role in various geologic and industrial applications. In geologic research, it is widely used for stratigraphic interpretations and age dating of sedimentary formations (Burst, 1958; McRae, 1972; Amorosi, 1997; Wigley & Compton, 2007). Its understanding has also been advantageous for the paleoenvironmental reconstructions (Banerjee et al., 2016; Banerjee et al., 2020; Starzec et al., 2023) and other scientific needs. Beyond geology, glauconite is highly valued in practical applications: for example, as a potassium-rich agricultural fertilizer (Tedrow, 2002; Santos et al., 2015; Kalinina et al., 2023) and an effective industrial sorbent (Belousov et al., 2022).

Recently, with the development of offshore wind farms along the east coast of the U.S., glauconite-bearing deposits of the Atlantic Outer Continental Shelf (OCS) started getting more attention as a potential geotechnical hazard. Here, challenges associated with the degradation of glauconite and elevated soil resistance to driving could be exacerbated by negative pore pressures, requiring careful material characterization to answer new design needs and reduce uncertainty and risk in pile installation and long-term performance (Lennon, 2023; NGI, 2024; Westgate et al., 2024).

Pile drivability issues have also been reported in other areas of glauconite deposition, even when its content was rather low. This was the case in Belgium (de Nijs et al., 2015) and North Sea (Perikleous et al., 2023) installations. Given the widespread distribution of glauconite deposits globally, particularly in shallow marine environments, its significance in geotechnical engineering is expected to grow alongside the expansion of the offshore sector. Note that only select sites of Paleogene formation, which comprises only up to 24 percent of the total record (Banerjee et al., 2016), are shown in Figure 1.1.

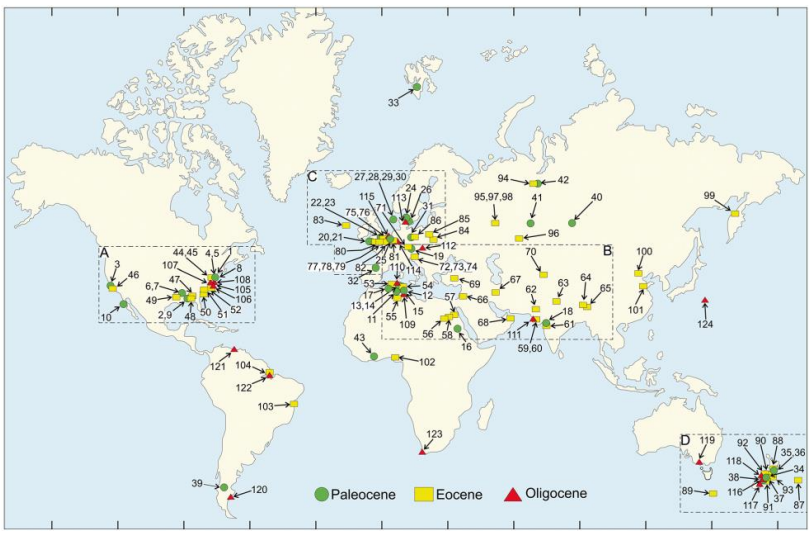

Figure 1.1. Global Distribution of Paleogene Glauconite from Banerjee et al. (2020)

Although the investigation of the (soil-steel) interface shear strength of glauconite-bearing sediments has recently gained attention in both the industry and academia, there is still no reliable database on high-quality test results that would support non-conservative estimation of the required pile design parameters (primarily, residual interface friction angle). Furthermore, with the limited number of experimental results available to date (Westgate et al., 2022; Westgate et al., 2023; Quinteros et al., 2023; Rezaei & Walkowska, 2024; Westgate et al., 2024; Piedrabuena, 2024), it is not fully clear how glauconite properties vary between the different depositional conditions and which aspects of its formation and geologic history require special attention in geotechnical characterization. Finally, there is no consistency in how glauconitic soils are studied in a laboratory setting. Therefore, a systematic evaluation is needed to establish a robust methodology for the assessment of glauconitic soils and accurate simulation of their behavior during and after pile installations.

1.2 Research Objectives

This thesis focuses on glauconitic sand to steel interface shear testing with the primary objective of deriving credible pile design parameters using two samples from Belgium. Achieving this goal necessitates the development of test procedures that would allow for a comprehensive evaluation of glauconitic sands capturing their transformation from the uncrushed coarse-grained material to a reworked state, simulating shear-induced degradation along the pile walls. To provide a basis for future research, various test conditions and methods needed to be considered.

Therefore, this study aims to address the existing gap in knowledge focusing on the given research question:

- What are the reliable interface shear strength parameters (e.g., residual interface friction angle range) for pile design in glauconitic soils from Belgium and how can they be effectively assessed in a laboratory setting?

Sub-questions defining direction of this research project are as follows:

- How do the properties, behavior, and interface shear strength of glauconitic sands change as glauconite undergoes crushing and degradation?
- How do specific properties of glauconitic sands such as glauconite content, maturity, and formation type, influence their interface shearing behavior and mechanical response?
- How do variations in applied test conditions, including interface roughness, shear rate, and normal stress, affect the interface shear strength of glauconitic sands?

Given the limited duration of an MSc thesis project and complexity of the assessed soil-structure interaction, these questions may not be fully addressed but served as a framework guiding the performed experimental program.

1.3 Research Methodology

The research aims to provide new insights into the interface shear strength and behavior of glauconitic sands for pile design through a systematic experimental program conducted in collaboration with the Norwegian Geotechnical Institute (NGI). The program was centered on soil-steel interface direct shear testing, divided into two primary phases. The first phase evaluated glauconitic sands in their natural state, as found in situ, establishing a baseline for the subsequent analysis of their degraded condition. The second phase investigated the effects of glauconite crushing and degradation, attempting to simulate shear-induced breakage occurring during pile installations. Both phases were supported by comprehensive material characterization, including standard geotechnical index tests and mineralogical evaluations, to link the observed behaviors to the intrinsic soil properties. In addition to the standard well-established procedures, alternative test methods were employed to explain responses exhibited by glauconitic sands.

The experimental program was primarily conducted at Delft University of Technology facilities. Testing was performed on two Belgian sand samples: Leuven sand, kindly provided by Bruno Stuyts from Ghent University, and Antwerp sand, supplied by Deltares.

1.4 Outline of the Report

The structure of this thesis report is organized as follows:

- Section 2 provides an overview of interface shear testing and shear behavior factors likely to influence the assessment of glauconitic sands in both their natural sand-like state and with the ongoing transformation into a fine-grained material. It also reviews the existing knowledge on glauconitic sands, with an emphasis on aspects relevant to geotechnical characterization.
- Section 3 introduces the two Belgian glauconitic sand samples evaluated in this study and outlines the relevant geologic background.
- Section 4 provides a detailed overview of the implemented material characterization methods.
- Section 5 discusses the results from the first phase of material characterization, focusing on glauconitic sands in their natural state.
- Section 6 covers further analyses of glauconitic sands with an emphasis on degradation effects.
- Section 7 highlights the limitations of the conducted experimental program and offers insights for future research on glauconitic sands.
- Section 8 presents the conclusions and recommendations drawn from the experimental program.

2 Literature Review

This section provides an in-depth review of the current interface shear testing practices and key factors affecting interface shear behavior of sands and clays. Kowing that glauconitic sands pose risk to pile installations due to their tendency to transform from coarse- to fine-grained material, both states should be considered to see if the existing understanding of soil-structure interaction fits with results obtained for the Belgian glauconitic sand samples (discussed in Sections 5 and 6). Following the overview of relevant experimental considerations, it shifts focus to the general understanding and geotechnical characteristics of glauconitic sands.

2.1 Shaft Resistance of Driven Piles

Accurate characterization of soil-structure interface shearing behavior is required for a wide range of offshore and onshore geotechnical structures. When considering axially driven piles, interface shear resistance is one of the major factors governing shaft capacity. To ensure their reliable performance, derivation of high-confidence site-specific interface shearing parameters is necessary (Jardine et al., 2005).

The analysis of soil-shaft interface shear resistance, or side friction, is based on the principle of sliding friction and may be evaluated with the use of either (1) total stress or (2) effective stress analyses. Both approaches are idealizations of the true mechanisms governing a much more complex problem and including some combination of friction and adhesion (Randolph, 2003; Coduto et al., 2016).

The total stress approach (alpha method), which still remains popular for estimation of the shaft capacity of piles in clay (Doherty & Gavin, 2011), links the average shaft resistance (τ_{av}) to the average undrained shear strength (s_u) of cohesive soil along the shaft through the adhesion factor (α):

$$\tau_{av} = \alpha s_u \tag{2.1}$$

The formulation of the method and the term “adhesion factor” may give an incorrect impression that side-friction resistance is considered to form due to a “glueing” effect between the soil and pile. Although some adhesion may be present in a considered case, the α value should be seen more as a correlation factor linking the frictional resistance to the undrained shear strength s_u (Coduto et al., 2016). The adhesion factor is determined empirically from pile load test results and has been shown to depend on many factors, i.e., to decrease with the increasing over consolidation ratio and clay content (Coduto et al., 2016) and decreasing plasticity index (PI) (Doherty & Gavin, 2011). However, despite a vast application and research contributing to the development of total stress methods, they remain fundamentally flawed as local shaft failure is not controlled by the initial undrained shear strength (s_u) characteristics that are modified by the pile installation and creation of a weaker interface zone. This, together with the difficulties in defining s_u and dependence of the developed shear resistance on interface roughness, led to an implementation of the effective stress design approach not only for piles installed in sand but also in clay (Jardine et al., 2005; Doherty & Gavin, 2011).

The effective stress design approach (beta method) proposed by Burland (1973) expresses local shaft resistance (τ_f) in terms of the radial effective stress at failure (σ'_{rf}) and the interface friction angle (δ), which is linked to the in situ vertical effective stress (σ'_{v0}) through an empirical parameter (β):

$$\tau_f = \beta\sigma'_{v0} = K\sigma'_{v0}tan\delta = \sigma'_{rf}tan\delta \tag{2.2}$$

Beta values are often back calculated from load test results or obtained from published sources based on values from static load tests or local experience on sites with similar subsurface conditions (Coduto et al., 2016).

Throughout the years of research both design methods have been improved and many new methods, such as the cone penetration testing (CPT)-based formulations (Lehane et al., 2022), have been developed. Since this project is intended to focus on characterization of interface shear strength of glauconitic sands and not the pile design applications, these advancements will not be discussed further. The given introduction into the methods for evaluation of the axial capacity is only intended to show why local shaft failure governed by the simple Coulomb

effective stress interface friction angle law (Eq. 2.2) is considered to apply for piles installed in both sands and clays. Moreover, this explains why derivation of the interface friction angles through direct and torsional (ring) shear laboratory tests has been a focus of studies on degrading glauconitic sands and their characterization for pile design. While the beta method can indirectly reflect the contribution of adhesion (the cohesive bonding between soil and structure that is especially relevant for fine-grained soils), it is not explicitly accounted for. This discussion will be relevant for the understanding of research limitations associated with the focus on frictional resistance and disregard of adhesion in Section 7.

2.2 Interface Shear Testing

The peak (δ_{peak}) and ultimate (δ_{ult}) or residual (δ_{res}) interface friction angles are measurable material parameters dependent on the soil type and properties, shearing history, and soil-structure interface characteristics. Soil interface shearing angles and behavior have been evaluated through direct shear, simple shear and torsional (ring) shear laboratory tests. The latter are considered preferential due to their ability to apply nominally unlimited shear displacements, impose uniform interface shear stresses, and include pre-conditioning stages representing pile installation effects (Head & Epps, 2011; Liu et al., 2019). However, direct shear (DS) tests used in this project are more widely available, standardized and offer a pragmatic approach for a relative parametric comparison of shear strength even considering their limitations such as the stress nonuniformities, poor boundary conditions, and limited tangential displacement range (Potts et al., 1987; Head & Epps, 2011).

In characterization for pile design, the interface direct shear test measures the shear resistance between a soil sample and a plate imitating pile surface. An applied normal load simulates the radial effective stresses expected to act on a pile in situ (i.e., the pressure exerted by surrounding soil perpendicular to the pile shaft). A horizontal force is applied during the test, representing axial loading on the pile, to induce sliding at the interface, mimicking how a pile resists vertical loads through friction and adhesion between its surface and the surrounding soil. In conventional direct shear tests, samples are sheared with the constant normal load (CNL) condition applied (Head & Epps, 2011).

Shearing results in sands depend on the state of packing of the grains. This is shown in Figure 2.1 originally created for shear characteristics in soil-soil tests (Head & Epps, 2011). If it is assumed that distortion and crushing of individual grains does not occur, in dense state, they will be forced to ride up and over the underlying particles, resulting in expansion observed through the upward movement of the top surface of the specimen. The resulting shear stress-displacement curve and volume change relationship are marked with letter D in Figure 2.1. The shear stress curve is shown to rise to a peak and fall off to a lower value with the excess of the peak (denoted by letter E) representing the extra work that has to be put in to produce the vertical movement due to dilatancy. This strain-softening response is typical for dense sands as well as the over-consolidated clays (Budhu, 2011; Head & Epps, 2011).

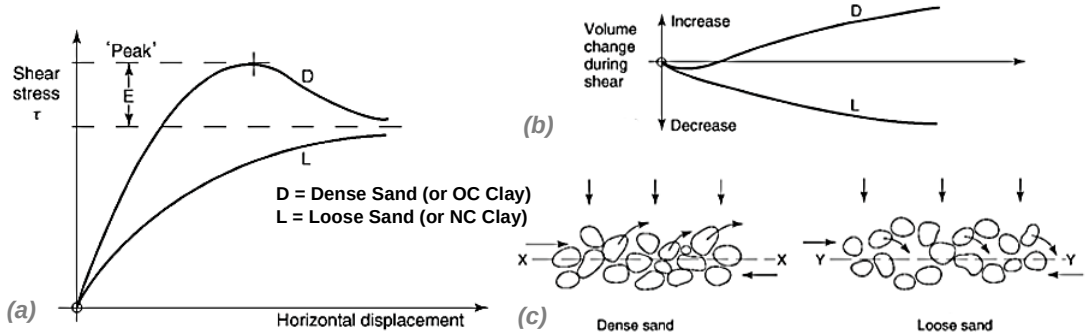

Figure 2.1. Shear Characteristics of Dense and Loose Sands: (a) Shear Stress vs. Horizontal Displacement; (b) Volume Change vs. Horizontal Displacement; and (c) Effect on Grain Structure from Head and Epps (2011)

In loose sands, shearing results in collapse of the open structure with grains moving into void spaces, causing downward movement of the top surface of the specimen. As shown in Figure 2.1, in this case (denoted with letter

L) there is no pronounced peak in the resulting shear stress-displacement curve. The shear stresses gradually increase with displacement (strain-hardening) until an approximately constant value is attained. The same response is observed for normally consolidated and lightly overconsolidated clays (Budhu, 2011).

When compared to soil-soil tests, volumetric response in interface direct shear tests may be more complex due to the introduction of roughness effects resulting in various failure modes and creation of a rigid boundary condition (Tsubakihara et al., 1993; Head & Epps, 2011; Guo et al., 2023). The effects of shear localization and volumetric response directly at the interface will be discussed in detail in Section 2.3.

From a set of tests on three identical specimens tested under different normal stresses, peak and residual interface friction angles (δ_{peak} and δ_{res}) can be derived from Coulomb envelopes as shown in Figure 2.2. The peak and residual shear strength are defined by the following equations:

$$\tau_f = c_{ap} + \sigma_n tan\delta_p \tag{2.3}$$

$$\tau_f = c_{ar} + \sigma_n tan\delta_{res} \tag{2.4}$$

In interface shear testing of non-cohesive or reconstituted soils and normally consolidated clays failure envelopes are often shown or expected to pass through the origin and tests may not be conducted at various normal stress levels (Rao et al., 1998; Rao et al., 2000; Martinez & Stutz, 2018; Westgate et al., 2023). Thus, the peak and residual adhesion ($c_{ap}$and c_{ar}) may be ignored as presumably negligent.

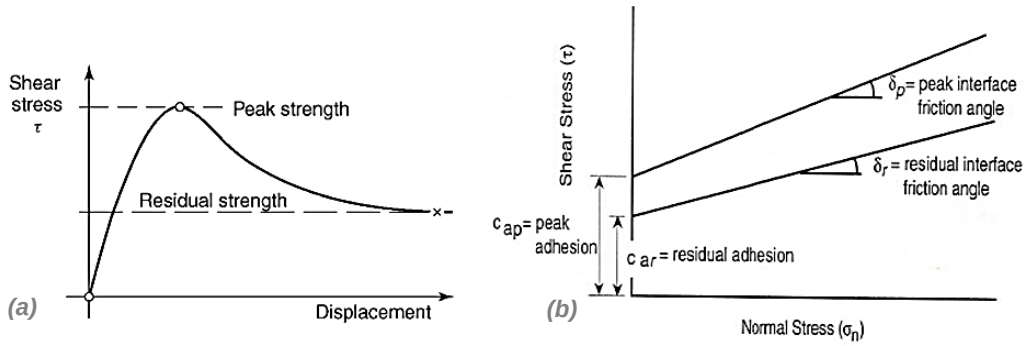

Figure 2.2. (a) Peak and Residual (Interface) Shear Strength and (b) Coulomb Envelopes for Peak and Residual Conditions from Head and Epps (2011) and Koerner (1998)

The operational interface angle of friction, or the constant volume value (δ_{cv}) for sands, is developed when the soil at the interface has ceased dilating or contracting (Jardine et al., 2005). The design value depends on the sand grain size, shape and mineral type, hardness of the particles, and roughness of the pile surface. The range of δ_{cv} values in commonly encountered (siliceous) sands is rather narrow and usually spans between 26 and 30 degrees (Jardine et al., 1992; Liu et al., 2019). In current design practice, δ_{cv} is usually assumed to be equal to 29 degrees for piles driven in marine sands (Jardine et al., 2005; Lehane et al., 2022).

For clays, the peak and ultimate friction angles (δ_{peak} and δ_{ult}) cover a wider range of values (8 to 36 degrees), depending on the soil type, prior loading history and interface properties (Jardine et al., 2005). Pile installation and shearing in a laboratory apparatus modifies soil fabric at the interface. When undergoing these shear-induced changes, some clays show a ductile pattern of interface failure with little difference between the peak and ultimate interface friction angles. In other cases, clay fabric close to the structural surface may be left in an imperfectly reoriented state, leading to a significant reduction from δ_{peak} to δ_{ult}. According to Jardine et al. (2005), the ICP field measurements indicated that the local interface friction angle values reduced from peak to ultimate conditions within just 5 mm of pile-soil slip displacement.

In the given discussion definition of the post-peak interface friction angles remained consistent with the referenced literature, distinguishing between the constant volume (δ_{cv}), ultimate (δ_{ult}), and residual (δ_{res}) values. Despite the slight differences in their definitions, future sections may collectively refer to these as the residual interface friction

angle (δ_{res}). However, in the given literature review, shear strength parameters will be mentioned as defined in the corresponding references.

Factors affecting the interface shear behavior and strength are further discussed below with the focus on sands in Section 2.3 and clays in Section 2.4. Since glauconitic sand is considered a challenging sediment due to its tendency to transform from the coarse-grained into fine-grained material with shear-induced particle crushing (Westgate et al., 2023), these literature review chapters are intended to support the understanding of its behavior in both states.

2.3 Interface Shear Behavior in Sands

This subsection reviews previous research on the shearing behavior of non-cohesive soils, with a focus on silica/quartz sands. While it does not provide an exhaustive list of factors relevant to pile design, it highlights those most pertinent to the tests conducted in this project.

Interface Roughness Effects

This discussion on roughness effects references vertical surface profiles, an example of which is shown in Figure 2.3. Various studies use different roughness indices: R_{max} represents the height difference between the highest peak and lowest trough (Tsubakihara & Kishida, 1993), R_a indicates the average roughness (Martinez & Frost, 2017), and R_{CLA} refers to the centerline average roughness specifically (Yang et al., 2010; Liu et al., 2019). Additionally, normalized roughness (R_n or R) may be introduced as the ratio of surface roughness to the median particle size (D_{50}) of a soil (Rao et al., 1998; Liu et al., 2019).

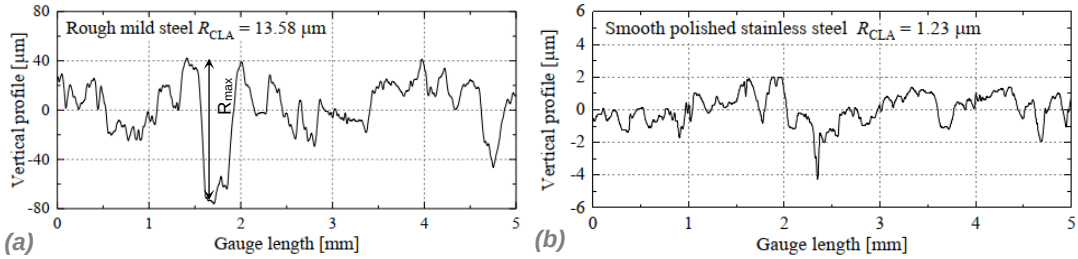

Figure 2.3. Examples of Vertical Surface Roughness Profiles of a) Rough and (b) Smooth Steel Surfaces from Liu et al. (2019)

The critical state or residual interface friction angle is known to increase with the increasing solid surface roughness (DeJong & Westgate, 2009; Martinez et al., 2015; Liu et al., 2019). A study conducted by Rao et al. (1998) showed that as relative roughness tends to zero, the critical interface friction angle can be as low as 12 degrees. As for the maximum limiting value, it corresponds to the critical state angle of internal friction (ϕ_{cv}) of the sheared sand (Rao et al., 1998). The variation of critical interface friction angle up to this threshold is shown in Figure 2.4.

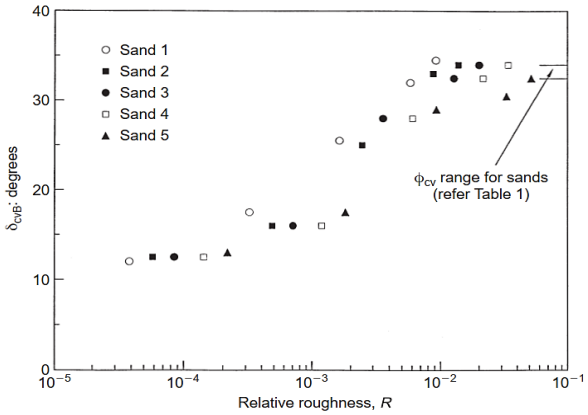

Figure 2.4. Variation of Critical State Interface Friction Angle with Relative Roughness from Rao et al. (1998)

A similar bilinear relationship (from Rao et al. (1998)) between interface strength and normalized roughness was previously quantified for different sands by Uesugi and Kishida (1986) and Jardine et al. (1992). It is worth noting that this trend may primarily apply to interface direct shear tests. As concluded by Liu et al. (2019) and demonstrated in Figure 2.5, in the case of ring shear tests, data points consistently plot above the bilinear DS trendline. This could be explained by the increased grain crushing and interface smoothening as well as the confining conditions being more representative of in situ stresses (Liu et al., 2019).

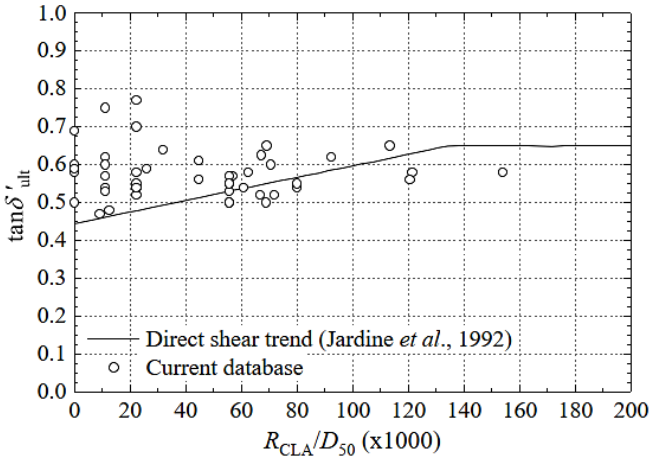

Figure 2.5 Correlation between tan(δ_{ult}) and pre-test normalized roughness R_{CLA}/D_{50} from Liu et al. (2019)

Uesugi et al. (1988) observed that in sand-steel shear tests, sand particles slipped, rolled, and moved vertically along a rough interface (R_n = 0.068), forming a shear zone about five times the particle diameter. On a smooth surface (R_n = 0.015), the sand mass slipped with minimal deformation. DeJong and Westgate (2009) made similar findings: in tests with smooth steel (R_a = 1.8 μm), shear and volumetric strains were concentrated within 0.5 to 1.5 mm of the interface, with nearly full slip occurring at particle contacts once a stable particle structure was formed. On rough surfaces, strains extended up to 6–8 mm, and slip reduced to about 30 percent of the full extent. The performed tests showed that in soil-structure shearing, surfaces of low roughness transfer load by friction while rough interfaces are capable of mobilizing additional passive resistances (DeJong & Westgate, 2009; Martinez & Frost, 2017). This change in response is clearly illustrated in the shear zone photographs from Martinez and Frost (2017) shown in Figure 2.6.

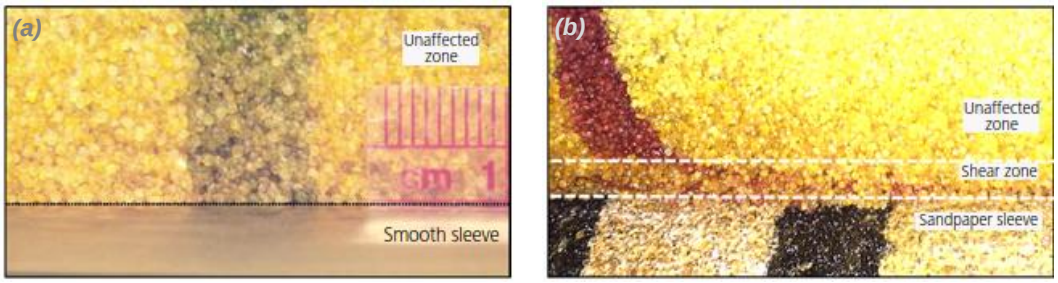

Figure 2.6. Photographs of Shear Zones Created During Shear with Surfaces of (a) Smooth and (b) Random Rough (Sandpaper) Roughness Forms from Martinez and Frost (2017)

The localized behavior of sand/steel interfaces was previously studied with the use of view windows in a modified interface direct shear setup (DeJong & Westgate, 2009) or by performing torsional axisymmetric tests (Martinez et al., 2015) allowing for the shear zone observation from above. These studies provided a better understanding of shear response at a rough or textured interface. When a granular specimen is sheared, the initial load is mostly carried by force chains developing through the entire specimen. Once the peak state is reached, the force chain columns begin to localize and orient with the shear zone formation. With failure they start to buckle and rearrange, resulting in fewer particle contacts and reduced shearing resistance. The global effect of this process is strain-

softening in the stress-strain curve. Locally, as the contacts collapse, particles are likely to push each other away and rearrange, leading to dilation of the soil mass.

In interface shearing, the shear zone forms at or near the soil-structure interface (Mitchell & Soga, 2005; Martinez et al., 2015), with its thickness influenced by relative density, particle angularity, and surface roughness, and reduced by increasing normal stress, particle hardness, and normal stiffness (DeJong & Westgate, 2009; Martinez et al., 2015). Higher interface roughness results in a more pronounced post-peak softening and is expected to cause a shift from contraction to dilation in both loose and dense specimens. However, dilation within the shear zone is not always recorded in the DS vertical displacement data because localization of shearing adjacent to the interface may cause underprediction of the actual rate of dilation occurring within the specimen. In cases indicating no volumetric expansion within the tested soil, it is likely that dilation occurs immediately at the interface and may be compensated by contraction in the specimen above (DeJong & Westgate, 2009). Thus, examination of a sheared specimen may be required to understand which shear mechanism took place and what level of deformation was achieved in a given test.

Impact of Gradation Characteristics

Gradation characteristics, which depend on depositional and stress history of a given soil, are one of the governing factors in soil-structure interface behavior. The median particle size and particle size distribution determine whether sand particles interlock, dilate in rotation, or translate laterally along an interface (Uesugi & Kishida, 1986). Median particle size, or D_{50}, is also correlated with the height of the local shear zone at the interface, which is typically around 5 times the median particle size (Uesugi et al., 1988).

In interface direct shear tests conducted previously δ'_{cv} was found to decrease with the increasing D_{50} (Jardine et al., 1992), likely due to the reduction in interlocking between the sand and steel asperities, limited rearrangement of the particles, and reduced contact area. Noteworthy, as shown in Figure 2.7, direct shear tests with smaller displacements and no pre-shearing stage seem to demonstrate more distinct variation of ultimate interface friction angles against D_{50} when compared to ring shear tests from the Imperial College London and NGI unified database (Liu et al., 2019).

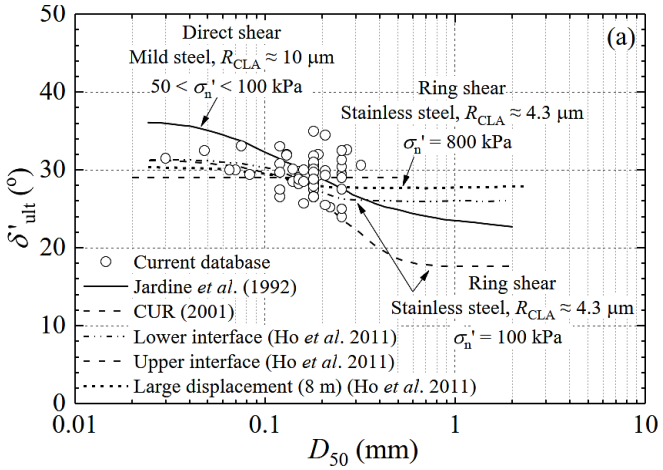

Figure 2.7. Published Trends for δ'_{ult} Against D_{50} from Liu et al. (2019)

Looking back at Figure 2.4 and Figure 2.7, for parametric comparison of interface shear tests results, it seems advantageous to consider relative roughness, which accounts for both surface asperities and grain size, rather than relying solely on D_{50}.

Impact of Particle Angularity and Hardness

In a series of monotonic direct interface shear tests by DeJong and Westgate (2009), particle hardness was found to have lower impact on interface response compared to particle angularity. Increased angularity led to greater

shear resistance and more pronounced dilation, reflecting enhanced interlocking. In loose specimens, dilation increased at the interface due to the additional soil-structure interlocking, while above the interface, contraction increased with greater particle rearrangement due to higher angularity.

However, the effects of particle hardness and crushability may become evident with the application of cyclic loading. Modified cyclic direct shear tests conducted by DeJong et al. (2003) showed that carbonate soil with the higher crushability than silica, exhibited a thicker shear band and increased cumulative contraction due to particle breakage, leading to greater degradation and increased slip at the interface.

Impact of Fines Content

The presence of fines in sands can have a significant influence on the exhibited shear strength behavior. Different types of intergranular matrix configuration defined by Thevanayangam and Martin (2002) are shown in Figure 2.8. In the first case fine particles fit in the void space with little effect on soil behavior due to external loads being transferred through contacts between coarse particles. In two intermediate scenarios fine particles start to separate the coarse grains, preventing them from forming direct contacts. Depending on properties and quantity of the fines, their presence may either reinforce the skeleton or make it unstable. As the proportion of fines shifts further, coarse particles start floating inside the matrix, and fine grains now control the mechanical behavior of soil. The threshold fines content defining transition to the fine-grained soil varies for each specific mixture but is typically in the range between 25 and 45 percent (Mitchell & Soga, 2005).

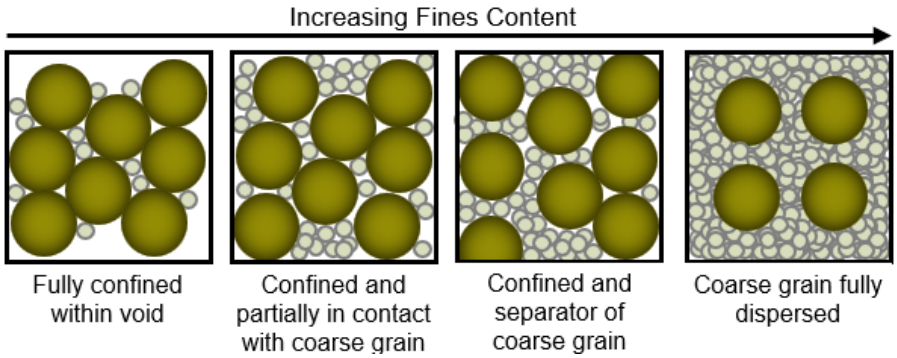

Figure 2.8. Granular Mix Classification Based on Thevanayangam and Martin (2002)

Although the effect of fines content on mechanical behavior of geomaterials has been studied extensively, there is still no consensus regarding its critical value and the influence on interface shear strength. It is generally believed that addition of a small amount of nonplastic fines (below about 15 percent) may increase both the peak and critical-state friction angles of the soil and result in a more dilative response of the sand through denser packing and additional interlocking between particles (Carraro et al., 2009). In interface shear testing, this influence of nonplastic fines on the ultimate interface friction angle had been experimentally demonstrated by Liu et al. (2019) through Bishop ring shear apparatus tests on silty sand soils as shown in Figure 2.9. While this figure does not indicate a clear increase in frictional resistance, it confirms that incorporation of up to 20 percent of non-plastic fines is unlikely to lead to its reduction.

In contrast, addition of the same percentage of plastic fines, such as kaolin clay, has been shown to lower both the peak and critical-state (residual) friction angles and impart a less dilative or more contractive response to the soil. This change is explained by clay acting as a lubricator and smoothing out the defects and asperities on the surface of the sand grains (Mitchell & Soga, 2005; Carraro et al., 2009). Further increase in fines content appears to decrease shear strength of the host sand and leads to transition in response from dilatancy to contraction for both plastic and nonplastic fines (Kim et al., 2018; Shen et al., 2021; Chen et al., 2023). In addition to content, the shape, mineralogy, and clay activity of fine particles influence soil stability, with more active clay fractions lowering the residual friction angle at a given clay size percentage (Mitchell & Soga, 2005). It is reasonable to believe that the same patterns would apply to the frictional interface shear behavior, although experimental base on mechanical response of clay-sand mixtures sheared along structural interfaces is very limited.

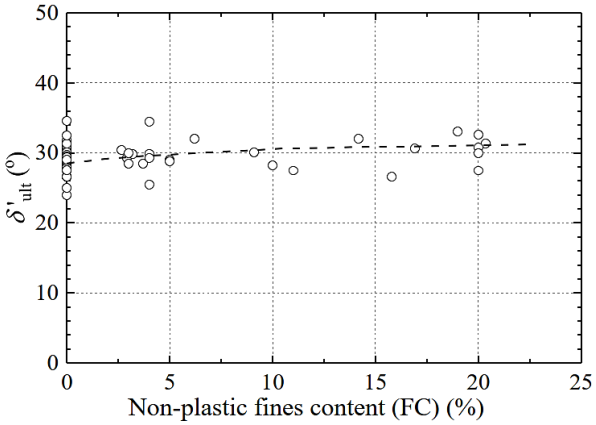

Figure 2.9. Correlation between δ_{ult} and FC from Liu et al. (2019)

Normal Stress Effects

Generally, increasing normal stress is expected to result in increased shear resistance, decreased strain-softening behavior, decreased dilation in dense sands, increased contraction in loose sands, and greater particle breakage in the soil (DeJong & Westgate, 2009).

A series of 2D constant normal stress sand-steel interface tests performed by Evgin and Fakharian (1996) under normal stresses of 100, 300, and 500 kPa (with R_{max} = 25 μm; R_n ~ 0.04) showed that while the peak stress ratio was higher at lower normal stresses, the residual stress ratio remained the same irrespective of the magnitude of the applied normal stress. In interface direct shear tests conducted by DeJong and Westgate (2009) (with R_a = 133 μm; R_{max} = 700 μm; and R_n ~ 0.95) increases in normal stress resulted in higher shear resistance but lower residual stress ratio, increased displacement to peak shear resistance, and suppressed dilation. The shear zone thickness was found to decrease at higher normal stresses due to the greater energy levels required for particle rearrangement. As shown in Figure 2.10, modest dependency of the ultimate interface friction angle on normal effective stress had also been observed in Bishop ring shear tests (with R_{CLA} of 8 – 13.5 μm) on silty sands from the unified database maintained by ICL and NGI (Liu et al., 2019).

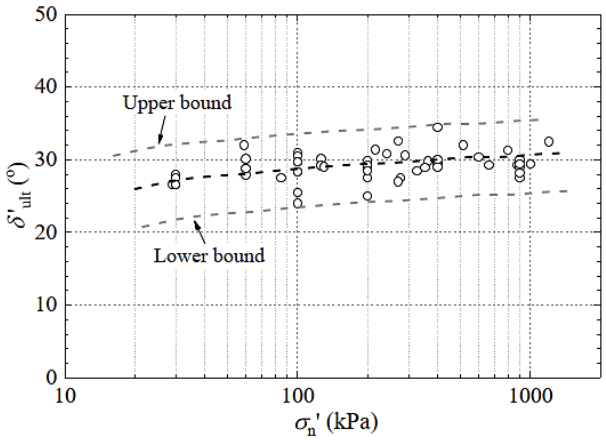

Figure 2.10. Correlation between δ_{ult} and σ'_n from Liu et al. (2019)

The review demonstrates that normal stress effects in DeJong and Westgate (2009) tests were studied with the use of interface roughness exceeding that expected for standard piles (typically within 5 to 15 μm (Jardine et al., 2005; Liu et al., 2019)), and that other programs indicated only modest dependency of δ_{ult} on the applied normal stress, if any. Thus, considering pile design applications, interface shear strength of relatively hard silica sands is not expected to be dominated by normal stress effects.

Shear Rate Effects

It is generally expected that at higher shear rates, shear strength of sand would increase with the greater frictional resistance between grains due to the lack of time for particle rearrangement (Beren et al., 2020). However, Quinteros et al. (2017) found that in ring shear tests, with fast pre-shearing applied, the resulting residual interface friction angles were relatively unaffected by the imposed shear rate. The same was true for ring shear tests conducted with the pre-conditioning stage on silty sands by Liu et al. (2019). This suggests that rate dependency may be influenced by the initial interparticle configuration and would likely be limited for silica sands. Please note that this discussion applies only to shear rates between 0.005 and 500 mm/min typically assigned for simulation of installation and serviceability loads for piles in the offshore wind sector.

2.4 Interface Shear Behavior in Clays

Although limited information exists on interface shearing of clays, particularly in direct shear (DS) testing, this section aims to enhance understanding of factors influencing the behavior of clayey soils, which may be relevant to the interpretation of shear response exhibited by degraded glauconitic sands.

Interface Roughness Effects

In interface shear tests on fine-grained soils stress distribution at the shear plane may be rather complex as a result of combined shearing and sliding of clay along the structural surface asperities. An experimental study of adhesion carried out by Littleton (1976) on a smooth steel surface (R_{CLA} = 0.18 µm) showed that less than 10 percent of the shearing area was attributed to direct clay-to-steel interaction, meaning that most shearing occurred along the clay-to-clay interface.

A similar conclusion was made by Tsubakihara and Kishida (1993) using simple and direct shear tests between normally consolidated clay and mild steel. However, the critical interface roughness, below which sliding would be the primary failure mode, was about 10 µm, lower than what would be observed for soils with higher sand fraction (Tsubakihara et al., 1993) and greater than the roughness at which most shearing already occurred withing the specimen in Littleton's tests (Littleton, 1976). As in the case of sands, when the steel roughness exceeded critical, shear failure occurred within the clay specimen itself.

In their further research Tsubakihara et al. (1993) recognized three modes of failure, namely full sliding at the interface (Mode 2), shear failure within the soil (Mode 1), and the mixed behavior where interface sliding and shear deformation of the soil specimen occur simultaneously (Mode 2). In the case of sand-clay mixtures, the latter mechanism was observed for steel roughness of 20 to 30 µm. The proposed idealized classification and boundaries between the failure modes are shown in Figure 2.11.

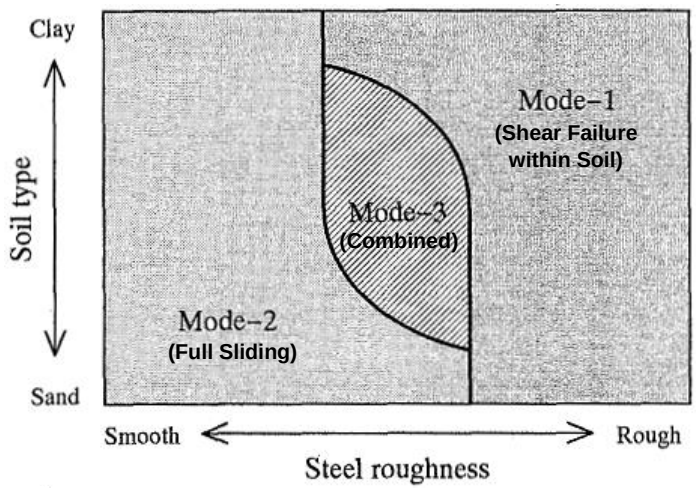

Figure 2.11. Idealized Failure Mode Classification from Tsubakihara et al. (1993)

Based on the conducted literature review, there is no consensus on definition of critical roughness for clays. The results may be highly variable between the independent studies due to differences in clay fraction, plasticity, mineralogy, etc. It is also difficult to implement normalized roughness as it is done for sands, because clay behavior at the interface may be driven by a combination of factors such as particle shape and reorientation, mineral composition, and cation exchange capacity (Lupini et al., 1981; Mitchell & Soga, 2005) rather than particle size relative to asperities. As in the case of sands, post-shearing interface assessment may be needed to understand the mobilized mechanism of failure.

Considering shear strength parameters, frictional resistance was found to consistently increase with the steel roughness, with the minimum interface friction angle derived for the smooth steel plates allowing for full sliding (Tsubakihara & Kishida, 1993). Similar increase in shear strength was observed in tests focusing on the effect of roughness on red clay-concrete interfaces. The increasing interface roughness led to mobilization of the higher interface friction angles approaching the internal friction angle of clay (Chen et al., 2015). Cohesive force, or adhesion, was also found to grow. The same observation was made based on tests for the Speswhite and Boom clay to stainless steel interfaces, which indicated an increase in adhesive shear strength with increasing roughness and pointed to a critical value falling between 2.4 and 4.7 μm (Zimnik et al., 2018).

Impact of Clay Fraction and Activity

Three residual shear modes, based on the percentage of clay-sized particles, are identified in the literature: turbulent, sliding, and transitional (Lupini et al., 1981; Lemos & Vaughan, 2000; Mitchell & Soga, 2005). The turbulent or rolling shear mode occurs in soils with high proportions of granular particles or high interparticle friction, preventing the formation of an oriented clay shear zone. These soils typically exhibit high residual strength, with the residual state reached at small shear displacements. However, if such soils are sheared against a smooth surface, partial sliding and lower residual strength may occur due to local reorientation of clay particles (Lemos & Vaughan, 2000).

The sliding mode (in soil-soil shearing), in contrast, forms a weak shear surface with oriented, low-friction clay particles, resulting in lower residual strength. This behavior is highly dependent on clay mineralogy, pore water chemistry, and interparticle friction. As clay plasticity increases, the particles develop a stronger preferred orientation, reducing residual strength and requiring greater displacement (up to 500 mm) to reach residual values (Lupini et al., 1981). A transitional mode, observed in soils with a lower clay content, combines features of both the turbulent and sliding modes. A schematic representation of the three failure modes and reduction of frictional resistance with clay content is provided in two graphs of Figure 2.12.

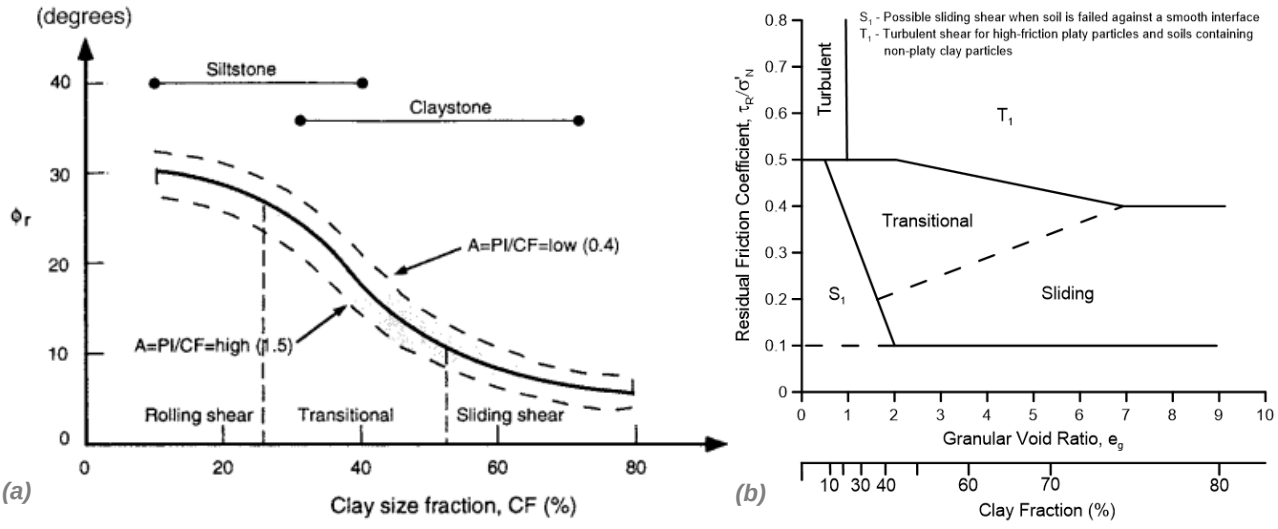

Figure 2.12. (a) Composite Relationship Showing Dependence of Residual Friction Angle on Soil Composition as Represented by Activity and Clay Size Fraction from Mitchell and Soga (2005); and (b) Possible Interface Shear by Sliding in Low-Plasticity Clays (after Lupini et al., 1981) from Lemos and Vaughan (2000)

As indicated in Figure 2.12(a), frictional resistance of clays is also affected by their activity, which is expressed as the ratio of the plasticity index (PI; range of water contents over which the soil deforms plastically) to the amount of clay fraction (Skempton, 1953). In general, the greater the activity of clay, the more important the influence of clay fraction on soil properties, and the more susceptible their values to changes in factors such as type of the exchangeable cations and pore fluid composition. In terms of the shear strength parameters, increasing plasticity and activity of clay result in increasing cohesion and decreasing friction (Mitchell & Soga, 2005). The same trend applies to the interface shear strength, which is illustrated in δ_{res} vs. PI plot modified by Jardine et al. (2005) after Saldivar-Moguel (2002) as shown in Figure 2.13. Similar to cohesion, adhesion is also expected to increase with the clay activity.

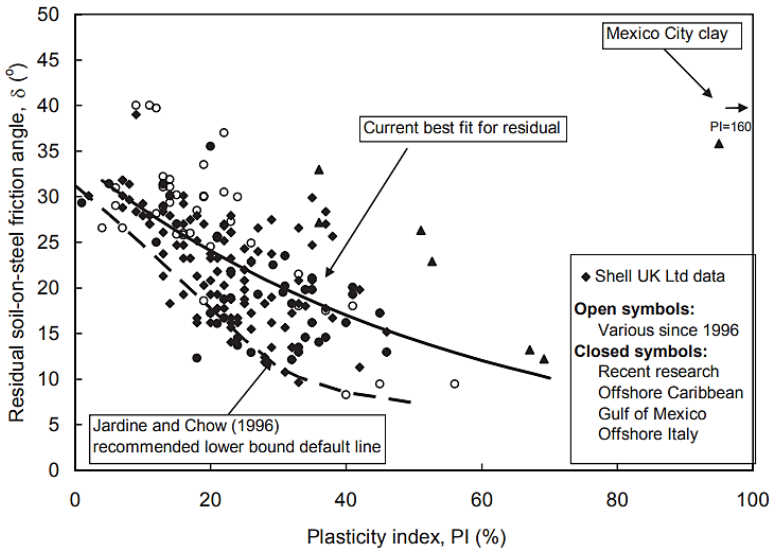

Figure 2.13. Ring Shear Residual Interface Friction Angle Results vs. Plasticity from Jardine et al. (2005)

Impact of Clay Mineralogy

According to Lupini et al. (1981), among the tests resulting in low residual interface friction angles, they were generally the lowest for montmorillonitic soils, and highest when soil mineralogy was dominated by illites and kaolinites. As shown in Figure 2.14, this is consistent with the earlier discussion and the fact that frictional resistance decreases with the increase in clay activity.

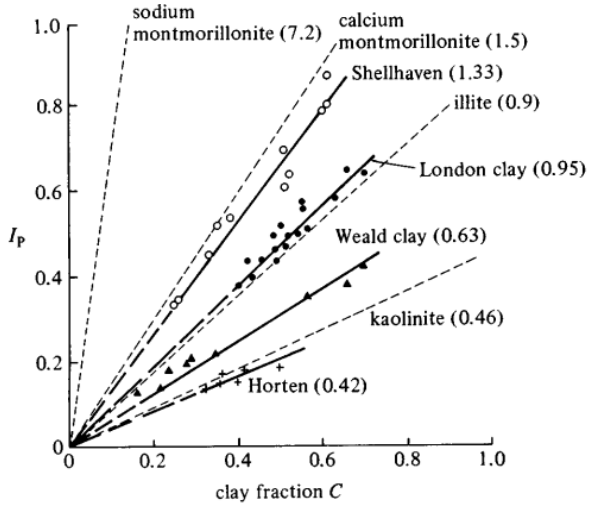

Figure 2.14. Relationship between PI and CF for Natural Clays and Clay Minerals with Values of Activity Indicated; from Wood (1990)

Normal Stress Effects

According to Littleton (1976), the failure mode (shearing vs. sliding) at a clay-steel interface is influenced by the normal stress applied. Lupini et al. (1981) observed that the residual friction angle in clay depends on the normal effective stress, with its impact being most significant in sliding behavior. This observation may also apply to the interface shearing behavior of clay-dominated soils, which has not been studied as extensively. Finally, the adhesive shear strength was found to increase with the increasing normal stress due to the greater bonding and contact surface of the Speswhite (mainly kaolinite) and Boom clays (Zimnik et al., 2018).

Shear Rate Effects

In fine-grained soils, as the shear rate increases, the response changes from drained, with no excess pore pressure generation, to partially drained, where only partial consolidation is occurring. Further increase in shear velocity leads to mobilization of undrained conditions, under which no consolidation takes place and excess pore pressures are accumulated. In the case of normally consolidated clays this rate effect follows the backbone curve shown in Figure 2.15 (Quinn et al., 2012; Martinez & Stutz, 2018). The shear rate at which the identified drainage conditions get mobilized mainly depends on mineralogy, plasticity, and the coefficient of consolidation.

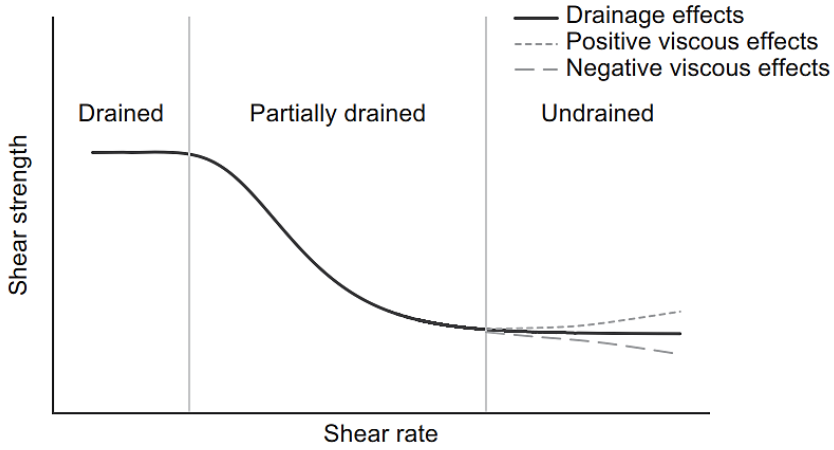

Figure 2.15. Schematic Representation of the Effect of Shearing Velocity on Shear Behavior of NC Clay from Martinez and Stutz (2018)

The existing research shows that rate and viscosity effects in shearing can have significant impact on the observed strength behavior (Briaud & Garland, 1985; Brown & Hyde, 2008). The physical reasoning behind the rate-dependent response and viscous effects in fine soils are based on contributions from the pore water, direct particle contacts, and water/soil interaction. Firstly, free water in the soil pores has viscosity significantly higher than that of the clays, meaning that higher water contents result in higher overall viscosity of the soil. Viscous behavior is also attributed to the inter-particle contacts that are formed by penetration of the mineral particle and its adsorbed water layer into the analogous layer of the other particle. Since viscosity of the adsorbed water is higher than that of the free water, deeper interparticle penetration as well as the higher adsorbed layer thickness expected of higher plasticity clays, would result in higher exhibited viscosity. Finally, water to soil skeleton interaction rate effects are explained by particles having time to deform along the path of least resistance at low shear rates, and, on the opposite, exhibiting higher resistance and, thus, higher viscosity at high shear rates (Briaud & Garland, 1985).

It would be reasonable to expect for the same rate dependence to be observed in interface shear tests. This was indeed the case in CNL (σ_n = 75 or 150 kPa) interface direct shear tests (conducted with the modified shear box device) on normally consolidated kaolin clay (LL = 59.8% and PI = 25.9%) sheared against stainless steel plates (Martinez & Stutz, 2018). However, the opposite trend of shear resistance increasing with the higher rate of displacement was observed in the same testing program for overconsolidated specimens and in shear box tests performed by Tsubakihara and Kishida (1993) on normally consolidated Kawasaki marine clay (LL = 86% and PI = 48.1%) sheared against a mild steel surface with the applied normal stress approaching 300 kPa. According to Martinez and Stutz (2018), discrepancy in trends observed for the normally consolidated specimens could be

attributed to differences in mineralogy of the studied clays. As for the OC specimens, the change in behavior was consistent with expectations. Negative pore pressures were generated, which led to an increase in shear strength at higher velocity.

Noteworthy, a couple effect between shearing velocity and surface roughness on the mobilized drainage conditions was observed in interface DS tests by Martinez and Stutz (2018). Larger velocities were required to transition from drained to partially drained conditions in tests on rough interfaces.

It is important to note that while some studies implement direct shear tests to assess fine-grained soil behavior in undrained conditions (Littleton, 1976; Martinez & Stutz, 2018; Lehane & Jardine, 1992), the standard DS apparatus is not suitable for their simulation due to the lack of drainage control. Even with the implementation of large shear rates the dissipation of some mobilized pore pressure cannot be ruled out. While methods to maintain constant volume during interface shearing, such as continuous adjustment of normal stresses or implementation of triaxial cell with drainage line closure (Rao et al., 2002) do exist, such experimental setups are not commonly available.

2.5 Glauconite/Glauconitic Sand Overview

This subsection provides an overview of the existing knowledge on glauconitic sands that could be relevant for interface shear testing. Currently, there are only a limited number of publications addressing this or closely related topics (Westgate et al., 2022; Westgate et al., 2023; Quinteros et al., 2023; Rezaei & Walkowska, 2024; Westgate et al., 2024; Piedrabuena, 2024). For instance, only two of them provide both the geotechnical index and strength characterization of glauconite-bearing sediments (Westgate et al., 2023; Rezaei & Walkowska, 2024). Both were focused on deposits from New Jersey. As a result, there is no clear understanding which properties in particular drive the varying responses of glauconitic soils from different sites and formations. It has been suggested by Westgate et al. (2023) that formation type, glauconite age and maturity may play a role in material susceptibility to crushing with shearing. Therefore, these factors are outlined below to explore any potential correlations with the properties of Belgian glauconitic sands further in the report.

Please note that throughout the literature review, several terms are used for glauconite and glauconite-bearing deposits. The same general morphological group may be identified as glauconite (McRae, 1972; Logvinenko, 1982), greensand (Tedrow, 2002), glaucony (Odin & Matter, 1981), glauconite sand (Westgate et al., 2023), and glauconitic sand (Quinteros et al., 2023) or soil. Different terms had been introduced in an attempt to avoid confusion between designations for the green pellets composed of various other components in addition to mineral glauconite, and the mineral species itself (McRae, 1972; Odin & Matter, 1981). There is still no clear consensus on the appropriate terminology. In this report “glauconitic sand” will be the primary term. However, in literature review, the original nomenclature may be maintained.

Glauconite/Glauconitic Sand

Glauconite sand, also known as ‘greensand’, refers to a soil containing peloidal sand-sized grains primarily comprised of mineral glauconite, an iron- and potassium-rich 2:1 interlayer-deficient mica. The mineralogy of glauconite pellets, however, rarely consists of pure glauconite mica. Instead, they commonly contain intermixtures of non-expandable (illitic) and expandable (generally smectitic) layers. Layers of kaolinite or amorphous clay are rare. Glauconite deposits are often found in a sand-sized peloidal form, with other mineral constituents, such as quartz, feldspar, etc. (McRae, 1972; McConchie & Lewis, 1978; Adriaens et al., 2014; López-Quirós et al., 2020; Westgate et al., 2023).

Glauconite Formation

There are two general types of sedimentary glauconite: authigenic (in situ) and allogenic (detrital) (Logvinenko, 1982). An intermediate perigenic form may also be recognized for locally transported grains (McConchie & Lewis, 1978).

Authigenic glauconite is a secondary in nature deposit that requires transformation of substrate particles including those of foraminifera, faecal pellets, biogenic and abiogenic clasts (Odin & Matter, 1981; Fernández-Landero &

Fernández-Caliani, 2021) in the presence of other detrital minerals, or cation exchange between the existing clay minerals found in a substrate (McConchie & Lewis, 1978; Westgate et al., 2022). Such formation occurs in environments where the rate of sedimentation is low, and conditions are suboxic and semiconfined. The required combination of factors is typically encountered in shallow marine environments. Authigenic glauconite is also found in estuaries and lagoons, where it is usually only present in low abundance, and sometimes along the continental slope and in deep water settings where it is moved by slides, slumps, and turbidity currents. Its formation is known to occur at the sediment-water boundary and further maturation requires sufficient exposure, mainly limited to few centimeters below the seafloor in clays and about a meter in sands (Odin & Matter, 1981; McConchie & Lewis, 1978; Banerjee et al., 2020). If the sediment is buried deeper, the maturation process halts. However, its re-exposure can lead to reinitialization of the glauconization process (Huggett, 2013; Westgate et al., 2022). Compared to allogenic, grains of authigenic glauconite appear to be softer and may have lighter green/grey-green color (Logvinenko, 1982). Authigenic deposits generally have higher percent glauconite and classify as glauconite sand, which is the term used for sands with glauconite content (GC) exceeding 30 percent.

Allogenic glauconite appears to be more widely distributed and is derived through erosion of the ancient glauconite-bearing rocks and authigenic glauconite that is reworked, transported and redeposited. It has been encountered in the Atlantic, Pacific, Indian, and Arctic oceans, as well as many seas (Logvinenko, 1982). Physical transport of glauconite pellets leads to their abrasion and appearance of large amounts of fragmented grains, or even further disintegration resulting of formation of clay-sized glauconite material (Amorosi, 1997; Tedrow, 2002; Adriaens et al., 2014). Allogenic deposits can be composed of either glauconitic (with less than 30 percent GC) or glauconite sands (Westgate et al., 2023). It is worth noting that while such classification exists, the two terms (glauconite/glauconitic sand) appear to be used interchangeably. Please note that to avoid confusion, following literature review, the term “glauconitic sand” will be primarily used independent of the estimated GC.

Criteria for differentiation between the authigenic and allogenic/perigenic glauconites was previously suggested by Amorosi (1997) as shown in Table 2.1. However, their application may be challenging considering the highly variable morphology demonstrated in photographs from Triplehorn (1966) in Figure 2.16.

Table 2.1. Criteria for Differentiation of Autochthonous (Authigenic) from Allochthonous (Allogenic/Perigenic) Glaucony from Amorosi (1997)

Geological feature	Autochthonous glaucony	Allochthonous glaucony
Host formation	Marine deposits	Marine and non-marine deposits
Habit	Film and granular facies	Granular facies
Thickness of the glaucony-bearing interval	Commonly low (less than a few meters)	Highly variable
Spatial distribution of glaucony	Non-selective	Selective
Grain size distribution relative to that of the detrital components	Commonly independent	Commonly similar
Sorting	Commonly low	Commonly high
Roundness	Commonly low	Commonly high
Morphological features	Fractures commonly present	Fractures commonly absent
Association with phosphate grains and fish teeth	Common	Uncommon
Association with biogenic structures	Common	Uncommon

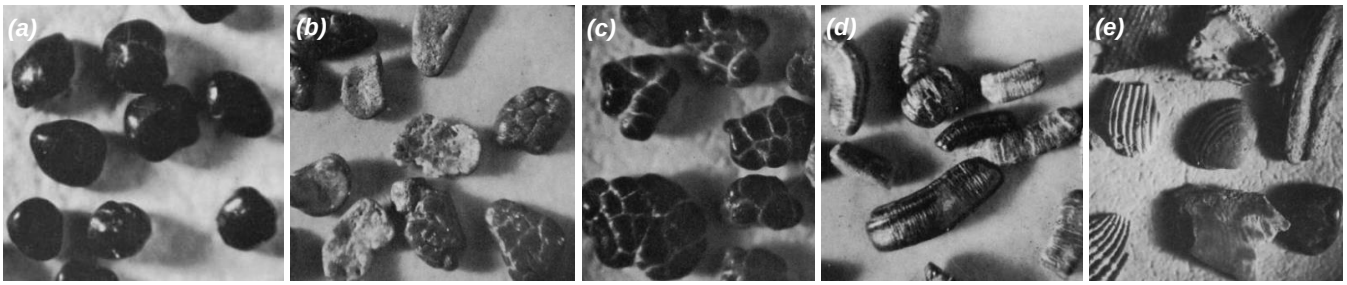

Figure 2.16. Glauconite Pellet Morphology Examples from Triplehorn (1966): (a) Spheroidal or Ovoidal Pellets; (b) Tabular or Discoidal Pellets; (c) Mammillated Pellets; (d) Vermicular Pellets; and (e) Fossil Replacements or Internal Molds

Glauconite Evolution

The time it takes for glauconite to form is still uncertain but presumed to vary from hundreds of thousands to a million years (Odin & Matter, 1981). For allogenic glauconites, the age has been estimated to range between 2 and 70 million years (Logvinenko, 1982).

The majority of glauconite formation (~73%) occurred within the last four Periods of Earth's history, namely the Quaternary, Neogene, Paleogene, and Cretaceous (Banerjee et al., 2016). The abundance of glaucony formation during certain geologic periods was associated with the warm climate and availability of suitable substrates. Noteworthy, faecal pellets and bioclasts are the most favorable substrates and comprise more than 76 percent of the overall record. Faecal pellets were also found to be the most favorable substrate for the evolution of glaucony, or glauconization.

A two-stage glauconization model (of the "precipitation-dissolution-recrystallization" theory) was proposed by Odin and Matter (1981). The model includes two major phases: (1) formation of a K-poor, Fe-rich glauconitic smectite and (2) gradual enrichment with K^+ (with intake from seawater above) leading to formation of a K-rich glauconitic mica. The degree of evolution, which as mentioned earlier, depends on the residence time of glauconite pellets in confined suboxic, partially reduced microenvironments, was thus classified primarily based on K_2O wt% (Odin & Matter, 1981; López-Quirós et al., 2020).

Four evolutionary morphological and chemical stages for glauconite formation were proposed to refine the model as shown in Figure 2.17 suggested by Obasi et al. (2011) based on work by Odin and Matter (1981). In this case iron concentration is not included as an index of glauconite maturity as it was concluded that iron intake (from the surrounding reactive detrital minerals) occurs mainly during the first stage of evolution. However, in other sources progression between glauconization stages is also accompanied by formation of ferric iron and decrease in aluminum (López-Quirós et al., 2020; Westgate et al., 2023).

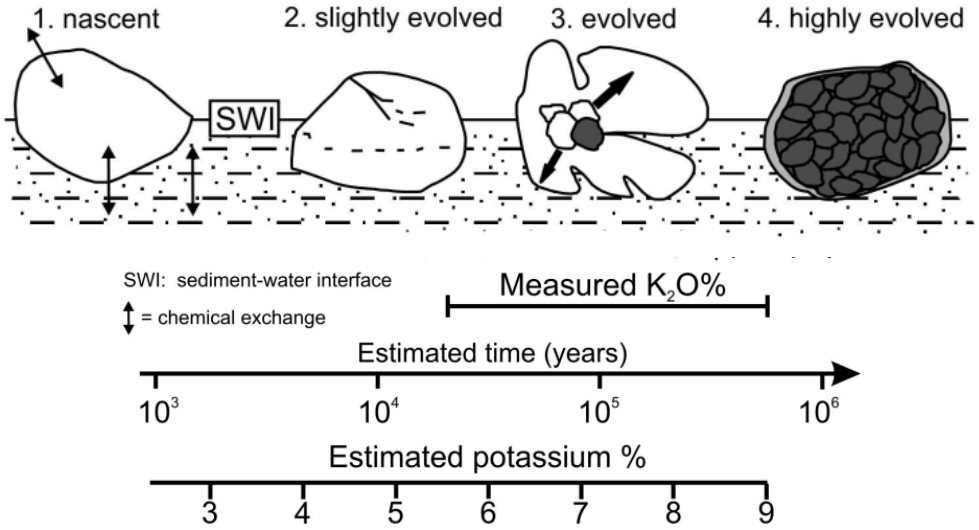

Figure 2.17. Glauconite Evolution Stages from Obasi et al. (2011)

As shown in Figure 2.17, the occurring oxidation, recrystallization, and the subsequent infilling of fissures and cracks can be recognized in particles that reached different stages of glauconite evolution. In many cases the degree of evolution can be recognized by color and texture as demonstrated in Figure 2.18. The nascent particles are light green, while the subsequent evolution results in development of a darker green color until polished black is reached at highly evolved stages. Noteworthy, glauconitic sands may be initially brownish if coated with iron oxide, which means that identification of glauconite by color alone may be misleading (McRae, 1972; Fernández-Landero & Fernández-Caliani, 2021; Quinteros et al., 2023). In addition to the observed color changes, angularity, size, and microporosity of glauconite pellets appear to increase with maturity (Odin & Matter, 1981; Westgate et al., 2022)

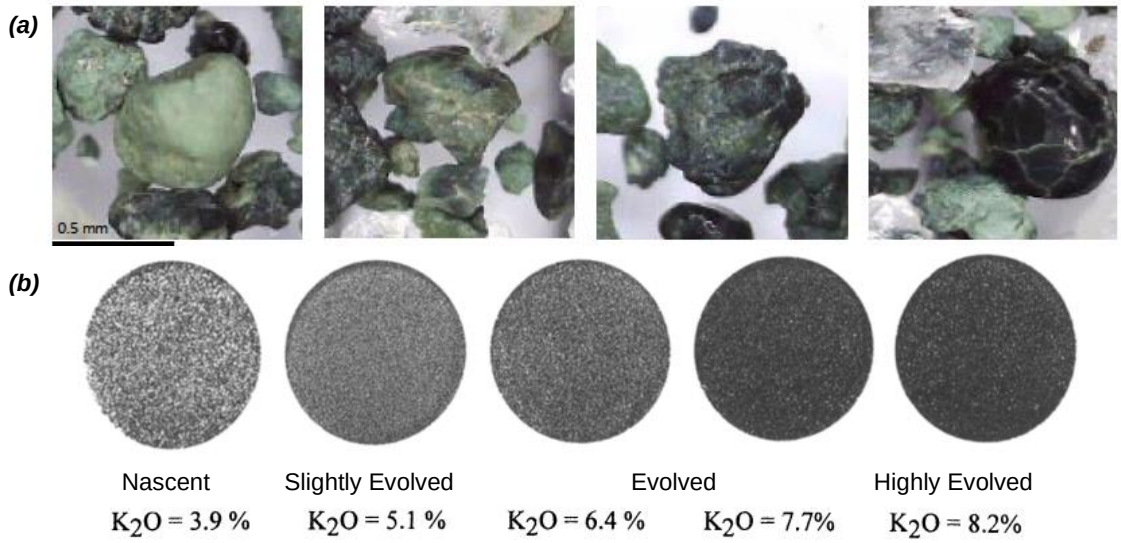

Figure 2.18. (a) Glauconite Evolution Based on Color and Texture from Westgate et al. (2022); (b) Changes in Superficial Color (Light to Dark Green) of Glaucony as a Function of Maturity of Grains from Amorosi (1997)

The degree of evolution may also be recognized based on the observed nanostructure as shown in Figure 2.19 (Odin & Matter, 1981; Wigley & Compton, 2007). Finally, in addition to the chemical, mineralogical, and visual inspection methods, maturity identification can be made based on magnetic characterization of glauconite pellets. With the use of a magnetic separator, glauconite pellets can be classified based on their paramagnetic susceptibility, which appears to be directly correlated with the K_2O content (Amorosi, 1997), confirming the increase in Fe_2O_3 concentration with maturity, as suggested by López-Quirós et al. (2020).

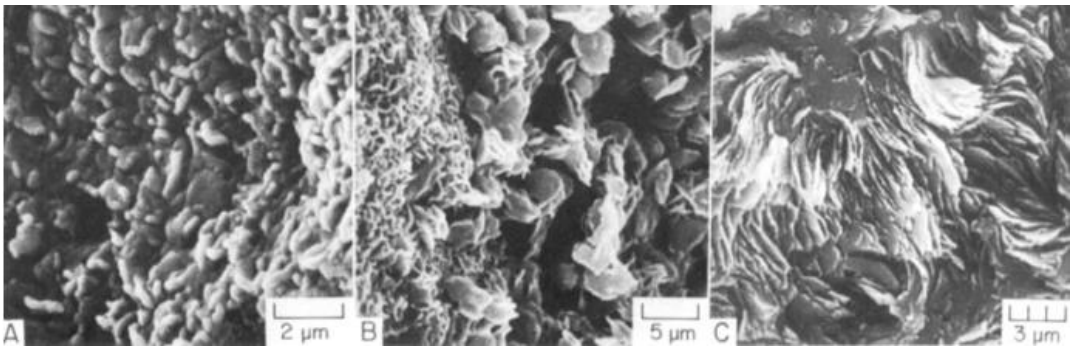

Figure 2.19. SEM Photomicrographs Showing the Main Types of Nanostructure of Glaucony: (A) Ill-defined globules and caterpillar structures typical of nascent glaucony (4% K_2O); (B) Boxwork and rosette structures of evolved glaucony (6.5% K_2O); and (C) Lamellar structure of highly evolved glaucony (8% K_2O); from Odin and Matter (1981)

As noted by Odin and Matter (1981), glauconitic grains within a bed are likely to be derived from different parent materials represented by several stages of glauconization. Thus, in a bulk analysis of a glauconitic sand, even if separated from other deposit constituents, authigenic glauconitic pellets are likely to be of varying maturity and mixed with the initial substrates. Fissures, cracks, and surface coatings observed in pellets may also incorporate trapped impurities.

Index and Mechanical Properties of Glauconitic Sands

Based on the literature review, glauconite pellet size (or median grain size) usually varies between about 100 and 500 µm (McRae, 1972; Odin & Matter, 1981; Amorosi, 1997). In some deposits, abundance of fine-grained glaucony in clay and/or silt-size range is known to be added through fragmentation of larger grains with transport (Amorosi,

1997; Adriaens et al., 2014). The separated glauconite fraction can be well or poorly graded, likely depending on the level of experienced abrasion (Adriaens et al., 2014; Westgate et al., 2023).

The Atterberg limits of glauconitic fines have not been widely studied. Based on results provided for New Jersey glauconite-dominated soils, in natural state they were either nonplastic or exhibited low to medium plasticity, if sufficient clay-sized fraction was naturally present in the deposit (Westgate et al., 2023; Rezaei & Walkowska, 2024).

Glauconite hardness measured on the Mohs scale was found to be around 2 (McRae, 1972; Van Raak, 2009; Westgate et al., 2022), although it may vary with microporosity and, thus, maturity of glauconite. This commonly reported value corresponds to the hardness level expected of gypsum, calcite, muscovite and biotite mica (Mitchell & Soga, 2005). Quartz commonly encountered in glauconitic sands shows hardness of about 7 on Mohs scale. Specific gravity of glauconite was found to range between 2.3 and 3.1 depending on its mineralogical composition (McRae, 1972; Odin & Matter, 1981; Van Raak, 2009; Westgate et al., 2022; Westgate et al., 2023; Piedrabuena, 2024).

During the literature review, several sources assessing the crushability of glauconite were encountered. However, due to the strong dependence of results on factors like glauconite content and preparation methods (details often missing from the reports) these studies will not be discussed in detail. In general, in some cases, glauconite exhibited crushability greater than that observed for calcareous and carbonate sands (Emidio et al., 2009; Westgate et al., 2023).

Glauconitic Sand as a Challenging Deposit for Pile Design

The limited availability of geotechnical data on glauconitic sands is associated with their challenging evaluation using in-situ investigation methods. Cone penetration testing (CPT) in glauconite and glauconitic sands result in a combination of high cone tip resistance (q_t) typical for sands, and high sleeve friction (f_s), which is expected of clays. The latter is caused by reworking of highly crushable glauconite pellets into fine-grained material with the deeper advancement of the cone and friction sleeve. The resulting friction ratio ($R_f = f_s/q_t$) can reach and exceed 10 percent, which falls outside of the boundaries of Robertson's SBTn (normalized soil behavior type) charts and makes CPT-based characterization of glauconite-bearing deposits complicated (Joustra & de Gijt, 1985; Van Raak, 2009; Robertson & Cabal, 2022; Westgate et al., 2023; Piedrabuena, 2024). The combined action of high tip resistance and sleeve friction is also likely to result in refusal of the cone.

The same combination of factors, namely the high tip resistance dominated by sand-sized fraction below the crushing zone and high shaft resistance caused by the addition of fines from degraded glauconite pellets within the interface shearing zone (shown in Figure 2.20), leads to the high soil resistance to driving. This, together with the strong thixotropy of degraded glauconitic sands causing pile-soil setup during redrives, increased risk of early pile refusals, and potentially complicated pile extraction, makes glauconite-bearing soils a challenging deposit for pile installations (Westgate et al., 2023; Westgate et al., 2024).

Figure 2.20. Glauconite Sand Degradation due to Drilling and Pile Driving from Westgate et al. (2023; 2024)

Noteworthy, drivability issues have been reported for glauconitic sands with relatively low GC. Presence of glauconite was shown to increase driving resistance in the North Sea (Perikleous et al., 2023) where GC did not exceed 20 percent and in proximity of Antwerp, Belgium (de Nijs et al., 2015), where GC is expected to be around 50 percent on average (Adriaens et al., 2014).

Other design aspects associated with the glauconite degradation and performance of piles during loading stage, such as the long-term axial capacity, and lateral pile-soil stiffness, are yet to be addressed in the ongoing Piling in Glauconitic Sand Joint Industry Project (JIP) (Westgate et al., 2024).

Previous Studies on Geotechnical Behavior of Glauconitic Sands

Effects of degradation on geotechnical behavior of glauconitic sands have mainly been studied on samples collected from New Jersey deposits with a high glauconite content (exceeding 85 percent) (Westgate et al., 2023; Quinteros et al., 2023; Westgate et al., 2024; Rezaei & Walkowska, 2024).

Various particle degradation methods, such as hand griding, Proctor testing, ball milling, and dispersion in a stirring apparatus have been assessed to investigate their effect on clay fraction and added fines content. The last method, dispersion in water, appeared to result in the most drastic change of material, and showed a significant transition from sand to clay, increase in plasticity, reduction is shear strength (soil-to-soil and interface) and increase in thixotropic hardening (Westgate et al., 2023). Drying of the sample appeared to exacerbate the effects of degradation. However, in degradation through dispersion duration of mixing was a dominant factor. In laboratory studies by Westgate et al. (2023) it varied between less than 1 minute and 8 hours, while samples recovered from the shaft in recent pile tests (Westgate et al., 2024) showed an increase in fines content corresponding to that achieved with 1 to 10 minutes of stirring. It is worth noting that this may be a lower estimate of degradation due to sampling limitations and the fact that a sufficient quantity of material could not be gathered immediately adjacent to the pile wall (Westgate et al., 2024).

Considering dispersion periods of up to 8 hours, the maximum addition of clay content recorded for the four New Jersey samples from different stratigraphic units ranged from 26 to more than 80 percent. Plasticity index (PI) and liquid limit (LL) increased by up to 42 and 47 percent, respectively. Clay activity either increased or remained at the initial level estimated for natural/uncrushed samples. Several tests indicated high thixotropy ratios that exceeded the range typical for most marine clays. The degree of change in index properties, and by extension, shear strength of the soil appeared to be dependent on glauconite age and maturity as well as the depositional environment (Westgate et al., 2023).

Direct shear and interface direct shear tests performed on New Jersey samples showed a significant effect of specimen degradation. Both the peak and residual shear stress ratios reduced significantly with the increased dispersion time, exhibiting behavior typical for clays. Tested specimens showed increasing strain softening behavior with continued dispersion. The derived residual interface friction angles (with failure envelope passing through the origin) for glauconitic sand sheared along a steel plate with R_a = 5 µm ranged from 21 degrees for natural specimens to 12 degrees for highly degraded. The angles of internal friction decreased from 31 to 18 degrees. All tests were conducted with a constant normal stress of 150 kPa with shear rates targeting drained conditions. (Westgate et al., 2023). Interface direct shear test results provided by Westgate et al. (2023) are shown in Figure 2.21.

In addition to results from the systematic study carried out by Westgate et al. (2023), interface ring shear test results have been published by Quinteros et al. (2023). The ring shear study showed that the residual interface friction angle decreased with the increasing fines content, glauconite content, and vertical effective stress. Across all conditions tested, values of δ_{res} derived for natural and pre-crushed glauconitic sands were consistently lower than 29 degrees recommended for design of piles driven in sand (Lehane et al., 2020; Quinteros et al., 2023).

Results for cyclic direct shear tests on New Jersey glauconite sands by Rezaei and Walkowska (2024) as well as the calibration chamber pile tests on Belgium glauconitic soil by Piedrabuena (2024) became available during the execution of experimental work for the given project. They will be referenced and discussed when applicable throughout the report.

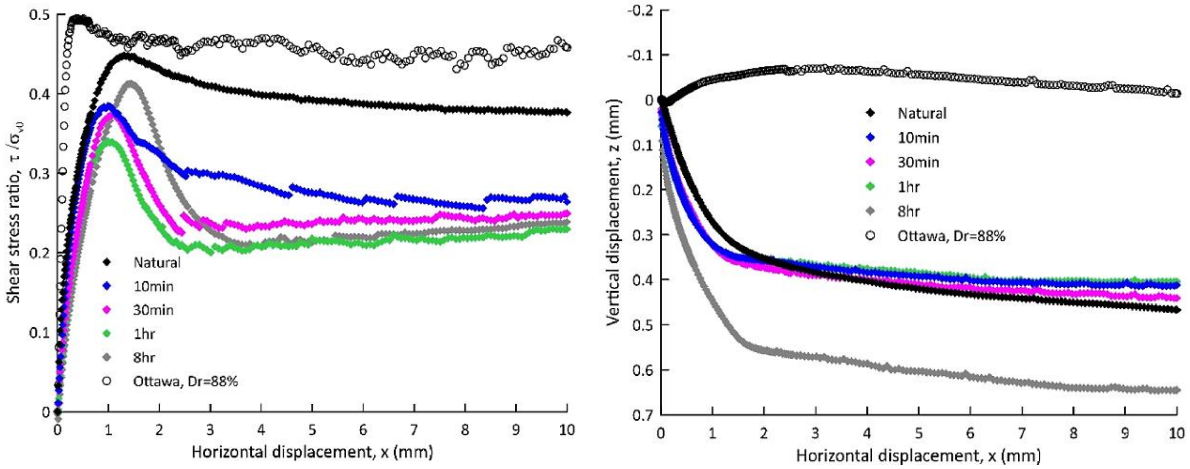

Figure 2.21. Direct Interface Shear Test Results on New Jersey Sewell Hornerstown Glauconitic Sand Sample from Westgate et al. (2023)

3 Belgian Glauconitic Sands

This section introduces the materials characterized in the project, outlining the geologic setting and summarizing key information about the studied deposits from available literature.

3.1 Leuven Sample – Diest Formation

The Diest Formation glauconitic sand was recovered from the Kesselberg in proximity of Leuven, Belgium. This material, the primary focus of the performed experimental program, will be referred to as the Leuven sample.

Geologic Background – Diest Formation

The Kesselberg is an elongated 75-meter-high hill located northeast of Leuven, Belgium. It is a part of a continuous row of Diestiaan hills typical for the Hageland region. According to the description of Kesselberg as a heritage object of Flanders, the subsurface in this area consists of a heterogeneous, glauconite-rich green to brown sand with limonite concretions from fossil soil formations and podzolic soil development. This subsurface stratum is recognized as part of the Diest Formation (Immovable Heritage Agency, 2014).

While the exact coordinates of glauconitic sand recovery are unknown, based on the Geologic Model for Flanders (GDI Flanders, 2024) as shown in Figure 3.1, Diest Formation (Hageland Diest Sand) is the most probable origin for this material. Unfortunately, no CPT data, which could provide stratigraphic interpretation for the area and show signatures characteristic of glauconite-bearing soils (as mentioned in the literature review), are available for the area identified in Figure 3.1.

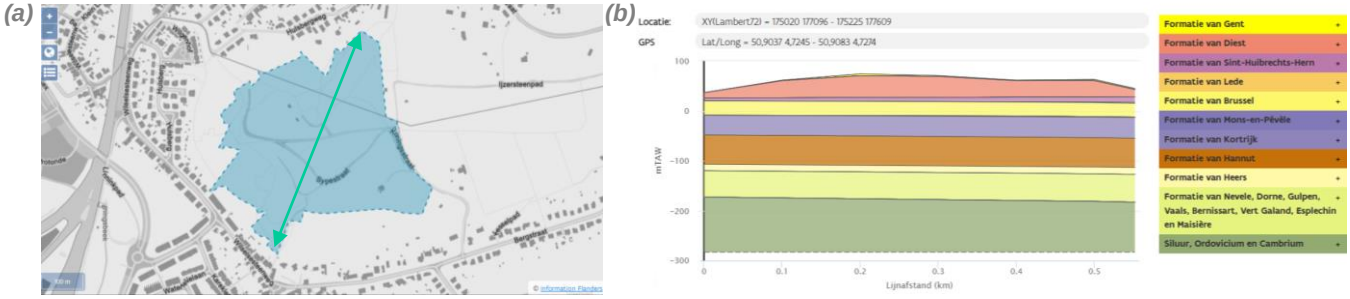

Figure 3.1. (a) Kesselberg Area and Cross-Section Location (Immovable Heritage Agency, 2014) and (b) Geologic 3D Model v3.1 (GDI Flanders, 2024)

The Diest Formation is a Neogene deposit in northeastern Belgium containing greyish green to brownish green locally clayey fine to coarse-grained glauconiferous sand. It is a marine deposit connected to the southern North Sea Basin and belonging to the late Miocene Tortonian (11.6 – 7.2 Ma) and earliest Messinian Age (7.2 – 5.3 Ma) (Houthuys et al., 2020). The Diest Formation was exposed to fully marine conditions that yield the anoxic environment necessary for the large amount of Fe and K uptake in its glauconitic structure (Adriaens et al., 2014).

The extent of the Diest Formation with the inclusion of Keselberg is shown in the outcrop and subcrop map in Figure 3.2. This figure also includes Kasterlee Sand and Kattendijk Sand units that represent two successive marine or marginal marine sedimentary deposits postdating the Diest Formation: the upper Miocene Kasterlee Formation and the lower Pliocene Kattendijk Formation (Houthuys et al., 2020). Glauconitic sand from the latter has recently been studied at TU Delft (Piedrabuena, 2024) in collaboration with Deltares. To support findings of the given project, this material was also tested for comparison with the Leuven sand results. A general description of this sample and its origin can be found in Section 3.2.

According to the 2020 review (Houthuys et al., 2020), the Diest Formation is dominated by poorly sorted very glauconiferous quartz sand with the median grain size mostly above 250-300 µm, approaching 500 µm locally. On average, glauconite pellets constitute between 35 and 40 percent of the deposit, with values up to 60 percent identified locally. These pellets are slightly finer than the quartz grains, pointing towards their higher weight allowing them to be transported along with the coarser quartz particles. The glauconite pellets in the Diest Formation appear

to be reworked based on comparison of K/Ar dating and age determination using micropaleontology (Houthuys et al., 2020). This observation is supported by Adriaens et al. (2014) who note that Diest sands show similar particle size distribution between the separated glauconite pellets and the remainder of the tested material, pointing towards the simultaneous transport of glauconites and detrital particles and indicating that the authigenic potential of glauconite is very low. Allogenic deposition would also explain the origin of large amounts of clay-sized glauconite in Hageland sands as the product of abrasion of glauconite pellets transported together with the harder quartz grains (Adriaens et al., 2014).

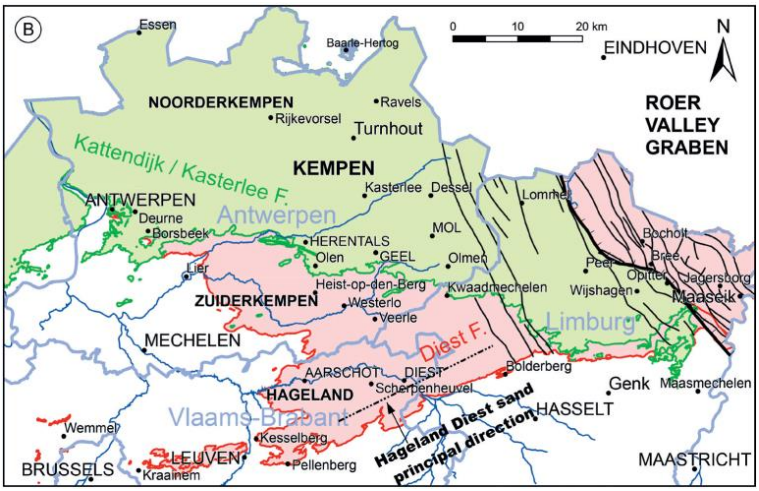

Figure 3.2. Diest Formation Outcrop and Subcrop Area (subcrop covered by the Kasterlee Formation) from Houthuys et al. (2020).

It is worth the note that due to the elevated topographic position of outcrops in Hageland (Kesselberg included), quartz grains often have limonite coating and glauconite pellets can be oxidized and altered at the surface. Due to the prolonged exposure to extensive oxidation, glauconitic sand has locally been altered from greyish green to brown colored (Houthuys et al., 2020).

Leuven Sample

Approximately 20 kilograms total of glauconitic sand in bulk were received from NGI in February and May 2024. The surficial material was gathered at the Kesselberg Diest Formation outcrop as shown in Figure 3.3. The sample was kindly provided by Bruno Stuyts from Ghent University for testing as part of the ongoing collaboration to investigate the behavior of glauconitic soils.

Figure 3.3. Leuven Sand Recovery Location (provided by Ghent University Professor Bruno Stuyts)

In its natural state shown in the left-most image of Figure 3.4 the received sample appeared to consist of primarily fine sand with some fines, and some gravel. When worked in hands, it developed a rather sticky texture.

Closer look at the gravel-sized fraction shown in the central and rightmost pictures of Figure 3.4, revealed that it consists of agglomerates of sand grains with the iron oxide coloring appearing inside the easily broken clumps. The as-received sample had a strong organic odor and included roots and tree bark pieces. Visible plant matter and iron-cemented clumps have been removed from the sample prior to carrying out the experimental program discussed further in the report.

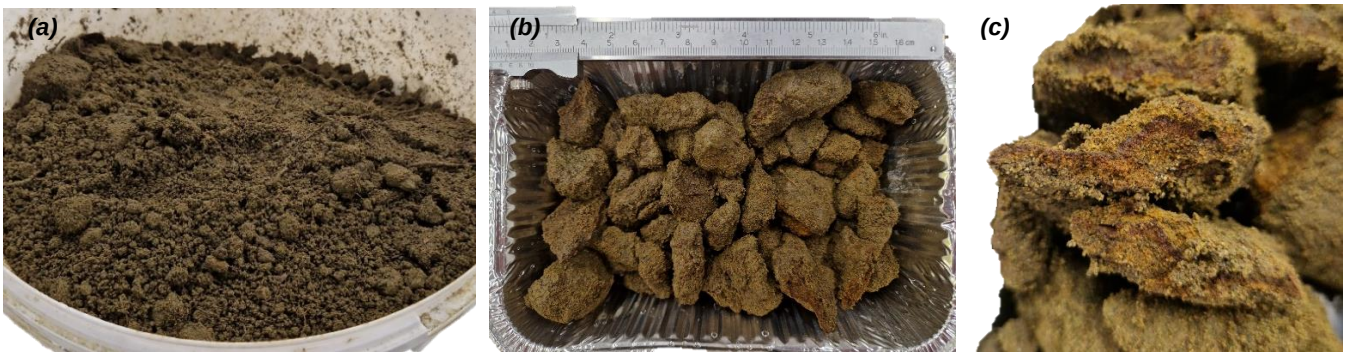

Figure 3.4. Leuven Sand Sample: (a) Full Fraction and (b-c) Oxidized Agglomerates

3.2 Antwerp Sample – Kattendijk Formation

This subsection provides a general description of the Kattendijk Formation sample kindly provided by Deltares to supplement results obtained for the Diest Formation (Leuven) glauconitic sand. Further information on this material can be found in the 2024 TU Delft master thesis by Piedrabuena (2024).

Geologic Background – Kattendijk Formation

The Neogene glauconite-bearing sands of the Kattendijk Formation, the extent of which is shown in Figure 3.2, were deposited during the early Pliocene (Zanclean; 5.3 – 3.6 Ma (Adriaens et al., 2014)), in a shallow marine environment of the southern part of the North Sea Basin. This unit has an average thickness of 10 meters and consists of fine- to medium-grained glauconitic sands with a varying clay fraction. The color of its deposits varies from dark grey to greenish grey. Glauconite content within the formation seems to reach up to 30 percent. The unit includes mollusks and brachiopods that appear either dispersed or in concentrated layers and basal gravel consisting of rounded quartz, flint, shark teeth, phosphatic nodules, and bones (Deckers & Louwye, 2020).

Antwerp Sample

The glauconitic sand belonging to the Kattendijk Formation was recovered from the Oosterweel connection project in Antwerp, Belgium (Piedrabuena, 2024). Two buckets of this air-dried sample were provided by Deltares in May 2024. The received material is shown below in Figure 3.5.

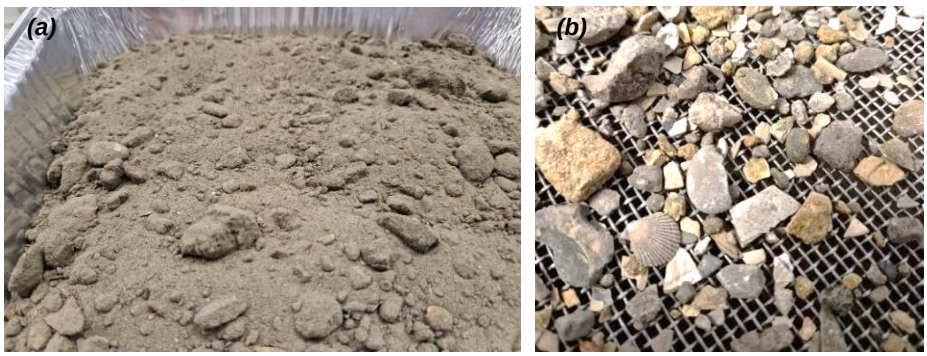

Figure 3.5. Antwerp Sand Sample: (a) Full Fraction and (b) Gravel Fraction

4 Experimental Methods and Program Overview

This section provides an overview of the implemented experimental methods and summarizes laboratory testing program carried out to support the glauconitic sand interface shear strength characterization. Detailed test results are provided and discussed in Sections 5 and 6.

4.1 Experimental Program Overview

Characterization methods included in this project were implemented following the experimental outline provided in Figure 4.1. The program was divided into two main parts. The first sequence was focused on glauconitic sand as found in situ, in its natural state. The second part included tests aimed to assess the degraded glauconitic sand in an attempt to characterize it as if it was reworked along a driven pile shaft, with the added fines content and increased plasticity.

Both experimental subsets included standard geotechnical index tests to determine physical properties of the natural and degraded soil. Mechanical tests assessed the glauconitic sand-steel interface shear strength and behavior in both states. Selective textural and mineralogical (comprehensive) characterization enhanced understanding of the material as well as the changes accompanying shearing and identified glauconite properties as a reference point for future research.

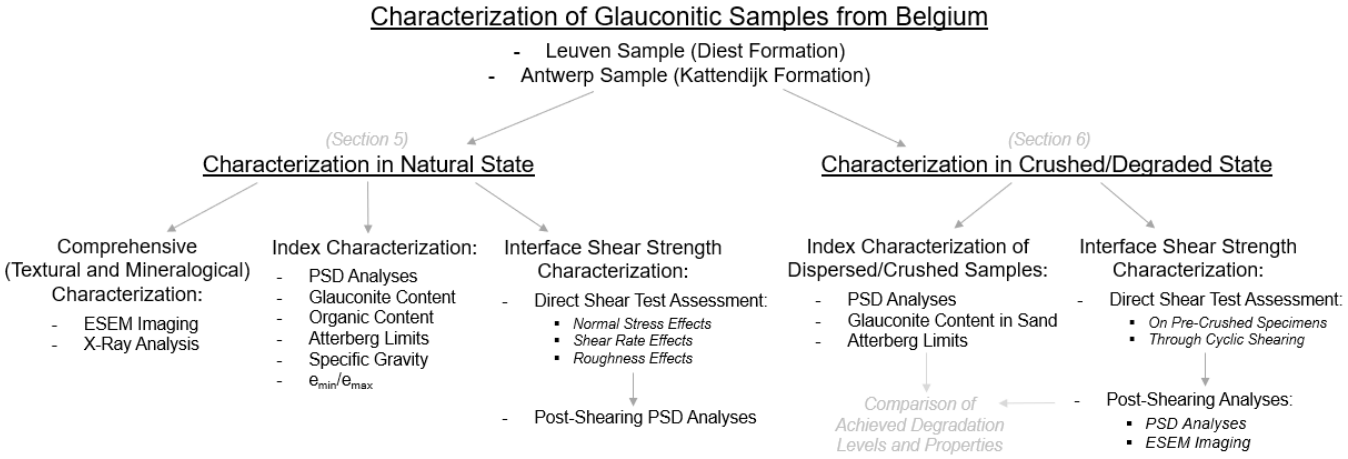

Figure 4.1. Experimental Program Outline

4.2 Comprehensive Glauconite Characterization Methods

To incorporate index and shear strength test results in the growing database on glauconitic sands and compare its characteristics with similar materials from New Jersey, North Sea, and other known sites of greensand deposition, it is important to consider its morphology, chemical composition, and mineralogical properties. Such characterization can be used to assess the corresponding glauconization stage, potential particle breakability, and for reasoning behind certain mechanical properties (e.g., plasticity, specific gravity, hardness, etc.) of the tested glauconite samples. Primary methods implemented to support this evaluation are summarized below.

Digital Microscopy

To provide fast and clear visualization of particles comprising the assessed material, digital microscopy was included in the program. It was primarily carried out with the use of a Leica digital microscope camera and, selectively, Keyence VHX-series digital microscope available at the faculty of Civil Engineering and Geosciences at TU Delft. No specific sample preparation was needed for this type of imaging. To achieve a higher magnification level and resolve fine structural details, scanning electron microscopy imaging was considered in addition to the digital as discussed below.

ESEM Analysis

Environmental scanning electron microscopy (ESEM) was implemented to take a closer look into the glauconite pellet structure and chemical composition of individual particles, allowing for their potential rough classification in terms of maturity and morphology. Imaging was completed with the use of FEI Quanta 50 FEG field emission scanning electron microscope available at the Microlab in the faculty of Civil Engineering and Geosciences. In addition to the high-resolution imaging, this setup allows for chemical analyses via energy-dispersive X-ray spectroscopy (EDX) (FEI, 2012). The ESEM system and glauconitic sand samples loaded in the specimen chamber are shown in Figure 4.2.

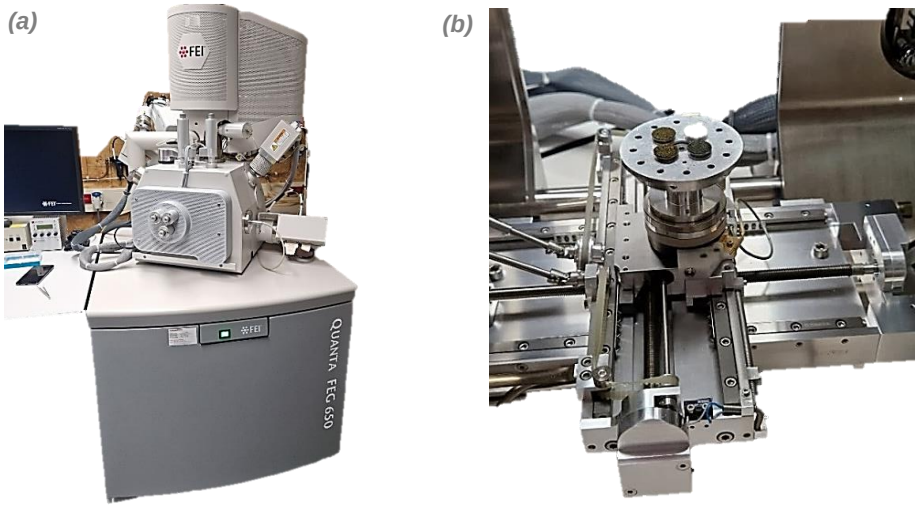

Figure 4.2. (a) ESEM Quanta FEG 650 and (b) Specimen Chamber

The ESEM is a scanning electron microscope (SEM) that allows for collection of electron micrographs for uncoated and wet specimens. It operates by projecting a focused beam of electrons onto the sample, where the beam interacts with the surface to produce backscattered and secondary electrons, which are used for high-resolution imaging. Additionally, the interaction generates characteristic X-rays (for each element with the exception of H and He) that enable elemental analyses through EDX. This combined imaging and elemental data provided by the ESEM enhance geo-engineering analyses, offering more in-depth information than digital microscopy alone (Welton, 2003; FEI, 2012; Goldstein et al., 2018).

To prepare natural sand specimens for the ESEM, the oven-dried full fraction was washed over the No. 200 (0.075-mm) sieve with demineralized water until the washings ran clear. The sample was then oven-dried again for 5 to 6 rounds of magnetic separation as explained in Section 4.3. Separated glauconite pellets were soaked in 1 M HCl solution for about 2 minutes to remove calcite coating visible in preliminary images (Figure 4.3) taken with the Keyence VHX-series digital microscope available in the Microlab. The pre-treatment solution was carefully washed off with a large volume of demineralized water. Samples were then oven-dried and left to cool in a desiccator. Extra care was taken to avoid any grease/oil contamination.

In the case of analyses carried out on magnetically separated uncrushed glauconite fraction, high-resolution imaging was accompanied by point element (EDX) analyses that were manually assigned to particles of varying topography and abrasion or fracturing level.

Additional ESEM imaging was carried out on degraded specimens of glauconitic sand subjected to shearing or dispersion and mixing for Atterberg limit tests (4.3). In this case, their moisture content was brough to a level above plastic limit with the addition of demineralized water to allow for proper mixing of a previously separated material. Moist samples were placed in the chamber for imaging with the moisture evaporating under vacuum conditions.

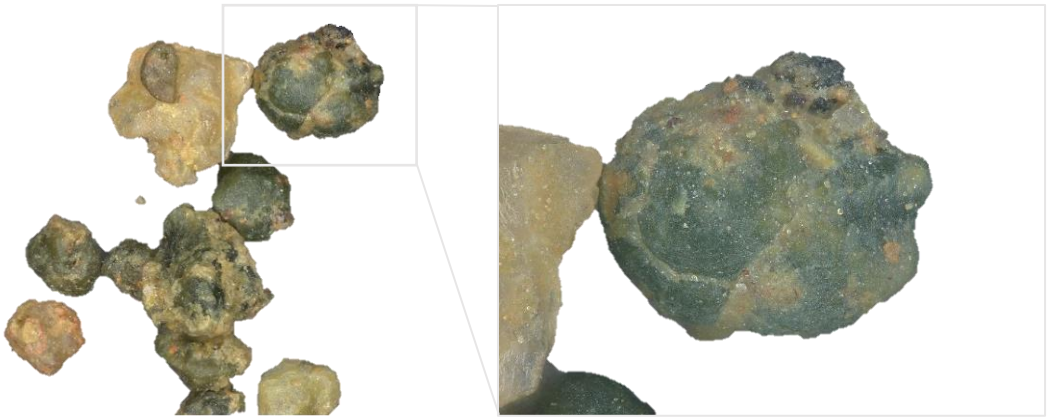

Figure 4.3. Digital Microscope Images of Glauconitic Sand Particles without the 1 M HCl Pre-treatment

X-Ray (XRD-XRF) Analysis

While selective point element method (EDX) was used as part of the ESEM, it would not allow for a bulk phase, structure, and elemental assessment achievable with the X-ray Diffraction (XRD) and X-ray Fluorescence (XRF) techniques. Therefore, additional X-ray analyses were included in the experimental program for comparison with published results on glauconitic sands from various formations (Adriaens et al., 2014; Westgate et al., 2023; Piedrabuena, 2024) and identification of mineralogical properties that could potentially affect the observed shearing behavior.

XRD is a non-destructive technique used to determine phase composition, crystal structure, and orientation of a material. In this method, a finely ground sample is placed in an instrument containing an X-ray source, sample holder, and detector. As the X-ray source and detector (or the sample stage and detector) move in sync, X-rays interact with the atomic planes of the sample, varying the angle 2θ between the incident and diffracted X-ray beams. Constructive interference occurs at specific angles (2θ), satisfying Bragg's Law. This interference produces distinct diffraction peaks, with 2θ positions corresponding to atomic plane spacings (d-spacings) in the crystal lattice. The diffraction pattern, where peak intensities generally indicate the quantity of crystallites with specific orientations and spacings, is then compared to reference databases for phase identification (Malvern Panalytical, 2024; ICDD, 2024; Iowa State University, 2024; Dinnebier & Billinge, 2008).

As a complementary method, XRF analyzes the chemical composition of a sample. High-energy X-rays excite the atoms in the sample, ejecting inner-shell electrons and creating an unstable state. When outer-shell electrons fill the vacancies, they emit X-rays characteristic to each element, allowing for the quantification of elemental abundances in the sample (Malvern Panalytical, 2024; Bruker, 2024).

The X-ray analyses for the given project were performed by Ruud Hendrikx at the Department of Materials Science and Engineering of the Delft University of Technology. The XRD was carried out using Bruker D8 Advance (Bruker, 2024) diffractometer (shown in Figure 4.4a) with Bragg-Brentano geometry. Phase identification was completed with the reference to ICDD PDF-5 (2024) and COD (2024) databases. The complementary XRF analysis was performed with the Panalytical Axios Max WD-XRF Spectrometer (Malvern Panalytical, 2024) shown in Figure 4.4b. Further instrumentation and sample preparation details can be found in a detailed X-Ray Facilities Group report provided in Appendix A.

The analyses at TU Delft focused on the Leuven sand sample, as Antwerp sand specimens had already been assessed at Qmineral as part of the graduation project by Piedrabuena (2024). Although comparable oxide weight percentages for maturity estimation were initially expected from both laboratories, direct comparison proved challenging due to varying glauconite content in the unseparated samples. To evaluate consistency in interpretation, XRD analysis was also conducted on the Antwerp samples at TU Delft, revealing significant mineralogical discrepancies compared to the Qmineral report. Despite uncertainties and limitations related to operator's technique and interpretation, the X-ray analysis results will be documented in Section 5.1 for future reference.

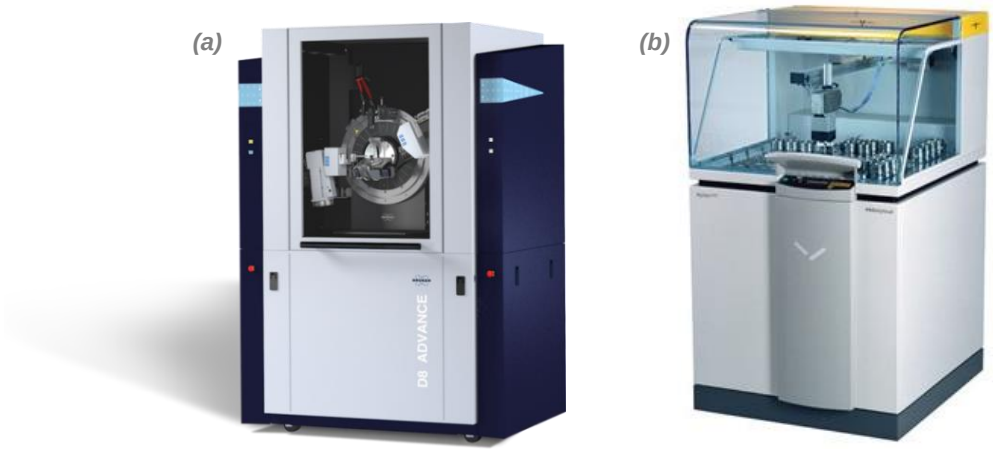

Figure 4.4. (a) Bruker D8 Advance X-Ray Diffractometer (Bruker, 2024) and (b) Panalytical Axios Max WD-XRF Spectrometer (Malvern Panalytical, 2024)

4.3 Index Test Characterization Methods

To support interface shear strength characterization and improve general understanding of the assessed material, a series of standard index tests was added to the experimental program. In addition to evaluating properties of glauconitic sands as found in-situ, it was important to consider how they would change between various sample preparation methods and with degradation of glauconitic pellets accompanying shearing. This subsection provides an overview of the methods implemented to achieve this. Index testing results for the natural and degraded samples are provided in Sections 5.2 and 6.1, respectively.

Particle Size Distribution (PSD)

As mentioned in the literature review of Section 2, gradation characteristics play an important role in soil-structure interaction. Considering the tendency of glauconitic sands to transform from coarse- to fine-grained soil with shearing, assessment of particle size distribution (PSD) is especially important for their characterization in both the natural and degraded states. Thus, PSD analyses were a crucial part of the discussed experimental program.

The primary particle size distribution analyses were carried out in accordance with ASTM D422 (ASTM, 2007), in which distribution of particle sizes larger than 75 μm is determined by sieving and PSD of the fraction smaller than 75 μm is assessed using hydrometer method based on Stoke's law governing the rate of sedimentation of particles suspended in water. The ASTM D422 analyses were performed focusing on fraction passing the No. 10 (2-mm) sieve (about 80 percent of total mass). The coarser portion of the PSD curve was not considered due to the limited quantity of soil available for testing. It was presumed that particle size distribution for the full fraction would not be representative of the sampled sand unless several kilograms of material were to be used to account for the nominal diameter of the largest particles exceeding 20 mm. Additionally, PSD results for the coarser fraction could be highly affected by clumping occurring with oven-drying of glauconitic soils and by the varying degree of agglomerate breakage (see Figure 3.4) accompanying dry sieving.

Following ASTM D422 for sandy samples, soil oven-dried at 105°C was separated on sieve No. 10. A 100-gram sample finer than 2 mm was then soaked in hexametaphosphate solution for at least 16 hours, dispersed in a stirring apparatus, and subjected to hydrometer testing. After the 24-hour reading, soil mixture was washed over the No. 200 (75-μm) sieve to remove the fines fraction. The retained portion of the sample was oven-dried and used for the dry sieve analysis to obtain a full PSD curve between the 0.001- and 2-mm grain sizes.

Figure 4.5 shows the setup for the ASTM D422 PSD analyses. Dispersion was completed using Hamilton Beach Scovill single spindle mixer on a medium setting. The fine fraction PSD was determined with the use of the ASTM hydrometer 151H. Dry sieving was carried out with a Haver & Boecker Haver EML Digital Plus sieve shaker and a standard set of square-mesh sieves. Each run was 10 minutes long with the amplitude maintained at 1 mm.

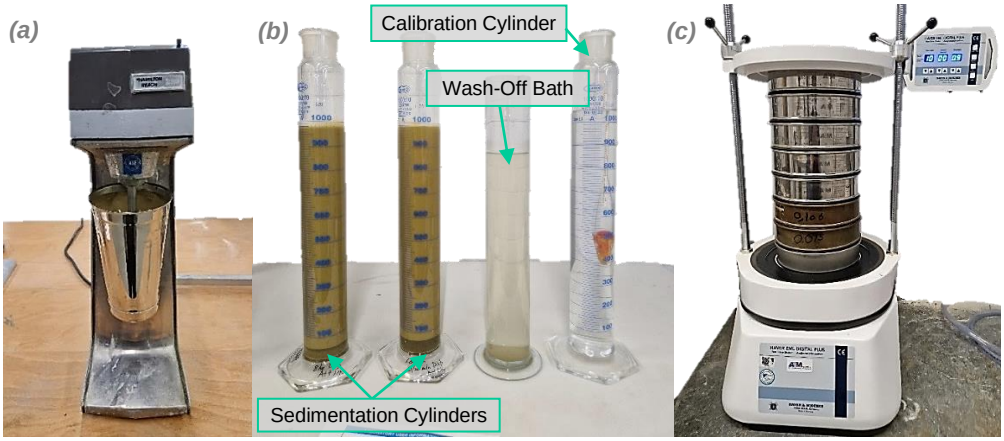

Figure 4.5. ASTM D422 Analysis: (a) Dispersion Mixer; (b) Hydrometer Test; and (c) Sieve Shaker with the Sieve Column

Supplementary PSD analyses were performed with the Microtrac BlueWave Particle Size Analyzer available at the Water Lab of the faculty of Civil Engineering and Geosciences of TU Delft. This laser diffraction method was preferred in cases when material quantity was insufficient for the standard ASTM D422 procedure. In particular, knowing that a specimen in interface direct shear tests (see Section 4.4 for the procedure) required 50 grams of dry sand, and that about 100 grams are needed for the analysis of a sandy specimen in accordance with ASTM D422, another testing method was necessary to evaluate gradation changes of an even smaller shear zone. In case of the implemented laser diffraction method, 2 grams of material would be enough to obtain a proper grain size distribution. The interface sample collection process is discussed further in Subsection 4.4.

The Microtrac BlueWave PSD analyzer (shown in Figure 4.6) utilizes light scattering technology, measures particle size from 0.01 to 2800 μm, and allows for calculations for non-spherical particles through the principle of Modified Mie calculations. The tri-laser system enables light-scattering measurements using three lasers and two fixed detector arrays. It features a sample circuit system with adjustable pump speed that allows for controllable homogenization and dispersion of the tested sample depending on its viscosity and sedimentation. When the light is diffracted by an ensemble of particles in the sample, the maxima and minima of the combined diffraction pattern are recorded by the detectors. An inversion algorithm is applied to separate the patterns that are then used for particle size distribution calculations via the system software (Microtrac, 2024).

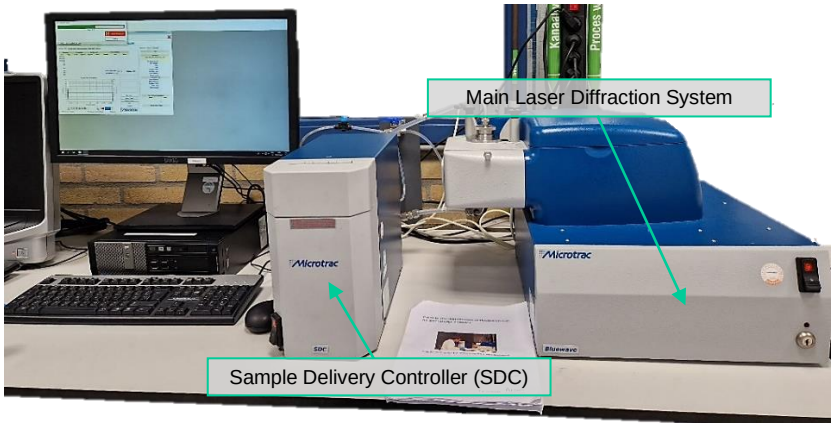

Figure 4.6. Microtrac BlueWave PSD Analyzer

It is important to note that results of the laser diffraction tests providing measurements by volume cannot be directly compared to the combined sieve and hydrometer output in percentages by weight. They may also vary depending on the user input settings. In the case of heterogeneous materials like glauconitic sand, flow rate for the sample circuit system may either be too low to capture the heavier sand-sized particles or too high to allow for the fine

fraction to be fully detected. Relying on comparison with the analogous tests carried out on the Antwerp sample at Deltares (Piedrabuena, 2024) and typical particle size distribution curves for both the evaluated materials, the optimal flow rate was established at 25 percent. Although this setting was considered most appropriate, it still resulted in a skewed PSD neglecting the clay-sized fraction as demonstrated in Subsection 5.2. Nevertheless, laser diffraction measurements were considered valuable for a relative comparison of gradations based on the fines fraction changes.

As in the case with hydrometer method, soil intended for the laser diffraction measurements was pre-soaked to ensure that all clumps appearing with oven-drying would be disintegrated prior to testing. Figure 4.7 clearly demonstrates how Leuven sand clumps would break down with the addition of water. It is worth noting here that because Antwerp sample was received in an air-dried state and with the naturally lower fines content, its particles were not binding together as much.

Figure 4.7. Oven-Dried Leuven Sand Clumps Breaking Down with Wetting

Glauconite Content (GC)

In order to understand the contribution of glauconite pellets susceptible to breakage to the overall interface shearing behavior of glauconitic sands, it is important to have an idea of their proportion relative to the remainder of the sample, which, in Belgium soils, consisted of quartz. In this study glauconite content (GC) was estimated relying on its paramagnetic susceptibility with the use of a manual magnetic separation method following procedure developed by University of Massachusetts Dartmouth (Sylvia, 2022) and relying on a high iron content in the tested sample. This method uses a glass jar with a metal lid and an 80 kg Neodymium magnet. Glauconite is separated from a small sample in several iterations with the test repeated at least three times to obtain a higher accuracy result. Material separation into the glauconite portion and quartz is shown in Figure 4.8.

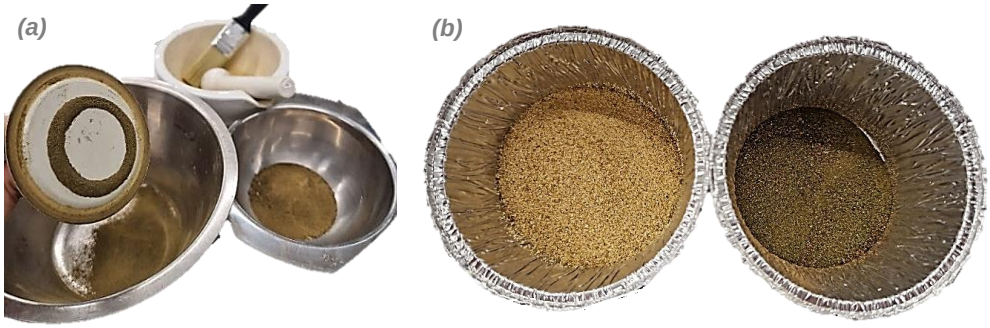

Figure 4.8. (a) GC Test Setup and (b) Separated Leuven Sand: Quartz and Glauconite

Noteworthy, glauconite pellets of lower maturity are expected to have lower paramagnetic susceptibility (Amorosi, 1997), and, thus, may not be well-captured in the adopted separation process.

Organic Content

Strong organic odor and surficial recovery of Leuven sample indicated that trace to little organics could be present in the tested material. To obtain a better estimate of the actual organic content, the loss of ignition (LOI) method was applied using two small sample sets of soil preliminary oven-dried at 65 and 105°C. The samples were then

ignited in a muffle furnace at 440°C (ASTM, 2020). Organic content was estimated using the difference between the pre- and post-ignition weight. Organic content estimation was not considered necessary for the Antwerp sample.

Atterberg Limits

The condition of clayey soil changes with moisture content (w). Each soil has a moisture content range within which it behaves plastically, defined by the Atterberg limits: the plastic limit (PL) as the lower bound, the liquid limit (LL) as the upper bound, and the plasticity index (PI) as their difference. Glauconite pellet breakage has been previously linked to the increases in fines content and plasticity (PI) exhibited by soil within the shear zone (Van Raak, 2009; Piedrabuena, 2024). Since higher overall plasticity and activity of clay is known to cause the reduction of frictional resistance and increase of the shear adhesion (Mitchell & Soga, 2005) and liquid limit (LL), for example, is tied to the increasing strain softening (Lupini et al., 1981), assessing Atterberg limits of the natural and crushed glauconitic sands is important for the understanding of their soil-steel interface shearing behavior. These basic properties can also provide additional insight into soil mineralogy and composition. Therefore, effects of sample preparation methods and glauconite degradation on plastic and liquid limits have been carefully considered in the given experimental program.

Atterberg limit tests were performed in accordance with the fall cone (liquid limit) test procedures described in Head's Soil Laboratory Testing manual (Head & Epps, 2011) and ASTM D4318 standard (ASTM, 2018) for plastic limit determination through rolling threads. To assess how these properties would be affected by the implemented sample preparation method, Atterberg limit tests were performed on fraction passing the No. 40 (425-µm) sieve after air-drying, oven-drying at 65 and 105°C, and in natural state without full drying allowed after washing of the fines.

To assess the impact of glauconite particle degradation, Atterberg limit tests were also performed on samples first subjected to crushing and degradation. In this case up to 300 grams of oven-dried 2-mm fraction suspended in demineralized water were stirred in the mixing apparatus. The mixture was then washed with demineralized water over the No. 40 (425-µm) sieve. The screened soil was carefully air-dried to moisture content just above the liquid limit, thoroughly mixed, and allowed to mature prior to testing.

Figure 4.9 provides a visualization for the carried out Atterberg limit tests.

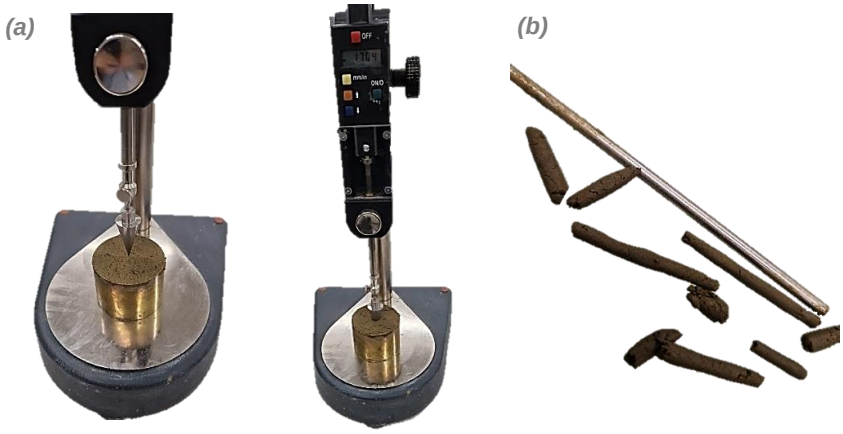

Figure 4.9. Atterberg Limit Tests: (a) Liquid Limit – Fall Cone Test and (b) Plastic Limit on Degraded Leuven Sand

Specific Gravity

Specific gravity (G_s) is the ratio of the mass of dry particles to the mass of water they displace. In geotechnical analyses it can provide insight into the mineralogical composition and microporosity of a given soil. In glauconitic sands, it can possibly be linked to their maturity as discussed in the literature review. Thus, specific gravity was considered for comparison of glauconitic sand samples from different recovery sites.

Specific gravity tests were performed in general accordance with ASTM D5550 (ASTM, 2023) using Anton Paar Ultrapyc 5000 Gas Pycnometer (shown in Figure 4.10) available at the Geoscience and Engineering Laboratory of TU Delft. Gas pycnometry is a non-destructive technique that uses gas displacement (helium in the given case) to measure the tested sample volume. The apparatus automatically determines specific gravity using the input sample mass. Multiple iterations set for the analysis allow to ensure accuracy and consistency in results. To accommodate for a sample size sufficient to account for variabilities in soil, a medium cell (50 cm^3) was used and filled to about 2/3 of the volume. Tests were conducted on various glauconitic sand fractions with the preliminary pulverization using pestle and mortar. Additional testing was carried out on the magnetically separated glauconite.

Figure 4.10. (a) Gas Pycnometer and (b) Medium Load Cell

Minimum and Maximum Index Density

To allow for determination of relative density (D_r) in interface direct shear tests, a degree of compactness relative to the loosest and densest conditions and a fundamental parameter in stress-strain behavior of soils, minimum and maximum index tests were performed on a Leuven glauconitic sand sample. Antwerp sand was not tested as it had been a part of the experimental assessment at Deltares (Piedrabuena, 2024).

To ensure that the implemented test method was reproducible and verified through the previous experimental trials, minimum and maximum index dry density was assessed at Deltares geotechnical laboratory. The implemented procedure is generally based on ASTM D4253 (ASTM, 2019) and D4254 (ASTM, 2016) but allows for a smaller sample size and applies surcharge weight and a hand-held vibratory device instead of a vibratory table for the maximum index density evaluation. The minimum index density test is a combination of Methods A and B of ASTM D4254 (ASTM, 2016). Each procedure was repeated at least 3 times until consistency in results was achieved. The setup for these tests is shown in Figure 4.11.

Minimum and maximum dry density needed for the future D_r estimation in interface shear tests was evaluated for the oven-dried fraction passing the No. 10 (2-mm) sieve since larger particle sizes would not be suitable for the intended direct shear test setup. Only the dry method was used as samples were to be air-pluviated and compacted without the addition of water that would have led to the breakdown of clumps as shown in Figure 4.7. This approach allowed for a consistent specimen preparation aiming for D_r ~ 70 percent. However, it was not sufficient for a continuous void ratio estimation during shearing as the sample carriage was flooded during consolidation.

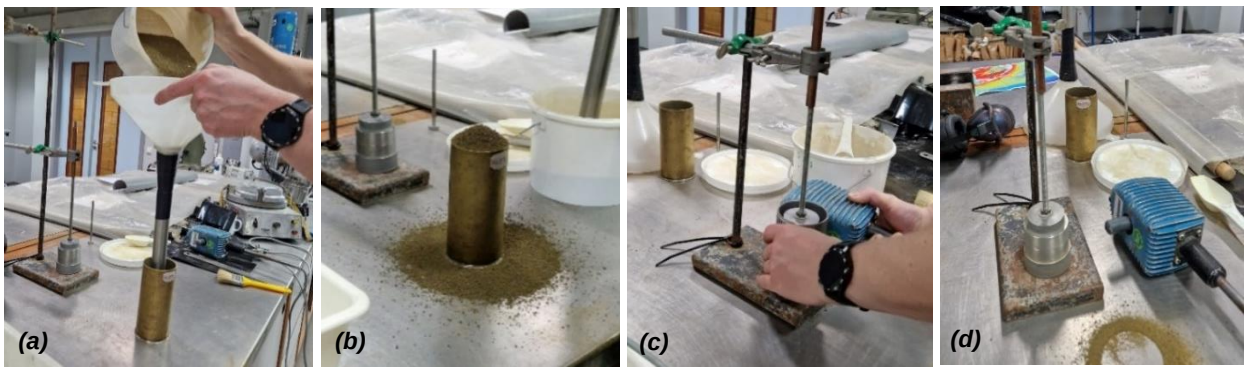

Figure 4.11. (a-b) Minimum and (c-d) Maximum Index Density Test Procedure

4.4 Interface Shear Strength Characterization Method

The primary component of the given project, i.e., soil-steel interface shear strength assessment, consisted of a sequence of interface direct shear (DS) tests. This section explains how the DS setup was modified for soil-to-steel interface evaluation and which steps were taken for the performed shear strength characterization.

Interface Shear Testing Program

In addition to evaluation of glauconitic sands in both their natural and degraded states, the imposed test parameters were systematically modified to replicate various scenarios applicable for monopile design. These variables, i.e. normal stress, shear rate, and surface roughness, were adjusted as shown in Figure 4.12 and discussed below.

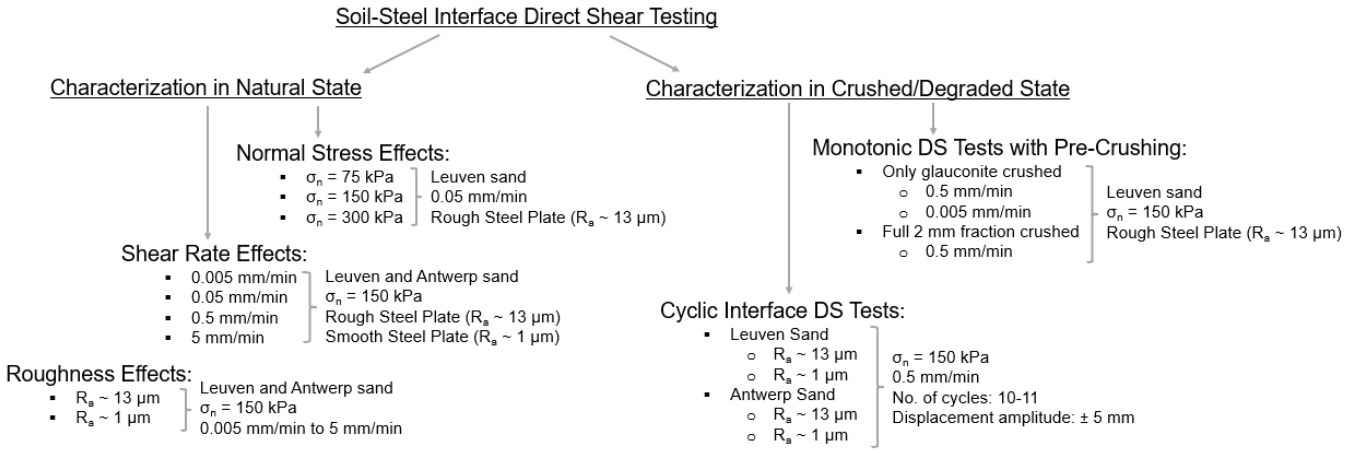

Figure 4.12. Interface Shear Testing Program

In interface shear testing under constant normal load (CNL) conditions, the applied vertical stress is set to replicate the in situ horizontal effective stress (σ'_{r0}) acting on a pile at a target depth. To simulate the overburden pressures at varying depths along a theoretical 20-meter pile, normal stress levels of 75, 150, and 300 kPa were selected. This range allows for the evaluation of how increasing vertical loads influence the resulting interface shear behavior, glauconite breakage, and residual strength. While CNL testing is limited in its ability to simulate realistic stress changes and installation effects, it provides valuable data for understanding of soil-structure interaction and evaluation of frictional resistance.

The DS tests were also performed at varying shear rates to assess the behavior of glauconitic sand-steel interfaces under conditions simulating both the rapid loading, as experienced during pile installation, and slow loading, representative of the long-term service stage. Given that standard DS testing is not well-suited for evaluation of soil-structure interaction under undrained conditions (Rao et al., 2002), the primary objective of these tests was to offer insights into the rate sensitivity of glauconitic sands rather than derive parameters for the pile installation phase calculations. With this goal in mind, displacement velocities of 5, 0.5, 0.05, and 0.005 mm/minute were considered.

As mentioned earlier, the conducted DS program also examined the effects of interface roughness. The objective of this evaluation was to assess the influence of pile surface finish on interfacial friction and behavior of glauconitic sands during shearing. Two cases were considered. The higher average roughness (R_a = 13 µm) was chosen to simulate surface finish typical for the offshore piles (Liu et al., 2019). The lower value (R_a = 1 µm), representative of physical modeling piles and a standard CPT cone surface, provided an opportunity to look into the behavior of glauconitic sands sheared along a smooth interface, outside of the standard range generally lying above 5 µm.

In addition to the discussed analyses, interface shear tests were performed on natural/uncrushed samples as well as glauconitic sands subjected to a higher level of degradation either through pre-crushing or cyclic shearing. These supplemental tests were added to simulate the behavior of material disturbed during pile installation as a standard direct shear apparatus does not allow for one-way displacement sufficient to achieve the same level of degradation on its own.

Interface Shear Test Setup

Shear strength characterization of glauconitic sands was performed at TU Delft Geoscience and Engineering laboratory in general accordance with ASTM D3080 (ASTM, 2012) and procedures provided in Head's Soil Laboratory Testing manual (Head & Epps, 2011). All tests were completed with the use of ELE International Digital Direct/Residual Shear Apparatus 26-2114. This equipment allows for a variable shear rate, ranging between 0.00001 and approx. 10 mm/minute. Normal load is applied by means of dead weights suspended from a counterbalancing hanger. The shear machine operates with the lever arm assembly arranged to multiply a given normal load by a factor of 10, allowing for the maximum normal load of 1000 kg and maximum shear force of 5 kN (ELE International, 2015).

Main components of the described direct shear apparatus are identified in Figure 4.13.

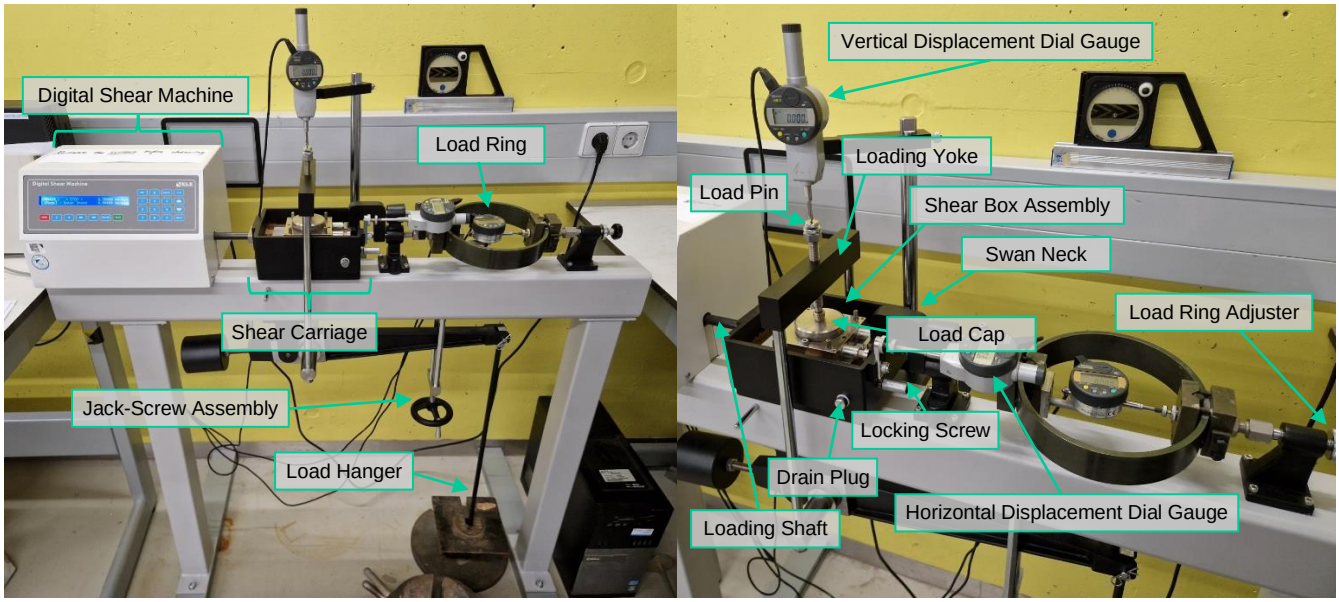

Figure 4.13. Direct Shear Test Apparatus

Shear Box Assembly Modifications

Soil-to-steel interface shear tests were carried out with the modified shear box assembly. A small shear box accommodating a circular specimen with a diameter of 63.5 mm was used as the basis. Its lower half was replaced with a steel plate that was about 12.8 cm long, 9.7 cm wide, and 2 cm thick. To ensure fixed position of the upper shear box body relative to the steel plate during consolidation, clamping screws were added outside of the shearing path as indicated in Figure 4.14. Four shear box separator screws with Teflon tips were used to maintain a consistent (~0.5 mm) gap between the metal surfaces throughout the shearing stage. In the case of a rough steel plate, 1.5 cm wide strips were manually sanded on each side parallel to the horizontal displacement range to ensure free sliding of the separator screw tips with shearing.

As mentioned above, to assess the effects of roughness on shear strength results, testing was performed on a "smooth" surface with an average roughness (R_a) of approximately 1 μm and a "rough" interface with R_a of about 13 μm. The smooth steel plate had been previously prepared for another experimental program conducted at TU Delft (Zimnik et al., 2018). To get the needed rough surface, new plates were ordered at Van Nobelen Delft B.V. and blasted with aluminum silicate using grit size of 1.4 – 2.8 mm. The resulting roughness was then assessed with the Keyence 3D Optical Profilometer (VR-series) available at The Stevin Laboratory of TU Delft. To obtain a representative roughness value, plate surface was first mapped and then analyzed with the reference plane setting applied. Roughness measurements were subsequently taken using both the surface and line calculations. Examples of the resulting roughness profiles are shown in Figure 4.15. Throughout the DS program, one measurement location was maintained for consistency in results.

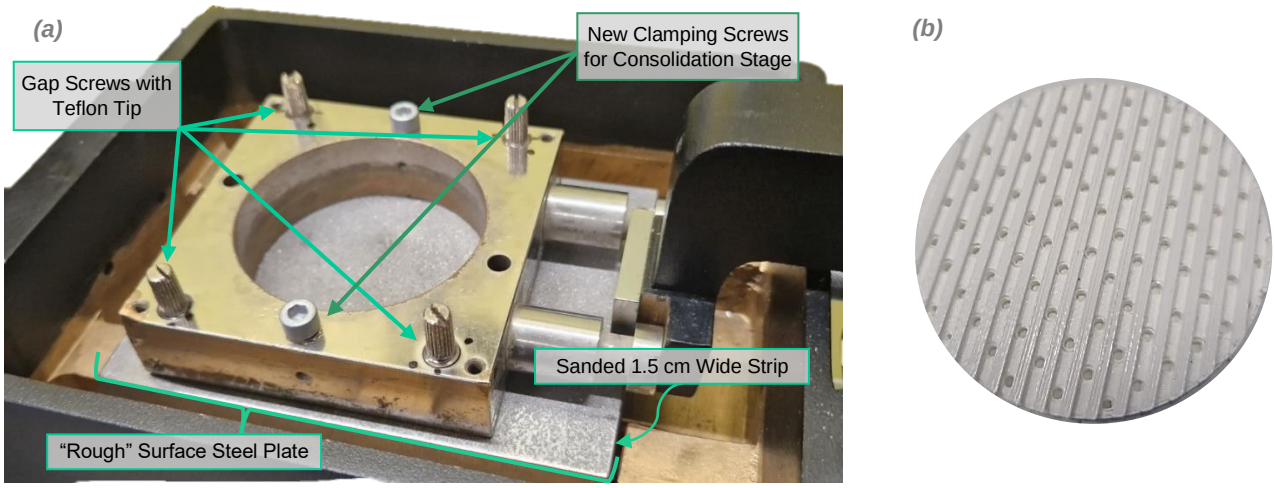

Figure 4.14. (a) Modified Shear Box Assembly and (b) 3D Printed Perforated Grid Plate

The original DS test setup allows for the load cap tilting with displacement. This rotation would also occur during interface shearing, especially with the horizontal displacement exceeding half of its full range (about 15 mm). Several attempts were made to minimize the tilt, but it appeared difficult to control, especially for tests on a rough (~13 μm) steel surface in which soil particles inevitably got trapped by the asperities. However, it has been previously shown that the difference in mobilized strength should not exceed 5 percent between tests conducted with fixed and non-fixed top caps (Potts et al., 1987).

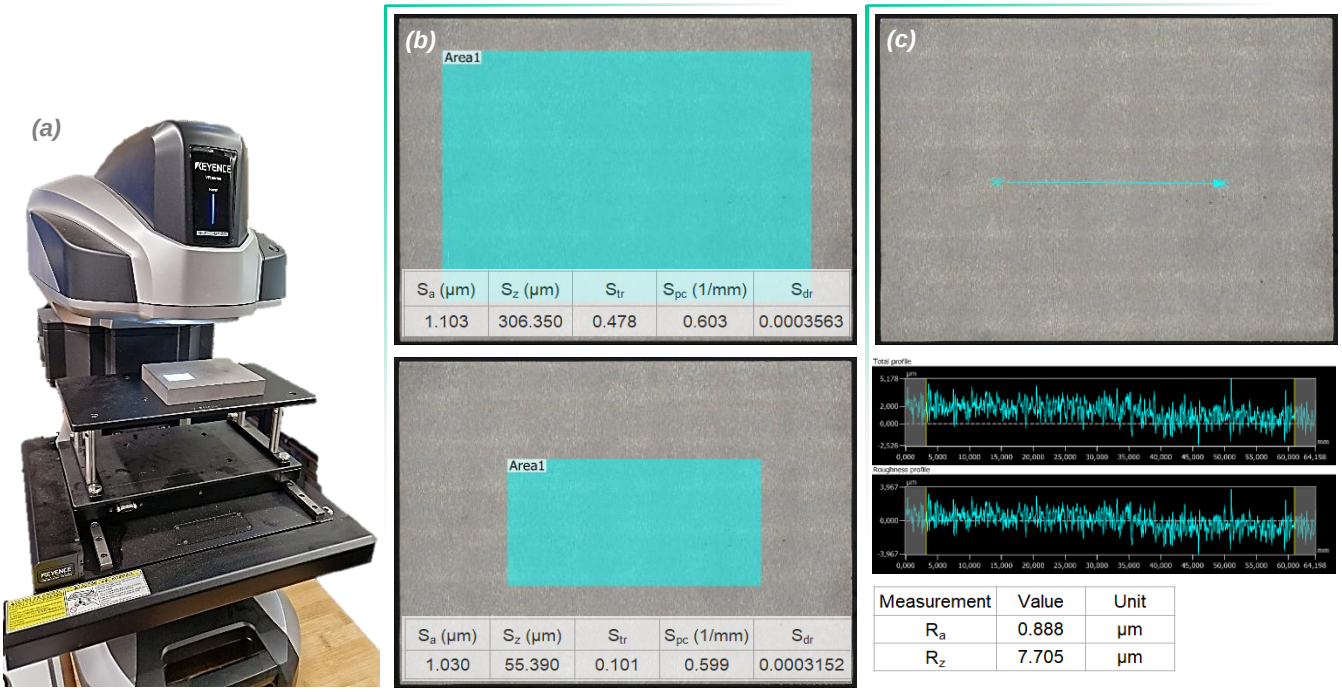

Figure 4.15. (a) Keyence 3D Optical Profilometer, (b) Example of Surface Roughness Measurement on a Smooth Steel Plate, and (c) Line Roughness Measurement on a Smooth Steel Plate

Specimen Preparation

Direct shear tests were conducted on soil oven-dried at 105°C and screened on a No. 10 (2-mm) sieve. To achieve a consistent level of compaction between the tests, dry glauconitic sand was carefully poured and compacted in the upper half of the shear box already resting on the assigned interface steel plate. While such procedure could break down clumps (shown in Figure 4.7) forming with oven-drying, it is highly unlikely that it would be damaging to

glauconite pellets since compression-induced breakage was shown to have lower significance compared to degradation with shearing (Westgate et al., 2022). As for the deterioration of clumps, it would not be an issue as they would fully break down with flooding of the carriage during consolidation.

Thus, DS samples were prepared in the shear box through air pluviation and dry compaction of a predetermined mass of soil until relative density (D_r) of approximately 70 percent was achieved. While this step was carried out with care, uneven clumping of glauconite pellets was likely to affect the degree of compaction between different tests. As the focus of this study is on residual interface shear strength that is independent of the initial soil density, this was not considered to be a significant limitation for this program.

Following recommendations by Head (Head & Epps, 2011), a perforated grid plate of a closely fitting size was 3D-printed as shown in Figure 4.14(b) and placed on compacted sand to enable shearing forces to be transmitted uniformly along the sample area. Porous stone on top of the grid plate was replaced with filter paper to provide sufficient space for the soil sample and avoid having the load cap stick out far above the top of the shear box. Together with the grooved loading cap, such setup would be efficient in allowing water to escape while also preventing particles from getting washed out through the grid plate perforations and minimizing tilting of the pressure pad. In the end it allowed for an initial specimen size of about 10 mm in height and 63.5 mm in diameter.

Direct Shear Test Procedure

Soil-steel interface shear strength characterization of samples from Belgium included both the monotonic and cyclic DS tests performed following a consistent experimental procedure. First, after the sample preparation, an initial normal stress of 50 kPa was applied for up to one hour. Following this, shear carriage was flooded with demineralized water, and the specimen was left to saturate for a minimum of 1.5 hours. Next, the sample was consolidated to the designated vertical stress, either in a single or multiple loading steps, depending on the final σ_v value. After consolidating overnight, the specimen was sheared under constant normal stress at the predetermined shear rate.

Monotonic shearing was allowed to proceed up to the engagement of end switch with the maximum shear path of about 15 mm. If there were time limitations for the slow shear tests, testing could be stopped at displacements exceeding 8 mm, a boundary at which load cap tilting would usually become noticeable. In cyclic tests discussed in Section 6.2, displacement amplitude was maintained at $\pm$5 mm. The assigned normal stress and shear rate varied depending on the particular test objectives as explained earlier.

Post-Shearing Evaluation

Following each test, loading yoke was removed from the sample with the carriage drained afterwards. The upper portion of the shear box was then carefully lifted, leaving soil specimen to rest on the steel surface. The carriage was subsequently brought to its original position, allowing for removal of the plate.

After the retrieved specimen was photographed, a small portion (~ 2 grams) was removed from its top right below the grid plate for laser diffraction PSD tests on material above the interface. The rest of the sample above the shear zone was then carefully trimmed with a rubber spatula and a wire saw and set aside for drying and storage.

As the shear zone specimen remaining on the plate (see Figure 4.16(a)) would be too large for the laser diffraction PSD tests, it was divided into three portions and carefully washed off the plate into the respective containers. In the case of smooth surface tests, specimens could sometimes be slid off the plate, allowing for the interface zone to be carefully trimmed off afterwards as shown in Figure 4.16(b). Material collected for post-shearing tests at and above the interface was then oven-dried at 65°C for storage until it would be selected for the PSD/ESEM tests.

After shearing, steel roughness was reassessed as surface measurements accounting for steel abrasion are recommended as best practice for the interface shear box testing (Westgate et al., 2021). For example, significant reduction in centerline interface roughness (R_{CLA}) was recorded for ring shear tests on glauconitic sands performed by Quinteros et al. (2023). Repeated measurements were not made for the smooth plate as there was no reason to expect any noticeable change to its surface.

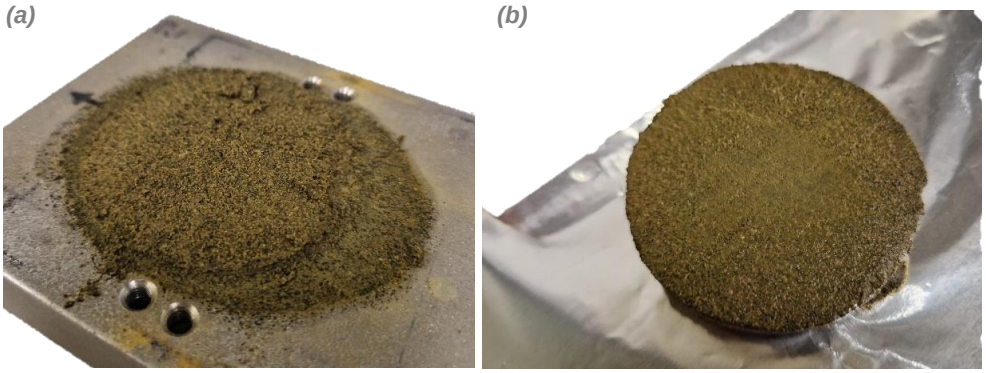

Figure 4.16. (a) Rough Plate Shear Zone for Post-Shearing Evaluation and (b) Smooth Plate Specimen Slid Off the Plate (Sheared Zone Upwards) for Shear Zone Removal

5 Natural Glauconitic Sand Characterization

This section provides results of material characterization as found in situ, in its natural state. Both Leuven (Diest Formation) and Antwerp (Kattendijk Formation) samples are considered.

5.1 Comprehensive Characterization

Representative digital microscopy images of magnetically separated, washed, and HCl-pretreated pellets from the Leuven and Antwerp samples are shown in Figure 5.1. The provided photos are not intended for size comparison but rather for the assessment of differences in peloidal gradation, color, and texture.

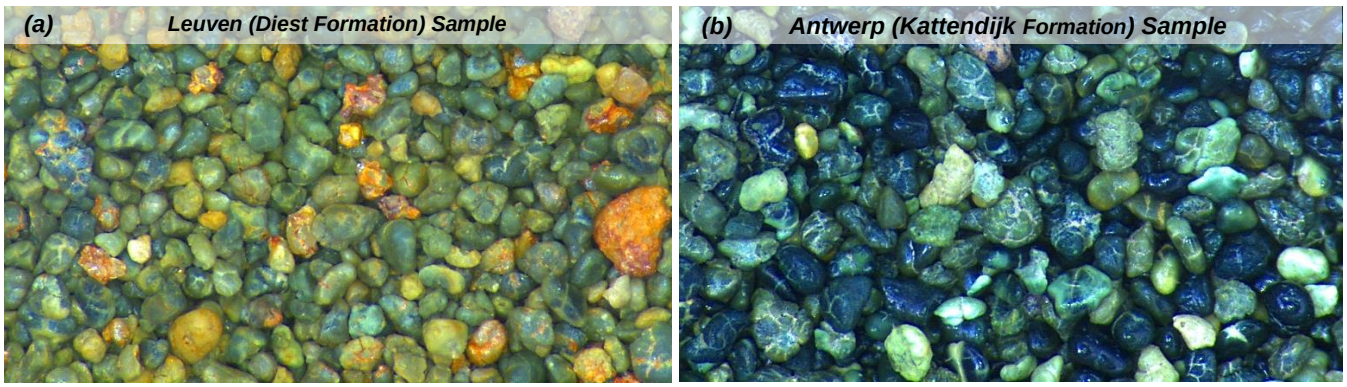

Figure 5.1. Digital Microscopy Images of Magnetically Separated, Washed, and HCl-Pretreated Glauconite from (a) Leuven and (b) Antwerp Samples (Magnification: 6x)

Based on visual examination alone, both samples contain glauconite pellets at different stages of evolution, from nascent (smooth-surfaced and light green) to highly evolved dark-green and even black in the case of Antwerp sand. Overall, Antwerp glauconite from the Kattendijk Formation appears to be more mature based on its darker color, higher density of infilled fissures, and relatively polished surface. Leuven glauconite from the Diest Formation seems to be more well-graded but shows less variation in evolution among its pellets. The lighter olive-green color and lower reflectivity suggest that its pellets are generally nascent to slightly evolved. However, the overall yellowish-green shade is likely associated with post-depositional alteration, weathering, and chemical processes in the shallow subsurface of the Kesselberg outcrop. For an instance, photo of a fresh Diest Formation core sample provided in Adriaens et al. (2014) shows a colder shade of green, resembling that of the Antwerp and New Jersey (Westgate et al., 2023) glauconites.

ESEM Analysis

The ESEM micrographs for the magnetically separated and pretreated 105°C and 65°C oven-dried glauconite pellets from the Leuven and Antwerp samples are shown in Figure 5.2 and Figure 5.3, respectively. The limited number of captured particles does not allow for a systematic image analysis and thorough comparison of the two samples but may still provide insight into their geologic history and evolution of glauconite.

Under the ESEM examination glauconite from both formations showed high morphological variability. Considering morphology types suggested by Triplehorn (1966) (with examples shown in Figure 2.16), ovoidal, mammillated, lobate, tabular, and composite pellets were observed. Many of the captured particles had deeply propagating cracks, fractures, dents, and chipped off-edges. At least some of these features may be the evidence of post-glauconization transport rather than textural changes accompanying recrystallization in situ.

When comparing glauconites from the two considered sites, Leuven sand pellets showed more signs of post-depositional alteration, such as weathering and fragmentation. Most cracks were open, without the clay precipitate infillings. Antwerp sand pellets from the Kattendijk Formation showed seemingly greater variation in morphology but appeared to be more intact. The observed cracks were both open and infilled. Based on visual examination alone, they seemed to be less prone to degradation with the application of external stresses.

In terms of the temperature effects, if present at all, they were expected to be subtle with only the limited range considered. However, it is possible that oven-drying at a higher temperature affected cracks infilled with the clay precipitates as either composite or mammillated/lobate pellets showed evidence of disintegration in Figure 5.3(a-b) for the Antwerp sand.

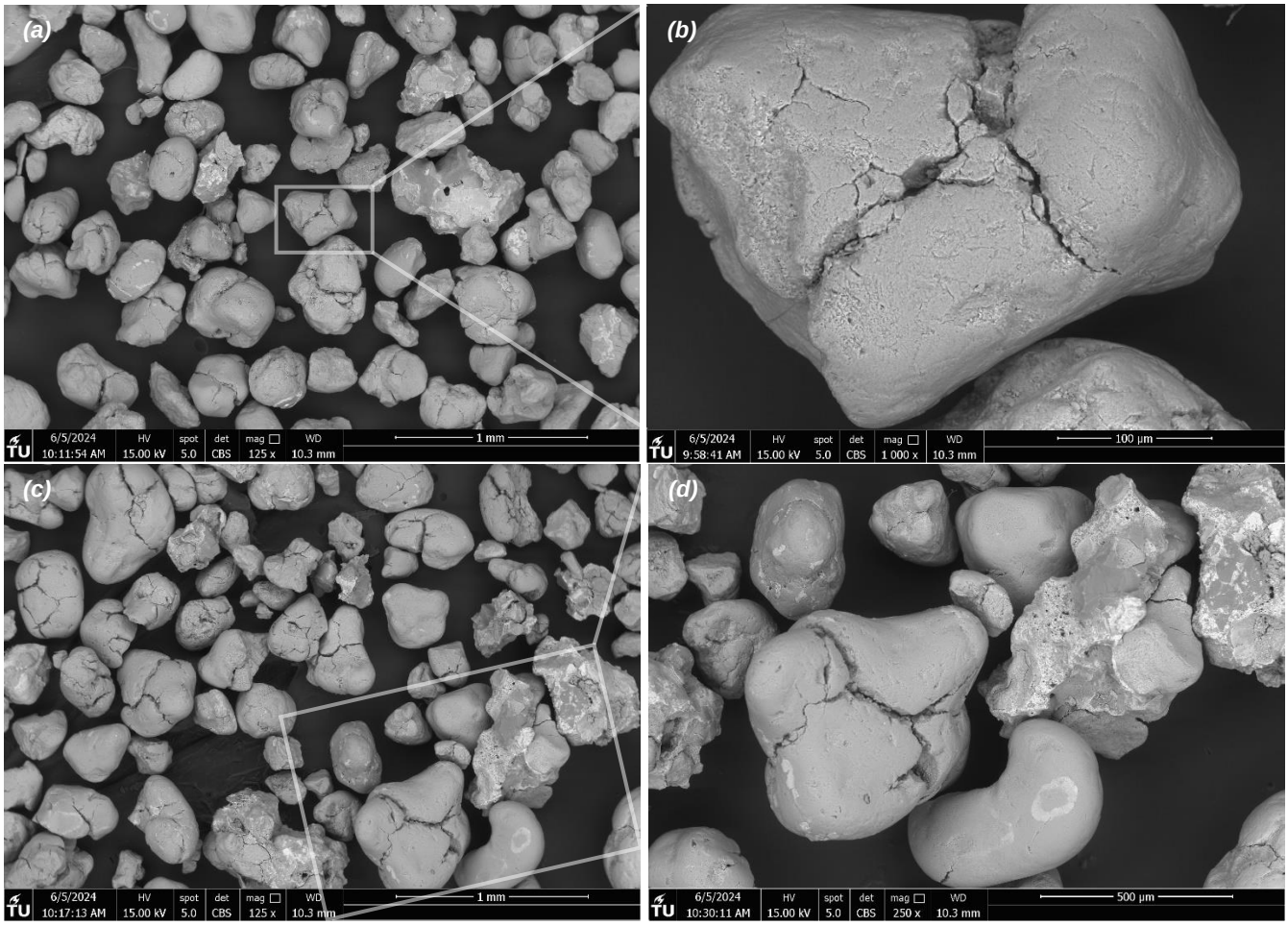

Figure 5.2. Leuven Sample Separated Glauconite ESEM Images for (a) 105°C oven-dried pellets at 125x magnification; (b) 105°C oven-dried pellets at 1000x magnification; (c) 65°C oven-dried pellets at 125x magnification; (d) 65°C oven-dried pellets at 250x magnification

In assessing the most likely stage of glauconization of the Leuven and Antwerp samples, nanostructures were observed for just a few pellets. However, rosette and lamellar structures (see Figure 2.19) indicative of evolved to highly evolved stages (Odin & Matter, 1981; Wigley & Compton, 2007), were evident along with low-maturity textures in some magnified images. According to Odin and Matter (1981), glauconization occurs as glauconitic smectite crystallizes within the substrate pores, later evolving into glauconitic mica through recrystallization. The resulting mature pellet, with visible micaceous cleavage (Triplehorn, 1966), may be seen in Figure 5.4(e) for the Antwerp sand. This particle is shown to display a lamellar nanostructure of mature glauconite in Figure 5.4(f). For comparison, Figure 5.4(g) shows a fractured, presumably lower-maturity pellet lacking the micaceous appearance, which was more common in both samples. The predominance of this type of structure could suggest that glauconitic clay formed from the Leuven and Antwerp sand pellets is more likely to exhibit plasticity and activity typical for smectites, which becomes important for characterization of degraded clayey soils in Section 6.

In general, based on classification from Figure 2.17, most pellets appeared to fit with the nascent to slightly evolved stages of glauconization for Leuven sand and slightly evolved to evolved stages for the Antwerp sample. This seems to be consistent with the contrasting colors of Figure 5.1.

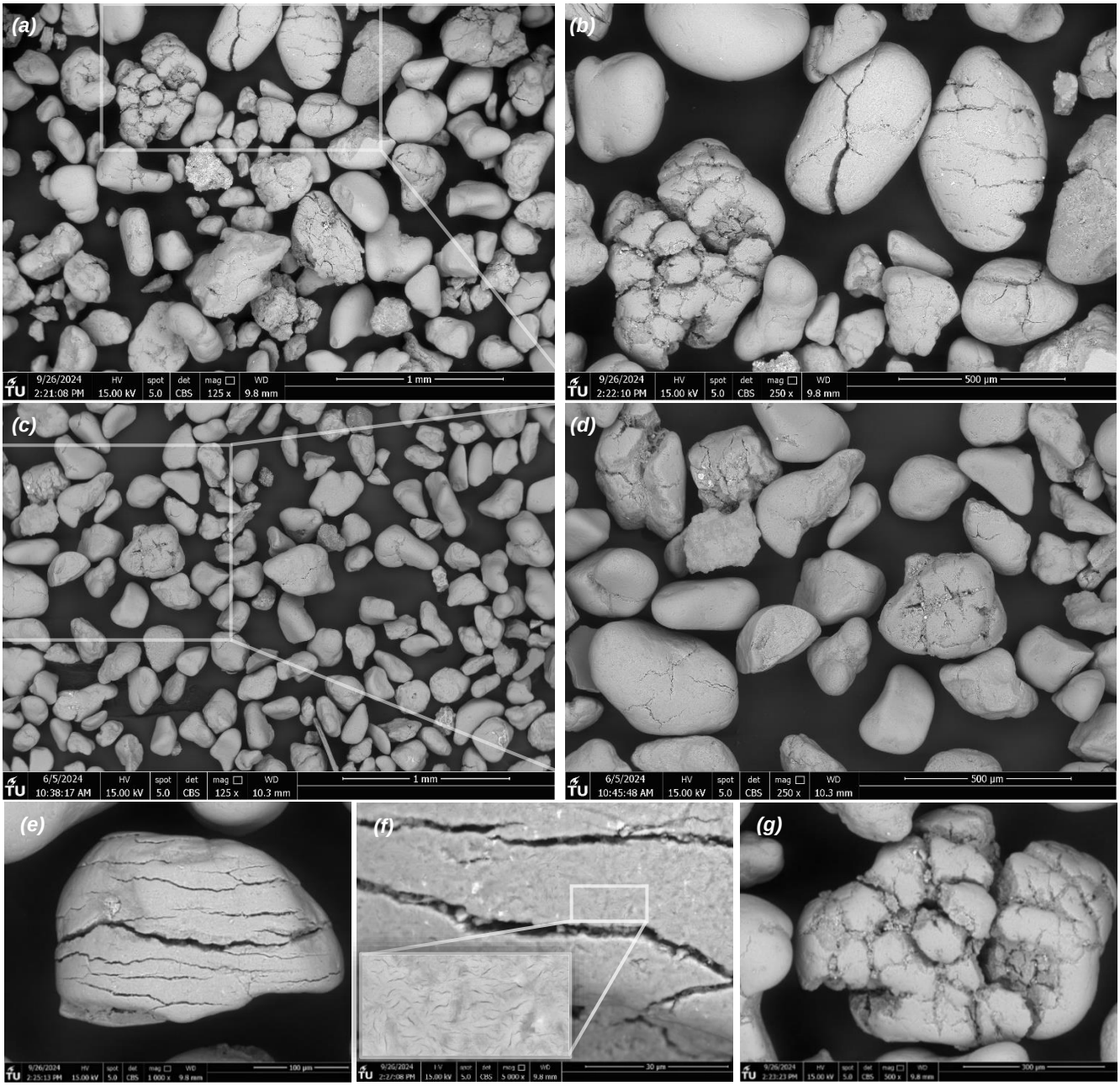

Figure 5.3. Antwerp Sample Separated Glauconite ESEM Images for (a) 105°C oven-dried pellets at 125x; (b) 105°C oven-dried pellets at 250x; (c) 65°C oven-dried pellets at 125x; (d) 65°C oven-dried pellets at 250x; (e) pellets with micaceous cleavage at 1000x; (f) lamellar nanostructure becoming visible at 5000x; and (g) pellets without micaceous cleavage at 500x magnification

As discussed in Subsection 4.2, ESEM assessment was supplemented by selective point-method EDX analyses. An example of the EDX spectroscopy results is shown in Figure 5.4. The detected composition closely matches that provided for glauconite in the SEM Petrology Atlas (Welton, 2003).

Evaluation points were assigned to pellets of different morphologies, degradation, structure, and surficial texture. With only several locations captured per frame and no systematic approach implemented for testing, these results are not intended for a quantitative comparison between the Leuven and Antwerp deposits. Instead, they can be used to support earlier conclusions regarding glauconite evolution and demonstrate high compositional variability within one sample.

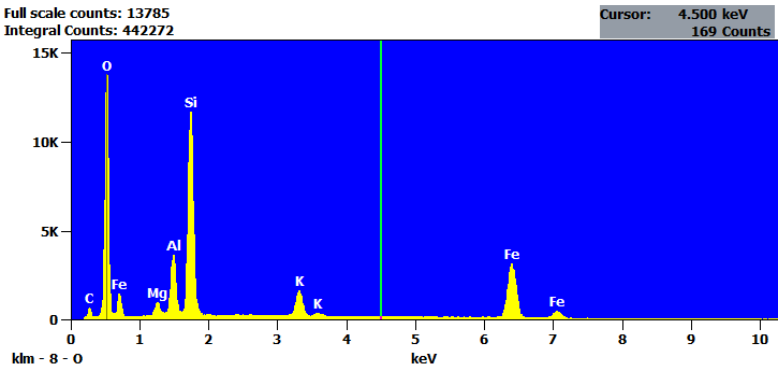

Figure 5.4. Glauconite Point Analysis EDX Spectroscopy Results; Example for Leuven Sand

Results for specific points from different frames in weight percentage are shown in Table 5.1.

Table 5.1. EDX Point Analysis Results for Leuven and Antwerp Glauconite Pellets

EDX Image	Elemental Analysis Bar Graph (wt%)
Leuven Glauconitic Sand Sample	
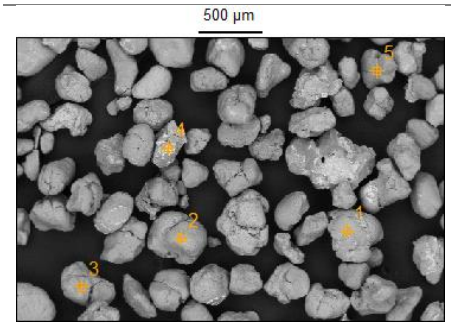 *Image 1*	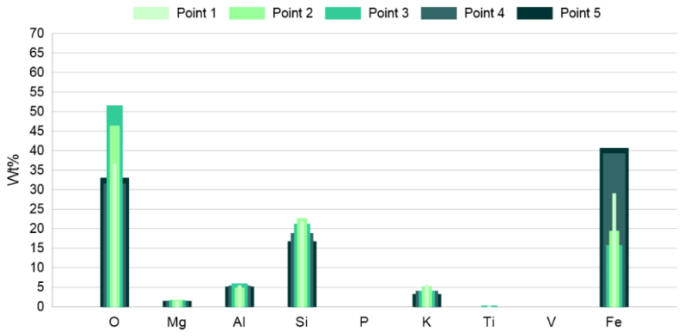
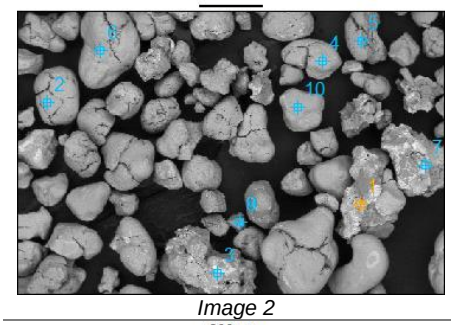 *Image 2*	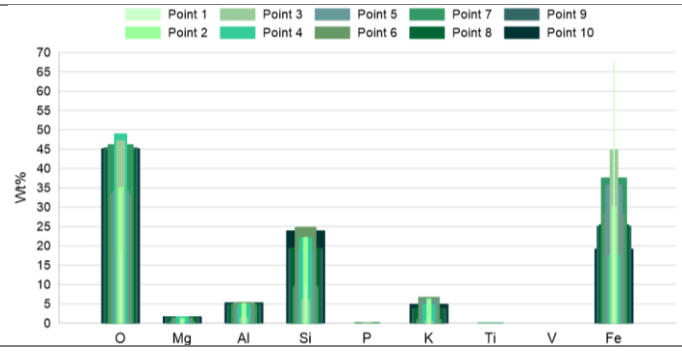
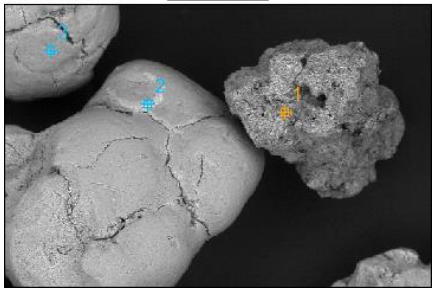 *Image 3*	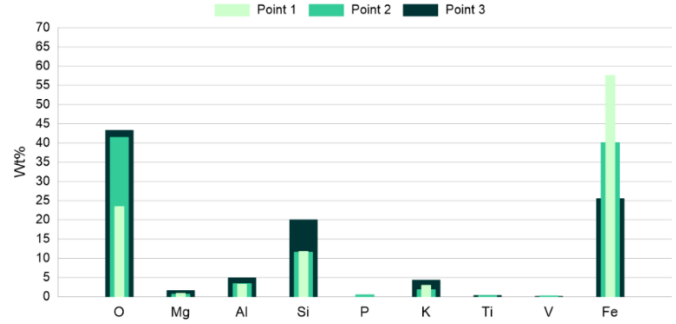

	O	Mg	Al	Si	P	K	Ti	V	Fe
Average:	39.2	1.3	4.5	17.8	0.2	3.9	0.2	0.2	33.3
Standard Deviation:	8.8	0.4	1.2	5.5	0.1	1.8	0.1	0.0	13.4

EDX Image	Elemental Analysis Bar Graph (wt%)
Antwerp Glauconitic Sand Sample	
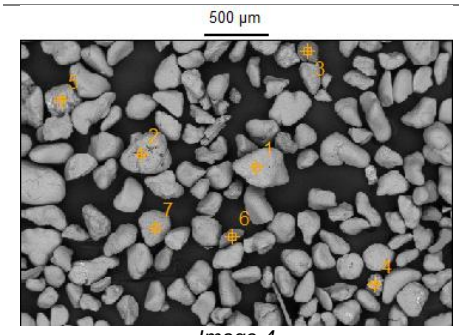 *Image 4*	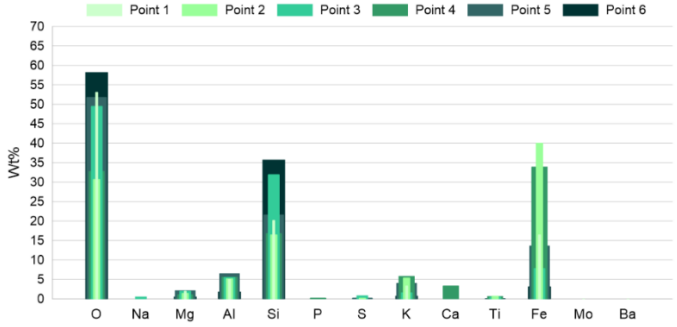
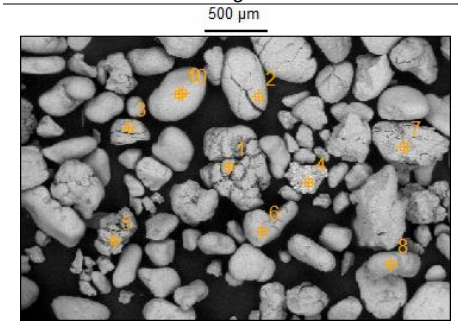 *Image 5*	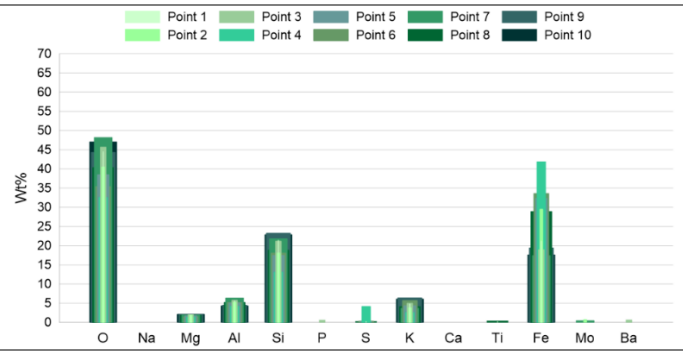

	O	Na	Mg	Al	Si	P	S	K	Ca	Ti	Fe	Mo	Ba
Average:	43.3	0.5	1.7	5.1	21.2	0.4	0.8	4.2	3.3	0.4	23.5	0.4	0.3
Standard Deviation:	7.7	0.0	0.4	1.0	5.5	0.2	1.3	1.6	0.0	0.2	10.9	0.3	0.3

The average potassium content measured at points from Table 5.1 aligns with the classification of a slightly evolved stage based on Figure 2.17. Potassium and aluminum levels appear relatively consistent across the pellets. The greatest variability is in iron content, with the peak values in Leuven sand likely attributed to oxidation that increases its relative weight percentage in EDX results. There may also be evidence of other alteration processes as indicated by point 4 from image 5 of Table 5.1 possibly corresponding to K-poor glauconite associated with jarosite (Fernández-Landero & Fernández-Caliani, 2021) in Antwerp sand sample.

Additional ESEM images not shown in the report can be found in Appendix B.

X-Ray Analyses

The XRD analysis was included for phase identification in the Leuven sample, considering that, for example, Qmineral findings (Piedrabuena, 2024) for the Antwerp sand detected other minerals (K-feldspar, plagioclase, calcite) alongside glauconite and quartz. Since evolution of glauconite is primarily assessed based on potassium oxide content (Odin & Matter, 1981; Amorosi, 1997; Obasi et al., 2011), it was important to understand whether other minerals may contribute to its weight percentage in a sample. The mass fraction of glauconite itself would also be a valuable output as the magnet jar separation method may not be suitable for identification of GC in a fine-grained form. Nevertheless, these goals have not been met as quantification of the compounds at TU Delft did not provide reliable results. Moreover, as mentioned in Subsection 4.2, supplemental tests on Antwerp sand revealed discrepancies in phase interpretations completed by the two laboratories, introducing additional uncertainties in mineralogical assessment of glauconitic sands from Belgium.

Based on results of the XRD analysis carried out at TU Delft, Leuven sand is primarily comprised of quartz (SiO_2), glauconite ($K(Fe,Al)_2(Si,Al)_4O_{10}(OH)_2$), and goethite ($Fe^{3+}O(OH)$). The presence of goethite is consistent with the visual state of the Kesselberg outcrop deposits subjected to oxidation. It had been previously shown that the end products of glauconite weathering are pseudomorphs of goethite and authigenic kaolinite and that staining and

goethite-quartz crust formation may result from the breakdown of goethite pseudomorphs (Wolff, 1967). The visual evidence of these processes may be seen in the ESEM images provided earlier.

Considering the lack of other detected potassium-bearing minerals in Leuven sand, XRF results for the natural GC sample may be sufficient to estimate its degree of evolvement based on potassium oxide content. With a bulk material assessment, that would be more dependable compared to the point EDX analysis results provided in Table 5.1. With the reference to Table 5.2, this results in K_2O content of approximately 5 percent by weight, which, according to the review from Subsection 2.5, corresponds to the slightly evolved stage of glauconization. Although deposits from other Diest Formation sites appear to be of a darker, colder green color and show higher K_2O content associated with the evolved stage (Adriaens et al., 2014), Leuven sand from the Kesselberg outcrop may have been removed from the exposed semiconfined suboxic conditions required for further glauconization before the same level of evolution was reached. As for the maturity of Antwerp sand, XRF results provided by Piedrabuena (2024) and summarized in Table 5.2 cannot be interpreted directly due to the presence of other potassium-bearing minerals, with K_2O content divided by GC resulting in the excessive 16 percent by weight.

Table 5.2. XRF Results for Leuven and Antwerp Samples

Sample	**GC (%)**	**Full Sample Chemical Composition – Concentration (wt%)**									
		SiO_2	**Al_2O_3**	**Fe_2O_3**	**SO_3**	**MgO**	**K_2O**	**CaO**	**P_2O_5**	**Na_2O**	**TiO_2**
Leuven Sample (Diest Formation)	~47	66.37	8.65	20.47	0.04	1.45	2.31	0.15	0.17	0.07	0.24
Antwerp Sample (Kattendijk Formation) (1)	~11	79.96	3.59	4.70	ND	0.68	1.75	3.10	0.08	0.32	0.38

(1) Results from MSc Thesis by Alba Piedrabuena (Piedrabuena, 2024).
(2) ND = not detected.

Considering these findings and their alignment with the literature, performing X-ray analyses on magnetically separated glauconite could be beneficial, as normalization with the estimated GC is not highly reliable. However, since interface shear testing in this project focuses on samples with the natural glauconite content, further analyses were deemed redundant. Furthermore, the DS results would be influenced by factors beyond glauconite composition, such as the high fines content and predominance of quartz.

X-Ray analysis reports provided by the X-Ray Facilities Group at TU Delft are included in Appendix A.

5.2 Index Test Characterization

The given subsection covers and analyses results of the standard index tests performed on uncrushed glauconitic sands from Belgium. Additional evaluation of basic properties can be found in Subsection 6.1 focused on testing of the degraded samples.

Particle Size Distribution (PSD)

Particle size distribution curves obtained for both the Diest (Leuven) and Kattendijk (Antwerp) Formation samples in their natural (uncrushed) state following ASTM D422 (ASTM, 2007) are shown in Figure 5.5. Several gradation analyses were performed on each sample to assess their variability and investigate the effect of drying on glauconite pellet breakage during dispersion.

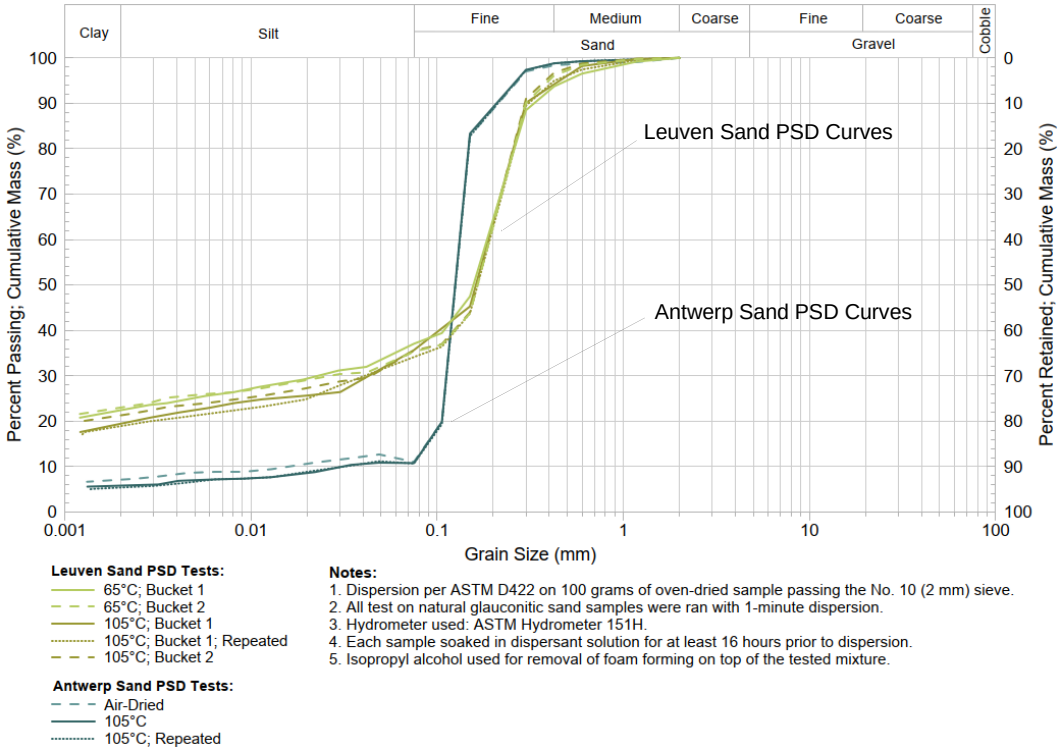

Figure 5.5. Natural Glauconitic Sand Particle Size Distribution Curves (ASTM D422 Method)

In both cases, results showed high consistency and appeared to demonstrate low impact of temperature on gradations. If there was any influence of the adopted preparation method, higher temperature could possibly increase the degree of clumping demonstrated previously in Figure 4.7. This would explain why samples subjected to air-drying and oven-drying at a lower temperature of 65°C showed slightly higher fines content in hydrometer tests than the sands oven-dried at 105°C. However, even if this was the case, the observed temperature effects appear to be negligible.

Gradation results from the chart are summarized in Table 5.3, showing fines content as high as 37 percent in natural Leuven sand and only about 11 percent in Antwerp sample. The reported PSD characteristics and well-graded classification of the Leuven sample fit well with the previous Diest Formation descriptions (Adriaens et al., 2014; Houthuys et al., 2020; Houthuys R. et al., 2023). Antwerp sample classifies as well- to poorly graded (C_u ~ 4) primarily fine slightly clayey sand, which is also consistent with the lithological description of Kattendijk Formation (Deckers & Louwye, 2020; Deckers J. et al., 2023).

To allow for comparison of PSD results between the two test methods (combined hydrometer and sieve vs. laser diffraction; see Section 4.3), natural samples were also evaluated with the Microtrac BlueWave PSD analyzer. The resulting curves are plotted in Figure 5.6.

The presented laser diffraction results show a similar relative distribution of grain sizes for the two glauconitic sand samples. However, contribution of the clay fraction is underestimated with the adopted flow rate of 25 percent as particles smaller than 1 µm have been omitted by Microtrac BlueWave. Adjustment of the flow rate to entries below or above 25 percent resulted in exclusion of either the finest or coarsest portion of the tested samples from PSDs. Noteworthy, both methods showed consistency with results provided by Alba Piedrabuena (2024) for the respective techniques applied on Antwerp sand at Deltares. Therefore, the established flow rate was maintained throughout the experimental program.

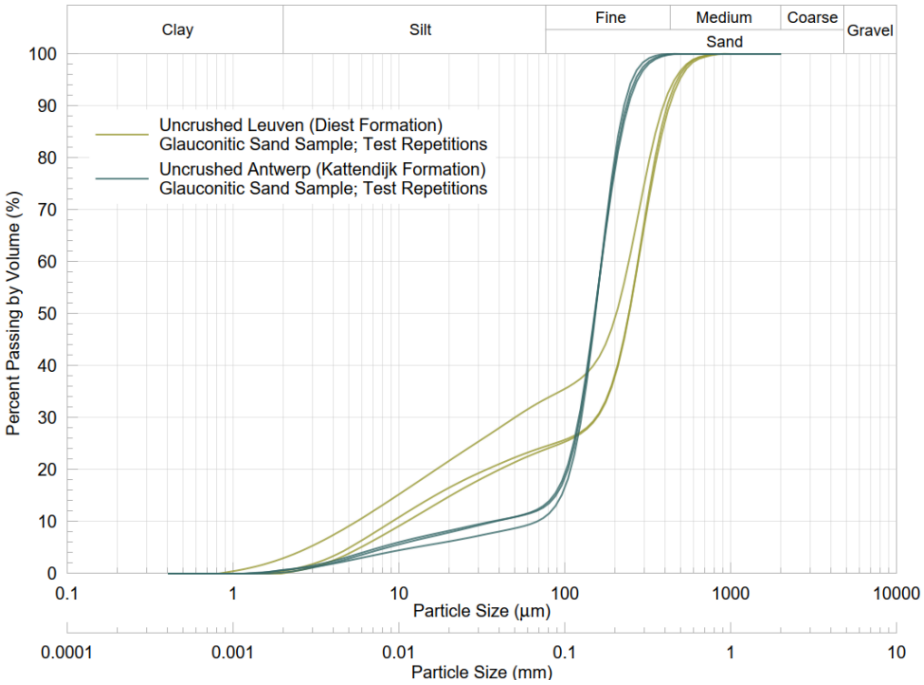

Figure 5.6. Natural Glauconitic Sand Particle Size Distribution Curves (Microtrac BlueWave Laser Diffraction Method)

As Table 5.3 with the PSD summary demonstrates, while clay fraction is not captured well via laser diffraction, this method provides fines content that is somewhat consistent with the ASTM D422 results, especially in the case of Antwerp sand. Nevertheless, the provided laser diffractometry results should be considered with scrutiny and will only be implemented as a supplementary method where the standardized PSD measurements would not be feasible. The discussed limitation will be of importance in post-shearing PSD evaluations in Subsections 5.3 and 6.2.

Table 5.3. PSD Summary for Natural Glauconitic Sand Samples

Sample	Medium Sand Fraction (%)	Fine Sand Fraction (%)	Silt-Sized Fraction (%)	Clay-Sized Fraction (%)	Fines Fraction (%)
		Percentage By Weight (ASTM D422)			
Leuven Sand	3.3 – 6.5	56.7 – 61.2	12.5 – 16.5	18.7 – 22.8	34.1 – 37.1
Antwerp Sand	1.2 – 1.6	87.3 – 88.1	3.9 – 5.3	5.3 – 7.1	10.7 – 11.0
		Percentage by Volume (Microtrac BlueWave)			
Leuven Sand	7.6 – 11.0	59.1 – 66.8	23.7 – 30.6	0.0 – 2.7	23.7 – 33.3
Antwerp Sand	~0.2	86.8 – 89.4	10.0 – 12.8	0.1 – 0.6	10.6 – 12.9

Additional PSD analyses following ASTM D422 (2007) were performed on the magnetically separated glauconite and separation tailings primarily composed of quartz. This evaluation was included to allow for a supplemental assessment of glauconite maturity by comparing the maximum pellet size in Leuven and Antwerp samples. The resulting gradations could also be used to better understand their depositional environments and abrasion susceptibility. For clarity, magnetic extraction results for the Leuven and Antwerp samples are shown separately in

Figure 5.7(a) and Figure 5.7(b), respectively. It is worth noting that in both test sets, fines content in separated fractions may not be representative of their actual composition as fine particles may not be easily extracted with a magnet.

As demonstrated in Figure 5.7(b), Antwerp PSD curves for the glauconite and quartz show a general overlap and identical median grain size of approximately 0.12 mm, suggesting either their common travel history (with the low experienced transport energy) and/or high resistance of glauconite pellets to abrasion. The separated glauconite curve is just slightly smoother and more well-graded, pointing towards the preserved state of glauconitic pellets in situ.

Different geologic history and/or glauconite pellet properties are hinted at by PSD curves from Figure 5.7(a) for the Leuven sand. Here, the magnetically separated fraction is consistently finer than the intermixed quartz (with D_{50} of 0.05 mm against 0.2 mm, respectively). While the maximum size of pellets is identical to that of the Antwerp sample, Leuven glauconite appears to be reworked further through selective transport or weathering. As concluded by Adriaens et al. (2014), the origin of at least a part of clay-sized particles in the sample is not authigenic but related to glauconite pellet abrasion and disintegration with transport. Thus, the performed analyses show that glauconite from Leuven has either been deposited in a higher-energy environment or shows higher susceptibility to breakage and degradation under similar stress conditions. Moreover, both hypotheses may be true.

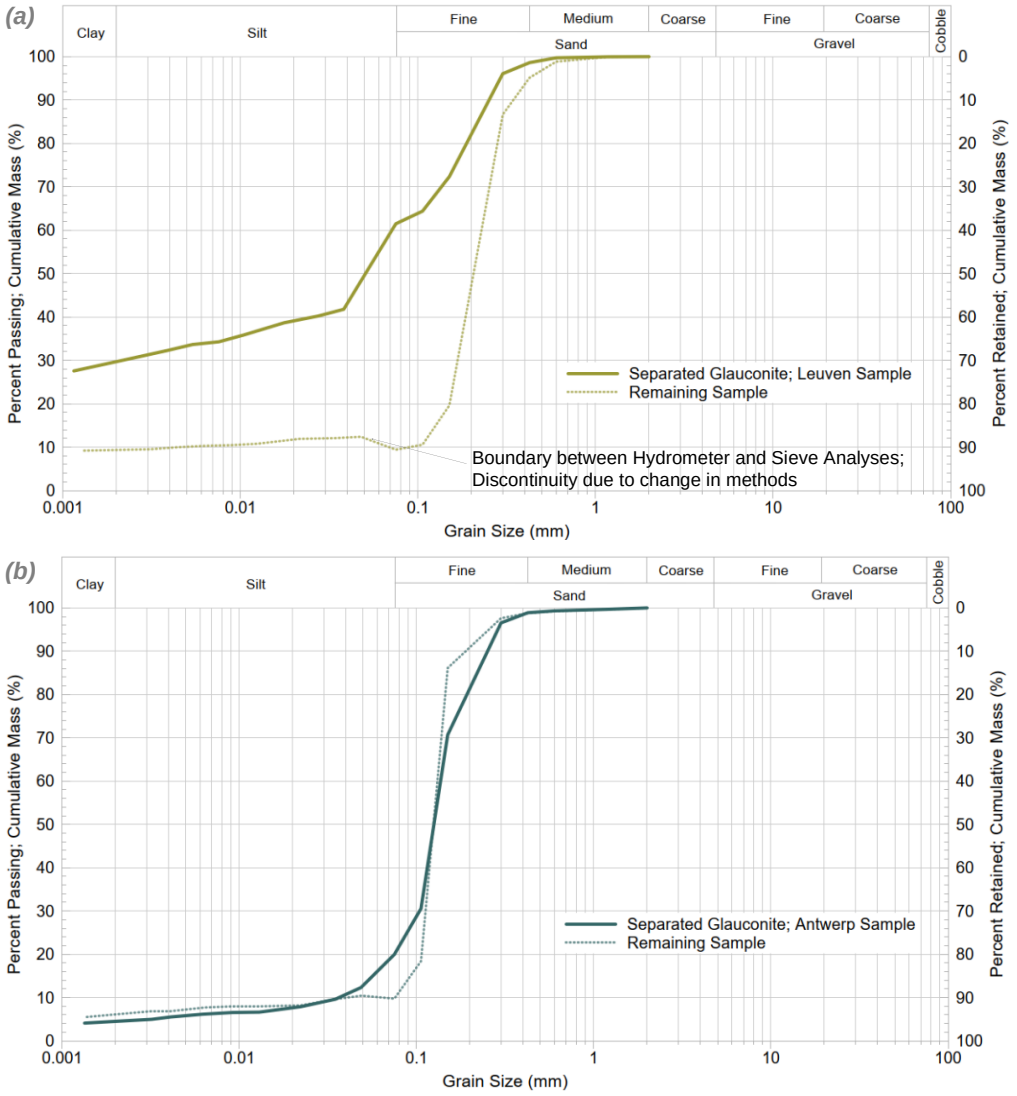

Figure 5.7. Magnetic Separation PSD Curves for (a) Leuven and (b) Antwerp Samples

To facilitate future discussions, PSD results discussed above are summarized in Table 5.4.

Table 5.4. ASTM D422 Test Result Summary for Magnetic Separation

Sample	Fraction	PSD Percentile Points (mm)					$C_u = \frac{D_{60}}{D_{10}}$	$C_c = \frac{(D_{30})^2}{D_{10} \times D_{60}}$	Gradation Classification
		D_{90}	D_{60}	D_{50}	D_{30}	D_{10}			
Leuven Sample	Glauconite	0.25	0.07	0.05	0.002	-	-	-	Well-Graded
	Quartz	0.35	0.23	0.20	0.17	0.09	2.55	1.40	Poorly Graded
	Full	0.31	0.19	0.16	0.04	-	-	-	Well-Graded
Antwerp Sample	Glauconite	0.25	0.14	0.12	0.10	0.04	3.50	1.79	Poorly Graded
	Quartz	0.19	0.13	0.12	0.11	0.08	1.63	1.16	Poorly Graded
	Full	0.21	0.13	0.12	0.11	0.03	4.33	3.10	Poorly Graded

Glauconite Content (GC)

Natural glauconite content (GC) was estimated for the oven-dried Leuven sample using both its full fraction and portion passing a No. 10 (2-mm) sieve. This resulted in GCs of 48 and 47 percent, respectively. These measurements are consistent with the range of glauconite content between 25 and 60 percent provided for the Diest Formation deposits in literature (Adriaens et al., 2014; Houthuys et al., 2020; Houthuys R. et al., 2023).

As for the more poorly graded Antwerp sample that does not contain coarse particles or clumps, its glauconite content was estimated only for material passing the No. 10 sieve, resulting in an average GC of 21 percent. The lower average value of 11 percent reported by Qmineral (Piedrabuena, 2024) for samples from the same site could be explained either by the difference in implemented magnetic separation methods (Frantz Isodynamic Magnetic separator used in this case) or by high variability of the excavated sand. Both results appear reasonable considering typical GC of approximately 20 percent reported for the Kattendijk Formation by The National Commission for Stratigraphy in Belgium (Deckers J. et al., 2023).

Additionally, results from Figure 5.7 and Table 5.4 indicate that Leuven glauconite is predominantly fine-grained in its natural state, whereas the Antwerp sample mainly consists of sand-sized pellets with only up to 20 percent fines by weight. As later shown in Subsection 6.1, both samples contain about 15 percent sand-sized glauconite pellets. This distinction between the sand- and fine-sized forms becomes important when evaluating shearing behavior and sand degradation in soil-steel interface direct shear tests.

Organic Content

The organic content was only looked into for the surficial Leuven sand sample. As a result, it was estimated to be around 4 percent with insignificant difference between samples prepared through oven-drying at 65°C and 105°C. The primary purpose of this estimation was to eliminate the possibility that organics would play a role in the proposed interface shear strength characterization. Since only trace organics were found, this was no longer a concern.

Atterberg Limits

Atterberg limit test results for the two uncrushed glauconitic sand samples are summarized in Table 5.5 and shown in plasticity chart in Figure 5.8. As expected of a soil with little fines, Antwerp sand exhibited low plasticity, classifying as silt (ML) based on Atterberg limits alone. In the case of Leuven sample, the resulting plasticity was higher, pointing to a borderline classification between CL and ML (lean clay to silt). It appears that both materials exhibited slightly higher plasticity when left to air-dry rather than being subjected to oven-drying. This could be explained by clumping of the heated particles and, thus, reduction of fines content in soil matrix. Nevertheless, the effect of sample preparation appears to be negligible. The differences between test results may also be explained by their sensitivity to operator's technique and experience.

Table 5.5. Atterberg Limit Results for Natural Glauconitic Sand Samples

Sample	LL (%)	PL (%)	PI (%)
Leuven Sand	32.7 – 38.3	23.2 – 26.2	8.5 – 13.0
Antwerp Sand	28.5	22.4 – 23.9	4.5 – 6.1

The obtained Atterberg limit values fit closely with results of analogous tests for New Jersey glauconite sands with GCs exceeding 90 percent published by Westgate et al. (2023). These samples were either non-plastic or exhibited low to medium plasticity depending on the fines content in their natural state.

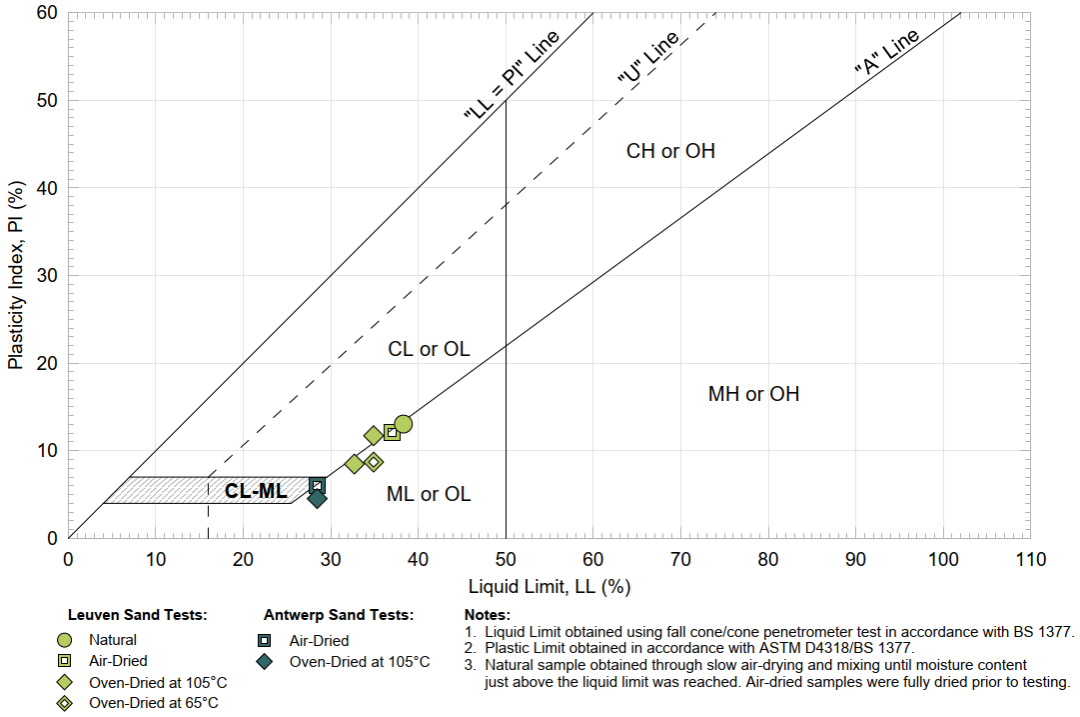

Figure 5.8. Natural Glauconitic Sand Plasticity Chart

Noteworthy, in the case of glauconitic sands one of the initial concerns with the Atterberg limit tests was that continued mixing of soil between each fall cone test run could affect its mechanical and water retaining properties. However, Figure 5.9 that shows the order in which the average depth of penetration results between 15 and 25 mm were obtained for a natural Leuven sand sample, demonstrates that there is no obvious trend of such sort. This was true for all the performed liquid limit tests.

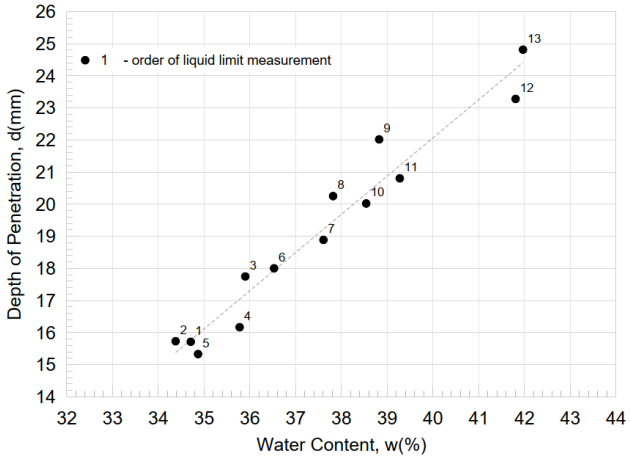

Figure 5.9. Example of Fall Cone Test Results for a Natural Sample

Specific Gravity

Summary of specific gravity results obtained for different Leuven and Antwerp sand fractions is provided in Table 5.6 and Figure 5.10.

Table 5.6. Specific Gravity (G_s) Results

Tested Sample	Leuven Sand	Antwerp Sand
Full Fraction	2.74	--
< 2 mm Fraction	2.65 – 2.71	2.69
Separated Glauconite with Fines	2.78	--
Separated Glauconite – Washed after Dispersion	2.71	2.79
Tailings (Quartz) after Dispersion	2.64	2.65

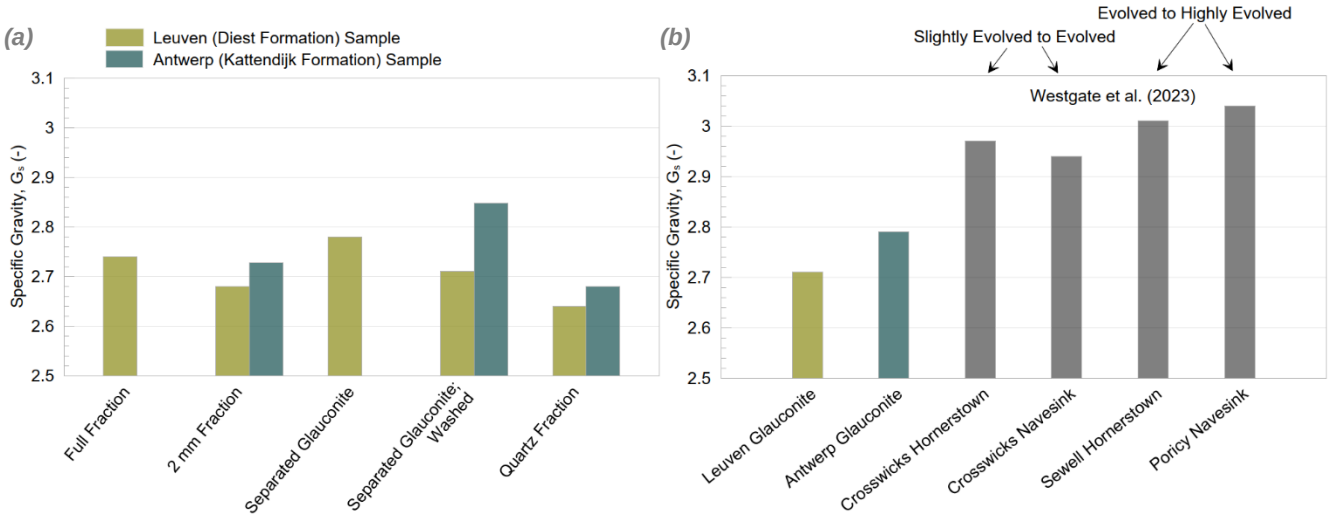

Figure 5.10. Specific Gravity (G_s): (a) Test Result Summary and (b) Comparison of Average Values with New Jersey Glauconitic Sand Results (Westgate et al., 2023)

As shown in Figure 5.10(a), to directly compare peloidal properties of the two formations, specific gravity tests were conducted on both the as-received material and extracted glauconite alone. For the Leuven sample, tests were performed on separated glauconite with the natural fines content and after washing of the sand with dispersion for the PSD tests. Exclusion of fines, which, as Adriaens et al. (2014) concluded, formed from reworked glauconite pellets, led to a decrease in specific gravity, likely due to their lower microporosity. For the Antwerp sample, specific gravity was only measured without the fines due to their low natural content. The separated specific gravity Leuven and Antwerp samples are shown in Figure 5.11.

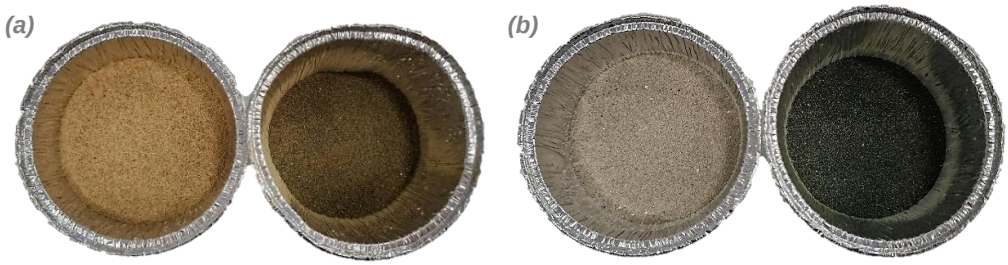

Figure 5.11. Separated Specific Gravity Samples: (a) Leuven and (b) Antwerp Sand

The gas pycnometer tests did not reveal any significant differences in composition or microporosity between the two characterized sands. The generally slightly higher G_s values for the Antwerp glauconite are consistent with its higher maturity established based on the color and chemical composition as discussed earlier in the report. Overall, the resulting G_s values of 2.7 to 2.8 are close to results provided for the Kattendijk (Piedrabuena, 2024) and Berchem (Westgate et al., 2022) Formations in Antwerp, Belgium.

As demonstrated in Figure 5.10(b), when comparing new results to literature, specific gravity appears to be higher for the slightly evolved to evolved and evolved to highly evolved New Jersey samples (Westgate et al., 2023). A reasonable hypothesis is that iron enrichment was greater in the substrate at New Jersey sites, causing the pellets

to be denser. When comparing bulk chemical data from the Diest and Kattendijk glauconite pellets (Adriaens et al., 2014) with samples tested by the U.S. research group, the latter generally show higher ferric oxide (Fe_2O_3) content. However, the Crosswicks Navesink sample has a closely matching iron oxide concentration (~ 19%) while still exhibiting higher specific gravity. If not the iron uptake, which commonly occurs during the first stage of glauconization and does not serve as a reliable index of glauconite maturity (Odin & Matter, 1981; Amorosi et al., 2007), increase in specific gravity at higher stages of evolution may be explained by the reduction in microporosity accompanying recrystallization.

Minimum and Maximum Index Density

Minimum and maximum index density results are summarized in Table 5.7 together with the values from an analogous test on the Kattendijk Formation (Antwerp) glauconitic sand sample carried out at Deltares (Piedrabuena, 2024). The comparison shows that minimum density test produced very similar results for the two materials. However, the resulting maximum density value was higher for the Leuven sample tested as part of this project. This could be explained by the higher presence of fines and, thus, increased clumping with oven-drying for the latter.

Table 5.7. Minimum/Maximum Index Density Test Results

Sample	Minimum Density Test			Maximum Density Test		
	ρ_{min} (g/cm^3)	$\gamma_{d,min}$ (kN/m^3)	e_{max}	ρ_{max} (g/cm^3)	$\gamma_{d,max}$ (kN/m^3)	e_{min}
Leuven Sand	1.07	10.55	1.55	1.46	14.31	0.88
Antwerp Sand; Dry Method; Full Fraction (Piedrabuena, 2024)	1.06	10.39	1.55	1.33	13.08	1.03

It is important to note that minimum and maximum index density tests are susceptible to errors and can yield varying results depending on the test method. This is particularly true for sands glauconitic fines, which tend to form clumps that degrade unevenly during compaction and other handling processes. In this project, results from Table 5.7 will only be used as a reference for consistent sample preparation in interface shear tests discussed in Sections 5.3 and 6.2.

5.3 Interface Shear Strength Characterization

The goal of the interface shear strength characterization on uncrushed samples was to determine the expected range of residual interface friction angles for natural glauconitic sands sheared against steel surfaces, simulating soil-pile interaction at low displacements, without a significant level of glauconite degradation reached. Performing these tests without shearbox reversal allowed for their comparison with the shearing behavior and strength results published by Westgate et al. (2023) for New Jersey glauconitic sands. Different test conditions were introduced to assess how variables such as the normal stress, shear rate, and steel roughness would affect peloidal breakage and the resulting soil-steel interface shearing behavior.

Table 5.8 serves as a summary of successful soil-steel direct shear tests conducted on uncrushed Leuven and Antwerp glauconitic sands. It provides the applied test conditions and the resulting interface friction angles, calculated from failure envelopes passing through the origin. Although some results may actually reflect the residual strength (δ_{res}) with steady values established at limited displacements, they are not explicitly identified as such. Instead, the term "post-peak" will be used to account for tests terminated before the residual condition was established.

Interface friction angles summarized in Table 5.8 were defined on a case-by-case basis considering tilting of the load cap occurring with continued shearing. Such rotation would affect load distribution at the interface as well as instigate material loss at the steel to soil contact surface. In tests on a rough steel plate (R_a ≈ 13 μm), relatively high tilting (up to 2 degrees) was usually observed after lateral displacement exceeded 8 mm. It could not be prevented with the material being inevitably lost to asperities in the blasted steel and remaining behind the sheared specimen as illustrated in Figure 5.12. Thus, post-peak interface friction angles for the “rough” interface tests were estimated as the average value between 4 and 8 mm of horizontal displacement.

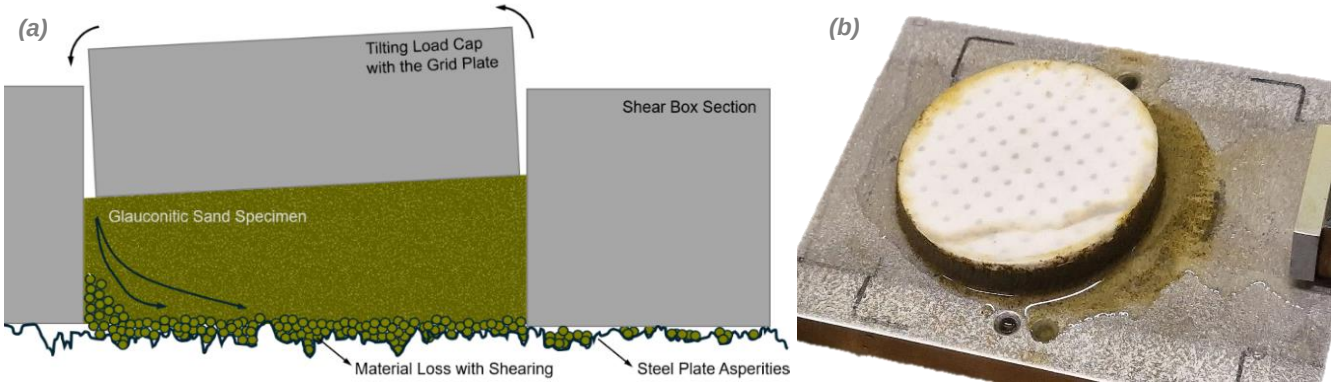

Figure 5.12. (a) Schematic Sketch of Load Cap Tilting Due to Material Loss and (b) Photo of the Leuven Sand Specimen with Material Lost to Asperities on a Rough Steel Plate

In tests conducted on a smooth steel surface (R_a ≈ 1 μm), asperities were too small to trap sand particles and cause material loss and, thus, load cap tilting was minimal. The associated interface friction angles were recorded as the average for lateral displacements between 8 and 15 mm. “Smooth” interface tests on Antwerp sample were the exclusion as in their case stabilization could not be achieved without shearbox reversals so the post-peak interface friction angle was taken as the average for the last 3 mm of shearing. In both cases, sharp reduction in shear stress at the end of the lateral displacement path was not considered in calculations.

In addition to the DS test results and variables discussed above, Table 5.8 includes average roughness (R_a) measurements for the steel plates taken before and after each interface shear test following procedure summarized in Section 4.4. In the end no remarkable reduction in roughness was observed throughout the conducted experimental program.

It is important to note that while end-of-consolidation void ratios were consistently estimated for quality control throughout the shear testing program, these values are not considered representative and will not be included in Table 5.8 or provided further in the report. This omission is justified by limitations associated with the uneven

disintegration of glauconitic clumps upon wetting, which would affect the pre-shearing density of a specimen. Given that the focus of this project is on residual interface shear strength, uncertainties in the initial dry density are acceptable, as they do not affect residual or post-peak shear strength results.

Table 5.8. Summary of Direct Shear Tests on Uncrushed Glauconitic Sand Samples

Sample	Steel Plate	Normal Stress (kPa)	Shear Rate (mm/min)	Steel Plate Average Roughness, R_a (μm)		Post-Peak Interface Stress Ratio (-)	Post-Peak Interface Friction Angle (deg)	Post-Peak Interface Friction Angle Summary (deg)
				Initial	Final			
Leuven (Diest Formation) Glauconitic Sand; 2 mm Fraction	Rough	75	0.05	12.80	12.74	0.55	28.8	*Average:* 29.2 deg *Std Dev:* 0.4 deg (2)
		150	0.05	12.79	12.76	0.57	29.6	
		300	0.05	12.84	12.74	0.55	29.0	
		150	5	12.69	12.70	0.57	29.8	
			0.5	12.86	12.84	0.56	29.3	
			0.05	12.76	12.86	0.55	28.7	
			0.005	13.00	12.80	0.56	29.1	
	Smooth	150	5	1.07 (1)		0.37	20.3	*Average:* 20.5 deg *Std Dev:* 0.4 deg (3)
			0.5			0.36	19.9	
			0.05			0.39	21.1	
			0.005			0.38	20.7	
Antwerp (Kattendijk Formation) Glauconitic Sand; 2 mm Fraction	Rough	150	0.5	12.74	12.79	0.57	29.5	*Average:* 29.5 deg *Std Dev:* 0.2 deg (2)
			0.005	12.79	12.82	0.57	29.7	
			0.005	12.82	12.79	0.56	29.2	
	Smooth	150	5	1.07 (1)		0.42	22.8	*Average:* 23.4 deg *Std Dev:* 0.7 deg (4)
			0.5			0.42	22.9	
			0.005			0.45	24.4	

(1) Smooth plate roughness was not re-measured after each test as any changes were expected to be negligible.
(2) For tests on rough steel plate post-peak (residual) interface friction angles were determined as the average value for horizontal displacements between 4 and 8 mm.
(3) For Leuven sand tests on smooth steel plate post-peak (residual) interface friction angles were determined as the average value for horizontal displacements between 8 and 15 mm.
(4) For Antwerp sand tests on smooth steel plate post-peak (residual) interface friction angles were determined as the average value for horizontal displacements between 12 and 15 mm.

Further subsections are intended to provide detailed results and analyses for each test sequence on uncrushed glauconitic sand samples as summarized in Table 5.8, focusing on one variable at a time. Note that in this report, negative vertical displacement values will signify contraction and positive - dilation.

Normal Stress Effects

Based on the performed literature review and observations from DeJong & Westgate (2009) in particular, it was originally expected that crushing of glauconite pellets induced at higher vertical stress levels would lead to changes in the exhibited shearing behavior and interface shear strength. In order to test this hypothesis, normal stresses of 75, 150, and 300 kPa were applied to the natural/uncrushed Leuven sand specimens under CNL conditions. To allow for their direct comparison, all tests were performed at a shear rate of 0.05 mm/min on a rough steel surface (R_a ≈ 13 μm). Antwerp sand was not included in this test sequence due to its lower glauconite content and, thus, lower possibility to observe changes in shearing behavior with peloidal breakage. Leuven sand DS data for the three normal stress cases are plotted in Figure 5.13.

As Figure 5.13 shows, increasing normal stress resulted in a greater shear resistance. However, results in terms of the shear stress ratio remained rather consistent between all three cases.

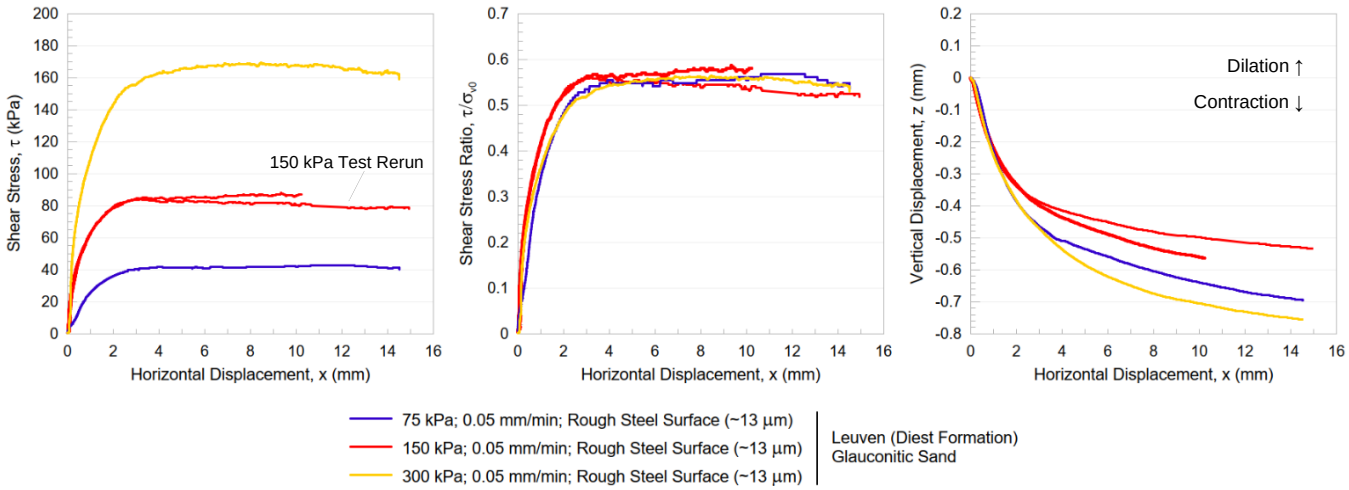

Figure 5.13. Direct Interface Shear Test Results for Evaluation of Normal Stress Effects

The natural Leuven sand exhibited contractive behavior with no distinct peak resistance, which agrees with findings from the literature. First, volumetric response at soil-structure interface is typically less dilative compared to that in sand-to-sand tests due to the sliding of grains, rigid boundary condition, and strain localization imposed by the rigid surface. This is supported by results from Westgate et al. (2023) and Guo et al. (2023) that clearly demonstrate the difference when comparing soil-steel and soil-soil DS tests performed on one material. Additionally, the recorded contractive response may be intensified by the degradation of glauconite pellets with shearing and loss of soil to asperities, a test limitation previously visualized in Figure 5.12.

As for the interpretation of a slight decrease in shear stress at horizontal displacements exceeding 8 mm, it may be ambiguous and the reduction could be explained either by reworking of sand particles with continued shearing or by redistribution of stresses accompanying material loss to the interfacial asperities. To ensure that tilting of the load cap resulting from soil loss on a rough steel plate would not influence the characterization, (residual) interface friction angle for uncrushed Leuven sand was derived using the average stress ratio for horizontal displacement range between 4 and 8 mm. The derived linear interface shear strength envelope passing through the origin as delineated in Figure 5.14 shows that normal stress effects at low displacements were minimal with the post-peak residual interface friction angle remaining at about 29 degrees.

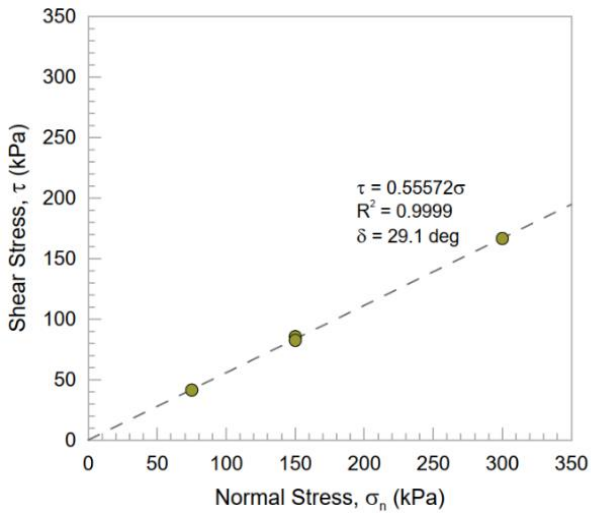

Notes:
1. Interface shear strength envelope plotted for tests performed on Leuven (Diest Formation) glauconitic sand sample sheared on a rough steel surface (~13 µm) at a shear rate of 0.05 mm/min.
2. Shear stress values correspond to the average results taken at intervals of lateral displacement between 4 and 8 mm, accounting for the load cap tilting typically observed with further shearing.

Figure 5.14. Interface Shear Strength Envelope for Leuven Sand Sample

The resulting value of approximately 29 degrees is consistent with the mean measured δ_{res} adopted in ICP (Jardine et al., 2005) and the new unified CPT-based (Lehane et al., 2022) methods for estimation of axial capacity of driven

piles in sand. Likewise, it concurs with the range of results from the unified database of ring shear steel-interface tests on sandy-silty soils maintained by the ICL and NGI (Liu et al., 2019).

Regarding the observed lack of change in residual stress ratios between tests conducted under the different normal stress levels, it is consistent with results for quartz sand sheared on a rough steel by Evgin and Fakharian (1996) and, in general, with the findings of a unified ring shear test database (Liu et al., 2019) shown in Figure 2.10. However, it is not in alignment with the higher roughness interface shear tests on silica sand from DeJong and Westgate (2009), which indicated a decrease in residual shear stress ratio with the increasing vertical load.

While both outcomes were shown possible for silica/quartz sands, cyclic interface direct shear tests on glauconite soils completed as part of the NTNU MSc thesis by Vahideh Rezaei and Dominika Walkowska (2024) support the second observation. In their case, after the total horizontal displacement exceeded 40 mm, difference in the residual interface friction angle between tests performed under normal stresses of 75 and 150 kPa became apparent with the greater values recorded for the lower normal stress level. It is worth noting that the angles were derived using shear strength envelopes passing through the origin and that their difference increased further with the continued tangential displacement.

Thus, Rezaei and Walkowska (2024) showed that in highly degradable glauconite-dominated sands (with GC above 90 percent), even with the limited range of normal stresses considered, particle breakage at the interface may increase with the higher vertical load application, causing reduction in the derived residual interface friction angle. For the natural Leuven sand, this effect was not clearly observed in monotonic interface DS test data either due to the significantly shorter shear path or the controlling quartz fraction remaining resistant to abrasion. To assess whether further reworking of glauconitic sands with the lower GC would impact the δ_{res} results, their degraded samples will be characterized separately in Section 6. In order to determine if, while not directly reflected in the DS results from Figure 5.13, glauconite pellet crushing was influenced by the increase in the applied normal load in monotonic shearing of the natural Leuven sand, laser diffraction PSD analyses were conducted after each run.

Several grams of a sheared sample were collected both from the interface and from the upper part of the specimen right below the grid plate that would not be subjected to shearing action, providing a baseline PSD. The collected material was tested using Microtrac BlueWave PSD analyzer as explained in Section 4.4. The results of this evaluation are shown in Figure 5.15.

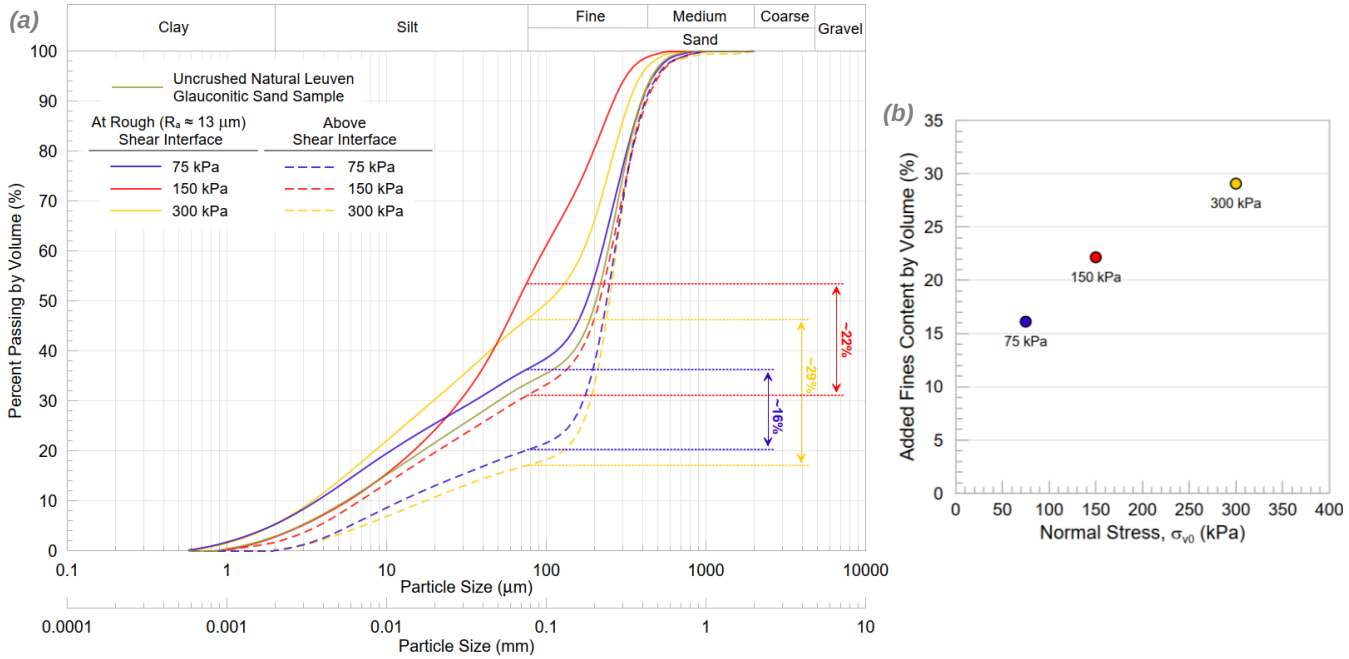

Figure 5.15. (a) Laser Diffraction PSD Analysis Results for Uncrushed Leuven Sand Sheared on Rough Steel under Various Normal Stress Levels and (b) Added Fines Content Summary

PSD curves from Figure 5.15 demonstrate a consistent increase in added fines fraction with the applied normal stress level. In the given experimental sequence, fines added after shearing comprised up to 16, 22, and 29 percent by volume under the normal stress of 75, 150, and 300 kPa, respectively. PSD curves for specimens collected above the interface zone and not subjected to shearing plot closely to results of analogous tests on uncrushed Leuven sand from Figure 5.6. This demonstrates that compression alone is unlikely to cause significant glauconite breakage in Leuven sample with the natural GC.

Noteworthy, the additional reworking of glauconite pellets with shearing at higher normal stress levels is not reflected in vertical vs. horizontal displacement plots of Figure 5.13. Although 150 kPa plot lines are expected to lie between the 75 and 300 kPa results, they actually show the lowest vertical displacement. This discrepancy may be caused by inconsistencies in sample preparation and variability of material that are difficult to gauge or prevent due to clumping of the oven-dried Leuven sand (see Figure 4.7) and their dissolution with flooding of the carriage.

To conclude, it was found that compression alone (with σ_n ≤ 300 kPa) is unlikely to instigate significant crushing of glauconite pellets in Leuven sand and that most of its degradation is caused by shearing against the interface. Although the increase in normal stress level was found to induce greater glauconite breakage within the shear zone, the resulting addition of fines was not reflected in the obtained shear stress ratios. The interface shear strength envelope defined based on the three normal stress points was shown to pass through the origin with no apparent adhesion identified. This indicates that either the experienced glauconite degradation was too low to be reflected in the DS test results or that the behavior of Leuven sand sheared along a rough steel surface was controlled by the predominant quartz fraction. A detailed discussion on contribution of quartz in the interface shear resistance behavior in Belgian samples will be provided further below in this section.

Shear Rate Effects

Based on results from Figure 5.13 and Figure 5.14, it was concluded that normal stress would not be the critical factor in assessment of glauconitic sands studied in this project. This allowed further analysis to focus on the effects of shear rate under a constant normal stress of 150 kPa. Displacement rates of 5, 0.5, 0.05, and 0.005 mm/min were considered for both the Leuven and Antwerp samples.

The obtained DS results plotted in Figure 5.16 indicate no clear correlation between the adopted shearing velocity and residual interface shear strength. Moderate variability observed in shear stress and vertical displacement progression between the tests is likely due to slight differences in specimen properties and preparation. The behavior of Leuven sand sample discussed in the subsection on normal stress effects also applies to results from Figure 5.16. As for the Antwerp sample, it exhibits slight dilation in the beginning, with a peak in shear stress at around 3 mm of horizontal displacement. Despite this, its volumetric behavior remains contractive throughout the entire shear path, though with less vertical displacement compared to Leuven sand, mainly due to the lower fines and glauconite content.

Similar to the effects of normal stress, rate effects may not be evident in natural Belgian glauconitic sands either due to the limited tangential displacement in monotonic DS tests, which prevented formation of a reworked shear zone, or because of the high quartz content. It is possible that dependence on the adopted shear rate would become noticeable with continued generation of glauconitic clay at the interface, leading to the change in shear resistance in line with the backbone curve from Figure 2.15. However, since natural Leuven and Antwerp samples exhibit behavior typical for the coarse-grained soils, negligible rate effects are consistent with findings for sands from the ICL and NGI ring shear programs (Quinteros et al., 2017; Liu et al., 2019) mentioned in Section 2.

Nevertheless, although not reflected in the DS data from Figure 5.16, shear rate changes may have affected glauconite pellet breakage at soil-steel interface. To see if this was indeed the case, post-shearing laser diffraction PSD analyses were performed for the Leuven specimens sheared against the rough (R_a ≈ 13 μm) interface with the obtained curves shown in Figure 5.18. The added fines content ranged between 15 and 22 percent without a clear correlation to shear rate. While the lowest velocity of horizontal displacement (0.005 mm/min) may have reduced degradation by allowing particles more time to readjust and deform, differences in results might also just reflect the natural material variability and limited sensitivity of laser diffraction method in detecting fines.

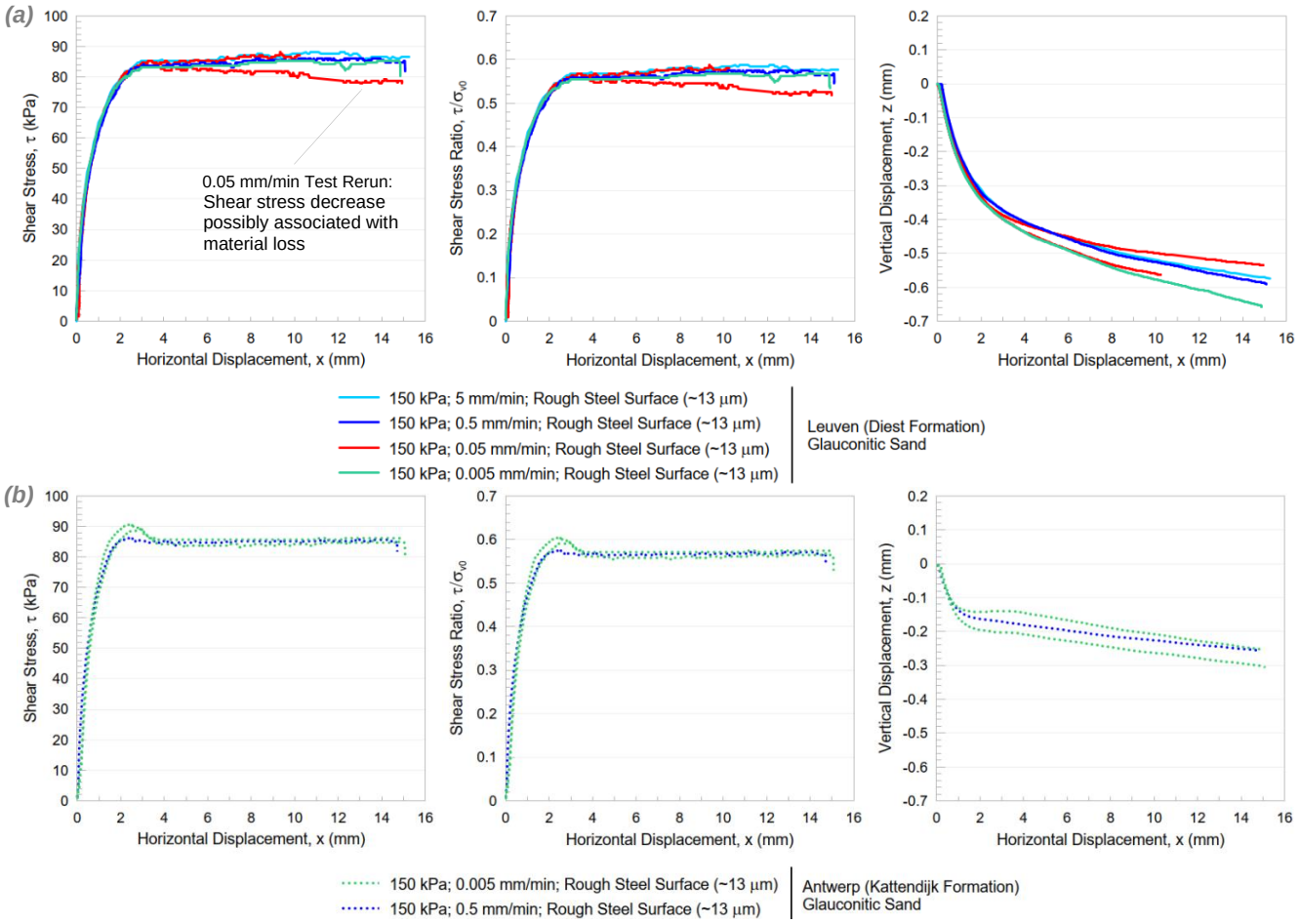

Figure 5.16. Direct Interface Shear Test Results for Evaluation of Shear Rate Effects on a Rough Steel Surface for (a) Leuven and (b) Antwerp Glauconitic Sand Samples in Natural (Uncrushed) State

As mentioned above, according to prior research (Quinn et al., 2012; Martinez & Stutz, 2018), formation of plastic fines at the interface is expected to lower shear strength as the rate of tangential displacement increases, resembling the backbone curve from Figure 2.15. However, the 2024 NTNU graduation project (Rezaei & Walkowska, 2024) reached an opposite conclusion. Findings from cyclic DS tests with the sequential shear rate adjustments on a single specimen, illustrated in Figure 5.17(a), indicated that the residual interface friction angle increased with the increasing velocity of horizontal displacement (as illustrated in Figure 5.17(b)). Yet, this approach introduces coupled effects and may hinder data interpretation, as the highest displacement rate was tested on a natural/uncrushed sample, with each subsequent velocity change being imposed on sand that had already been degraded by prior shearing cycles, with the growing fines fraction generated in the process. Therefore, shear rate effects could not be discerned from the impact of glauconite breakage.

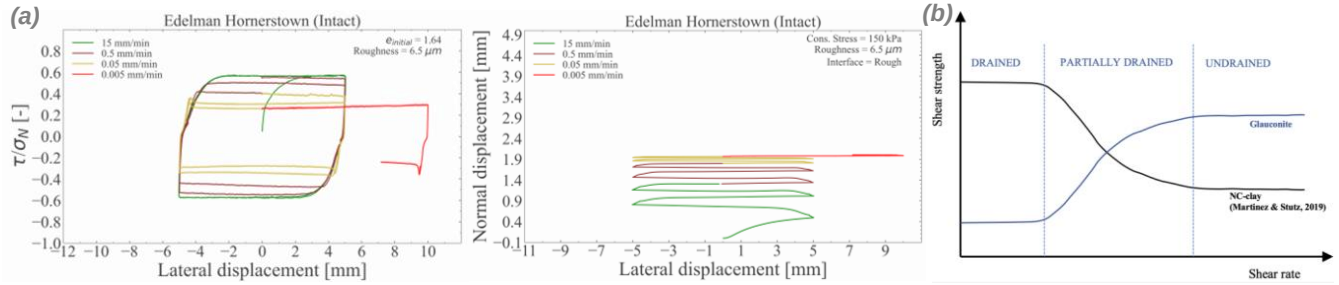

Figure 5.17. (a) Cyclic Interface Direct Shear Test Plots and (b) Shear Strength vs. Shear Rate Summary for New Jersey Glauconite Sands from the NTNU Master Thesis by Rezaei and Walkowska (2024)

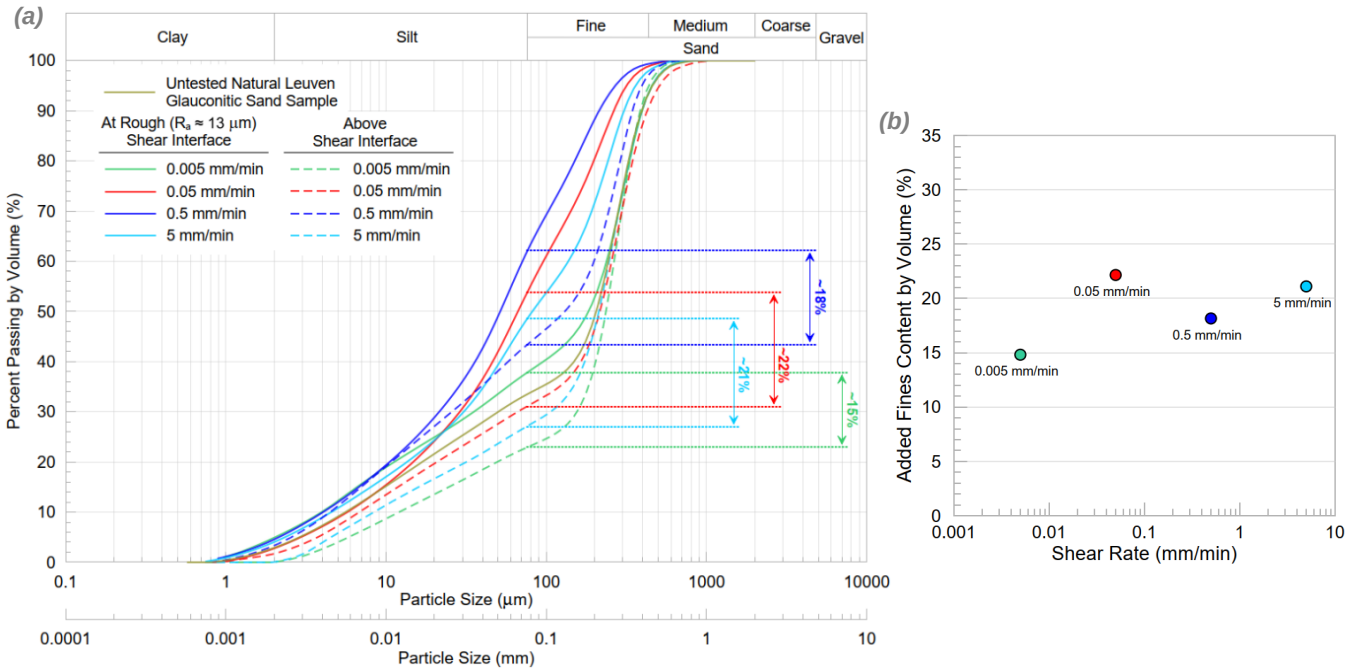

Figure 5.18. (a) Laser Diffraction PSD Analysis Results for Uncrushed Leuven Sand Sheared on Rough Steel under Various Shear Rates and (b) Added Fines Content Summary

Given the limitations of shear rate assessment at low tangential displacements in this project and the complexities of evaluation performed by Rezaei and Walkowska (2024), it is recommended to examine rate-dependence of glauconitic sands by testing each fixed rate on a separate, newly prepared specimen, allowing for an isolated analysis of further degradation effects. Additionally, post-shearing PSD tests proved valuable for capturing glauconite pellet reworking and comparing the degraded material response to shearing with the previous observations for sands, clays, and sand mixtures as outlined in Subsections 2.3 and 2.4.

In conclusion, while monotonic interface DS tests on Leuven and Antwerp sands indicted no obvious shear rate effects (as shown in Figure 5.19, which includes smooth interface tests discussed further below), this is unlikely to apply to full-scale pile installations, where glauconite degradation would be much greater. Therefore, further testing at higher displacements or on pre-crushed specimens is needed to draw relevant conclusions on shear rate effects for glauconitic sands from Belgium.

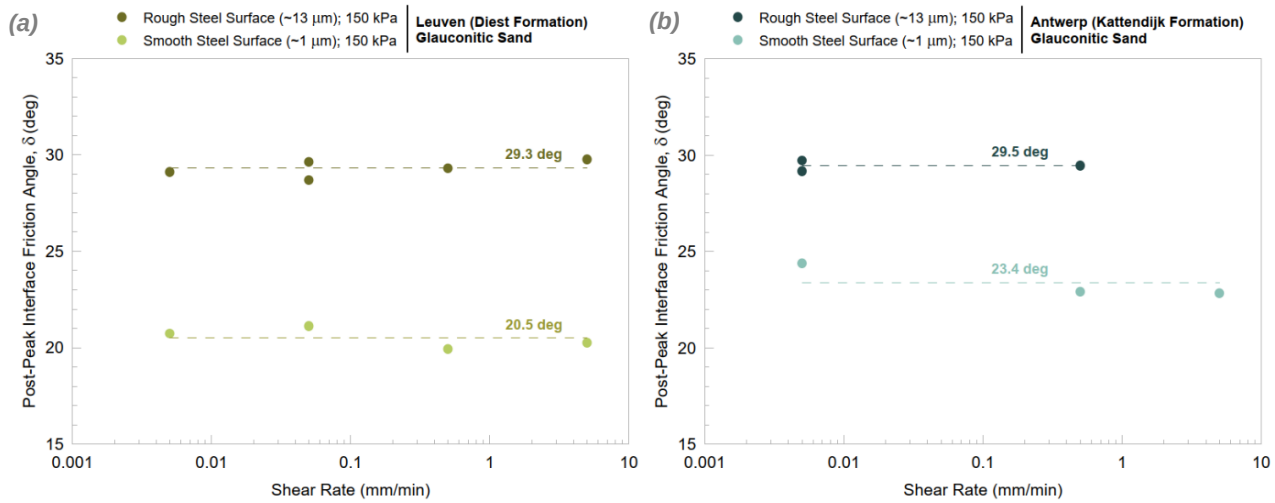

Figure 5.19. Shear Rate Effects Summary for (a) Leuven and (b) Antwerp Glauconitic Sand Samples in Natural (Uncrushed) State

Roughness Effects

For comparison with the rough (R_a ≈ 13 µm) interface results from Figure 5.16, plots for an analogous test sequence on a smooth (R_a ≈ 1 µm) steel surface are shown in Figure 5.20. As expected, a decrease in roughness caused a significant reduction in interface shear strength. The post-peak interface friction angle (derived from the shear strength envelope passing through the origin) dropped by approximately 9 degrees for Leuven sand and 6 degrees for the Antwerp sample.

In contrast to the rough surface tests, where failure was visibly progressing within the soil specimens or in a combined manner following Tsubakihara et al. (1993) (see Figure 2.11), smooth interface tests seemed to proceed with sliding of soil on steel, in line with observations by Martinez and Frost (2017) visualized in Figure 2.6. This change in shearing mode is suggested by stress-displacement curves for the Leuven sand from Figure 5.16 and Figure 5.20. Looking at the latter, in tests on a smooth interface, after horizontal displacement exceeded 2 mm, shear stress leveled off and remained relatively stable with minimal fluctuations, indicating a somewhat consistent level of resistance after yielding. This is in alignment with the slip at particle contacts controlling the response. In contrast, shearing along the rough interface produced more variation in shear stress with hardening evident after about 5 mm of horizontal displacement, pointing towards an ongoing gain in resistance beyond the yielding point. This is consistent with propagation of failure inside the specimen accompanied by interlocking, rearrangement, and degradation of particles within the shear zone.

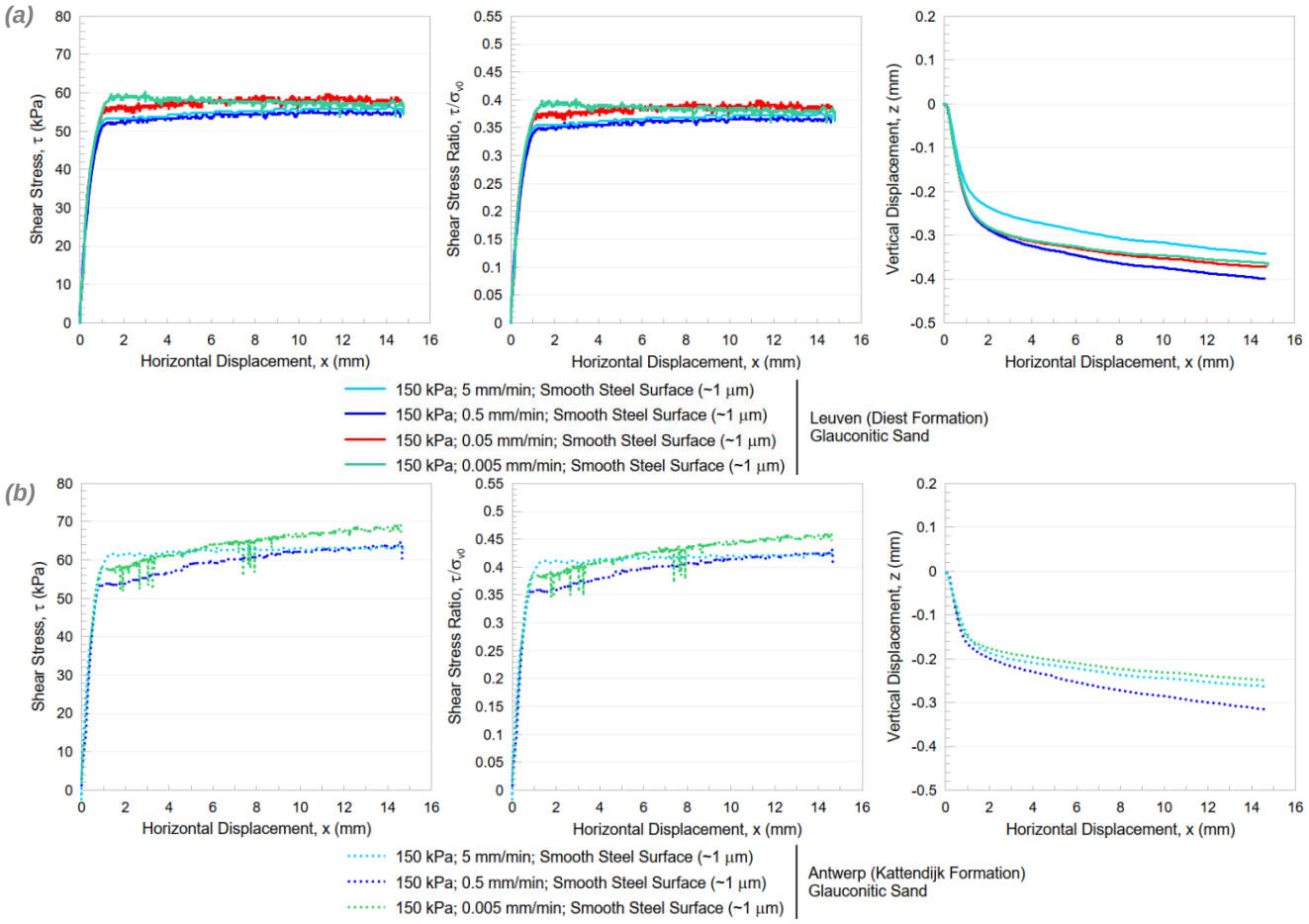

Figure 5.20. Direct Interface Shear Test Results for Evaluation of Shear Rate Effects on a Smooth Steel Surface for (a) Leuven and (b) Antwerp Glauconitic Sand Samples in Natural (Uncrushed) State

Understanding of the introduced shearing mechanisms allows for comparison of behaviors observed for the natural Leuven and Antwerp sands. Looking back at Figure 5.16 stress-displacement curves, even when sheared against a rough steel surface, Antwerp sand maintained a more consistent response, suggesting that it likely experienced

less alteration of the original structure. This is consistent with its poorly graded PSD, which would be less prone to particle rearrangement and densification, and low glauconite content leading to a relatively low degradation potential. As for the smooth interface DS data from Figure 5.20, the visible difference in post-peak shear resistance between the two materials could be attributed to the higher presence of plastic fines in natural Leuven sand. Nonetheless, the reason behind the substantial increase in shear stress with displacement in some of the interface DS tests on Antwerp sand specimens remains unclear.

Shifting focus to the vertical vs. horizontal displacement plots offers consistent conclusions regarding failure mechanisms triggered by shearing of Belgian sands on the smooth and rough steel plates. For instance, the poorly graded Antwerp sand experienced nearly identical total vertical displacement at the end of the shear path in both scenarios. However, in tests on the smooth interface volumetric response was more clearly contractive, without the tendency to dilate resulting in flattening of displacement curves between 1 and 4 mm of lateral movement (as seen in Figure 5.16). This points towards a full slip without any significant dilation-inducing particle rearrangement occurring at the smooth interface. A similar pattern is seen in the well-graded Leuven sand tests, but with significantly higher vertical displacement on the rough plate, indicating that localized stresses and particle interlocking within the forming shear zone led to perceivable glauconite pellet breakage.

The identified failure modes are evident in images of post-shearing zones remaining behind the specimens in Figure 5.21(a). Figure 5.21(b) provides further proof that clean sliding was taking place in tests on a smooth steel plate, while combined failure with shear deformation of the soil specimen was occurring in tests on a rough surface.

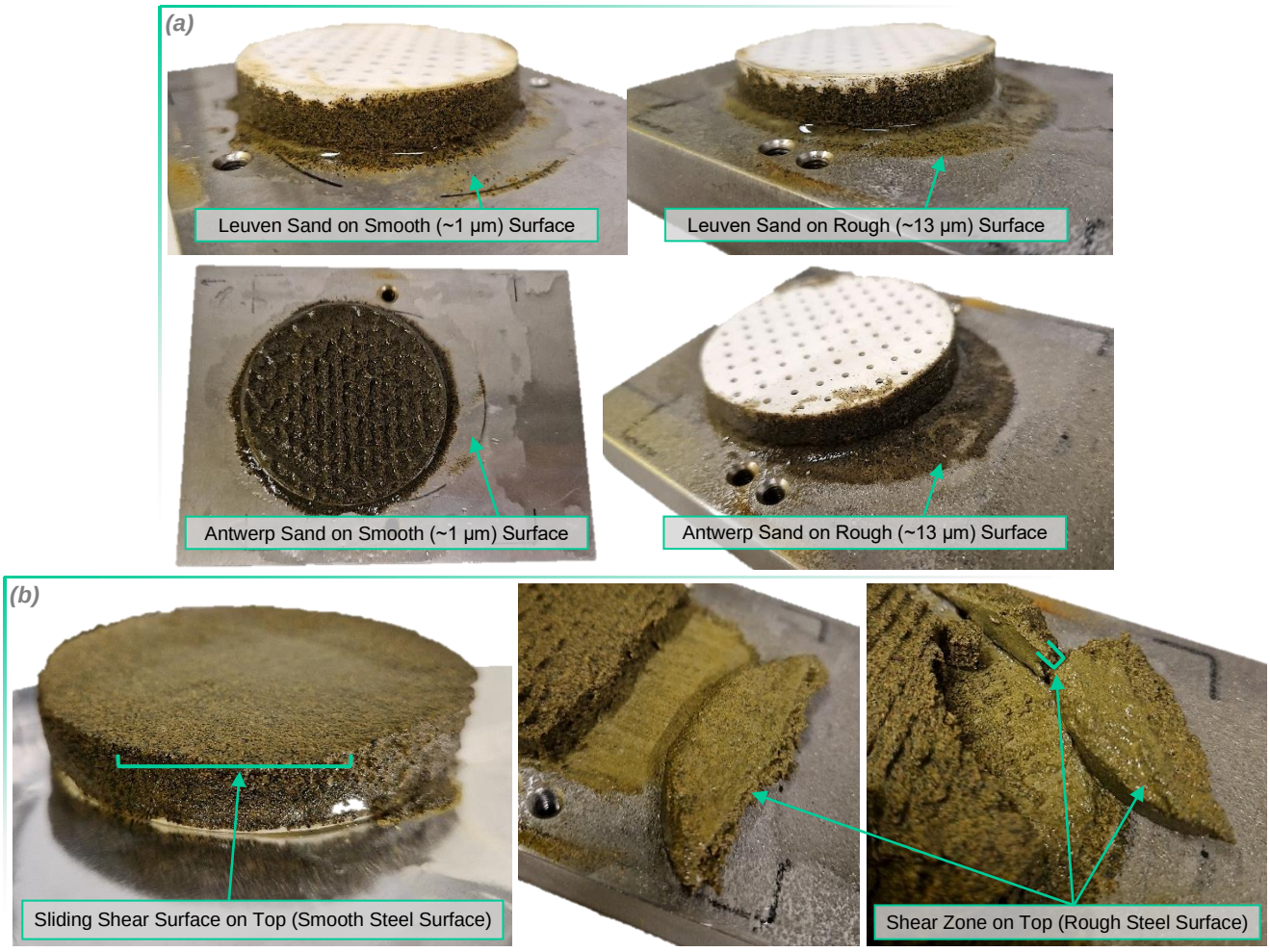

Figure 5.21. (a) Post-Shearing Photos for the Smooth and Rough Steel Plates (b) Leuven Sample Post-Shearing Photos with the Indication of Sliding Surface or Shear Zone(s)

Visual observations may also provide an explanation for the higher general variability in results for the smooth interface tests. A possible explanation is that, with full slippage, only particles in direct contact with the surface contribute to frictional resistance, making these tests more sensitive to material variability and, in turn, subject to greater uncertainty. Examples of two sliding surfaces with different protruding particles and composition are shown in Figure 5.22 to illustrate this idea.

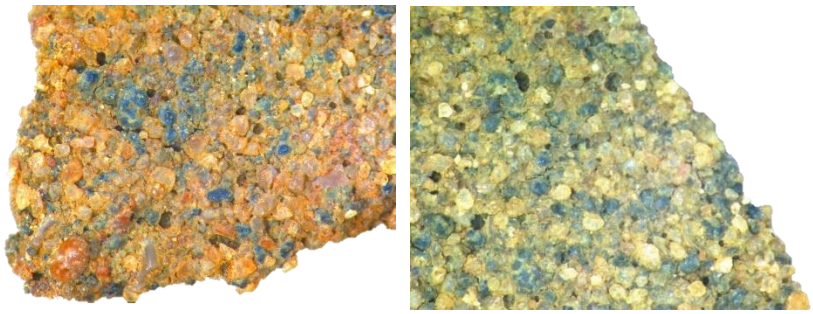

Figure 5.22. Digital Microscope Images of a Sliding Surface from Smooth Interface Tests on Leuven Sand

While Figure 5.22 can be used to show that glauconite pellets remained relatively intact when sliding of the specimen was the driving mechanism of failure, for comparison with the PSD changes summarized in Figure 5.18, an analogous tests sequence was added for the natural Leuven sand sheared on a smooth steel surface. The results showed a maximum increase in fines content of only 5 percent. Notably, the highest change was observed in sand subjected to slow shearing, while tests performed at displacement rates of 0.5 and 5 mm/min produced just 2 and 0.5 percent additional fines, respectively. This could indicate that the negligible crushing of glauconite pellets in smooth interface tests, if occurring at all, was mainly attributed to compression load that, in tests conducted at lower shear rates, was allowed to act for longer and with more time for the relative particle movement or deformation to take place.

To conclude the evaluation of roughness effects on natural glauconitic sands, all relevant test results are summarized in Figure 5.23. In addition to the previously provided average roughness (R_a), results are plotted for the relative roughness R, which is a ratio expressed as R_a over the median particle size, D_{50}. Please note that a clear relationship between the observed frictional resistance and (normalized) roughness cannot be established with only two cases considered per material.

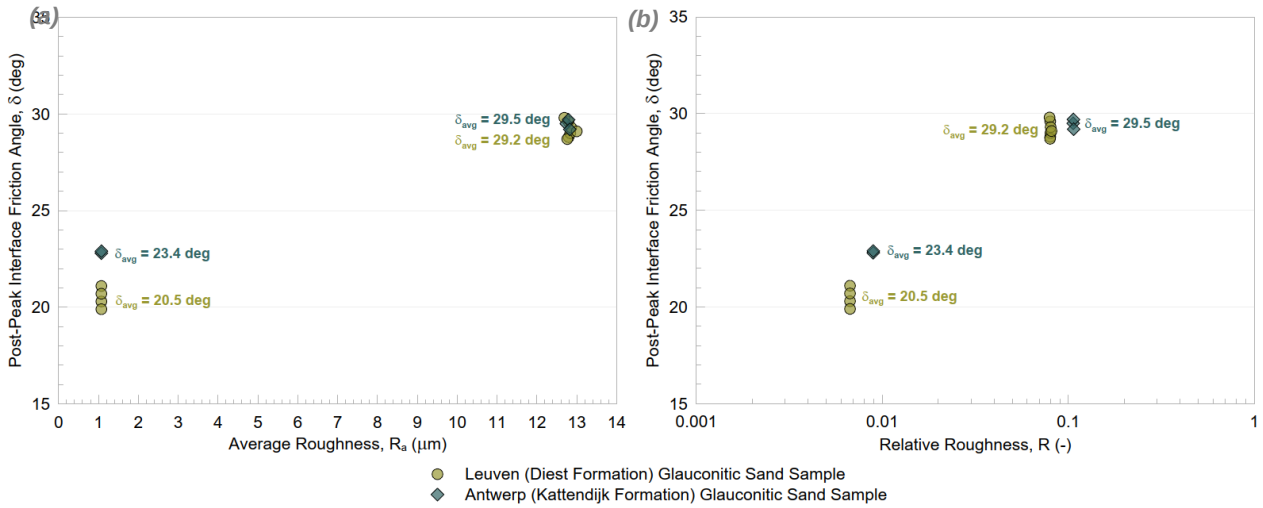

Figure 5.23. Post-Peak Interface Friction Angle vs. (a) Average Roughness and (b) Relative Roughness ($R = \frac{R_a}{D_{50}}$)

While the higher resulting post-peak interface friction angle for the Antwerp sample sheared on a smooth plate is consistent with its higher relative roughness (and higher angularity of quartz), this trend does not seem to apply to

the rough interface results. Here both sands exhibit similar resistance to shearing. First, looking back at Figure 2.4, this could indicate that critical roughness, at which residual interface friction angle (δ_{res}) becomes equal to the residual angle of internal friction (φ_{res}), has been reached. In general, this would be consistent with findings from other studies on sand-steel friction (Uesugi & Kishida, 1986; Uesugi et al., 1988; Rao et al., 1998; Liu et al., 2019). Ideally, evaluation of roughness effects would include a soil-to-soil direct shear test to determine whether ϕ_{res} is close to 29 degrees in the tested glauconitic sands. Unfortunately, these supplemental experiments were not completed due to a direct shear machine malfunction.

The acquired results indicate that as roughness increases, the shear mode transitions from full slip to internal failure within the specimen, accompanied by glauconite degradation in the shear zone. This shift in shear mode for the interfaces with higher roughness leads to greater resistance in glauconitic sands. Consequently, piles with a smooth surface finish may offer a solution to the existing drivability issues in glauconite-bearing soils by limiting the peloidal breakage and formation of added fines, provided they also perform adequately over their structural service life.

Quartz Fraction Effects

As discussed in Subsection 5.2, based on Figure 5.7, Leuven and Antwerp sands contain poorly graded quartz fraction with D_{50} of about 0.2 and 0.12 mm, respectively. As the PSD curves and Figure 5.24 show, in Leuven sand glauconite pellets are surrounded by the coarser and more angular (subrounded to subangular) quartz particles. In Antwerp sand glauconite pellets and quartz have roughly the same average size.

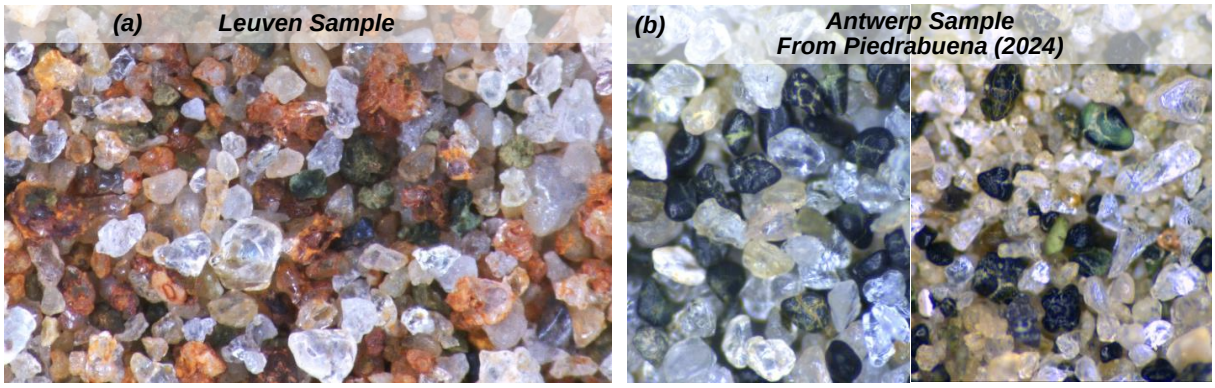

Figure 5.24. Images Showing Glauconite Pellets with Quartz Fraction for (a) Leuven and (b) Antwerp (Piedrabuena, 2024) Samples

Given that Leuven sand contains up to 53 percent of the coarser quartz fraction by weight, and Antwerp sand has only 20 percent glauconite in total, the interface shear strength and behavior of both these samples in their natural state could be mainly controlled by quartz. This would be in line with the 29-degree residual interface friction angle adopted in ICP (Jardine et al., 2005) and the new unified CPT-based (Lehane et al., 2022) design methods for driven piles in sand. Closely matching δ'_{20mm} values were also reported for non-glauconitic sands in the unified database of ring shear tests (Liu et al., 2019).

To provide a proper comparison with the relevant interface shear test results for quartz/silica sands from the literature (Reddy et al., 2000; Hu & Pu, 2004; Martinez & Frost, 2017; Liu et al., 2019; Guo et al., 2023; Westgate et al., 2023), interface friction angle and vertical displacement vs. horizontal displacement plots were added for the rough and smooth interface cases as shown in Figure 5.25(a) and (b), respectively.

Both figures include results from Westgate et al. (2023) for the New Jersey Sewell Hornerstown sample with GC exceeding 90 percent. The relative roughness (R ~ 0.013) in its interface shear strength evaluation was between the values estimated for the smooth and rough surface tests on Belgian sands from this project. However, the residual interface friction angle of 21 degrees was comparable to results for Leuven sand sheared on a smooth steel plate (R ~ 0.006). Given the limited displacement in monotonic DS tests performed in both experimental programs, the higher interface friction angles derived for Belgian sands likely result from the predominance of quartz rather than the lower degradation potential of glauconite when compared to the New Jersey sample.

The shearing behavior of Leuven and Antwerp glauconitic sands generally resembles that of the quartz sands tested under similar conditions. Although at relative density (D_r) of about 70 percent, sands are expected to exhibit dilation, in interface tests it is constrained by the solid plate. In Figure 5.25(a) this is demonstrated by displacement curve for the Geba sand (Guo et al., 2023). As expected, even greater (contractive) vertical displacement is shown by the Leuven sand specimens with the easily crushable glauconite pellets and higher fines content.

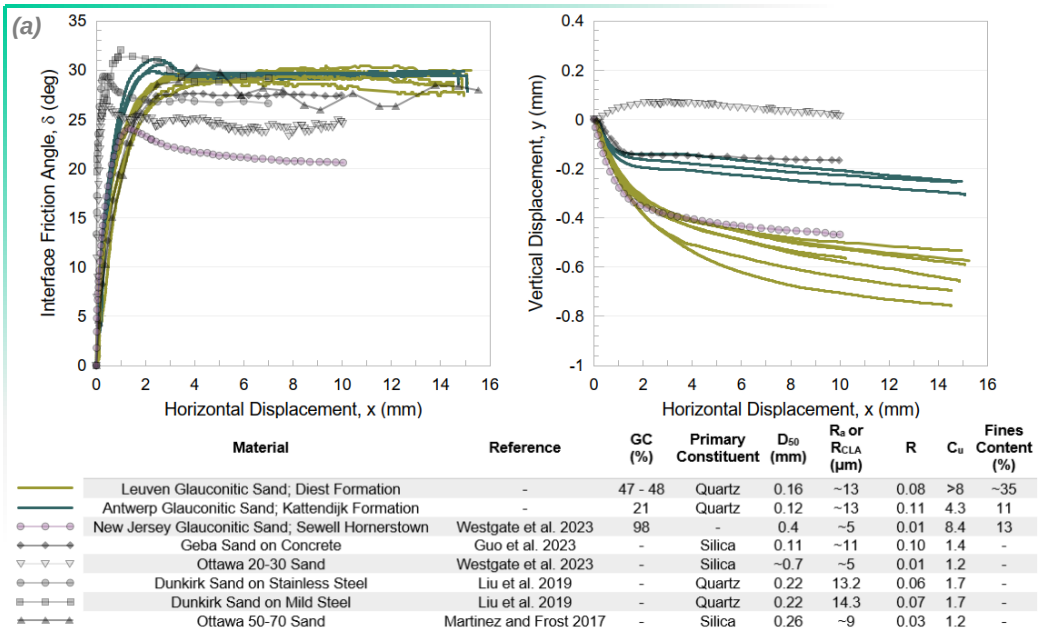

Material	Reference	GC (%)	Primary Constituent	D_{50} (mm)	R_a or R_{CLA} (µm)	R	C_u	Fines Content (%)
Leuven Glauconitic Sand; Diest Formation	-	47 - 48	Quartz	0.16	~13	0.08	>8	~35
Antwerp Glauconitic Sand; Kattendijk Formation	-	21	Quartz	0.12	~13	0.11	4.3	11
New Jersey Glauconitic Sand; Sewell Hornerstown	Westgate et al. 2023	98	-	0.4	~5	0.01	8.4	13
Geba Sand on Concrete	Guo et al. 2023	-	Silica	0.11	~11	0.10	1.4	-
Ottawa 20-30 Sand	Westgate et al. 2023	-	Silica	~0.7	~5	0.01	1.2	-
Dunkirk Sand on Stainless Steel	Liu et al. 2019	-	Quartz	0.22	13.2	0.06	1.7	-
Dunkirk Sand on Mild Steel	Liu et al. 2019	-	Quartz	0.22	14.3	0.07	1.7	-
Ottawa 50-70 Sand	Martinez and Frost 2017	-	Silica	0.26	~9	0.03	1.2	-

1. Results for Leuven and Antwerp sand samples are shown for tests perfromed under normal stresses of 75 to 300 kPa at shear rates ranging between 0.005 and 5 mm/min. D_r ~ 70%.
2. Test conditions for results from other researchers:
(Westgate et al. 2023): σ_n = 150 kPa; 0.1 mm/min; D_r ~ 70%; (Guo et al. 2023): σ_n = 150 kPa; 0.26 mm/min; D_r ~ 50%
(Liu et al. 2019): σ_n = 200 kPa; 0.1 mm/min; medium dense (e_0 = 0.740); (Martinez and Frost 2017): σ_n = 50 kPa; D_r ~ 60-65%

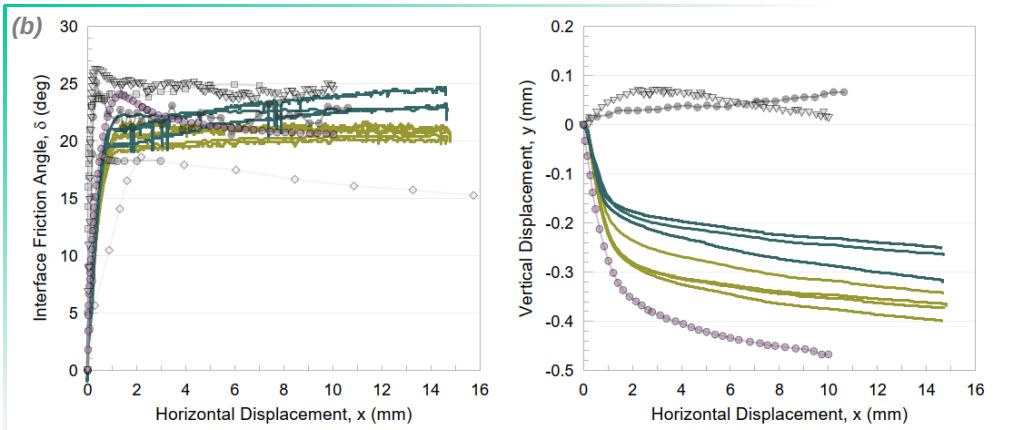

Material	Reference	GC (%)	Primary Constituent	D_{50} (mm)	R_a or R_{CLA} (µm)	R	C_u	Fines Content (%)
Leuven Glauconitic Sand; Diest Formation	-	47 - 48	Quartz	0.16	~1	0.006	>8	~35
Antwerp Glauconitic Sand; Kattendijk Formation	-	21	Quartz	0.12	~1	0.008	4.3	11
Dunkirk Sand on Stainless Steel	Liu et al. 2019	-	Quartz	0.22	1.2	0.005	1.7	-
Reddy et al.	Reddy et al. 2000	-	Silica	0.92	1.1	0.001	1.7	-
Ottawa 50-70 Sand	Martinez and Frost 2017	-	Silica	0.26	~1	0.004	1.2	-
Yongdinghe Sand	Hu and Pu 2004	-	Silica	~1.0	Smooth	-	2.1	-
New Jersey Glauconitic Sand; Sewell Hornerstown	Westgate et al. 2023	98	-	0.4	~5	0.013	8.4	13
Ottawa 20-30 Sand	Westgate et al. 2023	-	Silica	~0.7	~5	0.007	1.2	-

1. Results for Leuven and Antwerp sand samples are shown for tests perfromed under normal stress of 150 kPa at shear rates ranging between 0.005 and 5 mm/min. D_r ~ 70%.
2. Test conditions for results from other researchers:
(Liu et al. 2019): σ_n = 200 kPa; 0.1 mm/min; medium dense (e_0 = 0.740); (Reddy et al. 2000): σ_n = 150 kPa; D_r ~ 93%
(Martinez and Frost 2017): σ_n = 50 kPa; D_r ~ 60-65%; (Hu and Pu 2004): σ_n = 200 kPa; 0.6 mm/min; D_r ~ 90%
(Westgate et al. 2023): σ_n = 150 kPa; 0.1 mm/min

Figure 5.25. Interface Direct Shear Test Result Comparison with Literature: (a) Rough and (b) Smooth Structural Surface

To conclude, the observed interface shearing behavior of Belgium samples in their natural state is likely controlled or highly affected by quartz. While, on the one hand, predominance of quartz may hinder typical effects of glauconite breakage, its hard and angular particles may also induce reworking of glauconite pellets into fines, as it does in natural transport (Adriaens et al., 2014).

5.4 Natural State Characterization Summary

Based on the performed characterization, in accordance with the Unified Soil Classification System (USCS), natural (or uncrushed) Leuven and Antwerp samples classified as silty to clayey sand (SM to SC) and poorly graded sand with silt (SP-SM), respectively. The glauconite fraction in Leuven sand, comprising about 47 percent by weight, was shown to be finer than quartz. For Antwerp sand, glauconite content was estimated to be around 21 percent, with its gradation in close alignment with the particle size distribution of material (primarily quartz) remaining after the magnetic separation. Both samples showed low plasticity when uncrushed and had specific gravity within the 2.7 – 2.8 range.

Based on the literature review from Subsection 2.5, and results of this study, both Leuven and Antwerp samples appear to contain allogenic, or transported, glauconite. This is supported by findings from Adriaens et al. (2014), relatively low glauconite content, evidence of abrasion and fracturing, and pellet size at or below the D_{50} of quartz. Leuven sand appears to have been reworked to a lower D_{50} through higher exposure, weathering and, possibly, experienced energy of transport. The significant fines content in situ could also be explained by its greater degradation potential.

Using the potassium content from EDX (Table 5.1) and XRF (Table 5.2) analyses, along with data from Adriaens (2014), glauconite from both recovery sites can be classified as slightly evolved. Delving deeper, Leuven glauconite appears closer to the nascent boundary, while Antwerp sample leans more toward the evolved stage. This distinction primarily arises from differences in their color and texture. The general classification aligns with comparison to the higher maturity New Jersey deposits (Westgate et al., 2023; Westgate et al., 2024; Rezaei & Walkowska, 2024) as the Belgian sands exhibit lower angularity, have smaller median grain size, and potentially higher microporosity, indicative of an earlier evolutionary stage.

Although the difference in glauconization between Leuven and Antwerp samples appears minor, it is still expected to influence the interface shear test results when combined with distinctions in the USCS classification, glauconite content, and, possibly, degradation potential, which will be examined further in Section 6. This is why, considering the closely matching post-peak/residual interface friction angles derived for both sands, their behavior in soil-steel DS tests appears to be controlled by the predominant quartz fraction. This presumption is supported by the fact that the resulting δ_{res} value of 29 degrees (for the rough interface) is commonly reported and adopted for pile design in sand in the case of the standard surface roughness range (Jardine et al., 2005; Liu et al., 2019; Lehane et al., 2022). Additionally, volumetric response of Belgian samples differed, possibly suggesting a higher degree of reworking of the Leuven sand pellets, even though this was not clearly reflected in shear resistance.

Nevertheless, contribution of the added glauconite fines may become evident with continued shearing as a higher level of degradation is achieved. To investigate this, characterization of glauconitic sands undergoing further reworking of glauconite pellets is performed in the section below.

6 Degraded Glauconitic Sand Characterization Results

This section presents the material characterization of degraded Belgian samples to evaluate the geotechnical properties, behavior, and interface shear strength of glauconitic sands as if they were subjected to shearing during pile installation.

6.1 Index Test Characterization

In addition to the index characterization of natural glauconitic sand samples presented in Section 5.2, index tests were conducted on crushed and degraded sands to envision how their properties might change after pile installation and the breakage of glauconite pellets under continued shearing. Research methodology from works published by Westgate et al. (2023; 2024) was taken as the basis for this subprogram. This approach was adopted because the involved U.S.-based research group has an opportunity to compare crushed samples gathered around the augers or piles driven in glauconitic sands to degraded samples obtained in laboratory conditions. An example of one of such tube samples from Westgate et al. (2024) is shown in Figure 6.1.

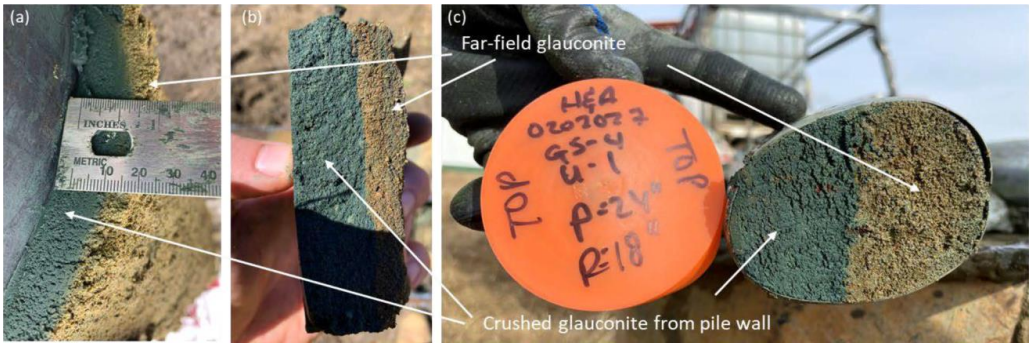

Figure 6.1. Samples of Crushed Glauconite from Pile Walls from Westgate et al. (2024)

Particle Size Distribution (PSD)

In order to assess the crushability of Belgian glauconitic sands, standard ASTM D422 procedure (ASTM, 2007) summarized in Section 4.3 was implemented with the modified duration of dispersion. The pre-soaked 2-mm sand was agitated in a stirring apparatus for time periods ranging between 10 seconds and 8 hours, replicating tests conducted by Westgate et al. (2023). The resulting curves are plotted in Figure 6.2(a) for the Leuven sand and Figure 6.2(b) for the Antwerp sample.

The visible increase in percent passing indicated by hydrometer analyses when compared to washings on a No. 200 (0.075-mm) sieve (pointed at by arrows in Figure 6.2) is not unexpected. This is because the sieving method accounts for an intermediate grain size, while hydrometer analysis measures the diameter of a sphere settling at the same rate as irregularly shaped particles like glauconite pellets. The greater discrepancy in samples stirred longer supports this, as continued abrasion likely creates more irregularly shaped fine particles. Despite this limitation, the results seem reasonable and will be used in future discussions on glauconite crushability.

In Leuven sand sample, the implemented degradation process added up to 8 percent fines by weight. The most significant change occurred in clay-sized fraction, which rose from 18 to 39 percent due to the breakdown of sand and silt-sized particles as shown in the fraction change summary of Figure 6.3. A part of this alteration could be explained by formation of clumps during oven-drying, and their disaggregation with continued agitation of the mixture. However, most of the aggregates appear to break down just from the addition of water as shown in Figure 4.7. This suggests that the observed increase in percentage of clay-sized particles was caused by the degradation of glauconite pellets, as with New Jersey sands tested by Westgate et al. (2023) and Campine Basin soils studied by Adriaens et al. (2014). This conclusion can be validated using glauconite content measured in washed sand fraction remaining after each hydrometer test (performed with a different dispersion period). As shown in Figure 6.3 for Leuven sample, curve added for GC in sand is parallel to that of the decreasing sand fraction, pointing towards the continuous crushing of sand-sized pellets into fines.

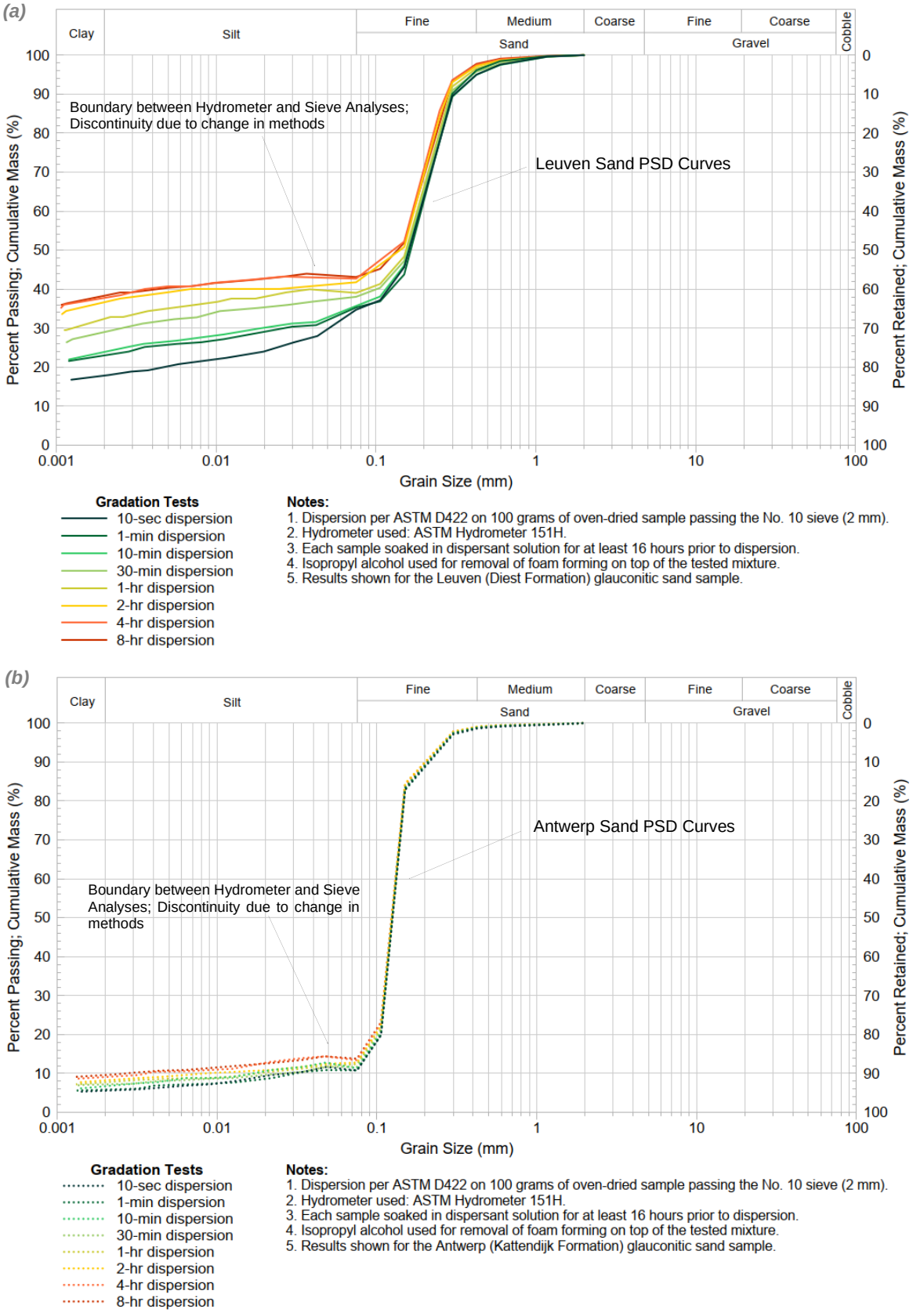

Figure 6.2. PSD Curves for Dispersed (a) Leuven and (b) Antwerp Sand Samples

In the case of Antwerp sand sample, the maximum increase in fines content that could be achieved following the same procedure was only about 3 percent by weight. The clay-sized fraction increased from 5.5 to 9.6 percent after 8 hours of stirring. However, glauconite content in sand fraction remained rather stable and decreased by no more than 1 percent by weight. This could indicate that the bulk of transformation from sand- to clay-sized fraction was actually caused by disintegration of clumps and detachment of fines from sand particles. Alternatively, there is a possibility that glauconite pellets that broke down with further dispersion were not initially captured by magnet due to their lower magnetic susceptibility likely associated with the lower stage of evolvement (Amorosi, 1997).

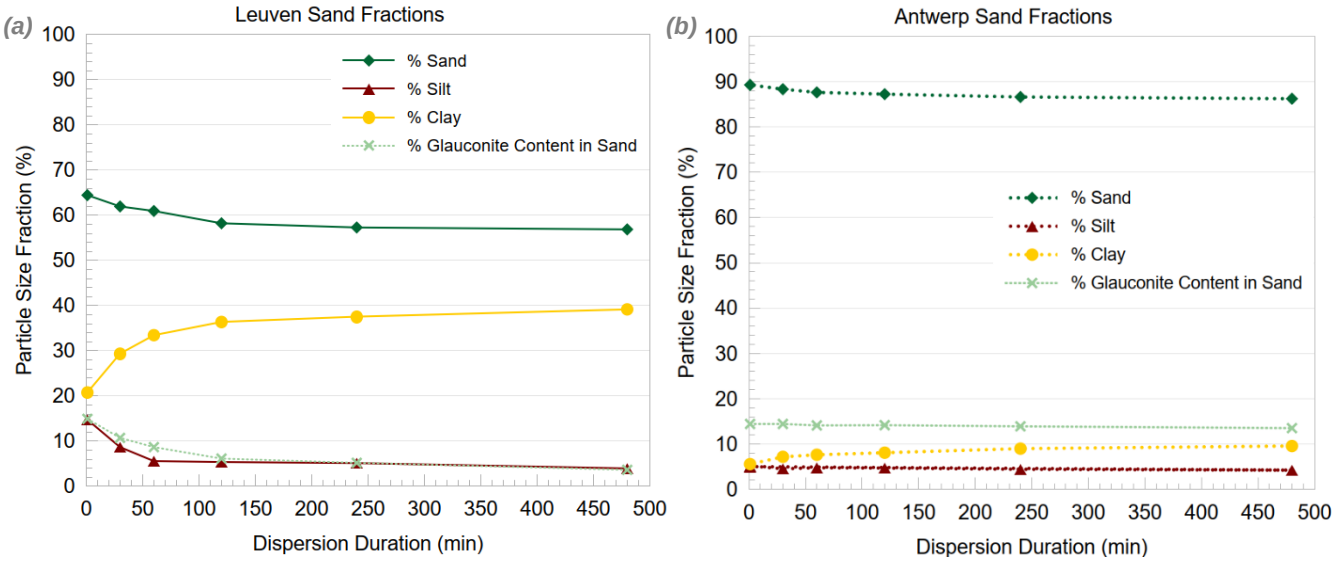

Figure 6.3. Summary of Dispersion Results for (a) Leuven and (a) Antwerp Sand Samples

Glauconite Content (GC) in Sand Fraction

As mentioned above and shown in Figure 6.3, an additional evaluation step was taken when assessing the crushability of glauconite pellets, and glauconite content was measured in washed sand fraction following each PSD test using the magnetic jar method. Figure 6.4 presents plots illustrating degradation of sand-sized glauconite with dispersion, previously shown in Figure 6.3, but combined here to facilitate a direct comparison between the Leuven and Antwerp samples. Additionally, data points for the natural GC measurements discussed in Subsection 5.2 are included to visualize the relative proportion of glauconitic fines in uncrushed Belgian sands (in situ).

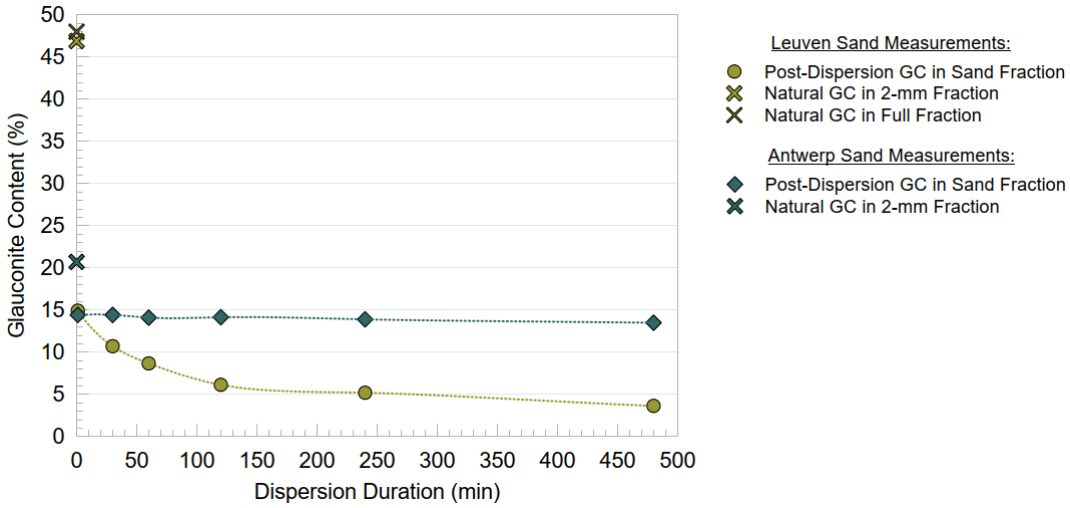

Figure 6.4. Summary of Sand-Sized Glauconite Content Measurements for Natural and Dispersed Leuven and Antwerp Sands

Figure 6.4 demonstrates that Leuven and Antwerp samples had an identical glauconite content in peloidal (sand-sized) form as indicated by the PSD tests ran in accordance with ASTM D422 following 1-minute dispersion. Therefore, in its natural state as found in situ, Leuven sand appears to include about 32 percent of glauconitic fines that can be separated by magnet. In Antwerp sand, only up to 6 percent of the total mass may be comprised of fine-grained glauconite.

According to the study by Adriaens et al. (2014) that included a Diest (Hageland) Formation sample from the Kesselberg outcrop, a large majority of clay-sized glauconite is naturally present in Campine Basin samples. As mentioned earlier, authors suggest that its origin is not authigenic but related to the mechanism of glauconite pellet abrasion and disintegration upon transport together with the quartz sand (Adriaens et al., 2014). This observation is consistent with the relative percentages of glauconitic fines in natural Leuven and Antwerp sands reflecting their degradation potential as indicated in Figure 6.4. After 8 hours of stirring, considering the initial peloidal glauconite content (approximately 15 percent), more than 76 percent of sand-sized pellets broke down into fines in Leuven sand, and only 6 percent in the Antwerp sample.

To demonstrate how the 76 percent degradation looks in Leuven sand, Figure 6.5 provides microscopic images of the washed sand fraction after 1-minute and 8-hr dispersion periods.

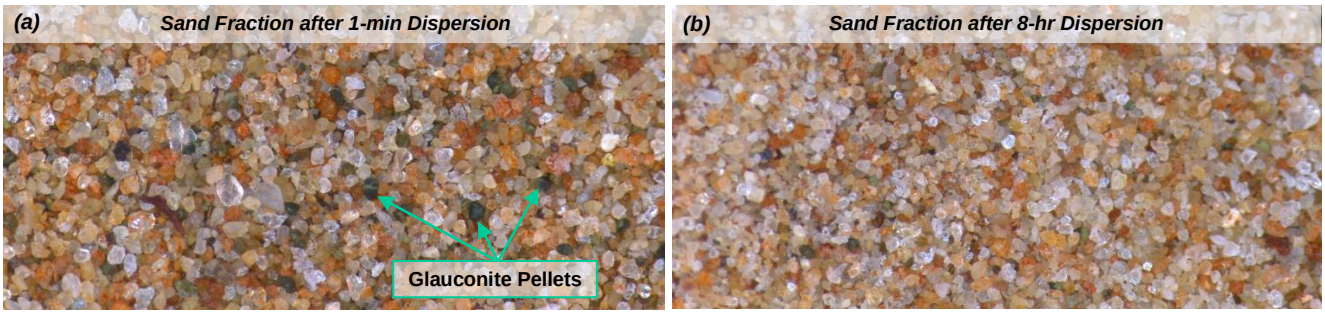

Figure 6.5. Leuven Sample Sand Fraction after Hydrometer Tests Using (a) 1-min and (b) 8-hr Dispersion

The degradation of glauconite pellets from Belgian samples can also be compared to the percentage of reworked sand-sized particles in New Jersey soils using 1-hour dispersion results, which is attempted in Table 6.1. It is worth noting that this comparison is limited by differences in laboratory dispersion methods and equipment as well as the potential influence of quartz fraction on abrasion in Leuven and Antwerp sands.

Table 6.1. Comparison of Glauconite Crushability and Coefficient of Uniformity for Belgium and New Jersey Sands

Sample	C_u	GC (%)	Peloidal GC (%)	FC (%)	Sand Fraction Reduction (%) (1)	Reworked Glauconite Pellets (%) (2)
Leuven (Diest Formation)	>70	47	~15	~36	3.5	23
Antwerp (Kattendijk Formation)	3.5	21	~15	~11	1.7	11
Navesink (Westgate et al., 2024)	37	-	~95 (3)	~19	26.5 - 28	28 – 29
Hornerstown (Westgate et al., 2024)	231	-	~95 (3)	~30	38.5 - 43	40 - 45

(1) After 1-hr Dispersion.
(2) Sand fraction reduction (%) divided by peloidal GC (%).
(3) Only coarse-grained content provided in Westgate et al. (2024).

Based on the summary from Table 6.1, Antwerp sand showed the highest resistance to abrasion, which appears to coincide with the lowest coefficient of uniformity (C_u). To further explore this relationship between the initial particle size distribution and degradation potential exhibited by glauconite, Figure 6.6 includes gradations for the magnetically separated material from Leuven and Antwerp samples. Full-fraction results are plotted for New Jersey sands as their GC (coarse-grained) exceeds 95 percent (Westgate et al., 2024) and, thus, can be directly compared to glauconite extracted from Belgian soils.

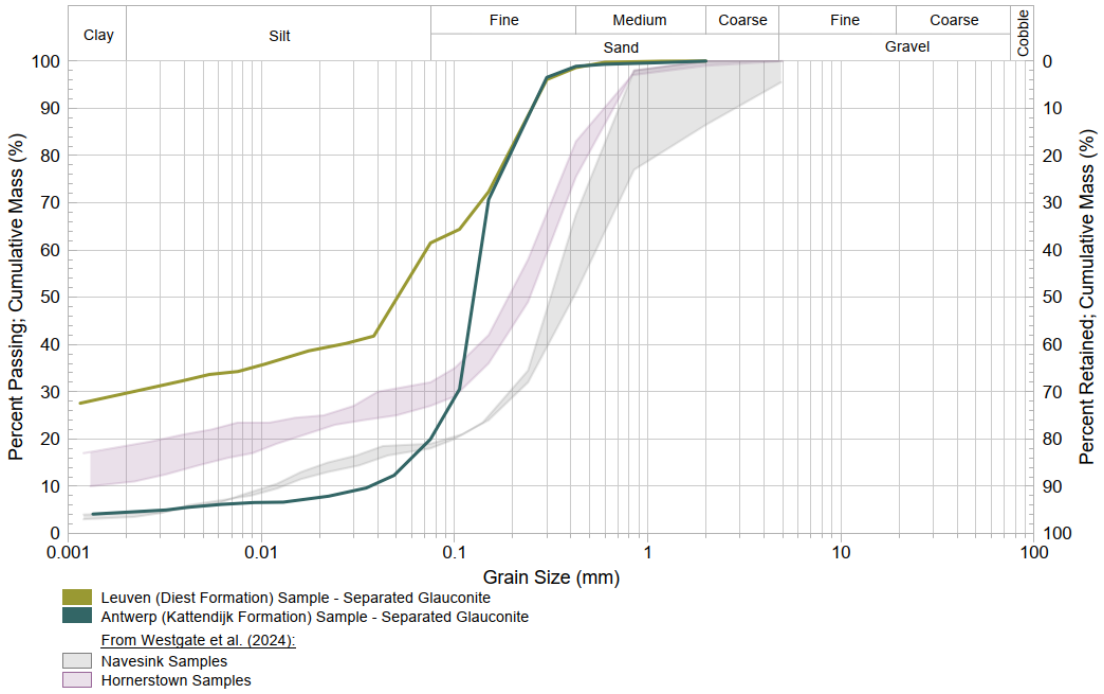

Figure 6.6. Glauconite Fraction PSDs – Comparison with Results from Westgate et al. (2024)

Although glauconite maturity depends on the extent of diagenetic process and is not solely determined by the age of deposition, the maximum size of pellets indicated by PSDs from Figure 6.6 is generally consistent with the geologic age and approximated glauconization stage of their parent formations (Obasi et al., 2011; Houthuys et al., 2020; Deckers & Louwye, 2020; Westgate et al., 2024). In descending order of D_{90}, gradations plot for:

- Navesink Formation from the Upper Cretaceous (ca. 66-72 Ma)
- Hornerstown Formation from the Paleocene (ca. 62-66 Ma)
- Diest Formation from the Late Miocene Tortonian (ca. 11.6-7.2 Ma) to earliest Messinian (ca. 7.2-5.3 Ma)
- Kattendijk Formation from the Early Pliocene (ca. 5.3 – 3.6 Ma).

Nevertheless, there is no clear correlation between glauconite evolution and crushability demonstrated during dispersion. Instead, degradation potential seems to increase with higher C_u values, reflecting a wider particle size range. This aligns with dispersion results from Westgate et al. (2023), where poorly graded sands, such as the Poricy Navesink sample, exhibited lower relative degradation. Similarly, Adriaens et al. (2014) found that clay-sized glauconite was a proxy for the transport intensity of pelletal glauconite. However, in this case, formation of clay-sized fraction is linked to the properties and breakability of glauconitic sand rather than the energy of transport.

In conclusion, while depositional history, allogenic vs. authigenic nature of glauconites, and inevitable differences in sample preparation and degradation methods between the different experimental programs should be kept in mind, natural gradation of glauconite may be a valuable preliminary indicator of its degradation potential.

Atterberg Limits and Clay Activity

Index characterization on degraded samples included Atterberg limit tests. Due to the time restrictions and limited quantity of delivered material, only select dispersion periods were considered for this assessment. Each sample was first oven-dried, screened on a 2-mm sieve, soaked over-night in demineralized water, stirred in a mixer for a pre-determined time period with no more than 300 grams used at a time, wet-sieved on a 425-µm sieve, and air-dried to the needed consistency. The remaining steps were carried out in accordance with the fall cone (liquid limit) test procedures described in Head's Soil Laboratory Testing manual (Head & Epps, 2011) and ASTM D4318 standard (ASTM, 2018) for plastic limit determination. Some tests were performed twice to evaluate their repeatability, which was found to be satisfactory. Results for both Belgian samples are summarized in Figure 6.7.

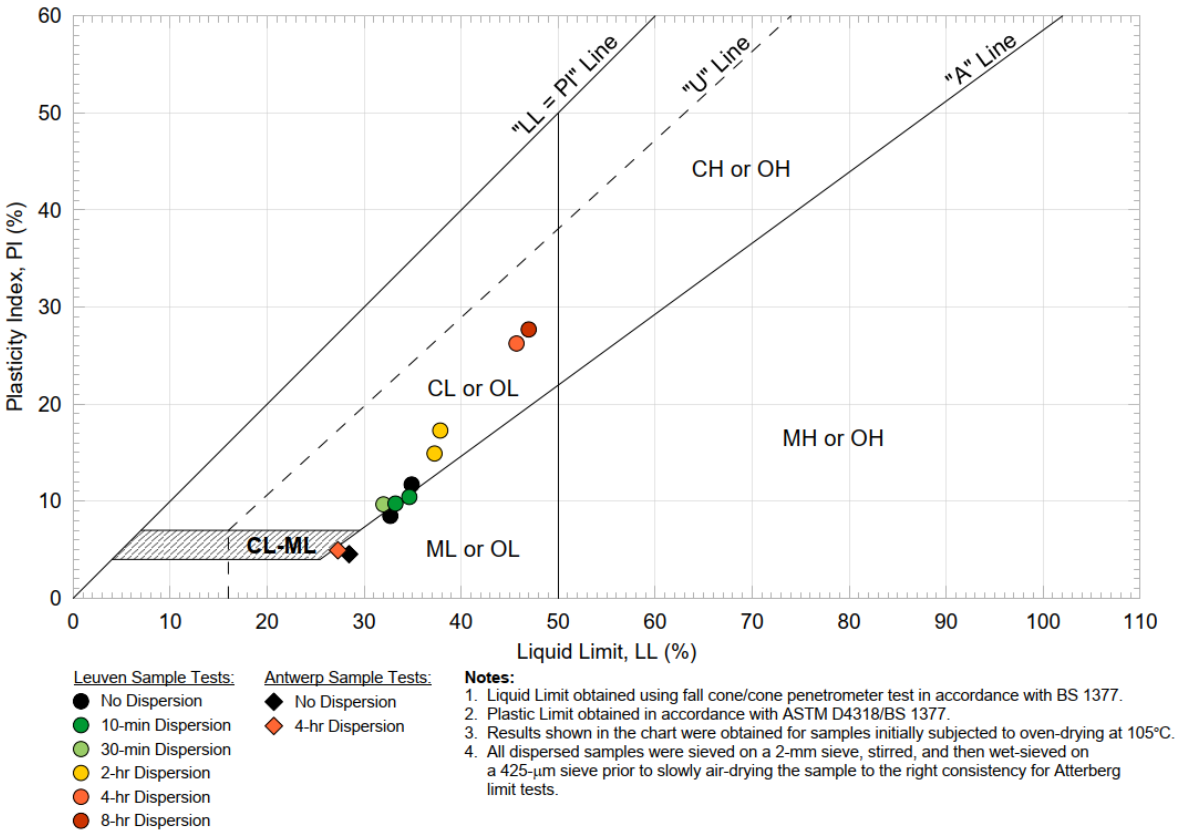

Figure 6.7. Degraded Glauconitic Sand Plasticity Chart

As indicated by Figure 6.7 points for Leuven sand, plasticity exhibited by soil dispersed for 10 to 30 minutes did not change compared to the natural state tests. However, stirring for longer than 2 hours resulted in transition from the low to medium plasticity classification corresponding to LL greater than 35 percent (Head & Epps, 2011). For Antwerp sand, prolonged degradation of the sample did not produce fines in quantity sufficient to affect the resulting Atterberg limits. While Leuven sand underwent a clearly visible change in soil texture with stirring as demonstrated in Figure 6.8, predominance of quartz in Antwerp sand did not allow for this level of alteration. This made further assessment of plasticity changes in its natural GC samples redundant.

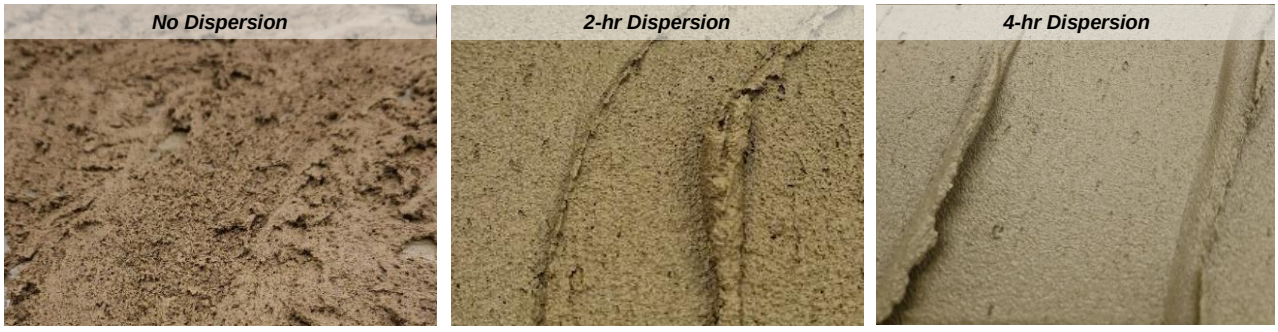

Figure 6.8. Photos of Degraded Leuven Sand; 425-µm Fraction Mixed for Atterberg Limit Tests

Even with degradation as significant as experienced by Leuven sand based on the textural alterations from Figure 6.8, it was characterized by Atterberg limits falling outside of the high plasticity range. Figure 6.9 demonstrates that the maximum change achieved with the breakdown of glauconite was moderate yet steep compared to that attained in analogous tests on New Jersey samples. While, in general, the trendline for Leuven sand results fits with its high quartz content, the role of glauconization in driving the behavioral changes in samples from different sites should be considered.

As pointed out in the legend of Figure 6.9, Atterberg limits for the degraded evolved to highly evolved New Jersey glauconite-dominated sands (Westgate et al., 2023) (in gray) tend to plot below the “A”- line, in a zone characteristic of the lower plasticity silty fines. In contrast, with continued dispersion, results for the slightly evolved to evolved specimens (in purple) tend towards the high plasticity clay zone, plotting parallel to the “U”-line. The degraded Leuven sands, representing earlier stages of evolution, show a steeper increase in plasticity with the continued glauconite degradation, approaching “U”-line as the liquid limit is pushed further.

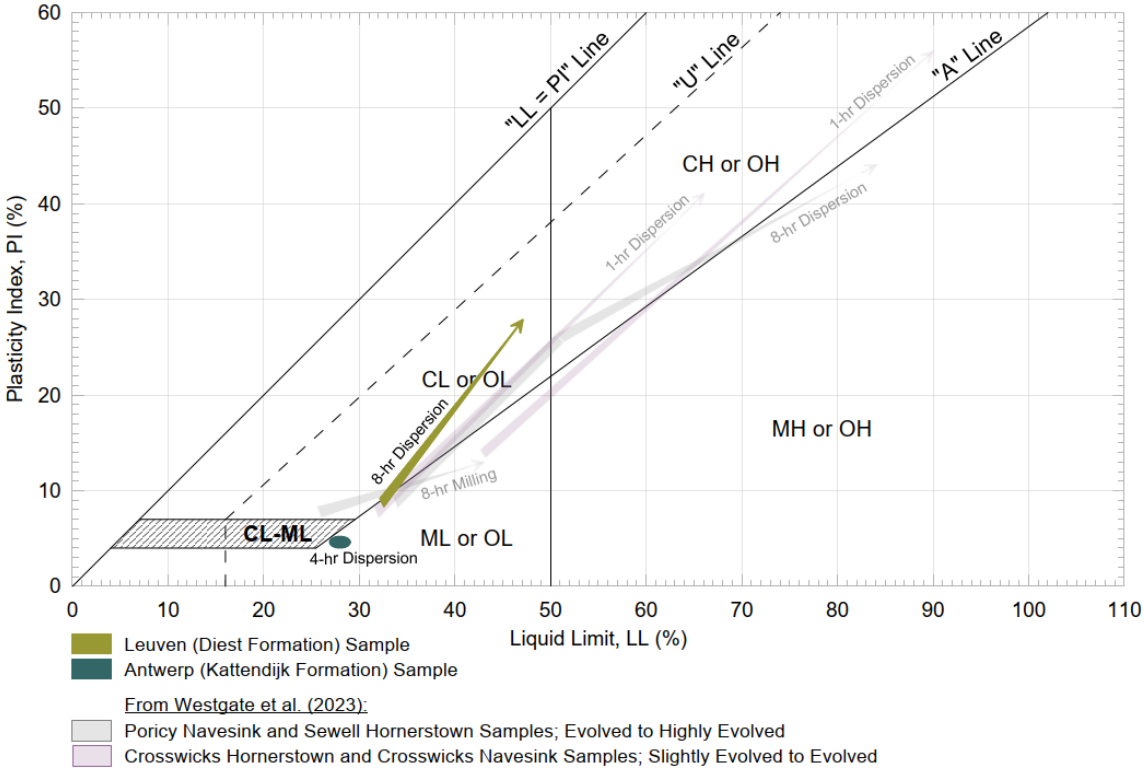

Figure 6.9. Plasticity Chart with Degradation Patterns for Samples from Belgium and New Jersey (Westgate et al., 2023)

Based on discussions from Subsections 2.5 and 5.1, glauconization involves transformation of glauconitic smectite into glauconitic mica through recrystallization (Odin & Matter, 1981). Thus, before it reaches the highly evolved stage from Figure 2.17, properties of the derived glauconitic fines are likely to resemble those of smectites and, subsequently, exhibit behaviors characteristic of micaceous clays. A recent study on the latter (Zhang et al., 2019) concluded that liquid and plastic limits tend to increase with mica content. However, since the rate of increase is greater for plastic limit, plasticity index starts to lower until clay fraction becomes non-plastic and cohesionless. This change in behavior aligns with the highly evolved (gray) Atterberg limits trendlines plotting shallower than the “LL = PI” boundary and the highest degradation level prompting reduction in plasticity.

Based on the PSD curves for Leuven and Antwerp sands from Figure 6.2, 425-μm fraction used in Atterberg limit tests contains a large quantity of quartz, which inevitably reduces plasticity exhibited by Belgian samples relative to the higher GC sediments. Thus, for a proper comparison with results from Westgate et al. (2023), plasticity index (PI) should be normalized to the clay fraction (CF). The resulting activity of clay, a ratio previously covered in literature review from Subsection 2.4, is summarized in Table 6.2, accounting for the imposed dispersion periods.

Clay activity for the Leuven and Antwerp samples was estimated using Atterberg limits from Figure 6.7 and PSDs derived for the tested and mixed materials in accordance with ASTM D422 following each fall cone test (not shown in the report). In the case of Leuven sand, clay activity increased almost linearly with the extended duration of dispersion and the resulting generation of plastic fines, transitioning from the inactive to normal activity range, which is consistent with values expected for marine clays (Head & Epps, 2011; Mitchell & Soga, 2005). Due to the low

production of fines in both the natural and degraded states, results for the Antwerp sample remained within the inactive range typical for kaolinite and illite (Mitchell & Soga, 2005).

Table 6.2. Activity of Clay Summary for Leuven Samples

Sample	425-µm Fraction		
	Plasticity Index (%)	Clay Fraction (%)	Activity (-)
Leuven Sand Atterberg Limit Samples			
No Dispersion	10.1	27.9	0.36
10-min Dispersion	9.8	28.6	0.34
10-min Dispersion (Rep.)	10.4	26.8	0.39
2-hr Dispersion	14.9	32.6	0.46
2-hr Dispersion (Rep.)	17.3	33.9	0.51
4-hr Dispersion	26.2	38.1	0.69
8-hr Dispersion	27.7	37.3	0.74
Antwerp Sand Atterberg Limit Samples			
No Dispersion	4.5	8.7	0.52
4-hr Dispersion	4.9	11.8	0.42

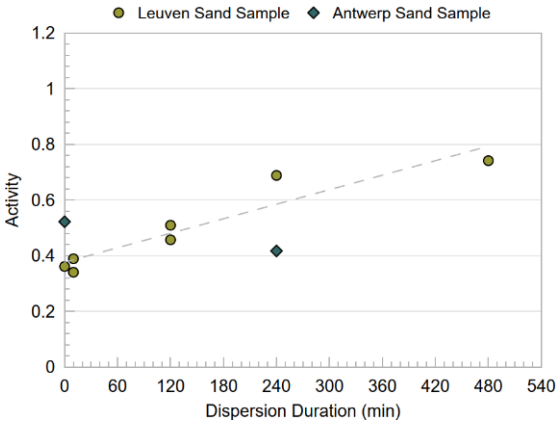

Figure 6.10 presents a PI vs. CF plot facilitating an easier comparison of clay activity (reflected by the slopes of the trendlines) between the Belgian and New Jersey samples. The resulting ratios can also be compared to those of natural clays from Figure 2.14, which was provided as part of the literature review.

The x-intercept of trendlines further confirms that in Belgian samples, clay activity gain with dispersion is stagnated by the high percentage of quartz. Based on the slope of the Leuven sand linear fit, its glauconite fraction, if tested separately, would likely exhibit activity within the range between 1 and 7, as expected for smectites (Mitchell & Soga, 2005). Results for the slightly evolved to evolved Crosswicks samples from New Jersey also fit within this range, while the highly evolved glauconites exhibit lower activity.

This supports the earlier conclusion: highly evolved glauconitic soils, when degraded, tend to show reduced plasticity and clay activity compared to their earlier stages of glauconization. As for the lower maturity glauconites, their properties appear to resemble those of the more active smectites.

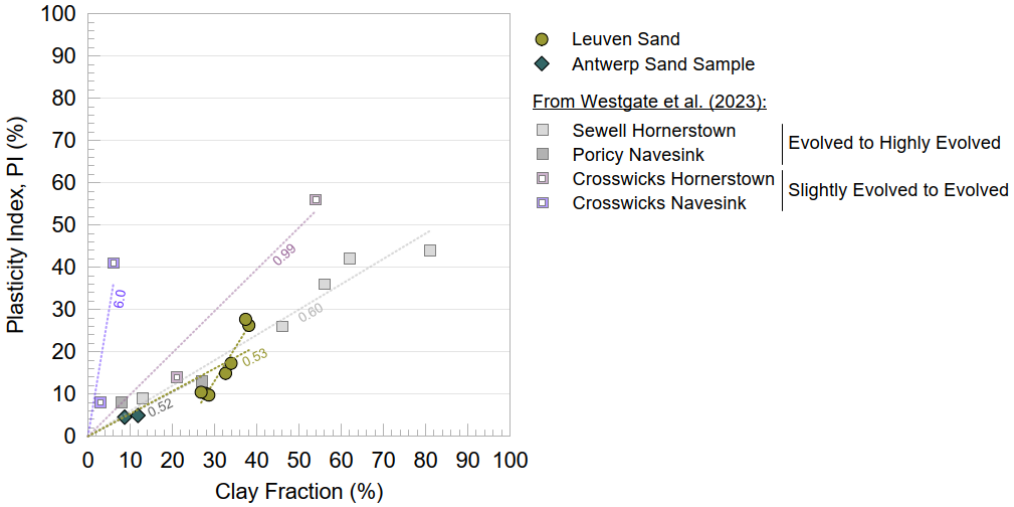

Figure 6.10. Activity of Clay Summary for Samples from Belgium and New Jersey (Westgate et al., 2023)

6.2 Interface Shear Strength Characterization

While direct shear test results for the natural glauconitic sands provided valuable insights into the interface shear resistance and supported the performed material characterization, they fall short in terms of the pile design needs. Large shear displacement, particle rearrangement, and breakage, which can be simulated in a ring shear apparatus with a fast-shearing stage, are not achievable in a monotonic direct shear test. Therefore, to capture sand degradation occurring with pile installations, samples must be either pre-crushed or tested over an extended displacement path through cyclic shearing. This section presents the results of tests conducted using these methods in an attempt to understand the behavior of glauconitic sands in their degraded state.

Pre-Crushing Approach

The high degradation potential of Leuven glauconitic sand demonstrated throughout the previous subsection suggested that it may be possible to rework its glauconite pellets and achieve a noticeable change in interface shear resistance with manual pre-treatment. The selected method involved crushing of small portions of soil with pestle and mortar for a period of 5 minutes. Two options were considered: one with glauconite fraction separated by magnet, pre-crushed and mixed back with the quartz, and another with the entire 2 mm sample ground in full. Texture obtained with the latter is shown in Figure 6.11(b).

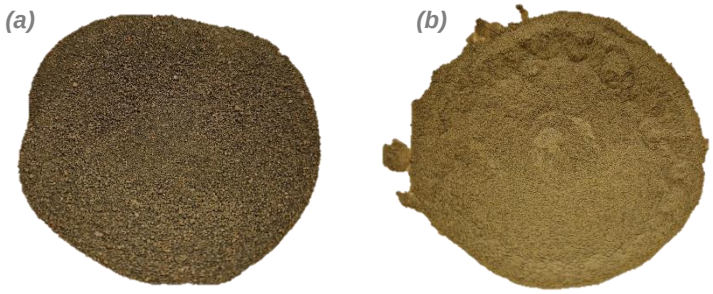

Figure 6.11. (a) Natural and (b) Pre-Crushed Leuven Sample

As summarized in Table 6.3, pre-crushed specimens were tested under the same conditions as implemented for the majority of DS tests on natural sands from Section 5.3. Two shear rates were considered to determine whether rate-dependence would become evident with the added fines content. Only the rough interface (R_a = 13 μm) was included in the given DS sequence. Antwerp sample was not tested due to its lower glauconite content and crushability.

Table 6.3. Summary of Direct Shear Tests on Crushed Glauconitic Sand Samples

Sample	Steel Plate	Normal Stress (kPa)	Shear Rate (mm/min)	Steel Plate Average Roughness, R_a (μm)		Interface Stress Ratio (-)	Interface Friction Angle (deg)	Interface Friction Angle Summary (deg)
				Initial	Final			
Leuven (Diest Formation) Glauconitic Sand; 2 mm Fraction	*Magnetically Separated Glauconite Crushed with Pestle and Mortar and Mixed Back in with Quartz*							
	Rough	150	0.005	12.82	12.78	0.56	29.2	*Average: 29.1 deg Std Dev: 0.2 deg*
	Rough	150	0.5	12.78	12.77	0.55	28.9	
	Full 2 mm Sample Crushed with Pestle and Mortar							
	Rough	150	0.5	12.69	12.77	0.55	28.9	

(1) For tests on rough steel plate (residual) interface friction angles were determined as the average value for horizontal displacements between 4 and 8 mm.
(2) Crushing with pestle and mortar was carried out for 5 minutes with up to 3 tablespoons of material crushed at a time.

Results from Table 6.3 are shown together with those from the comparable tests on natural samples in Figure 6.12. Only a minimal reduction in post-peak shear stress could be observed for the pre-crushed specimens. A small peak in resistance became apparent at 2 mm of horizontal displacement, which is consistent with the increasing strain

softening behavior exhibited by specimens subjected to further degradation in experiments by Westgate et al. (2023). Shear rate effects remained negligible.

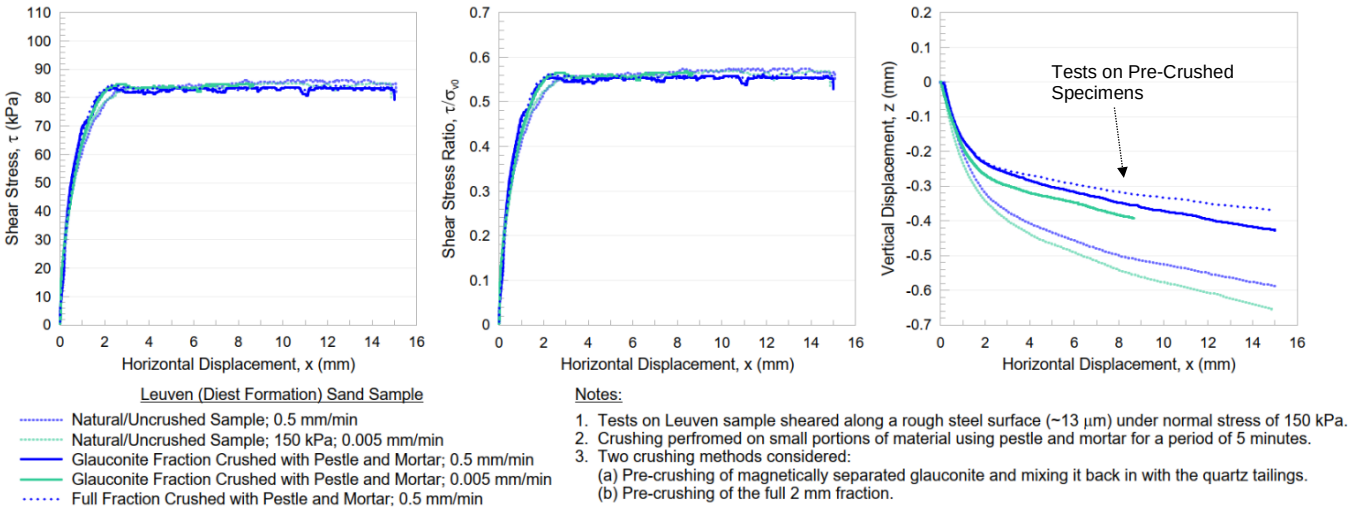

Figure 6.12. Direct Interface Shear Test Results for Pre-Crushed Leuven Sand Specimens

Although the effect of reworking of glauconite pellets with the pestle and mortar method is clearly evident in volumetric response of pre-crushed specimens from the vertical vs. horizontal displacement plot of Figure 6.12, additional PSD analyses were performed to determine where it lies in comparison to dispersion results from Section 6.1. The achieved peloidal breakage appears to be too low to be representative of glauconite degradation occurring along the pile walls. For comparison, in Antwerp full scale drivability tests, fines fraction doubled with the sheetpile installation in a deposit with similar glauconite content (de Nijs et al., 2015).

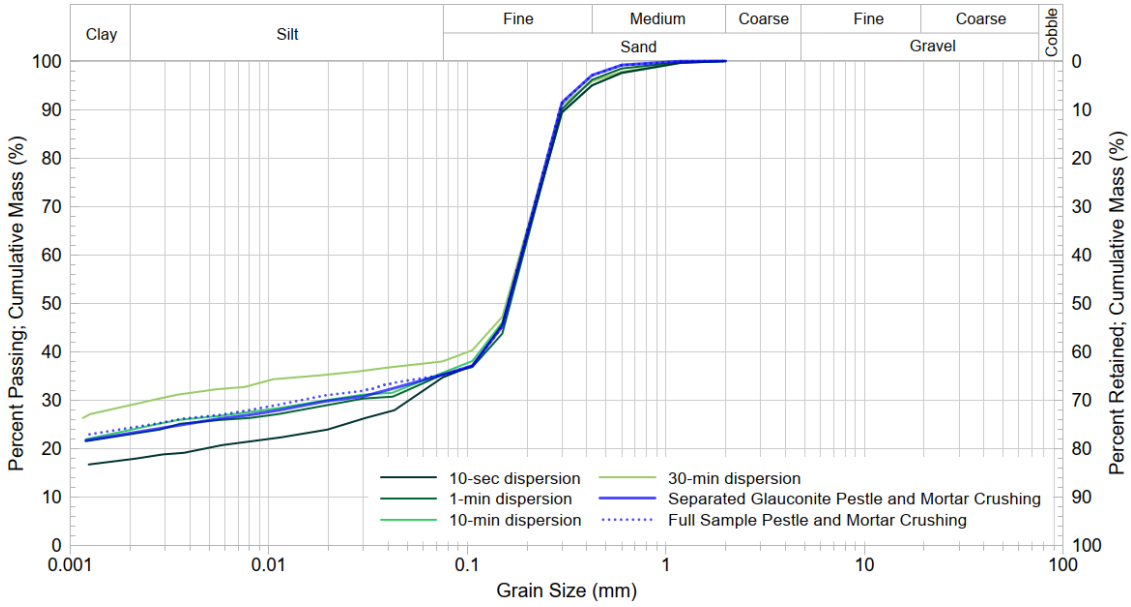

Figure 6.13. PSDs for Pre-Crushed Leuven Glauconitic Sand Specimens

The initial experimental plan included tests on material subjected to dispersion for periods longer than 10 minutes. However, the DS apparatus at TU Delft Faculty of Civil Engineering and Geosciences broke down before interface shearing could be performed. Before that happened, cyclic shearing tests were conducted on both samples as discussed in the subsection below.

Cyclic Shearing Approach

The disadvantage of sample pre-treatment approach is in implementation of degradation mechanisms that are not representative of the actual abrasion processes accompanying pile installations. Ideally, interface shear testing should be performed on material recovered from drilling augers or pile tests. Alternatively, ring shear tests can be conducted since they have capability to simulate pile installation effects and reach displacements needed for residual conditions to be ensured. Because such apparatus is not available at TU Delft, the next best option is performing cyclic direct shear tests.

Two-way cyclic shearing tests with a displacement amplitude of $\pm$ 5 mm were performed on the natural Leuven and Antwerp samples on both the smooth (R_a ≈ 1 μm) and rough (R_a ≈ 13 μm) steel plates as summarized in Table 6.4. Sample preparation and consolidation steps remained the same as mentioned earlier in Section 4.4. Since Figure 6.12 indicated no significant rate effects with crushing of glauconite, shear rate of 0.5 mm/min was used in all four tests. This was the minimum displacement velocity allowing for a sufficient number of cycles with the manual control of the system. After completion of 10 cycles, each specimen was subjected to overnight reconsolidation followed by monotonic shearing up to the end-lock engagement. All tests were performed with the constant normal stress of 150 kPa. To facilitate the comparison, results for the four evaluated interfaces are plotted together in Figure 6.14.

Table 6.4. Summary of Cyclic Direct Shear Tests on Glauconitic Sand Samples

Sample	Steel Plate	Normal Stress (kPa)	Shear Rate (mm/min)	Steel Plate Average Roughness, R_a (μm)		Number of Cycles	Interface Stress Ratio (-)		Interface Friction Angle (deg)	
				Initial	Final		Initial (2)	Final (3)	Initial (2)	Final (3)
Leuven (Diest Formation) Glauconitic Sand; 2 mm Fraction	Rough	150	0.5	12.78	12.69	10	0.55	0.48	28.9	25.7
	Smooth			1.07 (1)		11	0.39	0.33	21.1	18.3
Antwerp (Kattendijk Formation) Glauconitic Sand; 2 mm Fraction	Rough			12.77	12.82	10	0.56	0.55	29.2	28.6
	Smooth			1.07 (1)		10	0.43 (4)	0.49	23.0 (4)	26.1

(1) Smooth plate roughness was not re-measured after each test as any changes were expected to be negligible.
(2) Initial values taken as the average from 4 to 5 mm displacement for the first cycle prior to strain reversal.
(3) Final values taken as the average from 4 mm to final displacement in shearing stage conducted after the over-night consolidation period.
(4) With the first cycle showing very low stress ratio, the value was taken from 4 to 5 mm (or -4 to -5 mm) displacement after the first strain reversal in a range that appeared to be more representative of the tested interface.

As shown in Table 6.4 and Figure 6.14, when defined as passing through the origin, the post-peak interface friction angles mobilized after 10 cycles dropped compared to the monotonic DS values in both the rough and smooth interface tests on Leuven specimens (see Table 5.8). In both cases the reduction equaled approximately 3 degrees, although shearing on the smooth interface was unintentionally terminated after an additional 11th cycle. The reason behind the decreasing shear stress is ambiguous as it could be attributed to the establishment of residual condition, crushing of glauconite pellets with continued shearing, and/or loss of material to asperities that was exacerbated in all cyclic tests from Figure 6.14. As an example, excessive sample loss is captured in a photo from Figure 6.15(a), taken after its removal from the carriage.

As previously discussed and illustrated in Figure 5.12, entrapment of sand particles by asperities is inevitable in DS tests on textured structures. In cyclic tests the loss is worsened as, after being returned back to the original position, shear box starts sliding on top of soil pushed outside of the specimen. After only few cycles the upper half of the shear box is raised above its original position that is initially maintained by the gap screws. Considering these changes, the interface area calculated for the circular shear box may widen as normal stress could be transferred unevenly outside of the specimen perimeter. This is a major limitation of the interface cyclic DS tests, which predominantly applies to the rough steel surfaces, as suggested by vertical displacement results plotted in Figure

6.14. This constraint is also relevant for tests conducted at other laboratories as confirmed by post-shearing specimen photos taken at NGI (Rezaei & Walkowska, 2024).

Nevertheless, in spite of material loss appearing excessive for the Antwerp sand specimen sheared on rough steel, in this case the reduction in shear stress and the derived residual interface friction angle was insignificant. As for the smooth interface, shear resistance continued to accumulate until the last three cycles, where the shear stress finally stabilized.

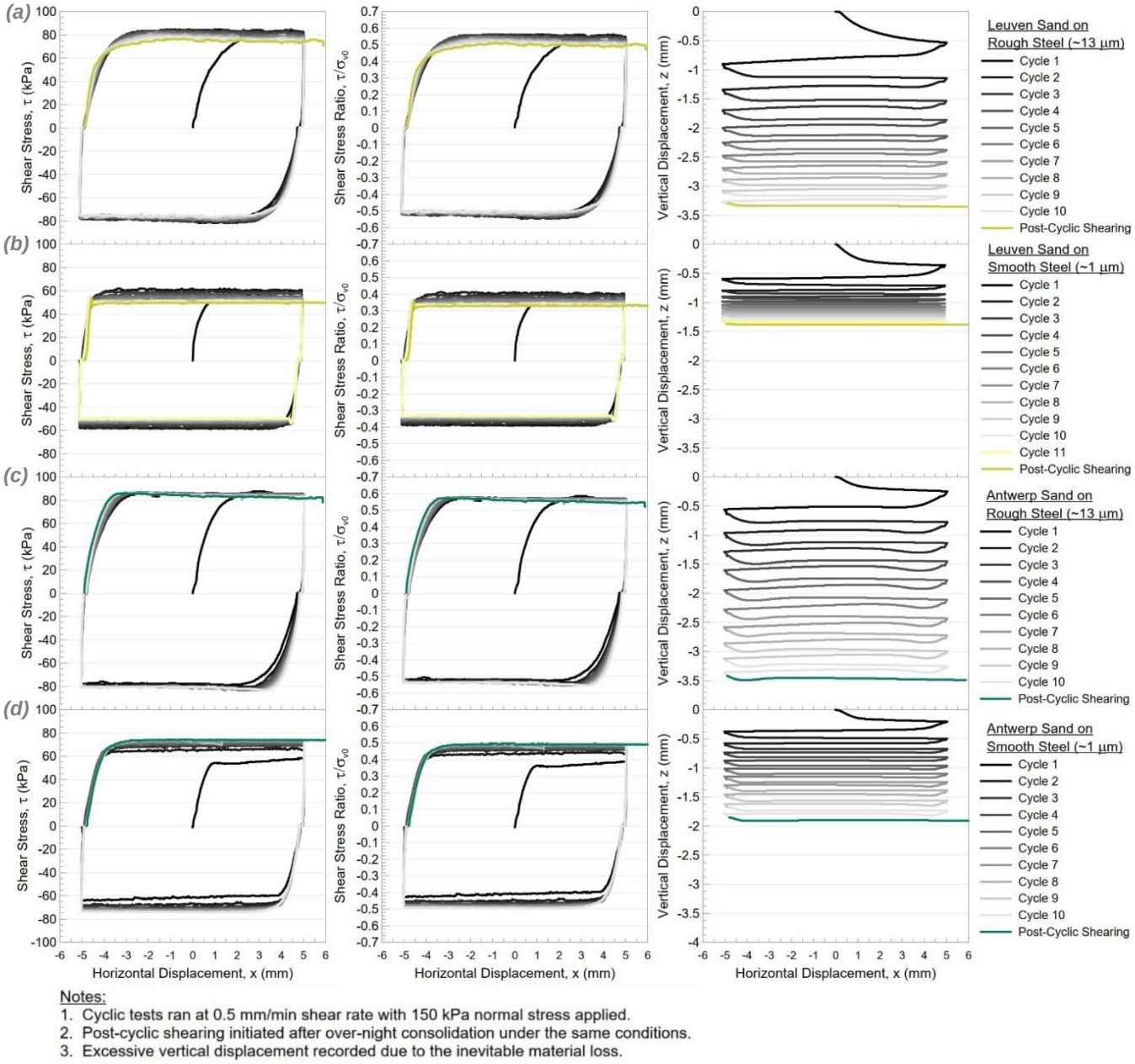

Figure 6.14. Interface Cyclic Direct Shear Test Results for: (a) Leuven Sand on Rough ($R_a \approx 13$ µm) Steel; (b) Leuven Sand on Smooth ($R_a \approx 1$ µm) Steel; (a) Antwerp Sand on Rough ($R_a \approx 13$ µm) Steel; and (d) Antwerp Sand on Smooth ($R_a \approx 1$ µm) Steel

While it is important to acknowledge the limitations associated with material loss, cyclic DS tests can still offer valuable insights into the behavior of degraded glauconitic sands. To enable such an assessment, the extent of achieved degradation should be carefully considered. Based on the visual inspection alone, sheared specimens

removed from the rough interface appeared to be clearly reworked, but in different ways. The Antwerp specimen remained sandy, with a slightly greener color showing directly above the steel plate. In contrast, Leuven sand was broken down into a sticky clayey light-brown material. These changes can be seen in photos from Figure 6.15 (b and c). As expected, evidence of glauconite degradation was less pronounced in soils sheared against the smooth steel plate, especially in the Antwerp sand specimen dominated by quartz. However, in the case of Leuven sand, it was more obvious compared to the Figure 5.21 observations for monotonic tests with the reworked cohesive material sticking to structural surface upon further shearing (Figure 6.15(e)). The experienced soil loss pointed towards partial transition from sliding after several displacement cycles.

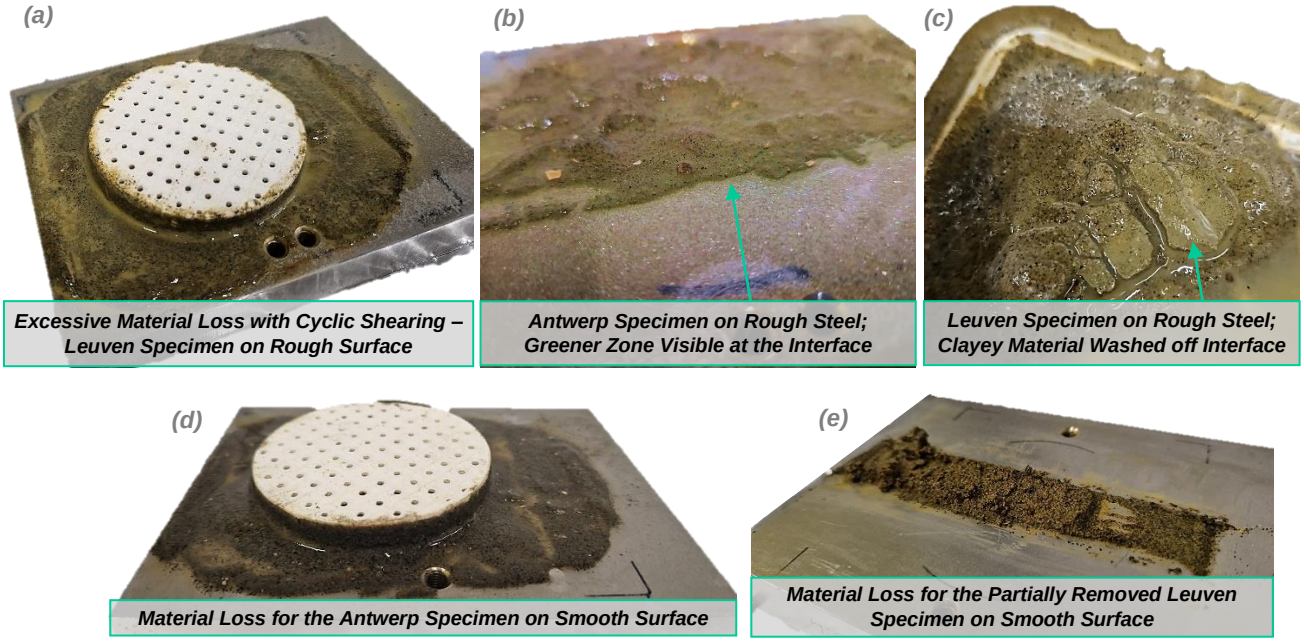

Figure 6.15. Interface Cyclic DS Test Observations: (a) Leuven Sand on Rough Steel; (b) Antwerp Sand on Rough Steel; and (c) Washed-Off Leuven Sample Shear Zone on Rough Steel; (d) Antwerp Sand on Smooth Steel; and (e) Partially Removed Leuven Sample on Smooth Steel

In an attempt to quantify the discussed visual changes, Microtrac BlueWave laser diffraction measurements were added for each sheared specimen as explained in Section 4. The resulting PSD curves are shown in Figure 6.16.

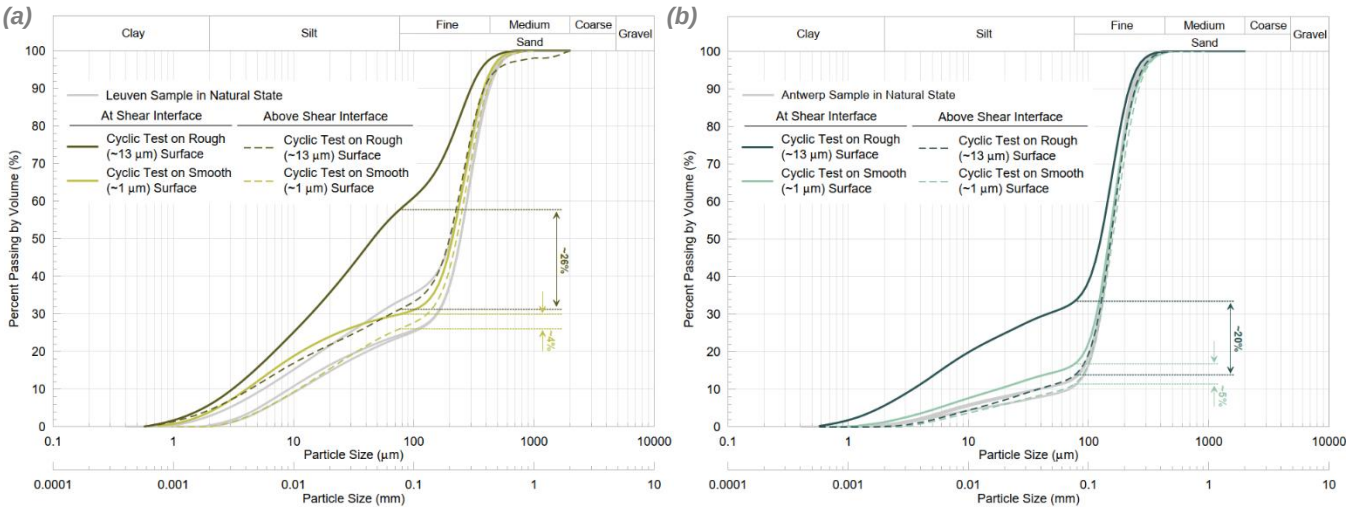

Figure 6.16. Laser Diffraction PSD Analysis Results for the Interface Cyclic DS Test Specimens from: (a) Leuven and (b) Antwerp Samples

When compared to the gray curves representing natural state specimens in Figure 6.16, material collected above the interface (outside the shear zone) showed no significant change in particle size distribution. This supports the earlier conclusion from Section 5 that compression alone does not contribute to noticeable crushing of the glauconite pellets in Belgian sands.

According to the laser diffraction measurements, in the cyclic Leuven sand to rough steel DS test, fines content increased by 26 percent, making it predominantly fine-grained. The PSD curve for an analogous test on Antwerp sample showed a comparable addition of fines, suggesting its transformation into a silty/clayey sand based on the produced gradation alone. Tests on the smooth interface indicated a smaller change of only 4 to 5 percent for both specimens. It is important to note that, as mentioned earlier, a direct comparison of the added fines content in Leuven and Antwerp sands is rather unreliable due to the generated clay-sized fraction remaining undetected in the implemented laser diffraction method. However, although subject to high level of uncertainty, the obtained results appear to agree with the shear zone changes visible in Figure 6.15.

To visualize shear-induced breakage as it would appear in soil matrix and verify findings of the laser diffraction PSD assessment, ESEM imaging was conducted on Leuven and Antwerp samples subjected to the highest level of degradation through cyclic DS tests on the rough (R_a = 13 μm) steel plate. Due to scheduling conflicts, it was impractical to arrange for the ESEM immediately after the DS tests. As a result, specimens had to be dried for storage and then brought to a moisture content above the plastic limit for remixing. While this process did not preserve particle orientation at the interface, the images were expected to provide insight into granular mix behavior that was previously covered in Section 2.3.

Figure 6.17 shows images of the Leuven specimens taken above and directly at the interface. Their comparison reveals that shear-induced degradation resulted in sand grains being fully coated by cohesive fines. As noted in literature, this continuous coating likely acted as a lubricant, smoothing out defects and asperities in steel and sand grains floating within the soil matrix and leading to a reduction in interface shear strength (Mitchell & Soga, 2005; Carraro et al., 2009). Noteworthy, surface cracking visible in both images is due to drying under vacuum in the ESEM chamber.

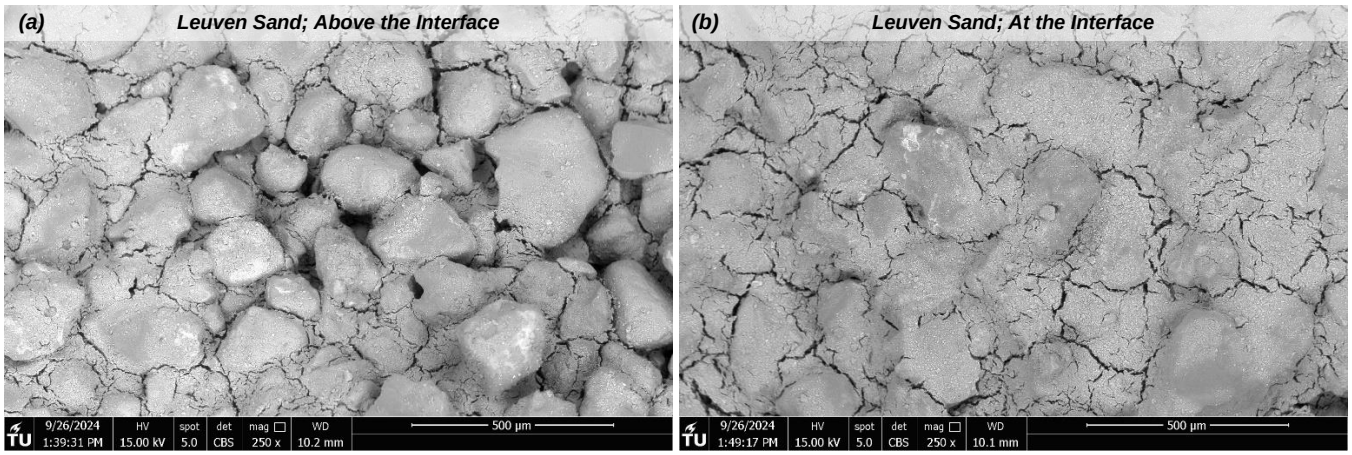

Figure 6.17. ESEM Images at 250x Magnification Showing the Remixed Cyclic Interface DS Leuven Sand Specimens Collected (a) Above and (b) at Soil-Steel Interface

Analogous images for the Antwerp sample are presented in Figure 6.18. Here, the post-shearing increase in fines fraction is visibly much more limited with the fines only locally confined between the sand grains. These slight matrix changes fit well with the lack of significant reduction in interface shear strength pointed out in Table 6.4. In general, sand grains comprising the Antwerp sample have higher angularity, which is consistent with the higher derived interface friction angle likely controlled by quartz.

A comparison of the ESEM images for the two sands suggests that the measured fines content for Antwerp sand sheared against the rough steel surface (Figure 6.16) may be overestimated. This could be attributed to the

inconsistent sample collection procedures or limitations inherent to the laser diffraction testing method. Alternatively, the lower fines content observed in Figure 6.18 may reflect inhomogeneities in the mixed soil. Notably, the former explanation aligns more closely with the low degradation potential of Antwerp sand, as indicated by the dispersion results in Figure 6.2 and Figure 6.3.

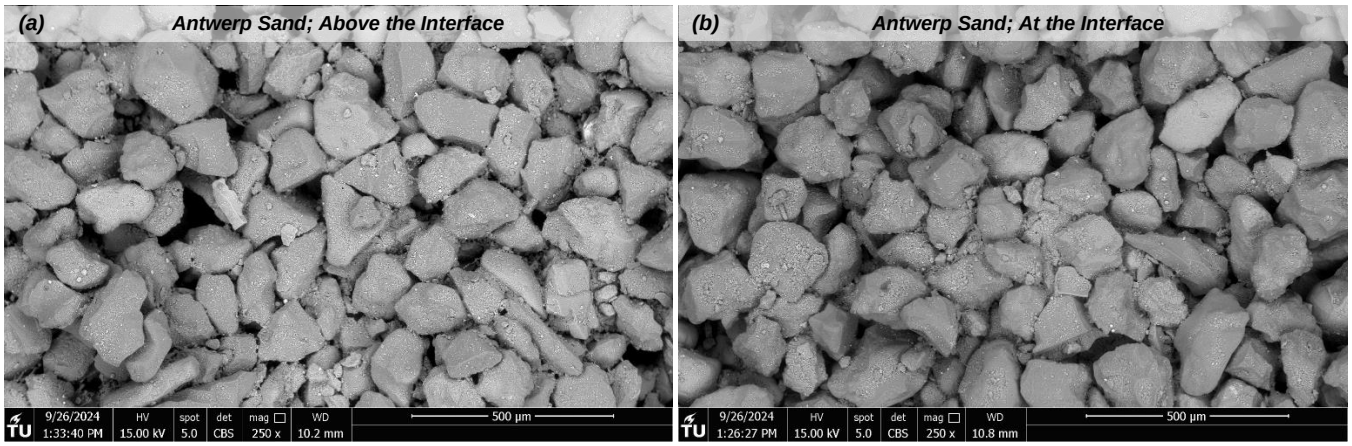

Figure 6.18. ESEM Images at 250x Magnification Showing the Remixed Cyclic Interface DS Antwerp Sand Specimens Collected (a) Above and (b) at Soil-Steel Interface

Overall, visual observations as well as the PSD and ESEM image assessment confirmed that, in terms of glauconite degradation, interface cyclic DS tests were more efficient than pre-crushing of the specimens for monotonic tests. Given the level of degradation, which appears to exceed that achieved through 30 minutes of dispersion in a stirring apparatus, adhesion may have increased in tests from Figure 6.14, at least for the Leuven sample. Thus, even though shearing after reconsolidation showed no evidence of pore pressure accumulation, results are presented as the interface shear stress vs. cumulative horizontal displacement as shown in Figure 6.19.

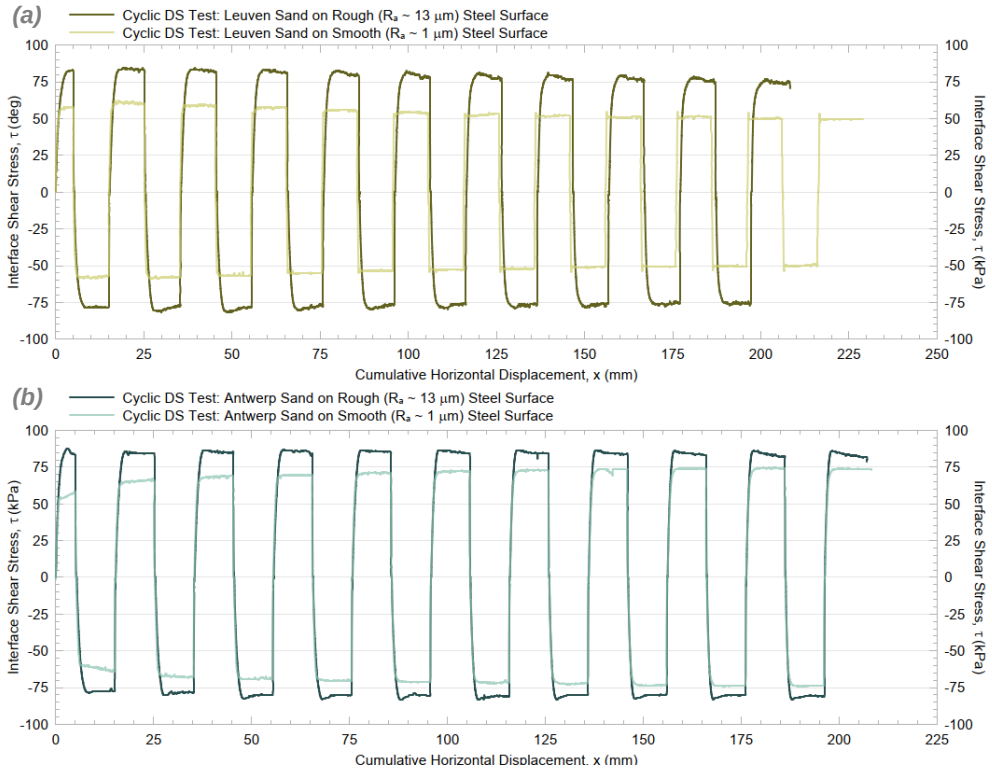

Figure 6.19. Cyclic Interface DS Tests; Interface Shear Stress vs. Cumulative Horizontal Displacement for: (a) Leuven and (b) Antwerp Sand

Figure 6.19 demonstrates more clearly that in the case of rough interfaces, increasing strain softening behavior became evident after about 25 mm of horizontal displacement. The Antwerp sand showed a moderate reduction in post-peak interface shear strength with the peak resistance remaining consistent between the cycles, likely indicating that the residual state was approached without a significant degradation of the soil. Meanwhile, Leuven sand demonstrated reduction in both the peak and post-peak, or residual, interface shear strength.

Going back to Figure 2.21 from the literature review, strain-softening in cyclic tests on Belgian sands was less pronounced compared to the pre-dispersed specimens of Sewell Hornerstown deposits from Westgate et al. (2023). This aligns with Lupini et al. (1981) who noted that in clayey soils, the strength drop from peak to residual increases with the liquid limit. Based on Figure 6.20 for Leuven sand, degradation from 210 mm of interface shearing with the application of σ_n = 150 kPa did not exceed that attained via 4 hours of dispersion for the Atterberg limit tests. Therefore, according to Figure 6.7, the PI and LL of clay within the shear band should not have surpassed 28 and 47 percent, respectively. In contrast, Sewell Hornerstown sample (GC ~ 98 percent) exhibited a higher LL after just 10 minutes of dispersion (Westgate et al., 2023). Noteworthy, significant reduction in post-peak interface friction angles derived for New Jersey soils could also be attributed to crushing of glauconitic mica in glauconites of higher maturity. It had been previously shown that shear strength of micaceous soils undergoes a significant decrease with crushing due to the changing geometric arrangement of mica and silt/sand particles (Sachan et al., 2019).

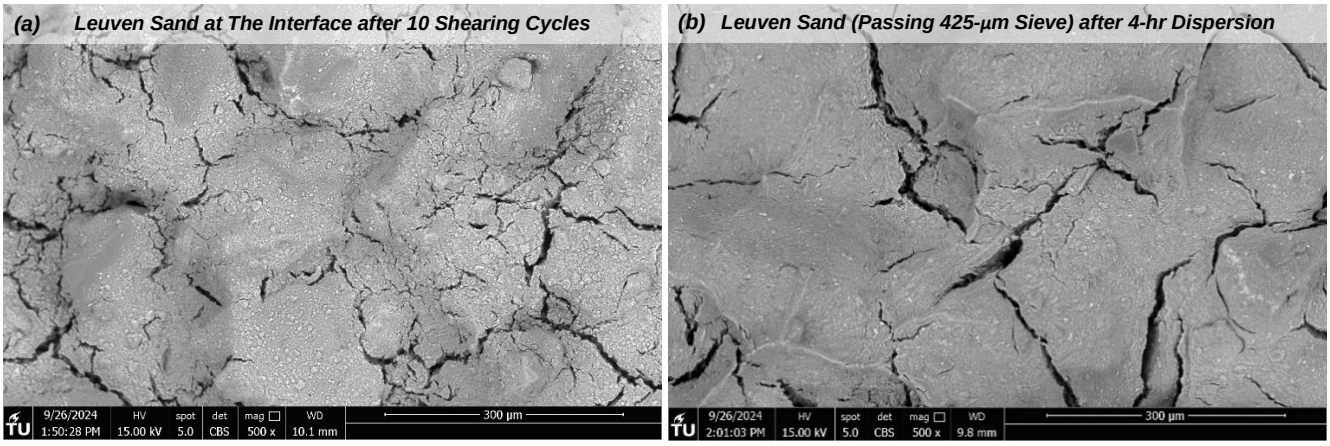

Figure 6.20. ESEM Images of Leuven Sand at 500x Magnification; (a) Collected at the Interface after Cyclic DS Test on a Rough Steel Surface and (b) Dispersed for 4 Hours as Part of the Atterberg Limit Tests

Looking at Figure 6.19, in the smooth interface tests, Antwerp sample exhibited a consistent accumulation of shear resistance, seemingly unaffected by reworking of the glauconite pellets. This strain-hardening behavior aligns with the findings from monotonic shear tests on sand reported by Zhang et al. (2021). Shearing performed after reconsolidation indicated that it was not driven by pore pressure buildup but rather densification that was initially enabled by the lack of interlocking between soil particles and the steel surface. The residual interface friction angle derived from the DS data was comparable to values reported for large-displacement ring shear tests on Fontainebleau sand sheared along the smooth stainless-steel surfaces (R_{CLA} ~ 2 to 3 µm), as documented by Yang et al. (2010). Thus, considering the abovementioned observations, shearing behavior of the Antwerp sand was likely dominated by quartz and did not reflect the breakdown of glauconite pellets. This conclusion seems to apply to both the rough and smooth interface tests.

In contrast, for Leuven sand, the high percentage of plastic glauconitic fines caused a continuous reduction in mobilized shear resistance, consistent with findings for glauconite sands with the higher GC (Rezaei & Walkowska, 2024). Therefore, after several cycles, the breakdown of glauconite and/or local reorientation of glauconitic clay particles at the interface became key factors influencing the mobilized shear resistance.

In conclusion, cyclic shearing was found to be an effective approach for the shear strength assessment of degraded glauconitic sands. In spite of its limitations associated with material loss and stress redistribution, it provided valuable insights into the behavior of glauconitic sands subjected to breakdown of the peloidal structure and

generation of glauconitic fines. The derived results generally agreed with the previously published values for samples and interfaces with similar characteristics obtained via ring shear testing by Quinteros et al. (2023).

6.3 Degraded State Characterization Summary

Index characterization of degraded Belgian sands was conducted following the methodology outlined in Westgate et al. (2023), using a stirring apparatus to disperse and break down glauconite. Results revealed significant differences in crushability. Up to 76 percent of sand-sized pellets in Leuven sample were reworked into fines after 8 hours of dispersion. In comparison, only 6 percent broke down in an analogous test on the Antwerp sand. Further characterization of the degraded samples, alongside published results for New Jersey sediments, suggested a potential correlation between the initial in-situ gradation of glauconite and its degradation potential. Additionally, a possible link was noted between the overall maturity of glauconitic sand and changes in clay activity caused by its abrasion and the resulting generation of fines.

The interface shear strength characterization focused on Belgian sands subjected to further degradation was performed using two methods: manual pre-crushing for monotonic shearing and cyclic interface DS tests. The second method, which extended the shear path to induce glauconite crushing, proved more effective, yielding results indicative of material being reworked at the interface.

Cyclic interface DS testing showed that Antwerp sand (GC ~ 21 percent) experienced low degradation, barely affecting soil shear resistance. Reductions in the residual interface friction angle were minimal or absent, and behavior in both the rough and smooth interface tests was dominated by quartz. Therefore, the imposed test conditions were likely insufficient to induce the level of crushing expected in full-scale or model pile installations.

In contrast, Leuven sand (GC ~ 47 percent) showed significant reductions in shear stress and residual interface friction angle during cyclic shearing in both the rough and smooth interface tests. Glauconite pellets and their fragments at the interface were visibly reworked into plastic fines. However, compared to New Jersey sands studied by Westgate et al. (2023) and Rezaei and Walkowska (2024), the reduction in frictional resistance was moderate to low, likely due to the high quartz fraction, relatively low glauconite content, and lower plasticity and clay activity exhibited by the degraded Leuven sample.

Although post-shearing analyses were limited and require further refinement, they provided valuable insights into the behavior of glauconitic sands. These findings, combined with prior characterization, highlighted connections between the soil-steel interface shearing behavior and properties of glauconite.

7 Experimental Program Limitations

Multiple limitations of the conducted experimental program have been revealed throughout the report. The main ones are summarized below in hope that they may provide useful insight for future research on glauconitic sands:

- Partial Experimental Program

As pointed out throughout the analysis, interface shear testing conducted on natural (uncrushed) specimens was only a part of the intended shear strength characterization program. It was supposed to serve as a baseline, or reference point for tests on pre-dispersed glauconitic sands. Since the direct shear machine broke down, shear rate, normal stress, and roughness effects could not be assessed on degraded glauconitic soils exhibiting clay-like behavior. Thus, parametric assessment was limited in its applicability for monopile design, which needs to account for both material states.

- Disregarding Adhesion in Interpretation of the DS Tests on Degraded Sands

The reviewed experimental programs focusing on soil-structure interaction in glauconite-rich deposits (Westgate et al., 2023; Quinteros et al., 2023; Rezaei & Walkowska, 2024) tend to ignore adhesion in interpretation of the interface shear test results. The interface friction angles are reported as derived with failure envelopes passing through the origin even for the highly degraded glauconitic soils leaning towards the clay-like behavior. For comparison with literature, the same approach was applied in the given project. Nevertheless, although appropriate for uncrushed sands, it is not theoretically sound for the characterization of degraded samples and may be a major limitation in understanding of glauconitic soil-structure interaction during pile installations and service life.

In the given study, failure envelope was derived only for the intact Leuven sample (see Figure 5.14), which exhibited behavior governed by frictional resistance. Due to the DS apparatus malfunction, the same test sequence could not be performed for degraded specimens with the higher activity of clay. Therefore, interface friction angles were derived ignoring adhesion that could become apparent with the addition of fines. However, looking, for example, at Figure 6.15(e) for a smooth interface test on Leuven sand, there is evidence of transition from the sliding shearing mode to partial failure propagation into the specimen. With the derived interface friction angle values decreasing, this change in behavior, if confirmed, could be explained by an increase in adhesion.

In order to support this observation, using cyclic interface DS results provided in the NTNU master thesis for the Edelman Hornerstown sand sheared under the normal stresses of 75 and 150 kPa (Rezaei & Walkowska, 2024), failure envelopes can be estimated for a degraded glauconitic soil undergoing transition to cohesive behavior. This is done in Figure 7.1, which shows that, assuming a linear envelope, the vertical intercept on the shear stress axis increases with the total tangential displacement, or the achieved degradation level. Note that the effect of shear rate changes is presumed to be limited compared to the impact of glauconite reworking. The adopted displacement velocities are provided only to show where the data points are taken from when considering the NTNU cyclic shearing sequence from Figure 5.17.

Figure 7.1 serves only as an indication that adhesion should be considered in glauconitic sands undergoing degradation. However, due to the use of varying shear rates and the consideration of only two normal stress levels, it does not support a proper interface shear strength interpretation. For future testing, it is recommended to establish well-defined failure envelopes using three normal stress levels and consistent test conditions.

In summary, ignoring adhesion from glauconite breakage at the pile surface can lead to misleading conclusions. While reworking glauconite pellets reduces interface friction angles, this alone does not account for drivability issues at glauconite deposition sites. However, the increase in adhesion may align with the reported observations, such as the 3-cm-thick clay plaster remaining on the retrieved sheet pile installed in the Berchem Formation glauconitic deposits (de Nijs et al., 2015) or significant pile setup recorded for piles installed in Navesink and Hornerstown deposits (Westgate et al., 2024). Knowing that adhesive shear strength increases with steel surface roughness, contact time between the clayey surface and structure and is highly dependent

on mineralogy due to the different bonding types (Zimnik et al., 2018), its assessment appears to be of foremost importance for pile design given the recently reported observations from the field.

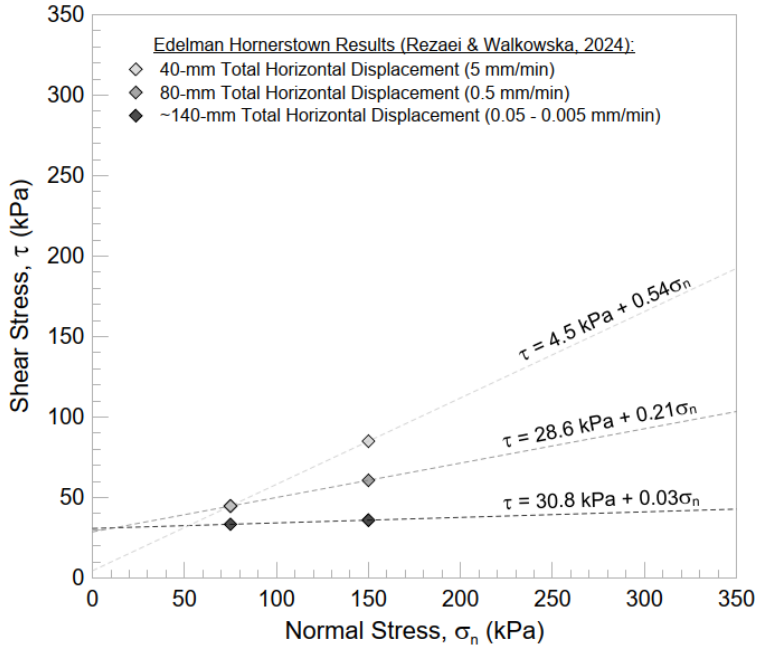

Figure 7.1. Failure Envelopes Based on Results Provided for the Edelman Hornerstown Sample in the NTNU Master Thesis Report; Plotted based on Figure 6.7 (Intact) from Rezaei and Walkowska (2024)

- Inherent Direct Shear Test Limitations

Even if frictional strength is considered the primary contributor to shear resistance of piles in glauconitic sands, direct shear tests have several limitations. First, they cannot simulate large displacement (fast) pre-conditioning, which is crucial for replicating friction fatigue and shear-induced particle rearrangement and breakage (Liu et al., 2019; Quinteros et al., 2023). Second, direct shear tests are limited in measuring true residual friction due to finite displacement and are prone to stress non-uniformities, worsened by load cap tilting and material loss at the interface (Head & Epps, 2011).

The inability to control drainage conditions during shearing in DS tests limits their applicability in evaluation of pile installation effects at high shear rates and understanding of the nature of interfacial resistance and adhesion with glauconite degradation (Rao et al., 2002). Considering these limitations and current gaps in assessment of the glauconitic soil behavior, it may be reasonable to focus future experimental efforts on a more comprehensive soil characterization, including triaxial shear, consolidation, and permeability tests.

- Limited Degradation Level Induced

Tests on the Antwerp sample allow for comparison with the calibration chamber program conducted by Piedrabuena (2024) at Deltares, as provided in Figure 7.2. Despite the removal of fines prior to testing in order to avoid liquefaction, static and cyclic CPTu tests, along with the impact driving and jacking installation of an instrumented model pile, generated up to 48 percent additional fines as shown in Figure 7.2(b). Increased plasticity was noted in high breakage zones (Piedrabuena, 2024).

Therefore, considering the lower added fines content in the smooth interface DS tests and the shear zone not being altered as shown in Figure 7.2(a), degradation methods implemented in this project may have been insufficient to simulate glauconite breakage accompanying pile installations. Further attempts to capture the occurring degradation should consider higher normal stresses, shear rates, and, possibly, number of cycles. For an instance, the highest degradation level in model pile tests from Piedrabuena (2024) was achieved with

the number of cycles reaching 400. In recent cyclic CPT tests in New Jersey, 15 implemented cycles showed only moderate degradation in sleeve friction (Westgate et al., 2024).

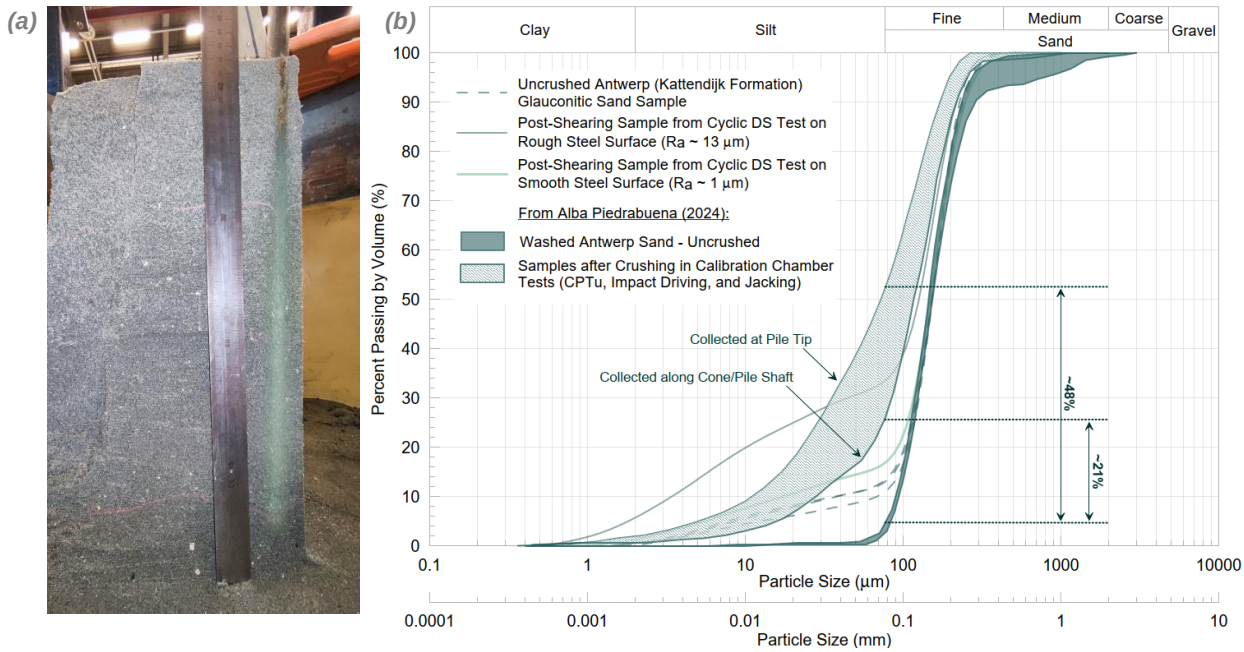

Figure 7.2. (a) Zone of High Particle Breakage in Calibration Chamber Test (Piedrabuena, 2024) and (b) Comparison of the Resulting PSDs with the Cyclic Interface DS Antwerp Sand Specimens

- Interpretation Challenges

The Belgian samples in this project present interpretational challenges due to the high natural content of quartz and glauconitic fines. In contrast, New Jersey specimens, with over 90 percent glauconite, allow for a more straightforward analysis. Additional complexity arises from roughness effects introduced during interface shear tests. To improve future evaluations of glauconitic sand mixtures, a comprehensive soil characterization is recommended as mentioned above. Extracting and testing 100 percent glauconite could also support comparison of pellets of varying maturity and composition.

- Ageing Effects and Implemented Steel Surfaces

The conducted direct shear tests did not consider long-term physiochemical processes affecting the direct shear tests interfaces. These effects would include soil thixotropy, potential cementation and microstructural changes in the sample with ageing as well as rusting of the steel surface and the resulting change in interface roughness (Lemos & Vaughan, 2000; Han et al., 2018; Liu et al., 2019; Igoe & Gavin, 2019). Such tests would be beneficial to model long-term service performance of piles installed in glauconitic sands.

Additionally, the use of aluminum silicate blasting to achieve a steel surface roughness of R_a ~ 13 µm may not accurately simulate the finish of industrial piles. For more realistic results in interface shearing tests, the steel plates should ideally be prepared using the same methods as the actual designed structures.

8 Conclusions and Recommendations

The conducted experimental program demonstrated that the primary research question posed in Section 1 cannot be conclusively answered in a single definitive manner. In the case of glauconitic soils, parameters derived for pile design are highly sensitive to the established degradation level. Considering the complex mechanical and physiochemical processes accompanying full-scale pile installations and loading, replication of glauconite breakage as occurring in situ in a laboratory setting is a challenging task that requires multiple iterations of trial and error to refine methodologies and gather reliable results. Hence, this project can only serve as one of the many foundational steps for future investigations.

Nevertheless, the performed testing revealed limitations in relevant studies published to date, implemented additional post-shearing and degradation level assessments, and offered new insights into the properties and behavior of Belgian glauconitic sands. Unlike most previously characterized glauconite soils, the analyzed samples showed relatively low glauconite content. As a result, this research project highlighted the interpretational challenges in characterization of glauconitic sands where quartz is the dominant component. The primary conclusions and recommendations for soil-steel interface shear testing of glauconitic sands derived from these findings are outlined below.

8.1 Conclusions

- Interface shear strength of Belgian glauconitic sands in their natural state, with the glauconite content below 50 percent, is highly affected by quartz, resulting in post-peak interface friction angles close to 29 degrees for surface roughness within the typical pile range.
- With the reduction of roughness below the typical pile range, failure mode transitions from shear within the soil to (at least partial) slip of the specimen on smooth steel surface, resulting in significant reduction of frictional resistance and minimized reworking of the glauconite pellets.
- No significant shear rate or normal stress effects are observed in monotonic interface direct shear tests (with the maximum shear path of 15 mm) on quartz-dominated Belgian sands. This is likely to change with further degradation of glauconite at the interface.
- In interface direct shear tests, glauconite breakage is controlled by shearing action and is negligible outside of the shear zone, where compression is predominant, up to the normal stress level of 300 kPa.
- In cyclic interface direct shear tests, degradation of glauconite pellets reduces frictional resistance through the addition of plastic fines at the interface. In Leuven sand, this required total fines content to exceed the initial 36 percent. In Antwerp sand, sufficient level of degradation was not achieved.
- Pile drivability issues reported to date may be linked to the increased adhesion caused by generation of plastic glauconitic fines, a factor that is not addressed in the existing experimental studies.
- The degradation potential estimates from dispersion tests aligned with the results of interface shearing of the two Belgian samples, demonstrating their effectiveness in preliminary evaluation of glauconite crushability.

8.2 Recommendations

- To assess the interface shear strength of glauconitic soils undergoing degradation, especially for sands with low glauconite content, greater tangential displacement range is recommended (via ring shear of cyclic direct shear tests).
- To promote greater glauconite breakage at the interface, in addition to the extended shear path, it is recommended to consider additional shearing cycles, higher normal stress levels, and faster displacement rates.

- Post-shearing PSD evaluation is recommended for all interface shear tests on glauconitic sands.
- To understand shear-imposed degradation potential of glauconite pellets of different types and maturity, testing on magnetically separated glauconite may be of interest.
- Reducing steel roughness could be explored as a potential mitigation strategy for the high drivability resistance of glauconitic sands. However, further evaluation of pile performance under loading conditions is necessary.
- To assess adhesion, a comprehensive material investigation with the inclusion of triaxial, permeability, and consolidation tests is recommended. Assessment of clay activity with degradation may also be insightful.

References

Adriaens, R., Vandenberghe, N., & Elsen, J. (2014). Natural Clay-Sized Glauconite in the Neogene Deposits of the Campine Basin (Belgium). *Clays and Clay Minerals, 62*(1), 35-52.

Amorosi, A. (1997). Detecting compositional, spatial, and tempral attributes of glaucony: a took for provenance research. *Sedimentary Geology, 109*, 135-153.

Amorosi, A., Sammartino, I., & Tateo, F. (2007). Evolution patterns of glaucony maturity: A mineralogical and geochemical approach. *Deep Sea Research Part II: Topical Studies in Oceanography, 54*(11-13), 1364-1374. https://doi.org/https://doi.org/10.1016/j.dsr2.2007.04.006.

ASTM. (2007). D422-63: Standard Test Method for Particle-Size Analysis of Soils. ASTM International.

ASTM. (2012). D3080-04: Standard Test Method for Direct Shear Test of Soils Under Consolidated Drained Conditions. ASTM International.

ASTM. (2016). D4254-16: Standard Test Methods for Minimum Index Density and Unit Weight of Soils and Calculation of Relative Density. ASTM International.

ASTM. (2018). D4318-17: Standard test Methods for Liquid Limit, Plastic Limit, and Plasticity Index of Soils. ASTM International.

ASTM. (2019). D4253-16e1: Standard Test Methods for Maximum Index Density and Unit Weight of Soils Using a Vibratory Table. ASTM International.

ASTM. (2020). D2974-20e1: Standard Test Methods for Determining the Water (Moisture) Content, Ash Content, and Organic Material of Peat and Other Organic Soils. ASTM International.

ASTM. (2023). D5550-14: Standard Test Method for Specific Gravity of Soil Solids by Gas Pycnometer. ASTM International.

Banerjee, S., Bansal, U., & Thorat, A. V. (2016). A review on palaeogeographic implications and temporal variation in glaucony composition. *Journal of Palaeogeography, 5*(1), 43-71. https://doi.org/http://dx.doi.org/10.1016/j.jop.2015.12.001

Banerjee, S., Choudhury, T. R., Saraswati, P. K., & Khanolkar, S. (2020). The formation of authigenic deposits during Paleogene warm climatic intervals: a review. *Journal of Palaeogeography, 9*(27). https://doi.org/https://doi.org/10.1186/s42501-020-00076-8

Belousov, P. E., Chupalenkov, N. M., Rudmin, M. A., & Krupskaya, V. V. (2022). Glauconite Deposits in Russia: Geological Position, Formation Conditions, and Development Perspectives. *Lithology and Mineral Resources, 57*(3), 234–247. https://doi.org/10.1134/S002449022202002X

Beren, M., Çobanoglu, I., Çelik, S., & Ündül, O. (2020). Shear Rate Effect on Strength Characteristics of Sandy Soils. *Soil Mechanics and Foundation Engineering, 57*(4). https://doi.org/DOI 10.1007/s11204-020-09667-y

Briaud, J.-L., & Garland, E. (1985). Loading Rate Method for Pile Response in Clay. *Journal of Geotechnical Engineering, 111*(3). https://doi.org/111(3): 319-335

Brown, M. J., & Hyde, A. F. (2008). Rate Effects from Pile Shaft Resistance Measurements. *Canadian Geotechnical Journal, 45*, 425-431. https://doi.org/111(3): 319-335

Bruker. (2024). *D8 ADVANCE*. Retrieved from X-ray diffractometers: https://www.bruker.com/en/products-and-solutions/diffractometers-and-x-ray-microscopes/x-ray-diffractometers/d8-advance-family/d8-advance.html

Bruker. (2024). *How does XRF Work? X-Ray Fluorescence (XRF) Spectrometry*. Retrieved from Elemental Analyzers: https://www.bruker.com/en/products-and-solutions/elemental-analyzers/xrf-spectrometers/how-does-xrf-work.html

Budhu, M. (2011). *Soil Mechanics and Foundations* (3 ed.). John Wiley & Sons.

Burland, J. B. (1973). Shaft friction of piles in clay - A simple fundamental approach. *Ground Engineering, 6*(3), 30-42.

Burst, J. F. (1958). “Glauconite” Pellets: Their Mineral Nature and Applications to Stratigraphic Interpretations. *AAPG Bulletin, 42*(2), 310–327. https://doi.org/https://doi.org/10.1306/0BDA5A7D-16BD-11D7-8645000102C1865D

Carraro, J. H., Prezzi, M., & Salgado, R. (2009). Shear Strength and Stiffness of Sands Containing Plastic or Nonplastic Fines. *Journal of Geotechnical and Geoenvironmental Engineering, 135*(9), 1167-1178. https://doi.org/https://doi.org/10.1061/(ASCE)1090-0241(2009)135:9(1167)

Chen, J., Yuan, J., Tong, H., Fang, Y., & Gu, R. (2023). Mechanism study on the soil mechanical behavior of the mixed soil based on energy multi-scale method. *Frontiers in Materials, 10*. https://doi.org/doi: 10.3389/fmats.2023.1270865

Chen, X., Zhang, J., Xiao, Y., & Li, J. (2015). Effect of roughness on shear behavior of red clay – concrete interface in large-scale direct shear tests. *Canadian Geotechnical Journal, 52*(8), 1122-1135. https://doi.org/https://doi.org/10.1139/cgj-2014-0399

COD. (2024). *Crystallography Open Database*. Retrieved from https://www.crystallography.net/cod/

Coduto, D. P., Kitch, W. A., & Yeung, M.-c. R. (2016). *Foundation Design: Principles and Practices* (3 ed.). Pearson.

de Nijs, R., Kaalberg, F., Osselaer, G., Couck, J., & van Royen, K. (2015). *Full scale field test (sheet)pile drivability in Antwerp (Belgium).*

Deckers, J., & Louwye, S. (2020). The Architecture of the Kattendijk Formation and The Implications of the Early Pliocene Depositional Evolution of the Souther Margin of the North Sea Basin. *Geologica Belgica, 23*(3-4), 323-331. https://doi.org/https://doi.org/10.20341/gb.2020.017

Deckers, J., Louwye, S., Goolaerts, S., & Everaert, S. (2023). *The Kattendijk Formation*. Retrieved from National Commission for Stratigraphy Belgium: http://ncs.naturalsciences.be/lithostratigraphy/Kattendijk-Formation

DeJong, J. T., & Westgate, Z. J. (2009). Role of Initial State, Material Properties, and Confinement Condition on Local and Gloabl Soil-Structure Interface Behavior. *Journal of Goetechnical and Geoenvirnomental Engineering, 135*(11), 1547-1778. https://doi.org/10.1061/(ASCE)1090-0241(2009)135:11(1646)

DeJong, J. T., Randolph, M. F., & White, D. J. (2003). Interface Load Transfer Degradation during Cyclic Loading: A Microscale Investigation. *Soils and Foundations, 43*(4), 81-93.

Delft University of Technology. (2020). TU Delft Code of Conduct.

Dinnebier, R. E., & Billinge, S. J. (2008). *Powder Diffraction: Theory and Practice.* Cambridge : Royal Society of Chemistry.

Doherty, P., & Gavin, K. (2011). The Shaft Capacity of Displacement Piles in Clay: A State of the Art Review. *Geotech Geol Eng, 29*, 389-410. https://doi.org/https://doi.org/10.1007/s10706-010-9389-2

ELE International. (2015). Operating Instructions; Digital Direct/Residual Shear Apparatus 26-2114. *Original Instructions(4), 9901X0248*. ELE International.

Emidio, G. D., Verástegui Flores, R. D., & Van Impe, W. F. (2009). Crushability of Granular Materials at High Stress Levels. *Proceedings of the 17th International Conference on Soil Mechanics and Geotechnical Engineering .* https://doi.org/doi:10.3233/978-1-60750-031-5-127

Evgin, E., & Fakharian, K. (1996). Effect of Stress Paths on the Behavior of Sand-Steel Interfaces. *Canadian Geotechnical Journal, 33*(6), 853-865. https://doi.org/https://doi.org/10.1139/t96-116-336

FEI. (2012). Quanta™ 650 FEG. *Product Data* .

Fernández-Landero, S., & Fernández-Caliani, J. C. (2021). Mineralogical and Crystal-Chemical Constraints on the Glauconite-Forming Process in Neogene Sediments of the Lower Guadalquivir Basin (SW Spain). *Minerals, 11*(6), 578. https://doi.org/10.3390/min11060578

GDI Flanders. (2024). *DATABANK ONDERGROND VLAANDEREN*. Retrieved from dov.vlaanderen.be: https://www.dov.vlaanderen.be/zoeken-ocdov/virtueelprofiel.html?xValues=175069.0430218562,175298.64302185693&yValues=177075.98822559882,177633.18822560058&resolution=100&layermodel=g3dv3_F#

Goldstein, J. I., Newbury, D. E., Michael, J. R., Ritchie, N. W., Scott, J. H., & Joy, D. C. (2018). *Scanning Electron Microscopy and X-Ray Microanalysis* (4 ed.). Springer. https://doi.org/https://doi.org/10.1007/978-1-4939-6676-9

Guo, Y., Golchin, A., Hicks, M. A., Liu, S., Zhang, G., & Vardon, P. J. (2023). Experimental investigation of soil–structure interface behaviour under monotonic and cyclic thermal loading. *Acta Geotechnica, 18*, 3585–3608. https://doi.org/https://doi.org/10.1007/s11440-022-01781-5(0123456789().,-volV)(0123456789().

Han, F., Ganju, E., Salgado, R., & Prezzi, M. (2018). Effects of Interface Roughness, Particle Geometry, and Gradation on the Sand–Steel Interface Friction Angle. *Journal of Geotechnical and Geoenvironmental Engineering, 144*(12). https://doi.org/10.1061/(ASCE)GT.1943-5606.000199

Head, K., & Epps, R. (2011). *Manual of Soil Laboratory Testing.* Whittles.

Houthuys, Adriaens, R., Goolaerts, S., Laga, P., Louwye, S., Matthijs, J., . . . Verhaegen, J. (2020). The Diest Fromation: a review of insights from the last decades. *Geologica Belgica, 23*(3-4), 199-218. https://doi.org/https://doi.org/10.20341/gb.2020.012

Houthuys, R., Adriaens, R., Goolaerts, S., Laga, P., Louwye, S., Matthijs, J., . . . Verhaegen, J. (2023). *The Diest Formation*. Retrieved from National Commission for Stratigraphy Belgium: http://ncs.naturalsciences.be/lithostratigraphy/Diest-Formation

Hu, L., & Pu, J. (2004). Testing and Modeling of Soil-Structure Interface. *Journal of Geotechnical and Geoenvironmental Engineering, 130*(8), 851-860. https://doi.org/10.1061/(ASCE)1090-0241(2004)130:8(851)

Huggett, J. M. (2013). Minerals: Glauconites and Green Clays. *Reference Module in Earth Systems and Environmental Sciences*. Elsevier. https://doi.org/https://doi.org/10.1016/B978-0-12-409548-9.02893-1

ICDD. (2024). *International Centre for Diffraction Data Database*. Retrieved from https://www.icdd.com/

Igoe, D., & Gavin, K. (2019). Characterization of the Blessington Sand Geotechnical Test Site. *AIMS Geosciences, 5*(2), 145-162. https://doi.org/10.3934/geosci.2019.2.145

Immovable Heritage Agency. (2014). *Heritage Object Kesselberg*. Retrieved from https://www.onroerenderfgoed.be/: https://id.erfgoed.net/erfgoedobjecten/302650

Iowa State University. (2024). *ACIDE X-Ray Diffraction Tutorial*. Retrieved from Chemical Instrumentation Facility: https://www.cif.iastate.edu/

Jardine, R. J., Lehane, B. M., & Everton, S. J. (1992). Friction Coefficients for Piles in Sands and Silts. *Offshore Site Investigation and Foundation Behaviour, 28*, pp. 661-677. https://doi.org/https://doi.org/10.1007/978-94-017-2473-9_31

Jardine, R., Chow, F., Overy, R., & Standing, J. (2005). *ICP design methods for driven piles in sands and clays.* ThomasTelford.

Joustra, K., & de Gijt, J. (1985). Results and Interpretation of Cone Penetration Tests in Soils of Different Mineralogic Composition. *Proc. 2nd Euro. Symp. Penetration Testing: ESOPT II, Amsterdam.*

Kalinina, N., Maximov, P., Makarov, B., Dasi, E., & Rudmin, M. (2023). Characterisation and Environmental Significance of Glauconite from Mining Waste of the Egorievsk Phosphorite Deposit. *Minerals, 13*, 1228. https://doi.org/https://doi.org/10.3390/min13091228

Kim, D., Nam, B., & Youn, H. (2018). Effect of clay content on the shear strength of clay–sand mixture. *International Journal of Geo-Engineering, 9*(19). https://doi.org/https://doi.org/10.1186/s40703-018-0087-x

King, T., Wuenscher, T., Griffiths, L., & Fraps, A. (2023). *A novel approach to quantifying glauconite content in soils using digital image analysis.* Norwegian Geotechnical Institute.

Koerner, R. M. (1998). *Designing with Geosynthetics.* Prentice Hall.

Lehane, B. M., & Jardine, R. J. (1992). Residual Strength Characteristics of Bothkennar Clay. *Géotechnique , 42*(2), 363-367. https://doi.org/10.1680/geot.1992.42.2.363

Lehane, B. M., Jardine, R., Frank, R., & Bond, A. (1993). Mechanisms of Shaft Friction in Sand from Instrumented Pile Tests. *Journal of Geotechnical Engineering*, 119: 19-35. https://doi.org/10.1061/(ASCE)0733-9410(1993)119:1(19)

Lehane, B., Bittar, E., Lacasse, S., Liu, Z., & Nadim, F. (2022). New CPT methods for evaluation of the axial capacity of driven piles. In G. Gottardi, & L. Tonni (Ed.), *Cone Penetration Testing 2022, Proceedings of the 5th International Symposium on Cone Penetration Testing (CPT'22), 8-10 June 2022.* Bologna, Italy: CRC Press. https://doi.org/10.1201/9781003308829-1

Lehane, B., Liu, Z., Bittar, E., Farrokh, N., Lacasse, S., Jardine, R., . . . Gavin, K. (2020). *A New 'Unified' CPT-Based Axial Pile Capacity Design Method for Driven Piles in Sand.* Proceedings Fourth International Symposium on Frontiers in Offshore Geotechnics.

Lemos, L. L., & Vaughan, P. R. (2000). Clay-Interface Shear Resistance. *Géotechnique, 50*(1), 55-64.

Lennon, A. E. (2023, October 19). *A tricky, sticky mineral that's challenging offshore wind developers*. Retrieved from The Bedford Light: https://newbedfordlight.org/a-tricky-sticky-mineral-thats-challenging-offshore-wind-developers/

Littleton, I. (1976). An Experimental Study of the Adhesion Between Clay and Steel. *Journal of Terramechanics, 13*(3), 141-152.

Liu, T., Chen, H., Buckley, M. R., Quinteros, S., & Jardine, R. J. (2019). Characterization of Sand-Steel Interface Shearing Behavior for the Interpretation of Driven Pile Behaviour in Sands. *7th International Symposium on Deformation Characteristics of Geomaterials (IS-Glasgow 2019). 92.* Glasgow: E3S Web of Conferences. https://doi.org/https://doi.org/10.1051/e3sconf/20199213001

Liu, T., Quinteros, S., Jardine, J., Carraro, A. H., & Robinson, J. (2019). A unified database of ring shear steel-interface tests on sandy-silty soils. *Proceedings of the XVII ECSMGE-2019 Geotechnical Engineering foundation of the future.* Reykjavik. https://doi.org/10.32075/17ECSMGE-2019-0268

Logvinenko, N. (1982). Origin of Glauconite in the Recent Bottom Sediments of the Ocean. *Sedimentary Geology, 31*, 43-48.

López-Quirós, A., Sánchez-Navas, A., Nieto, F., & Escutia, C. (2020). New insights into the nature of glauconite. *American Mineralogist, 105*, 674-686. https://doi.org/https://doi.org/10.2138/am-2020-7341

Lupini, J. F., Skinner, A. E., & Vaughan, P. R. (1981). The Drained Residual Strength of Cohesive Soils. *Géotechnique, 31*(2), 181-213.

Malvern Panalytical. (2024). *X-Ray Analysis*. Retrieved from Technology: https://www.malvernpanalytical.com/en/products/technology/xray-analysis

Martinez, A., & Frost, J. D. (2017). The Influence of Surface Roughness From on the Strength of Sand-Structure Interfaces. *Géotechnique Letters, 7*, 104-111. https://doi.org/http://dx.doi.org/10.1680/jgele.16.00169

Martinez, A., & Stutz, H. H. (2018). Rate Effects on the Interface Shear Behaviour of Normally and Overconsolidated Clay. *Geotechnique*. https://doi.org/10.1680/jgeot.17.p.311

Martinez, A., Frost, J., & Hebeler, G. L. (2015). Experimental Study of Shear Zones Fromed at Sands/Steel Interfaces in Axial and Torsional Axisymmetric Tests. *Geotechnical Testing Journal, 38*(4). https://doi.org/DOI: 10.1520/GTJ20140266

McConchie, D. M., & Lewis, D. W. (1978). Authigenic, perigenic, and allogenic glauconites from the Castle Hill Basin, North Canterbury, New Zealand. *New Zealand Journal of Geology and Geophysics, 21*(2), 199-214. https://doi.org/10.1080/00288306.1978.10424051

McRae, S. G. (1972). Glauconite. *Earth-Science Reviews, 8*, 397-440.

Microtrac. (2024). *PARTICLE SIZE ANALYZER BLUEWAVE*. Retrieved from microtrac.com: https://www.microtrac.com/products/particle-size-shape-analysis/laser-diffraction/bluewave/

Mitchell, K. J., & Soga, K. (2005). *Fundamentals of Soil Behavior* (3 ed.). John Wiley & Sons, Inc.

NGI. (2024). *PIGS - Piling in Glauconitic Sand Joint Industry Project (JIP)*. Retrieved from https://www.ngi.no/en/projects/pigs/

Obasi, C. C., Terry, D. O., Myer, G. H., & Grandstaff, D. E. (2011). Glauconite Composition and Morphology, Shocked Quartz, and the Origin of the Cretaceous (?) Main Fossiliferous Layer (MFL) in Southern New Jersey, U.S.A. *Journal of Sedimentary Research, 81*, 479-494. https://doi.org/10.2110/jsr.2011.42

Odin, G. S., & Matter, A. (1981). De glauconiarum origine. *Sedimentology, 28*, 611-641.

Perikleous, G., Meissl, S., Troya Diaz, A., Stergiou, T., & Ridgway-Hill, A. (2023). Monopile installation in glauconitic sands. *9th International Offshore Site Investigation and Geotechnics (OSIG): Innovative Getechnologies for Energy Transition*, (pp. 132–138).

Piedrabuena, A. R. (2024). First Steps in the Calibration Cnamer Pile Tests with Glauconitic Sands; On the Bahavior of the Sand Fraction from Glauconitic Sand of the Kattendijk Formation in Antwerp, Belgium. *Master Thesis*. Delft University of Technology.

Potts, D., Dounias, G. T., & Vaughan, P. (1987). Finite Element Analysis of the Direct Shear Box Test. *Géotechnique, 37*(1), 11-23. https://doi.org/https://doi.org/10.1680/geot.1987.37.1.11

Quinn, T., Robinson, S., & Brown, M. J. (2012). High Strain Rate Characterisation of Kaolin and Its Application to Rapid Load Pile Testing. *Proceedings of the 9th international conference on testing and design methods for deep foundations (IS Kanazawa 2012)*, (pp. 311 - 319). Kanazawa, Japan.

Quinteros, S., Dyvik, R., & Mortensen, N. (2017). *Geotechnical Frontiers 2017: Interface friction angle from Ring Shear tests on offshore North Sea sands.*

Quinteros, S., Westgate, Z., Vinck, K., Dantal, V., Lindtorp, A., & Toma, M. (2023). Interface friction angle of glauconitic sands for pile design. *9th International SUT OSIG Conference "Innovative Geotechnologies for Energy Transition".* London. Retrieved from https://www.researchgate.net/publication/374367631_Interface_friction_angle_of_glauconitic_sands_for_pile_design

Randolph, M. F. (2003). Science and Empiricism in Pile Foundation Design. *Géotechnique, 53*(10), 847-875. https://doi.org/https://doi.org/10.1680/geot.2003.53.10.847

Rao, S. K., Allam, M. M., & Robinson, R. G. (1998). Interfactial Friction Between Sands and Solid Surfaces. *Proceedings of the Institution of Civil Engineers - Geotechnical Engineering.* ICE Publishing. https://doi.org/10.1680/igeng.1998.30112

Rao, S. K., Allam, M. M., & Robinson, R. G. (2000). Drained Shear Strength of Fine-Grained Soil-Solid Surface Interfaces. *Proceedings of the Institution of Civil Engineers - Geotechnical Engineering.* https://doi.org/10.1680/geng.2000.143.2.75

Rao, S. K., Allam, M. M., & Robinson, R. G. (2002). An Apparatus for Evaluating Adhesion Between Soils and Solid Surfaces. *Journal of Testing and Evaluation, 30*(1), 27 - 36.

Reddy, S. E., Chapman, D. N., & Sastry, V. R. (2000). Direct Shear Interface Test for Shaft Capacity of Piles in Sand. *Geotechnical Testing Journal, 23*(2), 199-205.

Rezaei, V., & Walkowska, D. (2024). *Obtaining Relaiable Residual Interface Friction Angles in Glauconitic Soils for Monopile Design.* Norwegian University of Science and Technology, Department of Civil and Environmental Engineering . NTNU.

Robertson, P., & Cabal, K. (2022). *Guide to Cone Penetration Testing* (7th ed.). Gregg Drilling LLC.

Sachan, A., Seethalakshmi, P., & Mishra, M. C. (2019). Effect of Crushing on Stress-Strain and Pore Pressure Behavior of Micaceous Kutch Soil Under Monotonic Compression and Repeated Loading-Unloading Conditions. *Geotech Geol Eng, 37*, 5269–5283. https://doi.org/https://doi.org/10.1007/s10706-019-00979-x

Saldivar-Moguel, E. E. (2002). *Investigation into the behaviour of displacement piles under cyclic and seismic loads.* PhD Thesis, Imperial College, London.

Santos, W. O., Mattiello, E. M., da Costa, L. M., Abrahão, W. A., de Novais, R. F., & Cantarutti, R. B. (2015). Thermal and chemical solubilization of verdete for use as potassium fertilizer. *International Journal of Mineral Processing, 140*, 72-78. https://doi.org/https://doi.org/10.1016/j.minpro.2015.05.003.

Shen, J., Wang, X., Wang, X., Yao, T., Wei, H., & Zhu, C. (2021). Effect and mechanism of fines content on the shear strength of calcareous sand. *Bulletin of Engineering Geology and the Environment, 80*, 7899-7919. https://doi.org/https://doi.org/10.1007/s10064-021-02398-w

Skempton, A. W. (1953). The Colloidal Activity of Clays. *Proceedings of the third international conference on soil mechanics and foundation engineering* (pp. 57-61). Zurich: ICOSOMEF.

Starzec, K., Stadnik, R., Skiba, M., Bębenek, S., & Waśkowska, A. (2023). Origin and paleoenvironmental significance of Al-rich glauconite in the Ediacaran/Cambrian deposits of the Lublin Basin, Poland (SW margin of Baltica). *Precambrian Research, 397*, 107165. https://doi.org/https://doi.org/10.1016/j.precamres.2023.107165.

Sylvia, C. (2022). Evaluation of a magnetic jar separation test to determine glauconite content. Master's Project. UMass Dartmouth, College of Engineering.

Tedrow, J. C. (2002). *Greensand and Greensand Soil of New Jersey: A Review.* The State University of New Jersey Rutgers.

The Dutch Research Council (NWO). (2018). Netherlands Code of Conduct for Research Integrity. NWO.

Thevanayagam, S., & Martin, G. R. (2002). Liquefaction in silty soils—screening and remediation issues. *Soil Dynamics and Earthquake Engineering, 22*(9-12), 1035-1042. https://doi.org/https://doi.org/10.1016/S0267-7261(02)00128-8

Triplehorn, D. M. (1966). Morphology, Internal Structure, and Origin of Glauconite Pellets. *Sedimentology, 6*(4), 247-266. https://doi.org/https://doi.org/10.1111/j.1365-3091.1966.tb01894.x

Tsubakihara, Y., & Kishida, H. (1993). Frictional Behaviour Between Normally Consolidated Clay and Steel by Two Direct Shear Type Apparatuses. *Soils and Foundations, 33*(2), 1-13.

Tsubakihara, Y., Kishida, H., & Nishiyama, T. (1993). Friction Between Cohesive Soils and Steel. *Soild and Foundations, 33*(2), 145-156.

Uesugi, M., & Kishida, H. (1986). Frictional Resistance at Yield Between Dry Sand and Mild Steel. *Soils and Foundations, 26*(4), 139-149.

Uesugi, M., Kishida, H., & Tsubakihara, Y. (1988). Behavior of Sand Particles in Sand-Steel Friction. *Soils and Foundations, 28*(1), 107-118.

Van Raak, R. (2009). *Geotechnical properties of glauconitic sands.* Elsevier; Artesis Hogeschool Antwerpen, Paardenmarkt 92, 2000 Antwerpen, Belgium.

Welton, J. E. (2003). SEM Petrology Atlas. *Methods in Exploration Series No. 4*. Tulsa, Oklahoma, U.S.A.: The American Association of Petrolium Geologists.

Westgate, Z., Argiolas, R., Wallerand, R., & Ballard, J.-C. (2021). Experience with Interface Shear Box Testing for Pipe-Soil Interaction Assessment on Sand. *Offshore Technology Conference.* Houston, Texas. https://doi.org/https://doi.org/10.4043/31268-MS

Westgate, Z., DeGroot, D., McMullin, C., Zou, Y., Guo, D., Van Haren, S., . . . Browning, J. (2023). Effect of degradation on geotechnical behavior of glauconite sands from the U.S. Mid-Atlantic Coastal Plain. *Ocean Engineering, 283*. https://doi.org/https://doi.org/10.1016/j.oceaneng.2023.115081

Westgate, Z., McMullin, C., Zeppilli, D., Beemer, R., & DeGroot, D. (2022). Geological and geotechnical characteristics of glauconitic sands. *Geo-Congress 2022*, (pp. 113-121). https://doi.org/10.1061/9780784484036.012

Westgate, Z., Rahim, A., Senanayake, A., Pisanò, F., Maldonado, C., Ridgway-Hill, A., . . . Ghasemi, P. (2024). The Piling in Glauconitic Sands (PIGS) JIP: Reducing Geotechnical Uncertainty for U.S. Offshore Wind Development. *OTC-35483-MS; Offshore Technology Conference held in Houston, TX, USA, 6 – 9 May, 2024.* https://doi.org/https://doi.org/10.4043/35483-MS

Wigley, R., & Compton, J. S. (2007). Oligocene to Holocene glauconite–phosphorite grains from the Head of the Cape Canyon on the western margin of South Africa. *Deep Sea Research Part II Topical Studies in Oceanography, 54*(11), 1375-1395. https://doi.org/DOI: 10.1016/j.dsr2.2007.04.004

Wolff, R. G. (1967). X-Ray and Chemical Study of Weathering Glauconite. *The American Mineralogist, 52*.

Wood, D. M. (1990). *Soil Behavior and Critical State Mechanics.* Cambridge University Press.

Yang, Z., Jardine, R., Zhu, B., Foray, P., & Tsuha, C. (2010). Sand grain crushing and interface shearing during displacement pile installation in sand. *Geotechnique, 60*(6), 469 - 482 . https://doi.org/10.1680/geot.2010.60.6.469

Zhang, J., Soltani, A., Deng, A., & Jaksa, M. B. (2019). Mechnanical Behavior of Micaceous Clays. *Journal of Rock Mechanics and Geotechnical Engineering, 11*(5), 1044-1054. https://doi.org/https://doi.org/10.1016/j.jrmge.2019.04.001

Zhang, P., Ding, S., & Fei, K. (2021). Research on Shear Behavior of Sand-Structure Interface Based on Monotonic and Cyclic Tests. *Applied Sciences, 11, 11837*. https://doi.org/https://doi.org/10.3390/app112411837

Zimnik, A. R., Van Baalen, L. R., Verhoef, P. N., & Ngan-Tillard, D. J. (2018). The adherence of clay to steel surfaces. *ISRM International Symposium 2000, IS 2000.* International Society for Rock Mechanics.

Appendix A – X-Ray Analysis Reports

X-RAY FACILITIES GROUP

Dr. Amarante Böttger

Dhr. Ruud Hendrikx
Drs. Richard Huizenga

Delft University of Technology, Faculty of ME
Department of Materials Science and Engineering
Mekelweg 2, NL-2628 CD Delft, the Netherlands, phone +31(0)152789459

XRD identification of a glauconitic sand powder sample

Author	:	Ruud Hendrikx
Date	:	09 sep 2024
Researcher	:	Maria Tverdokhlebova, CITG

Sample
The sample is a mineral sand powder, presumably containing Glauconite.

Specimen
The sample was deposited as a thin layer on a Si510 zero-background wafer.

Experimental
Instrument: Bruker D8 Advance diffractometer Bragg-Brentano geometry and Lynxeye-XE-T position sensitive detector. Cu Kα radiation. Divergence slit V12, scatter screen height 5 mm, 40 kV 40 mA. Sample spinning. Detector settings "high resolution".

Measurements
Coupled θ -2θ scan 5° - 150°, step size 0.03 ° 2θ, counting time per step 1 s.

Data evaluation
Bruker software DiffracSuite.EVA vs 7.2.

Results
Figure 1 shows the measured XRD pattern in black, after background subtraction, between 10 and 110 ° 2θ. For better display of small peaks, the intensity scale is square root.
The colored sticks give the peak positions and intensities of the possibly present phases, using the ICDD pdf5 and COD databases, see table 1. Not all small peaks could be identified.

sample	*compound*	
Glauconitic sand	Quartz	SiO2
	Glauconite-1M	K(Fe,Al)2(Si,Al)4O10(OH)2
	Goethite	Fe+3O(OH)

Table 1

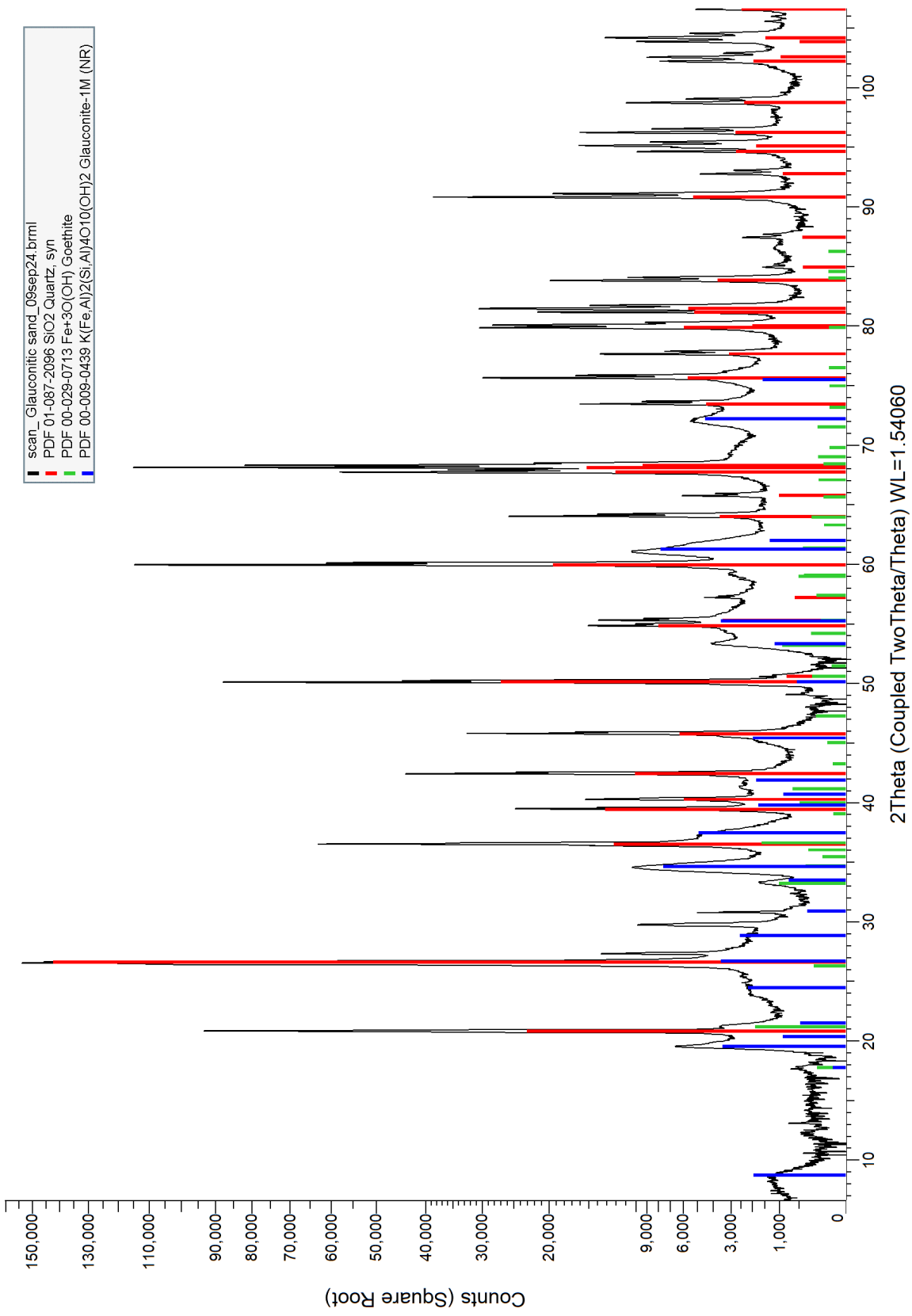

Figure 1 XRD pattern sample " Glauconitic sand", intensity scale is square root.

X-RAY FACILITIES GROUP

Dr. Amarante Böttger *A.J.Bottger@tudelft.nl*
phone +31(0)1527·82243
Dhr. Ruud Hendrikx *R.W.A.Hendrikx@tudelft.nl*
Drs. Richard Huizenga *R.M.Huizenga@tudelft.nl*

Delft University of Technology, Faculty of ME
Department of Materials Science and Engineering
Mekelweg 2, NL-2628 CD Delft, the Netherlands, phone +31(0)152789459

XRD identification of glauconitic sand powder samples

Author	:	Ruud Hendrikx
Date	:	16 sep 2024
Researcher	:	Maria Tverdokhlebova, CITG

Samples
The samples are mineral sand powders, presumably containing Glauconite.

Specimen
The sample was deposited as a thin layer on a Si510 zero-background wafer.

Experimental
Instrument: Bruker D8 Advance diffractometer Bragg-Brentano geometry and Lynxeye position sensitive detector. Cu Kα radiation. Divergence slit V12, scatter screen height 5 mm, 40 kV 40 mA. Sample spinning. Detector settings LL 0.19 W 0.06.

Measurements
Coupled θ -2θ scan 5° - 110°, step size 0.03 ° 2θ, counting time per step 2 s.

Data evaluation
Bruker software DiffracSuite.EVA vs 7.2.

Results
Figures 1 to 3 show the measured XRD patterns in black, after background subtraction. The colored sticks give the peak positions and intensities of the possibly present phases, using the ICDD pdf5 and COD databases, see table 1. Not all small peaks could be identified.

If the analysis is a significant part of a publication, a co-authorship is preferred.
In any case, it is useful to involve us in the preparation of any presentation to ensure optimum and correct use of the analysis results!
Whenever used in a publication, an acknowledgement will be appreciated, e.g.:
"personX at the Department of Materials Science and Engineering of the Delft University of Technology is acknowledged for the X-ray analysis".

sample	*compound*	
Leuven_Glauc_sep_65C_main	Quartz	SiO2
	Glauconite-1M (NR)	K(Fe,Al)2(Si,Al)4O10(OH)2
Antwerp_Glauc_sep_65C_S2	Quartz	SiO2
	Glauconite-1M (NR)	K(Fe,Al)2(Si,Al)4O10(OH)2
Antwerp_Glauc_Fwll_S3	Quartz	SiO2
	Glauconite-1M (NR)	K(Fe,Al)2(Si,Al)4O10(OH)2
	Calcite	CaCO3
	Goethite	Fe+3O(OH)

Table 1

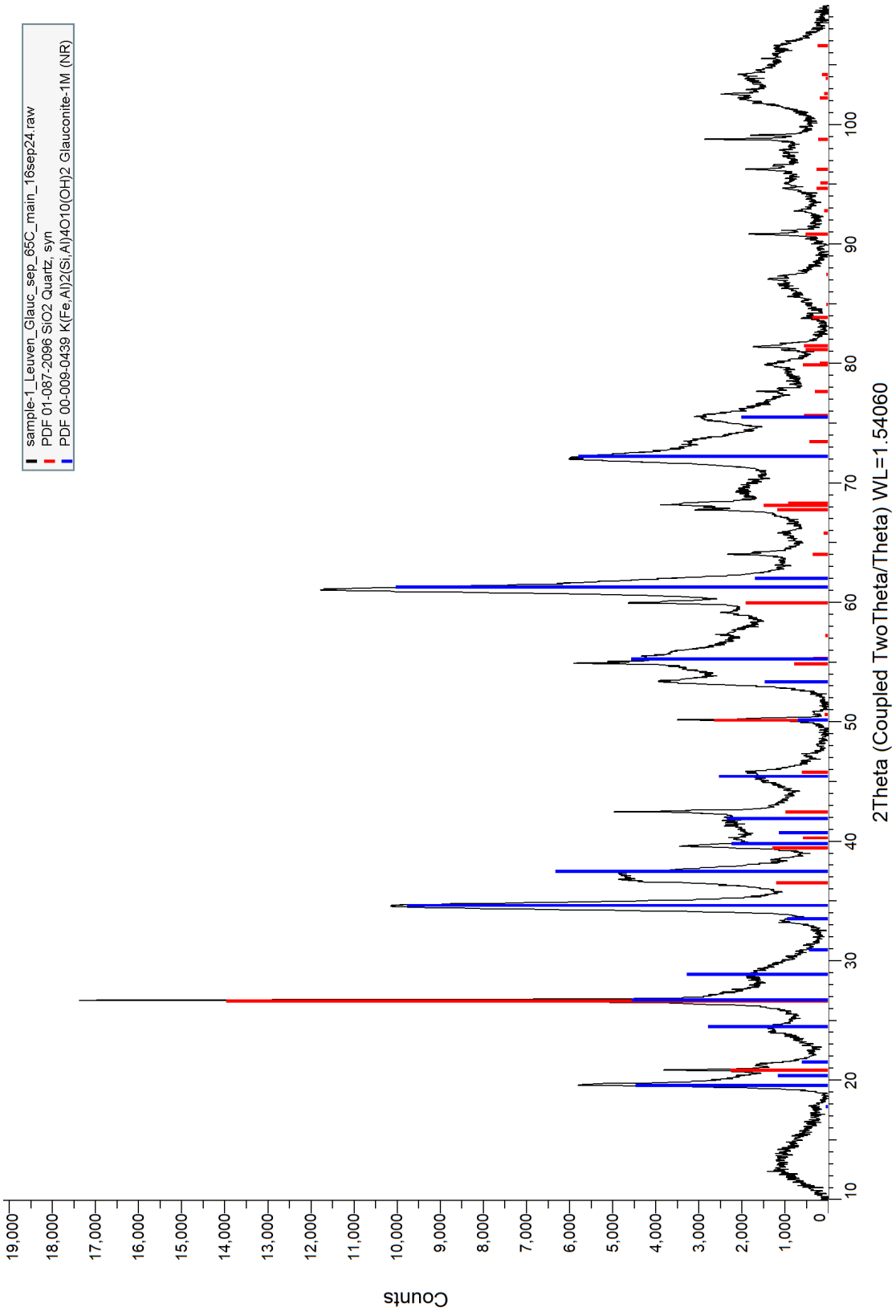

Figure 1 XRD pattern sample " Leuven_Glauc_sep_65C_main", intensity scale is linear

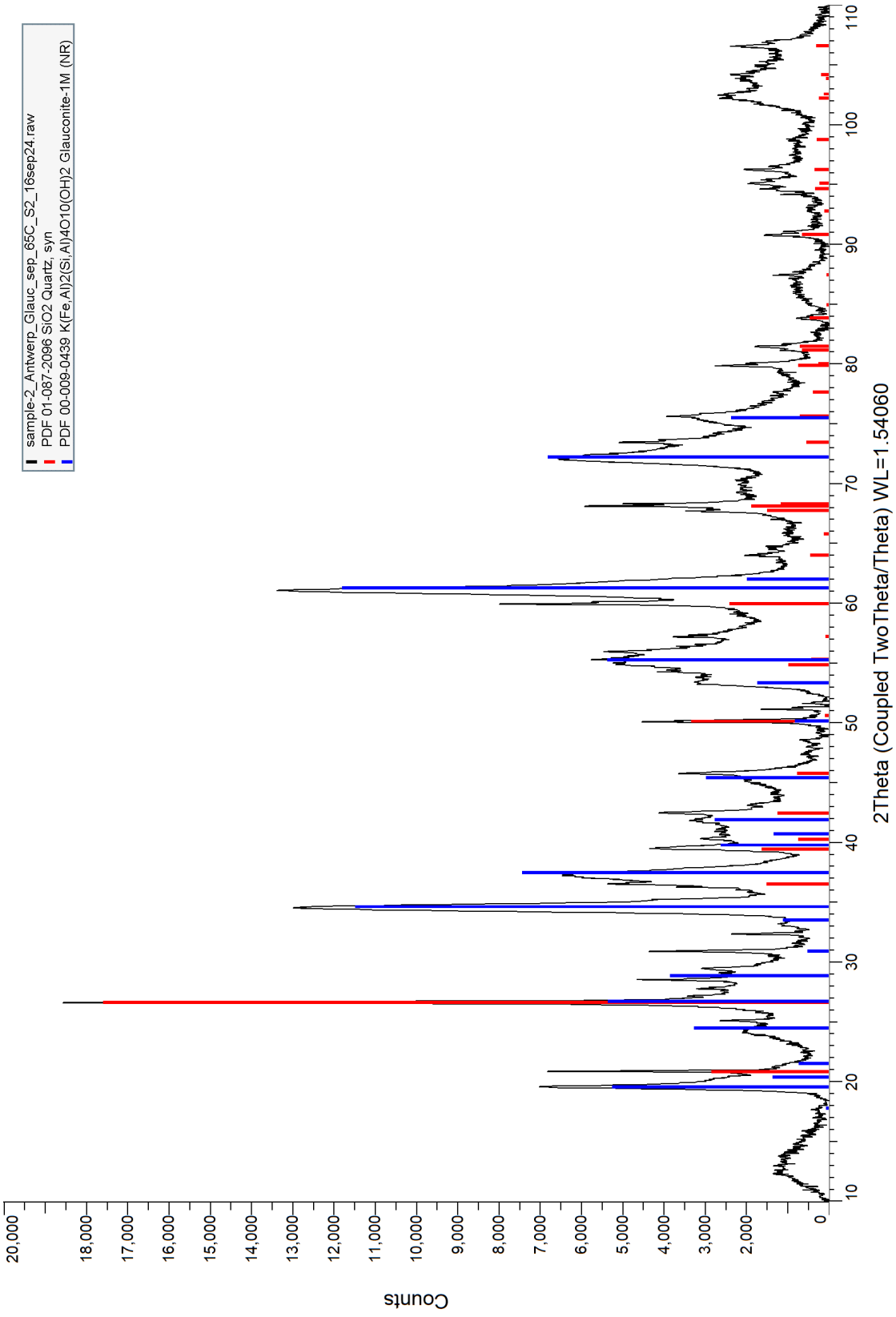

Figure 2 XRD pattern sample "Antwerp_Glauc_sep_65C_S2", intensity scale is linear

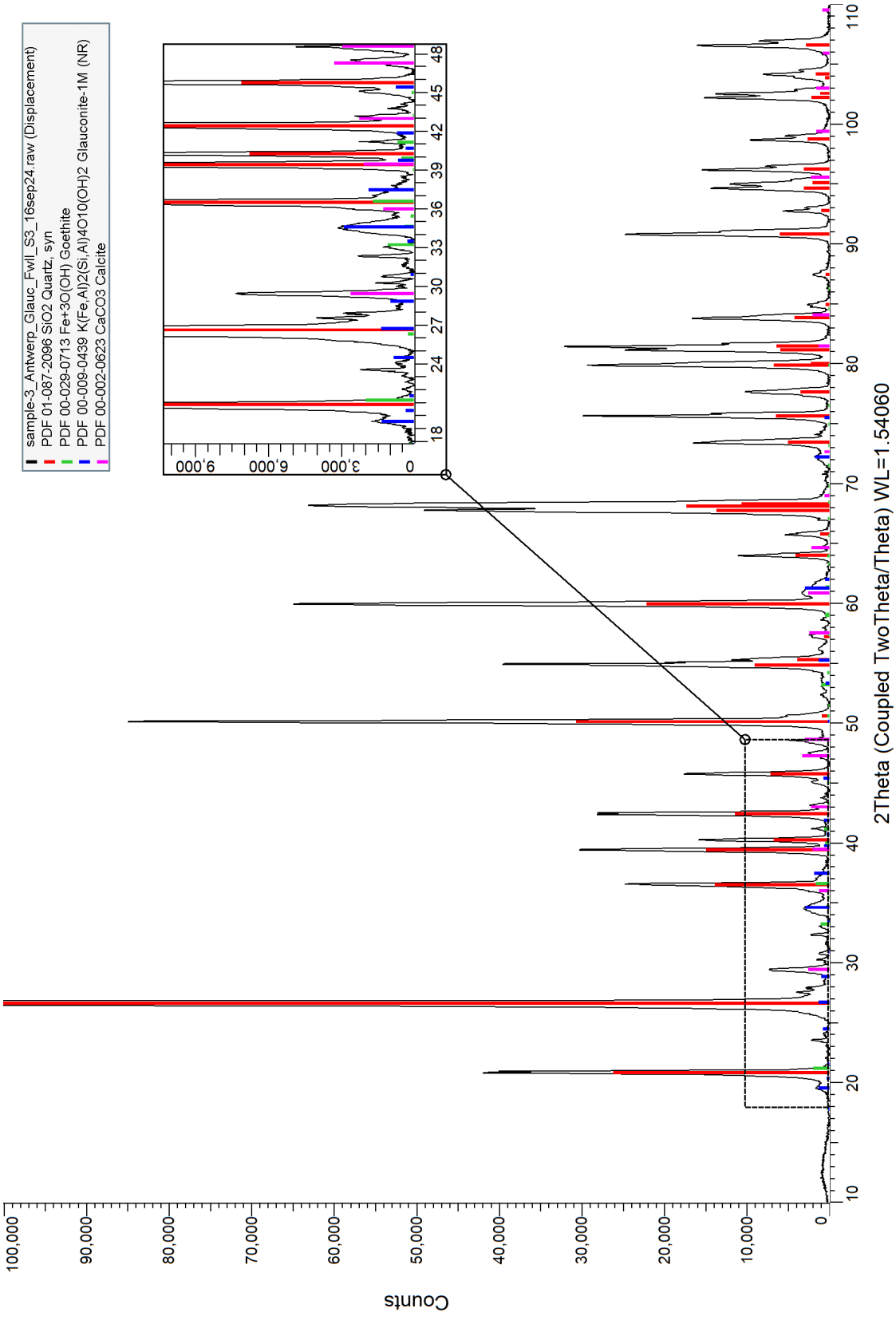

Figure 3 XRD pattern sample "Antwerp_Glauc_Fwll_S3 ", intensity scale is linear

Materials Science and Engineering
TUDelft, Faculty of 3mE
Mekelweg 2
2628 CD Delft, The Netherlands
Tel:015-2789459
Email: R.W.A.Hendrikx@tudelft.nl

X- ray diffraction facilities

Experimental conditions:

For XRF analysis the measurements were performed with a Panalytical Axios Max WD-XRF spectrometer and data evaluation was done with SuperQ5.0i/Omnian software. 18/12/2015 09:37:03

9/6/2024 4:48:45 PM

PANalytical

Quantification of sample Maria Tverdokhlebova, sample "Glauconitic sand", 06sep24

Sum before normalization: 105.2 wt%

Normalised to: 100.0 wt%

Sample type: Solid

	Compound Name	Conc. (wt%)	Absolute Error (wt%)
1	SiO2	66.375	0.1
2	Fe2O3	20.466	0.3
3	Al2O3	8.651	0.08
4	K2O	2.307	0.05
5	MgO	1.446	0.04
6	TiO2	0.235	0.01
7	P2O5	0.173	0.01
8	CaO	0.145	0.01
9	Na2O	0.066	0.008
10	V2O5	0.041	0.006
11	SO3	0.04	0.006
12	Cr2O3	0.019	0.004
13	ZrO2	0.012	0.003
14	Rb2O	0.011	0.003
15	ZnO	0.007	0.003
16	As2O3	0.005	0.002
17	SrO	0.003	0.002

Use of our XRD or XRF analysis:
In a publication: 'PersonX at the Department of Materials Science and Engineering of the Delft University of Technology is acknowledged for the X-ray analysis. If it is an important part of the publication: a co-authorship is preferred. It is useful to involve us in the preparation of any presentation!

Appendix B – ESEM Images

Image Description	*ESEM Image*
Leuven Sand: *2 mm Fraction with Quartz; No HCl Pretreatment; 125x Magnification*	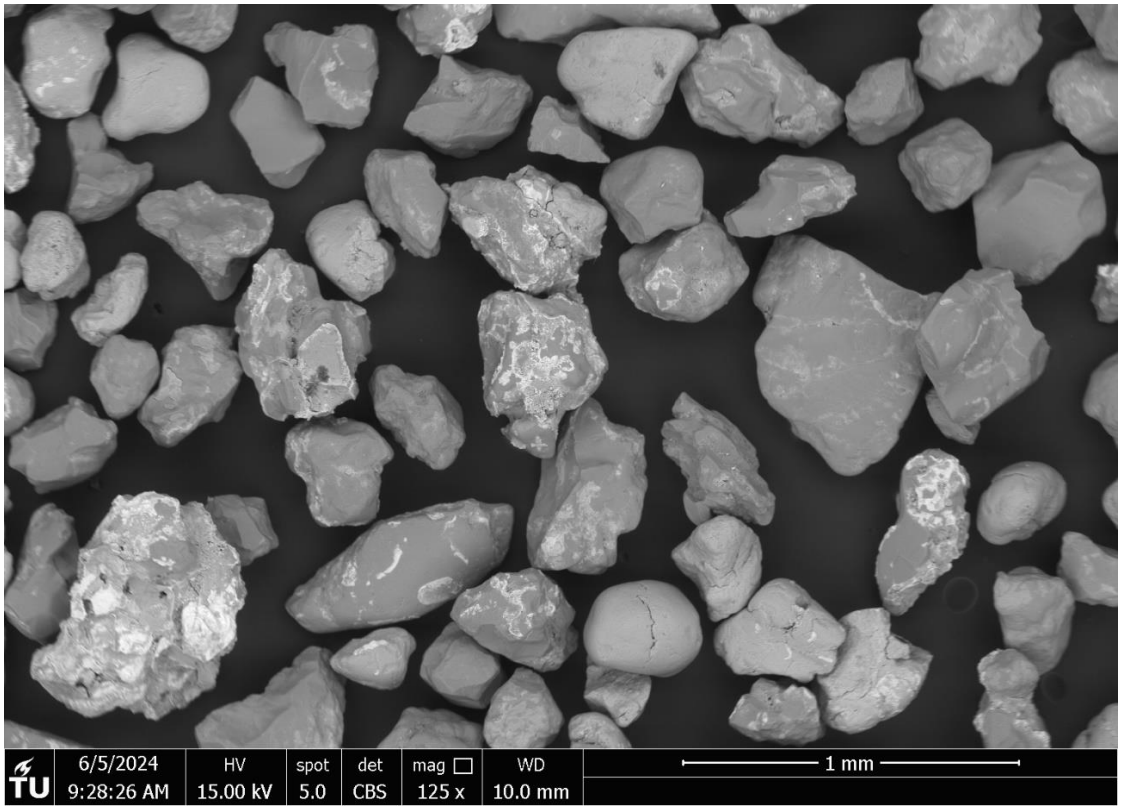
Leuven Sand: *2 mm Fraction with Quartz; No HCl Pretreatment; 250x Magnification*	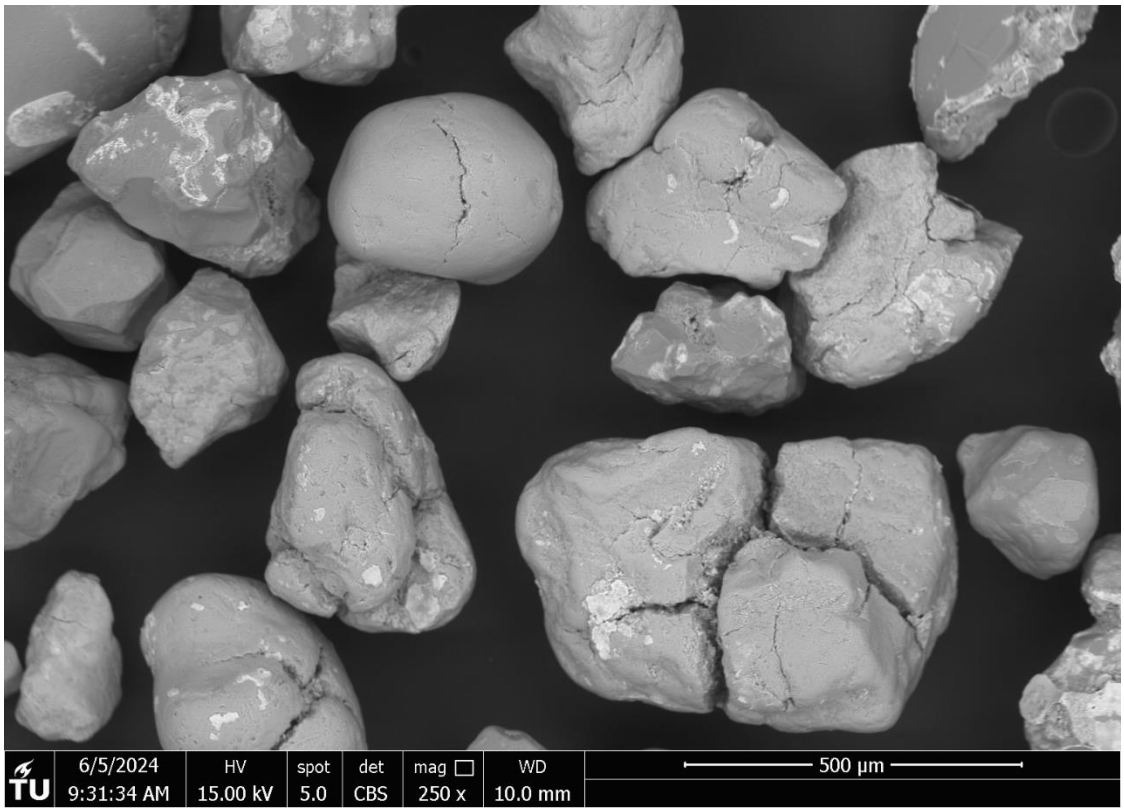

Image Description	*ESEM Image*
Leuven Sand: *2 mm Fraction with Quartz; No HCl Pretreatment; 2500x Magnification*	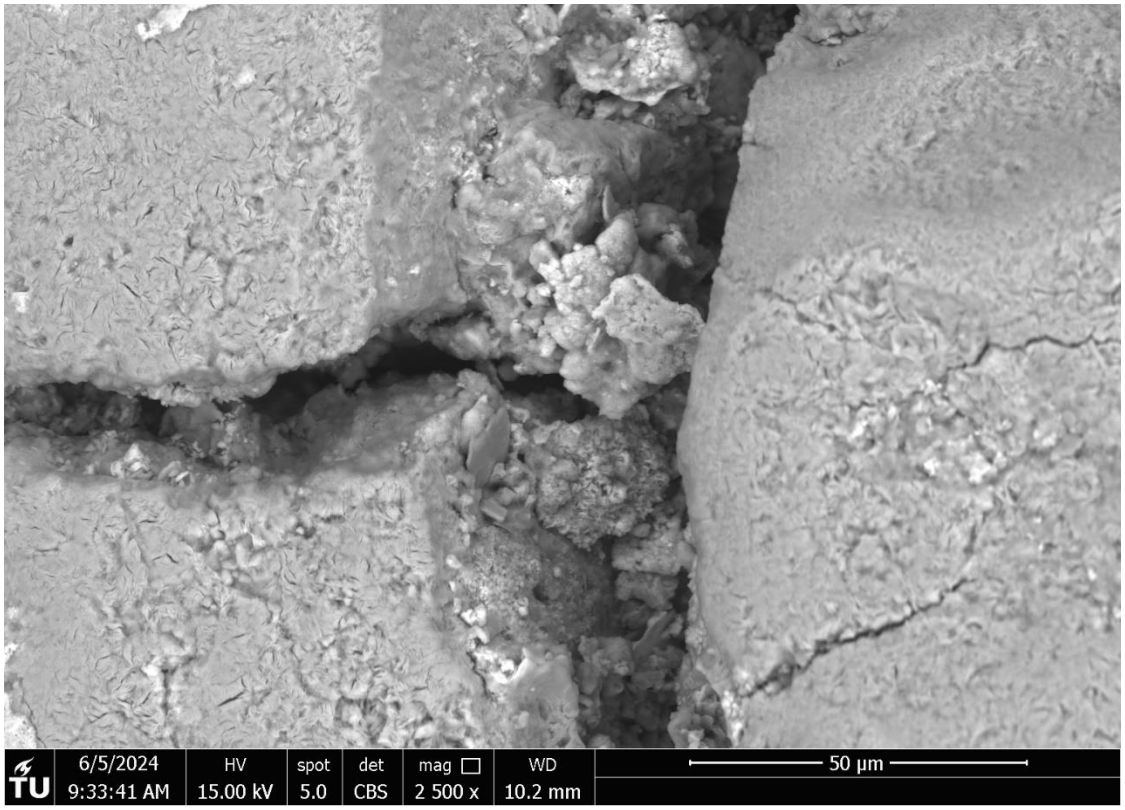
Leuven Sand: *Magnetically Separated Glauconite; With HCl Pretreatment; Oven-Drying at 65°C; 125x Magnification*	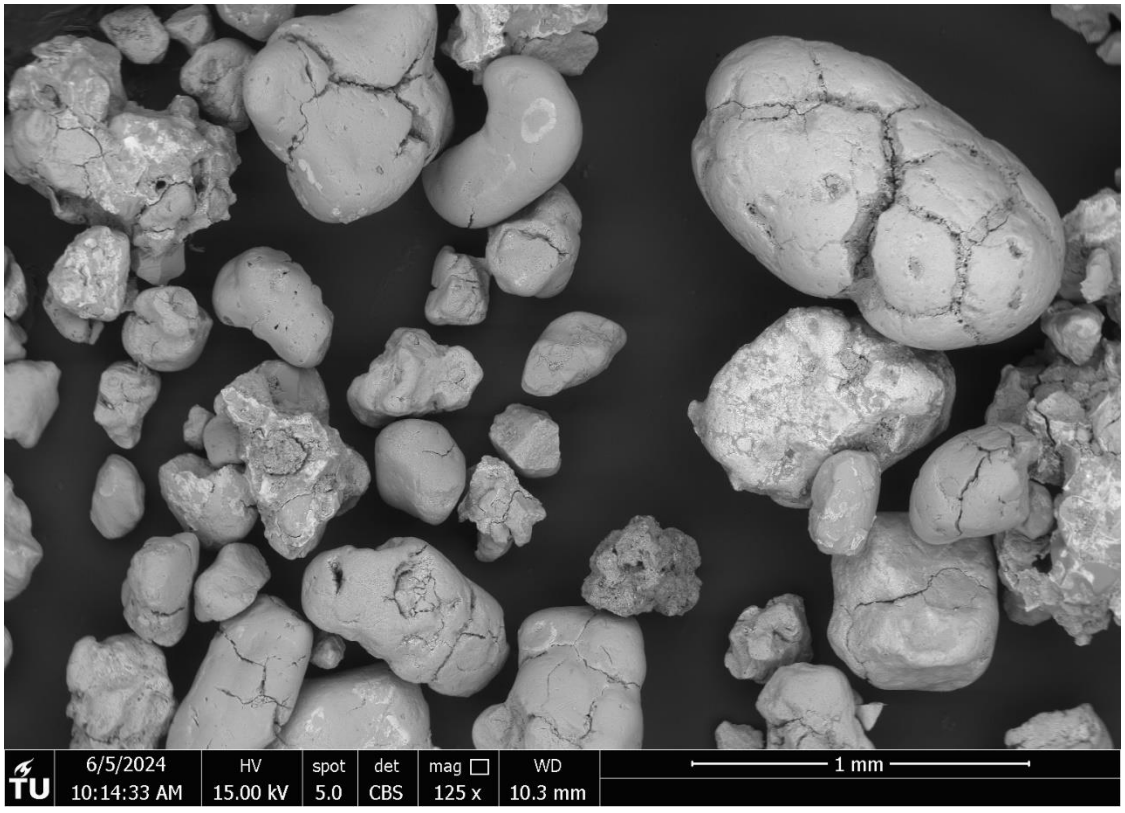

Image Description	*ESEM Image*
Leuven Sand: *Magnetically Separated Glauconite; With HCl Pretreatment; Oven-Drying at 65°C 125x Magnification*	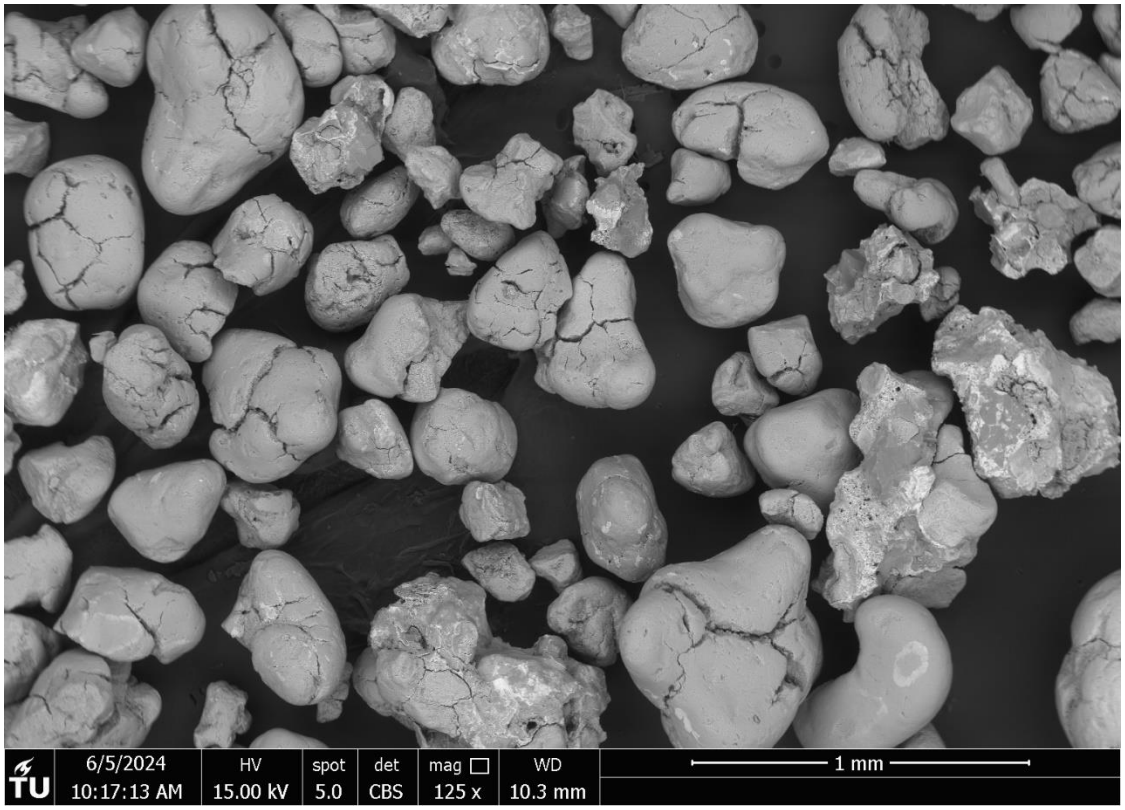
Leuven Sand: *Magnetically Separated Glauconite; With HCl Pretreatment; Oven-Drying at 65°C 250x Magnification*	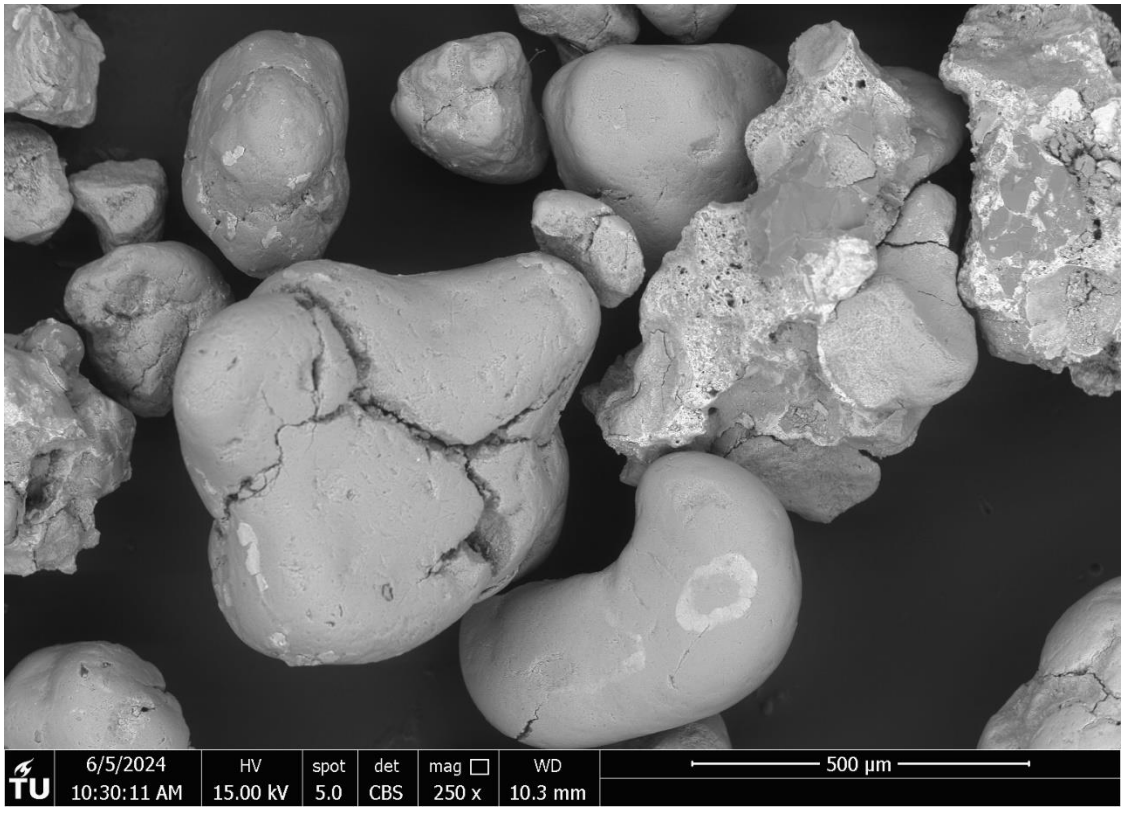

Image Description	*ESEM Image*
Leuven Sand: *Magnetically Separated Glauconite; With HCl Pretreatment; Oven-Drying at 65°C 500x Magnification*	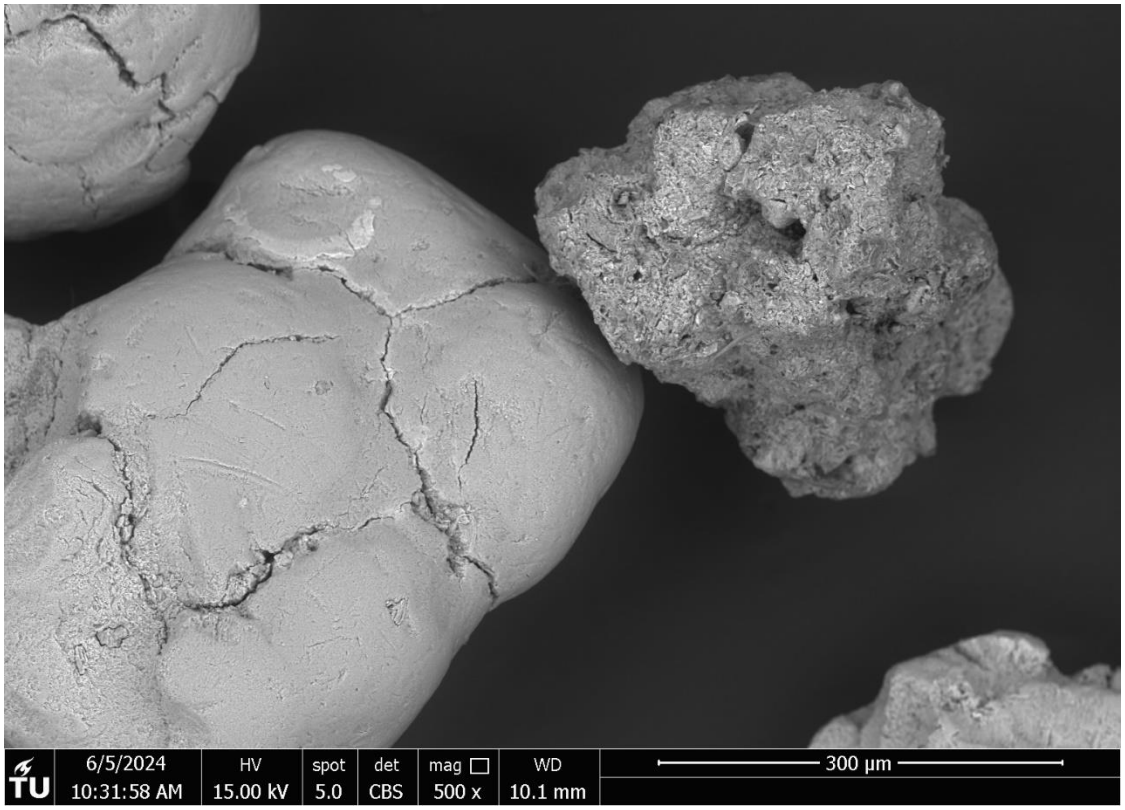
Leuven Sand: *Magnetically Separated Glauconite; With HCl Pretreatment; Oven-Drying at 105°C 125x Magnification*	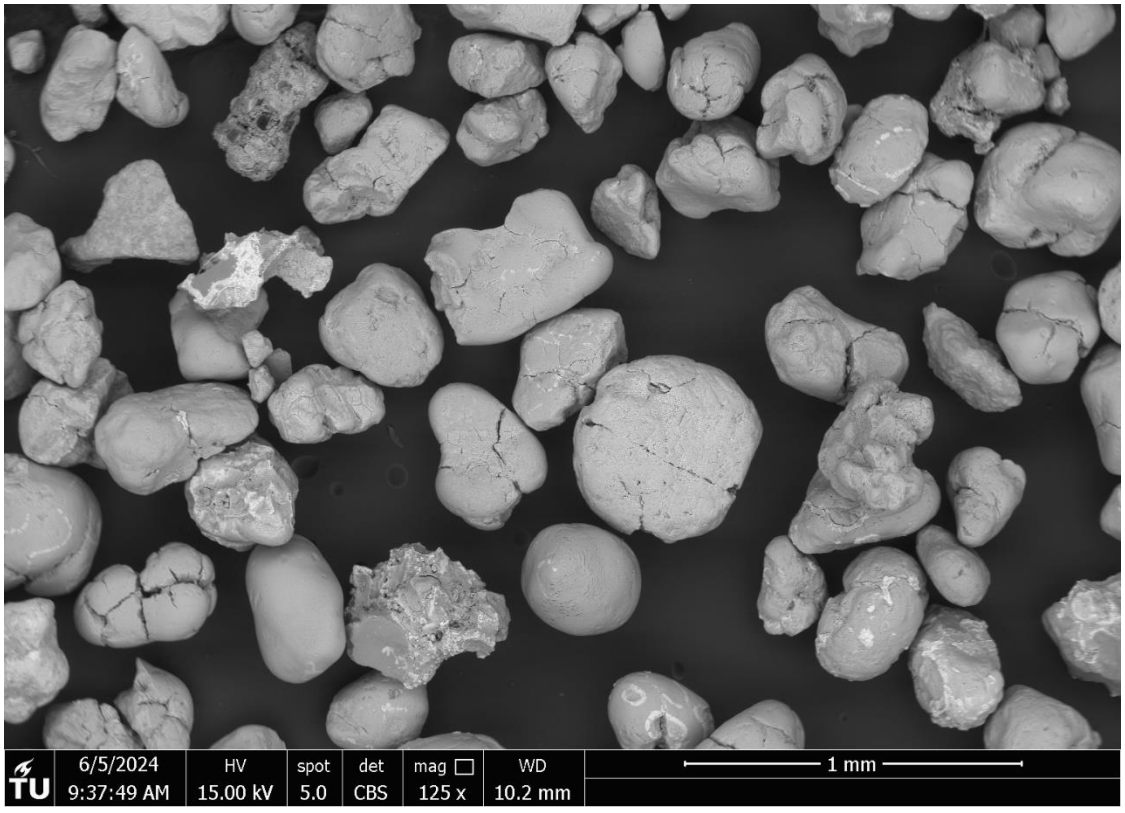

Image Description	*ESEM Image*
Leuven Sand: *Magnetically Separated Glauconite; With HCl Pretreatment; Oven-Drying at 105°C 250x Magnification*	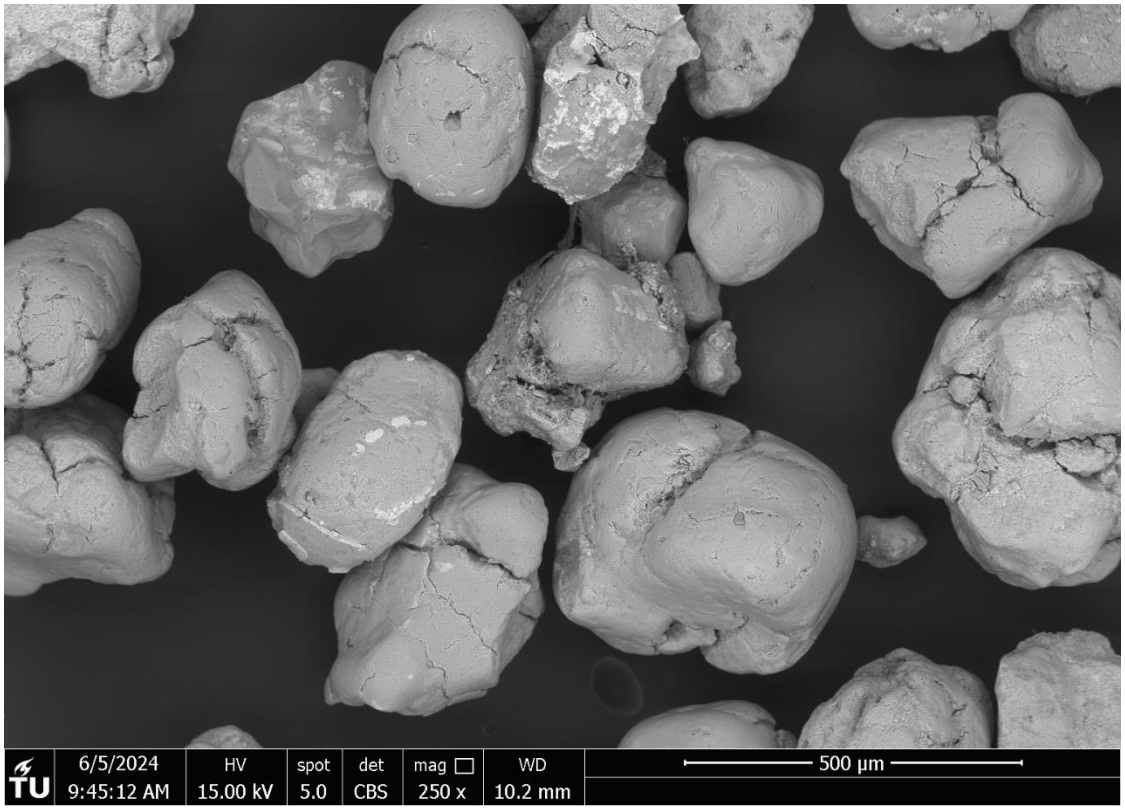
Leuven Sand: *Magnetically Separated Glauconite; With HCl Pretreatment; Oven-Drying at 105°C 1000x Magnification*	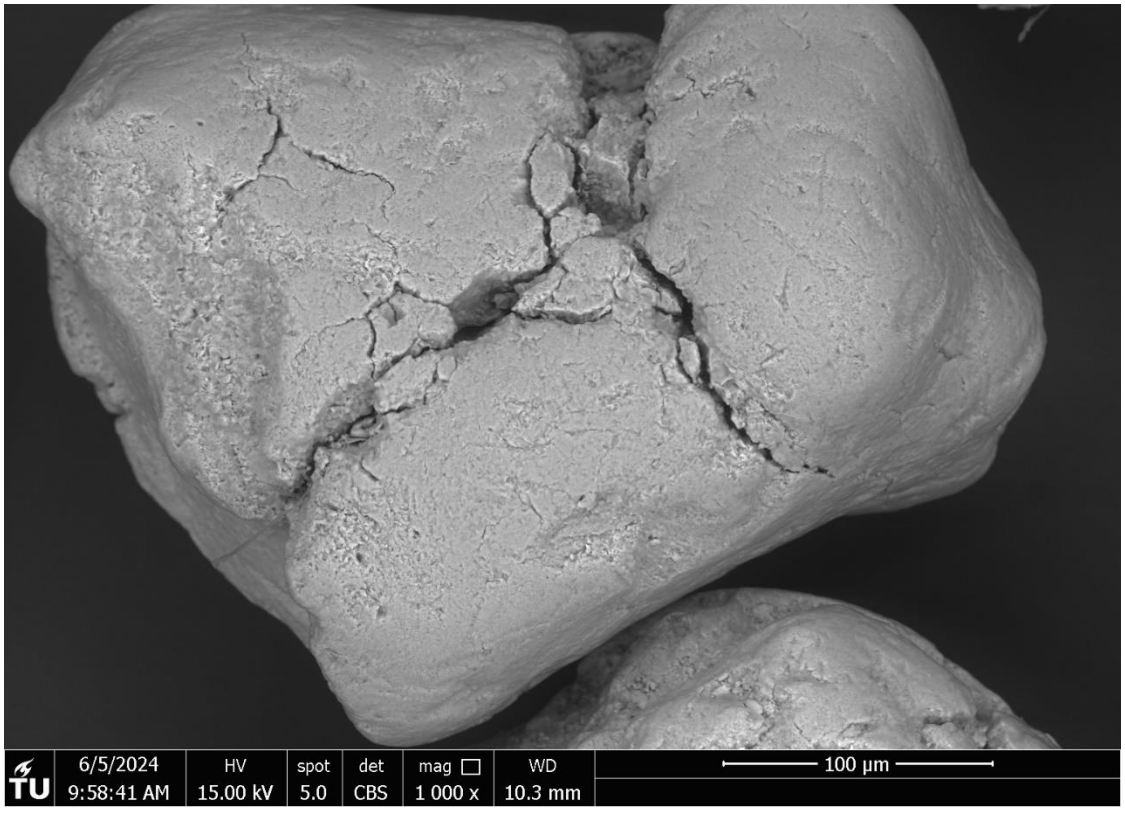

Image Description	*ESEM Image*
Leuven Sand: *Magnetically Separated Glauconite;* *With HCl Pretreatment;* *Oven-Drying at 105°C* *125x Magnification*	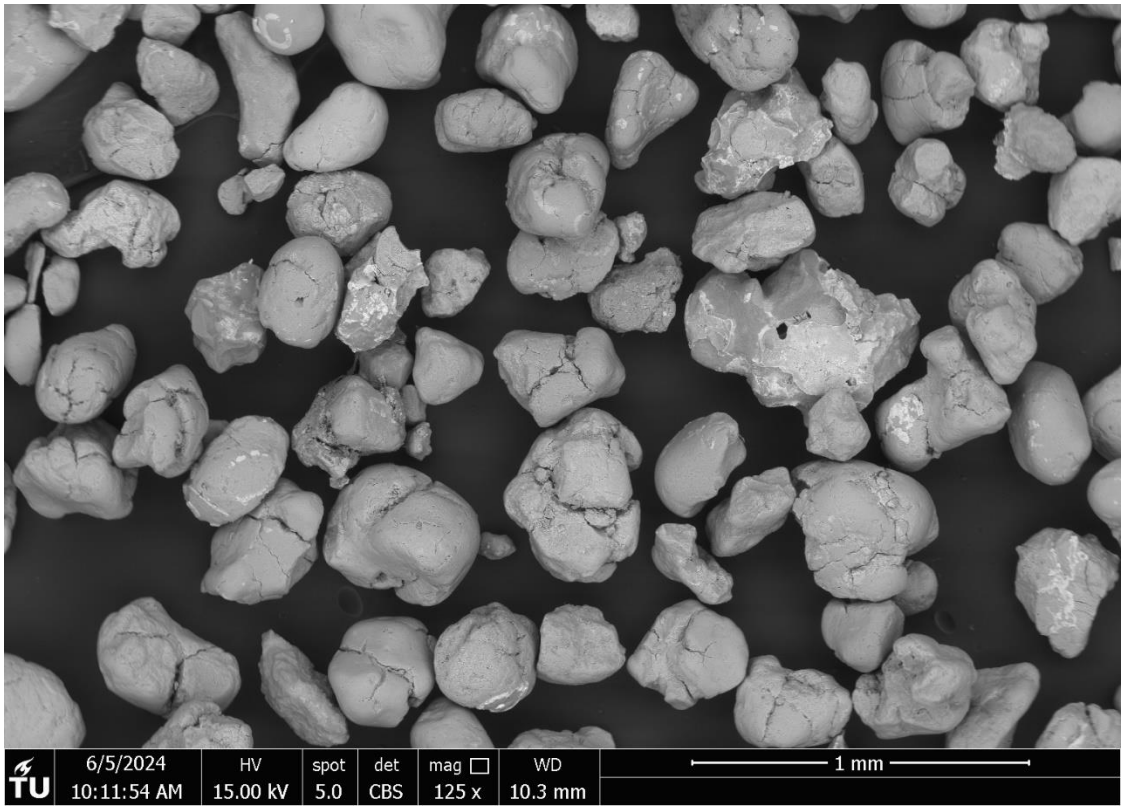
Antwerp Sand: *Magnetically Separated Glauconite;* *With HCl Pretreatment;* *Oven-Drying at 65°C* *125x Magnification*	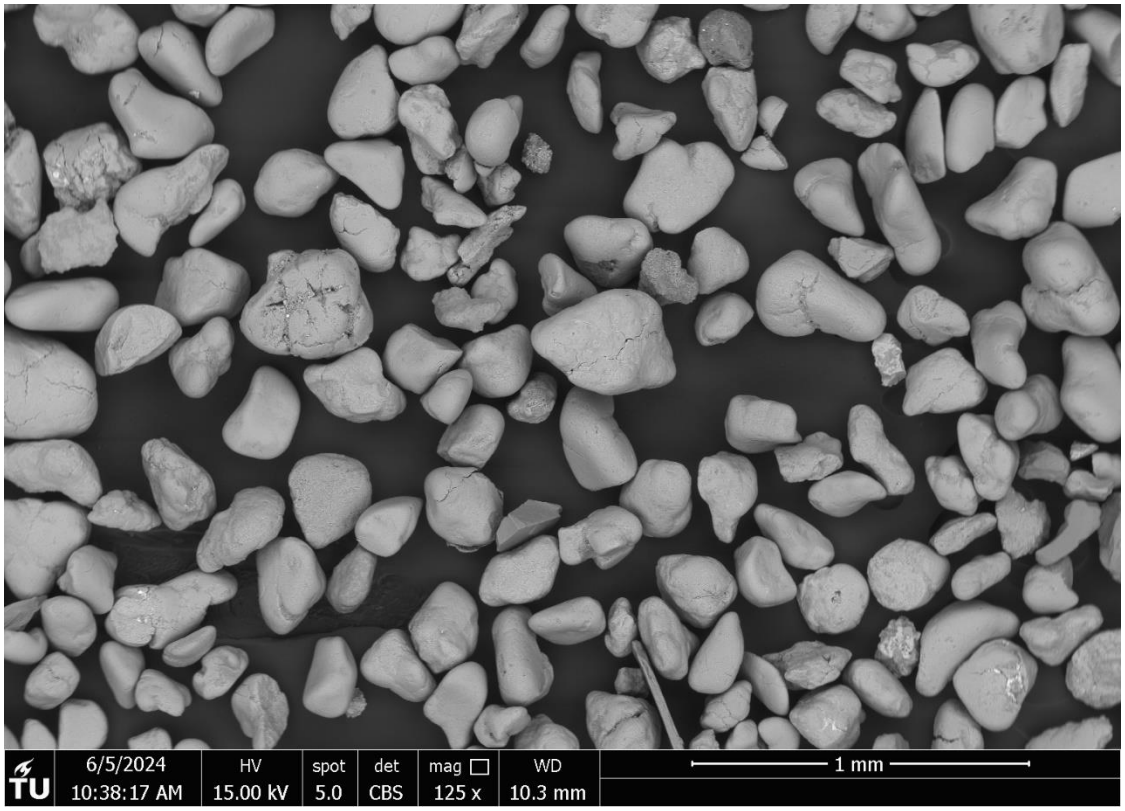

Image Description	*ESEM Image*
Antwerp Sand: *Magnetically Separated Glauconite; With HCl Pretreatment; Oven-Drying at 65°C 250x Magnification*	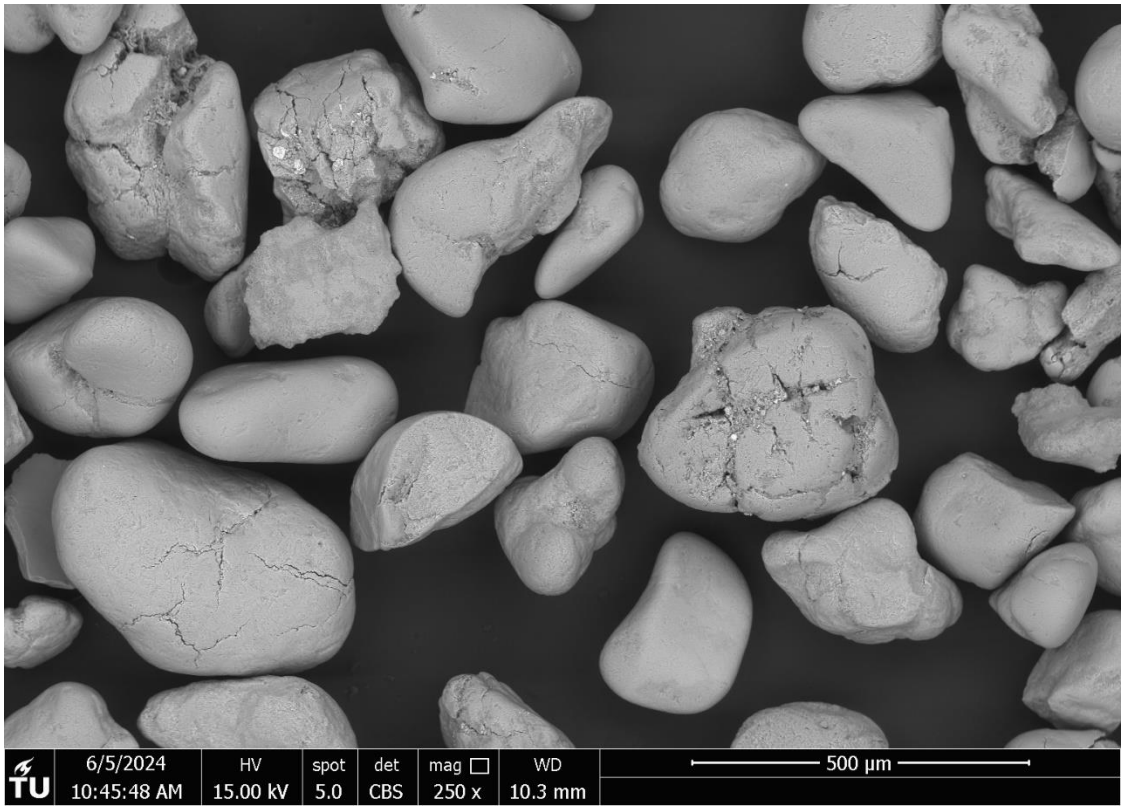
Antwerp Sand: *Magnetically Separated Glauconite; With HCl Pretreatment; Oven-Drying at 65°C 1000x Magnification*	

Image Description	*ESEM Image*
Antwerp Sand: *Magnetically Separated Glauconite; With HCl Pretreatment; Oven-Drying at 65°C 500x Magnification*	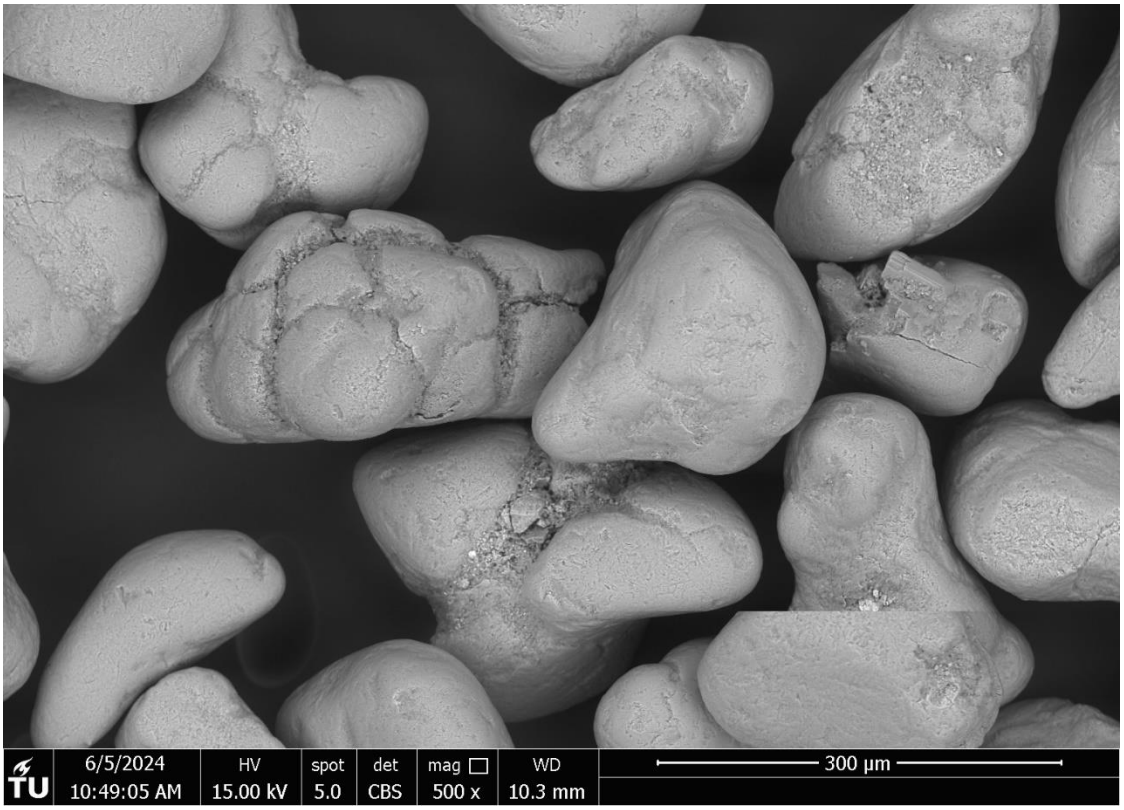
Antwerp Sand: *Magnetically Separated Glauconite; With HCl Pretreatment; Oven-Drying at 65°C 125x Magnification*	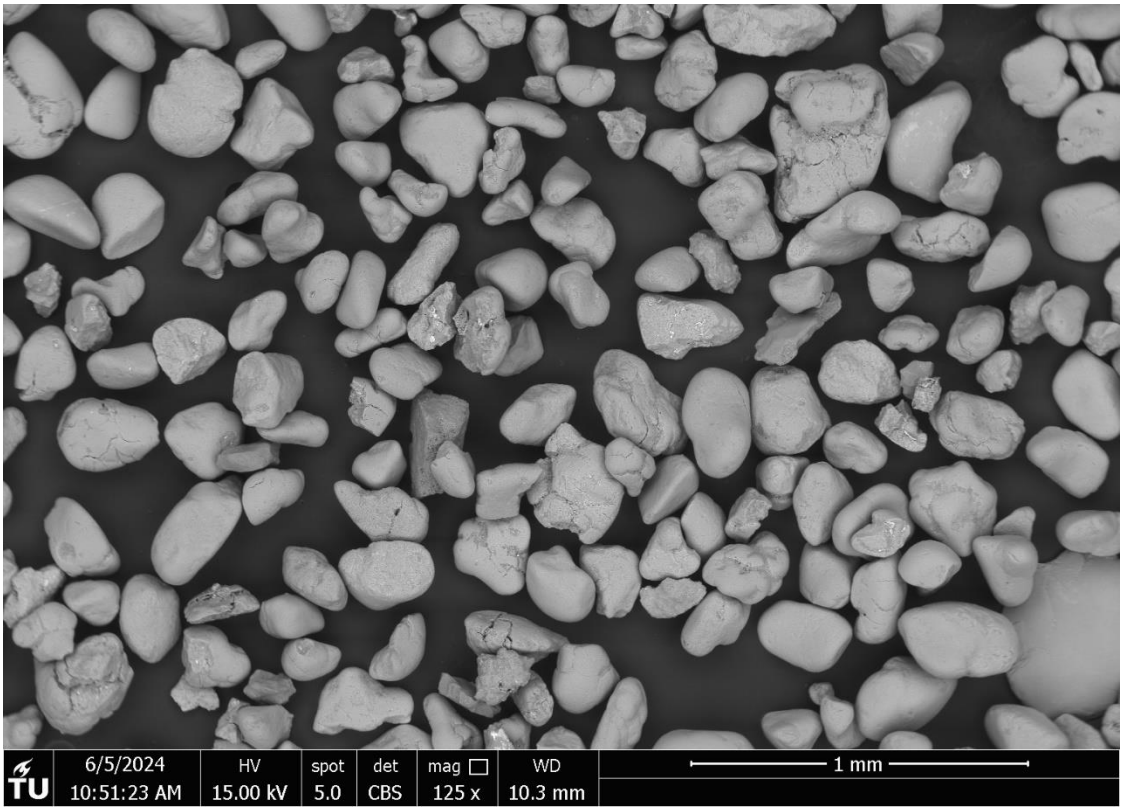

Image Description	*ESEM Image*
Antwerp Sand: *Magnetically Separated Glauconite; With HCl Pretreatment; Oven-Drying at 65°C 250x Magnification*	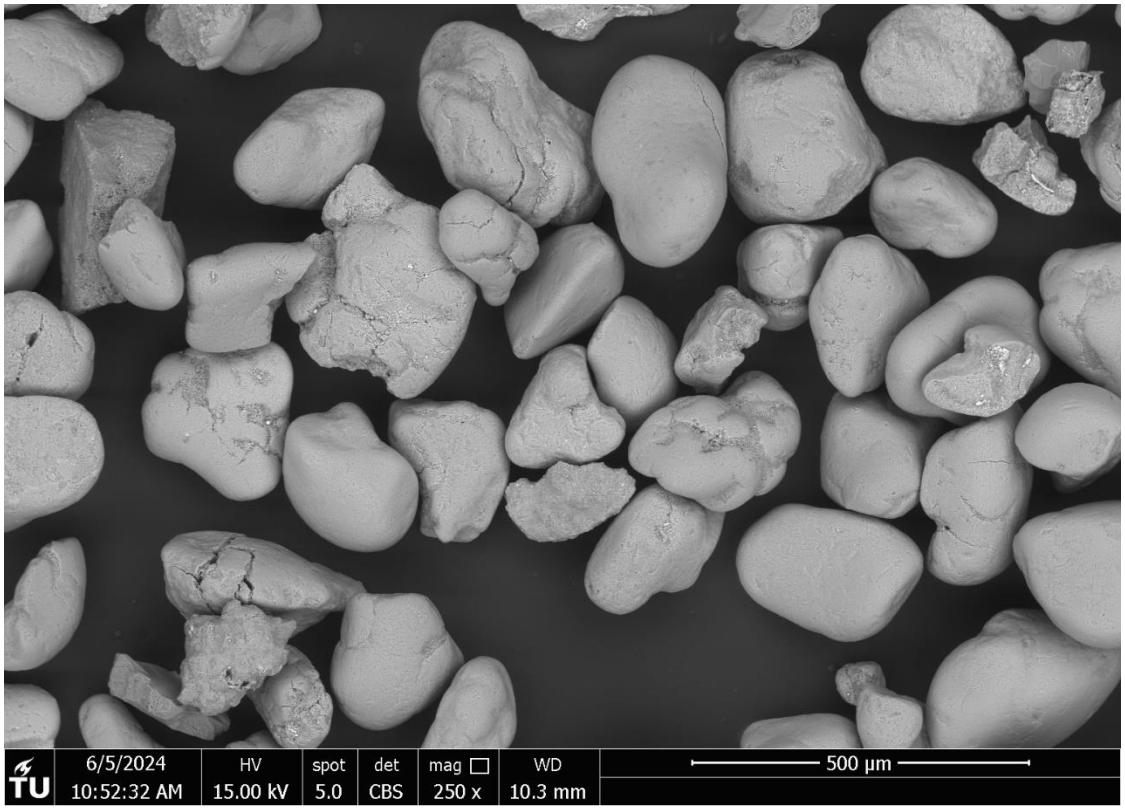
Antwerp Sand: *Magnetically Separated Glauconite; With HCl Pretreatment; Oven-Drying at 105°C 125x Magnification*	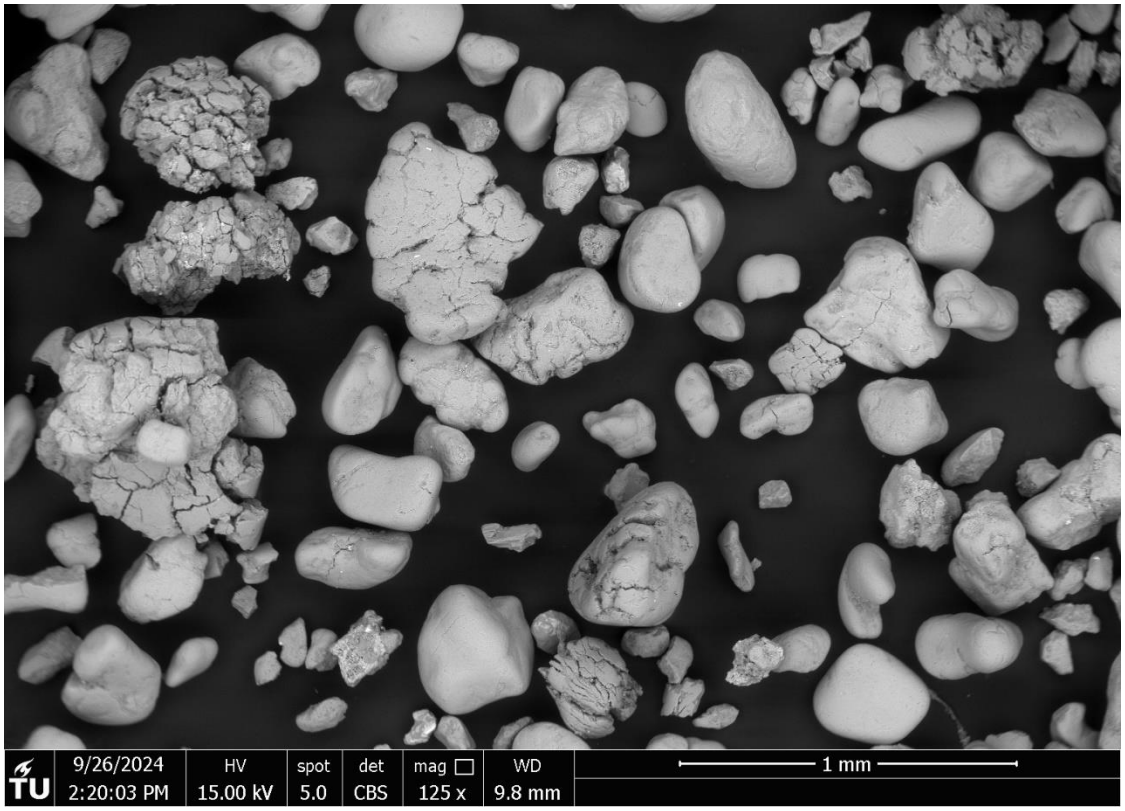

Image Description	*ESEM Image*
Antwerp Sand: *Magnetically Separated Glauconite; With HCl Pretreatment; Oven-Drying at 105°C 125x Magnification*	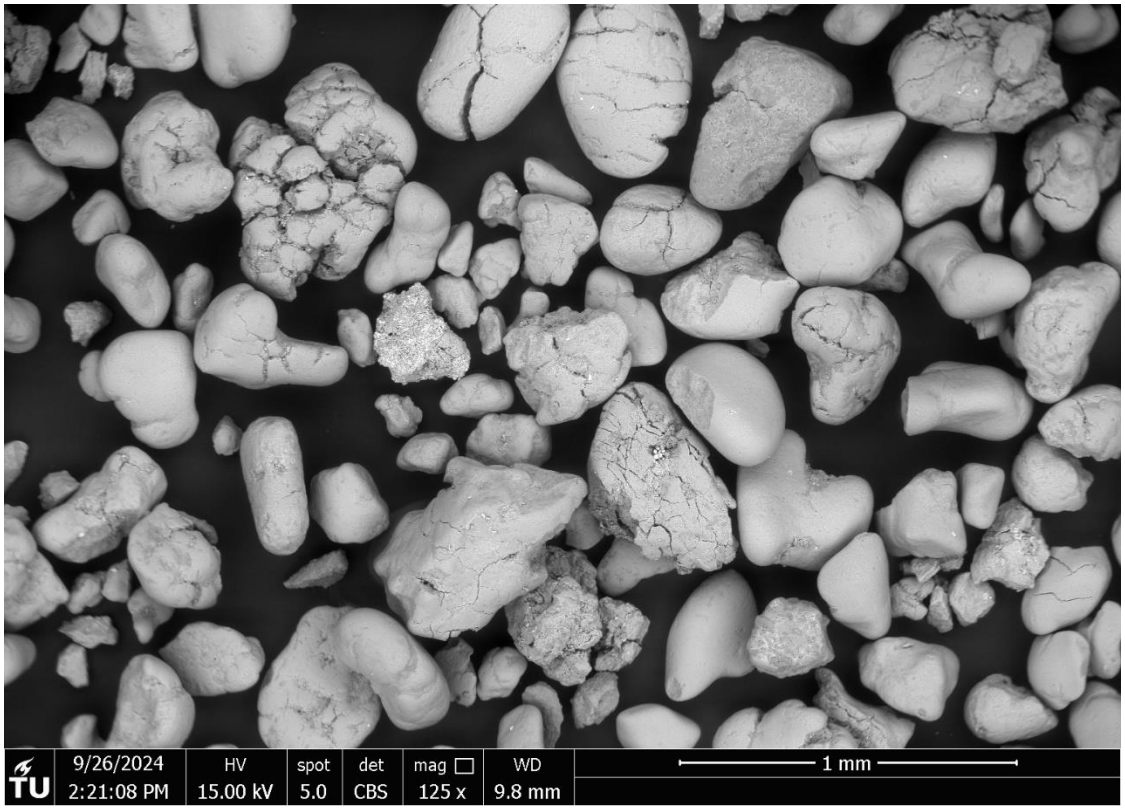
Antwerp Sand: *Magnetically Separated Glauconite; With HCl Pretreatment; Oven-Drying at 105°C 250x Magnification*	

Image Description	*ESEM Image*
Antwerp Sand: *Magnetically Separated Glauconite; With HCl Pretreatment; Oven-Drying at 105°C 500x Magnification*	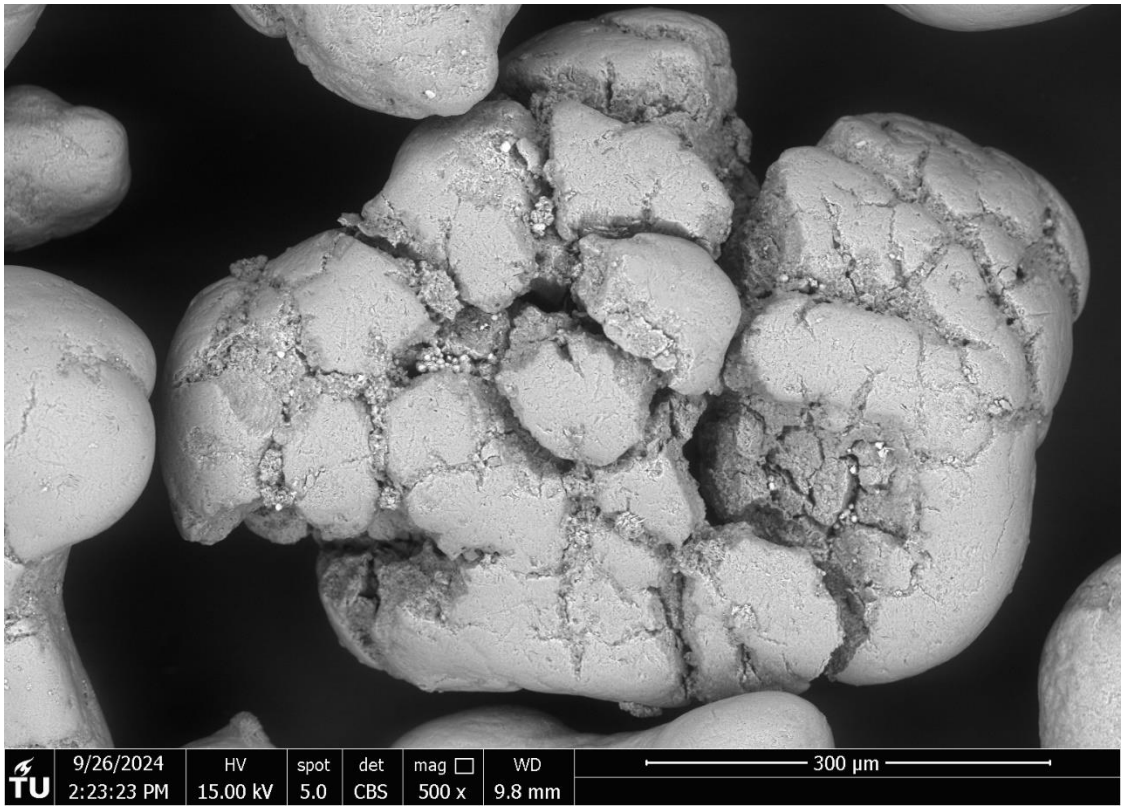
Antwerp Sand: *Magnetically Separated Glauconite; With HCl Pretreatment; Oven-Drying at 105°C 1000x Magnification*	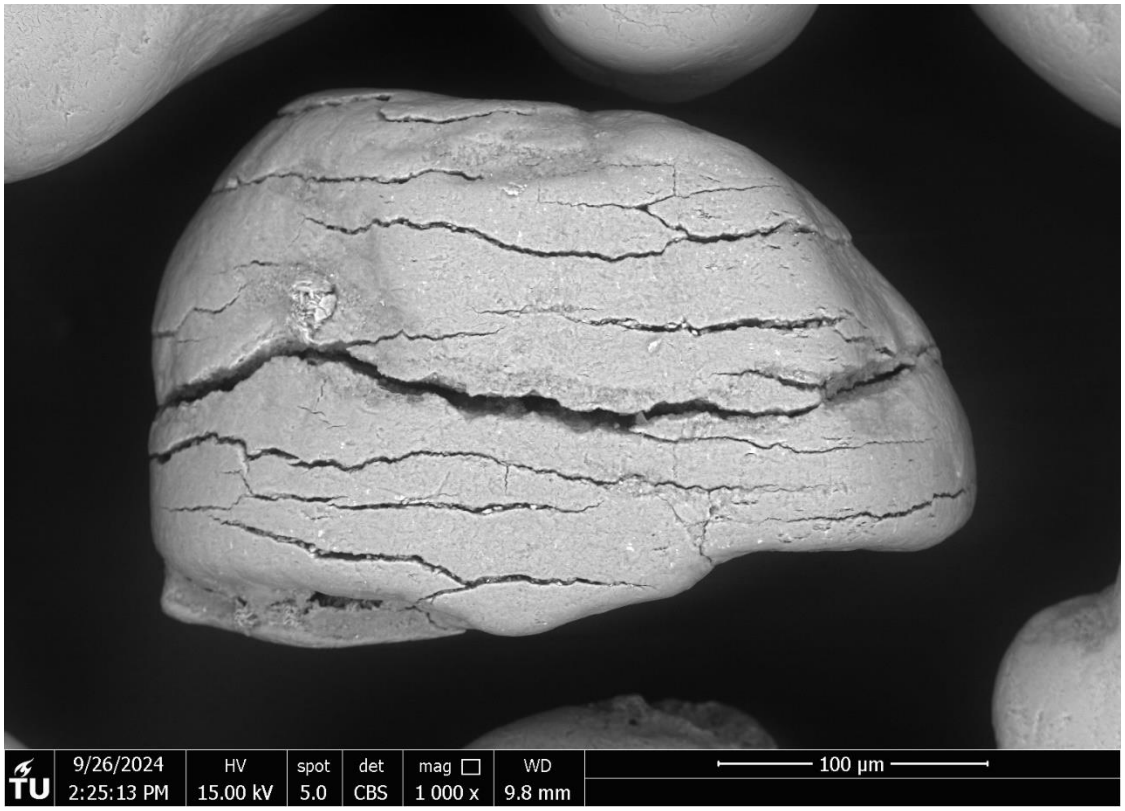

Image Description	*ESEM Image*
Antwerp Sand: *Magnetically Separated Glauconite; With HCl Pretreatment; Oven-Drying at 105°C 5000x Magnification*	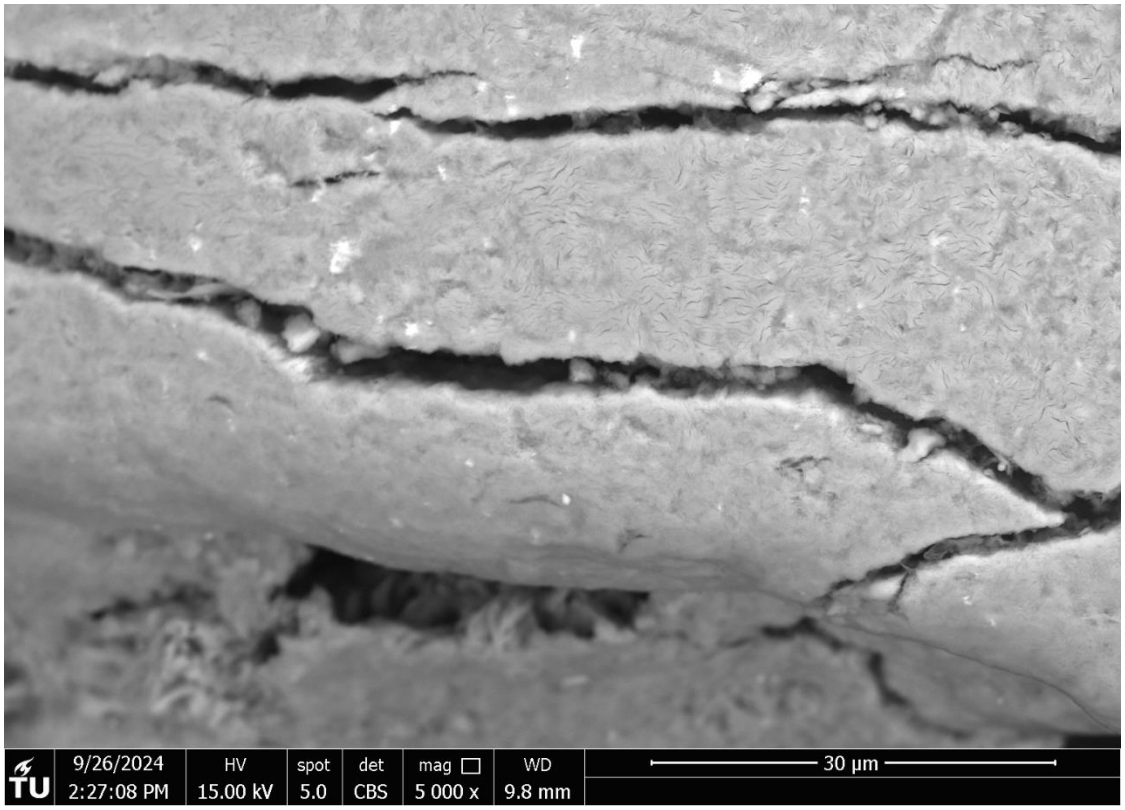
Leuven Sand: *Top of Specimen from Cyclic DS Test on Rough Interface; Dried and Remixed; 125x Magnification*	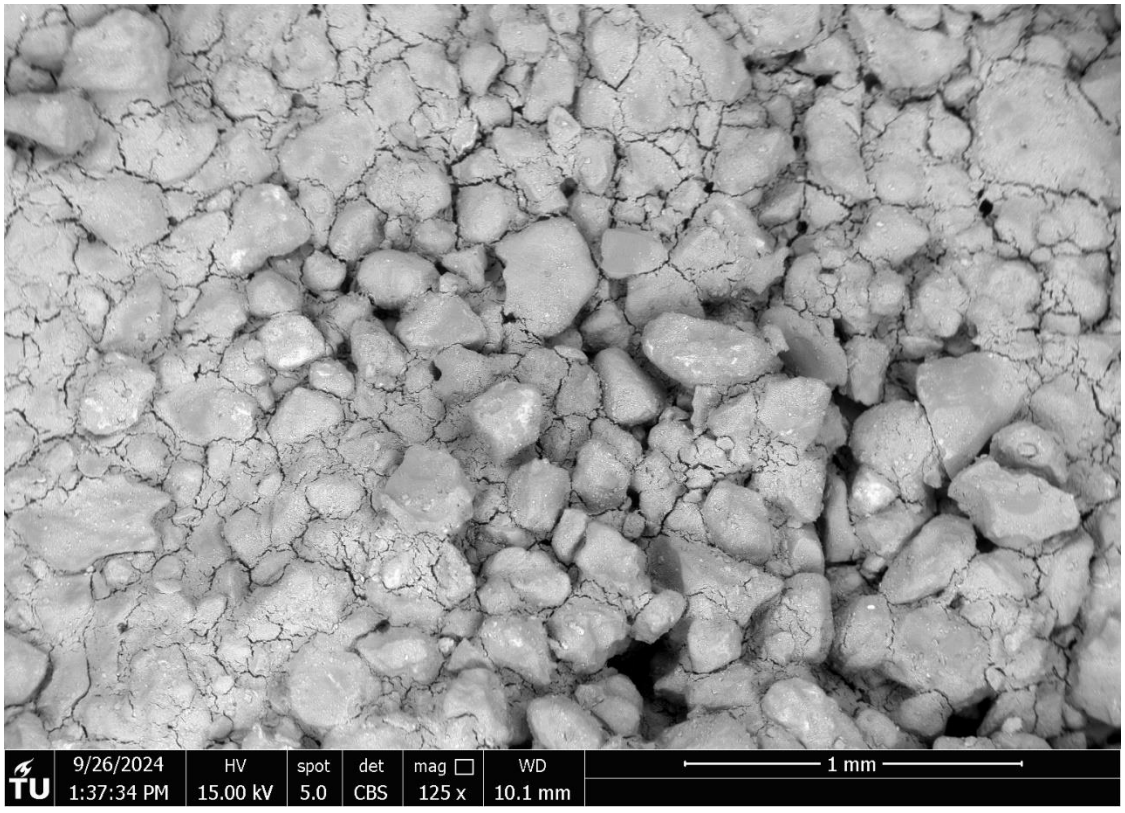

Image Description	*ESEM Image*
Leuven Sand: *Top of Specimen from Cyclic DS Test on Rough Interface; Dried and Remixed; 250x Magnification*	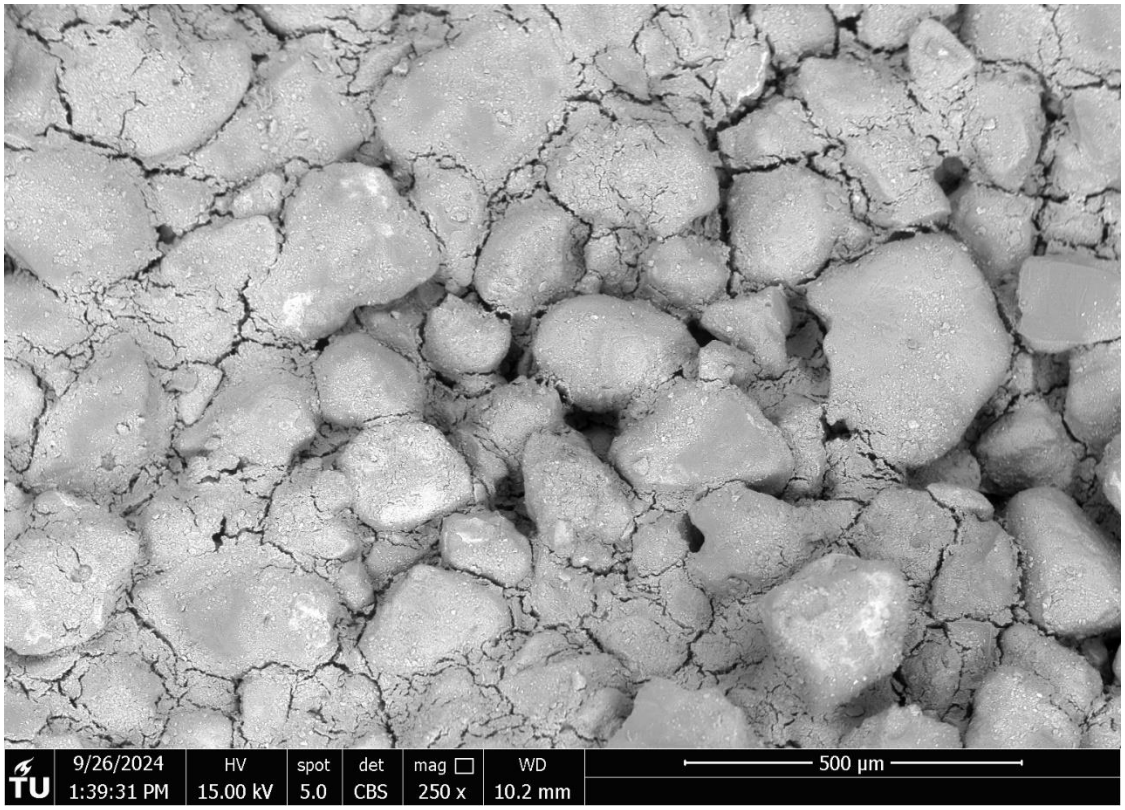
Leuven Sand: *Top of Specimen from Cyclic DS Test on Rough Interface; Dried and Remixed; 500x Magnification*	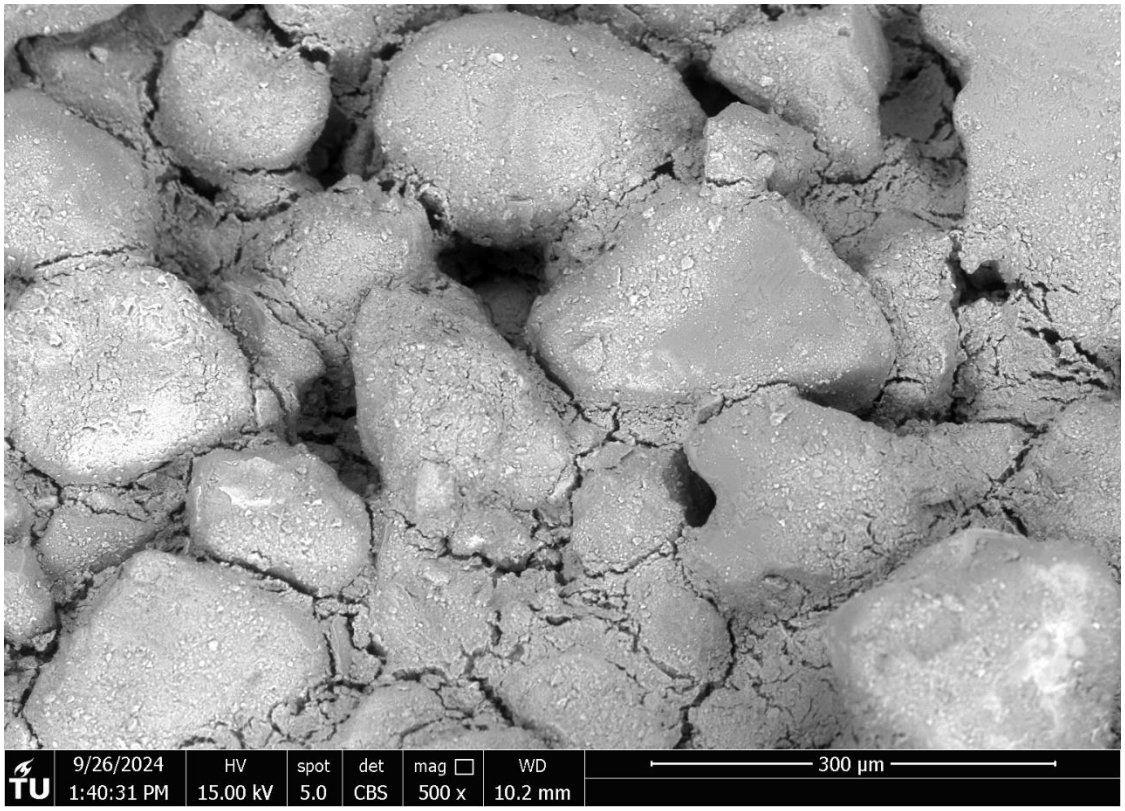

Image Description	*ESEM Image*
Leuven Sand: *Top of Specimen from Cyclic DS Test on Rough Interface; Dried and Remixed; 250x Magnification*	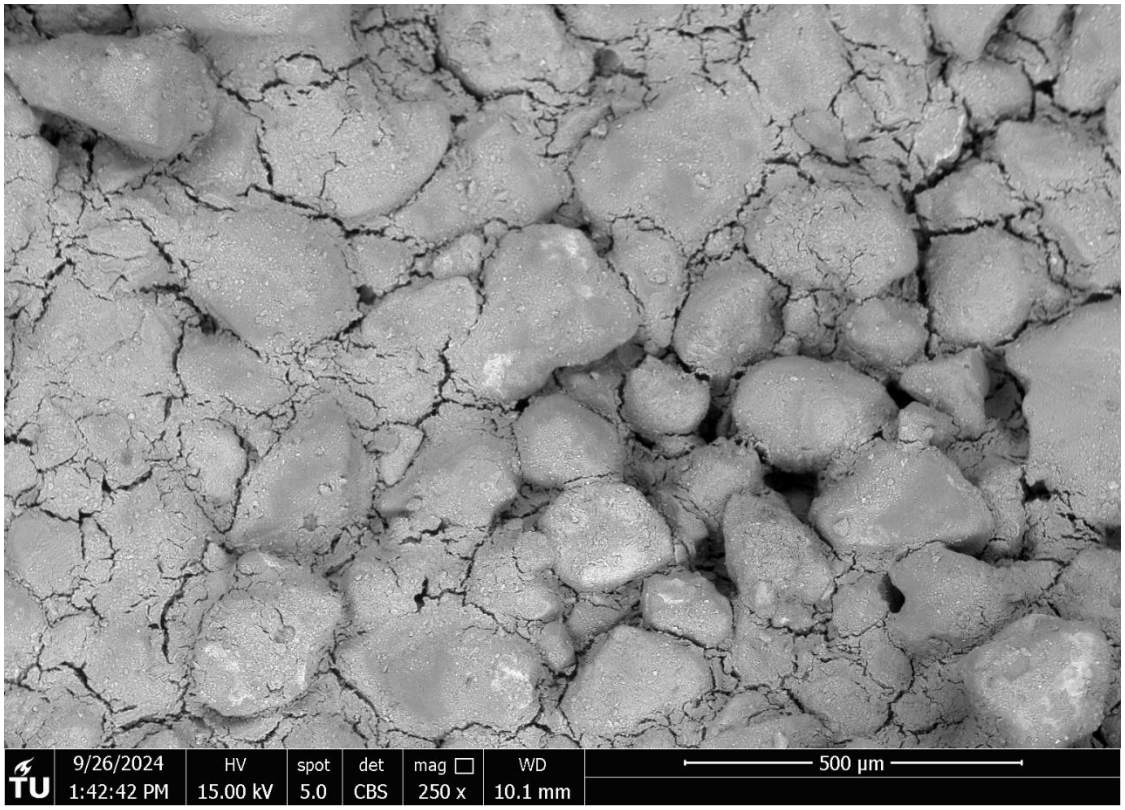
Leuven Sand: *Top of Specimen from Cyclic DS Test on Rough Interface; Dried and Remixed; 1000x Magnification*	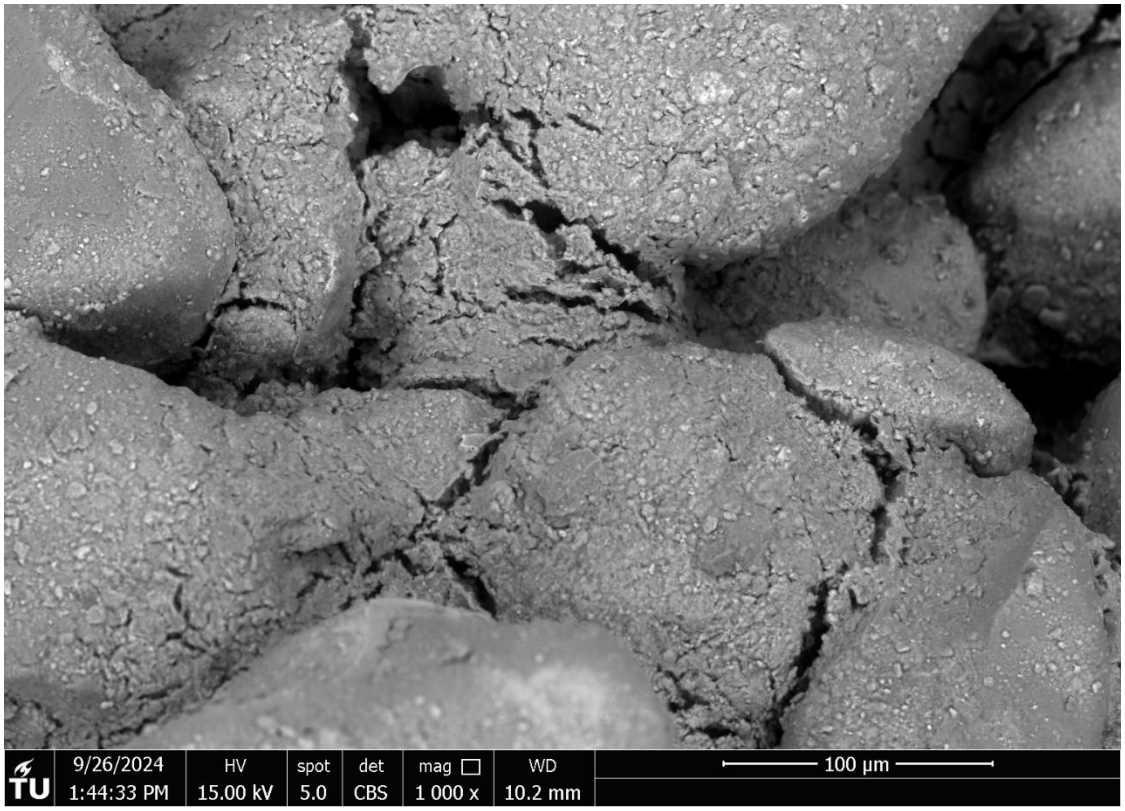

Image Description	*ESEM Image*
Leuven Sand: *Shear Zone Material from Cyclic DS Test on Rough Interface; Dried and Remixed; 125x Magnification*	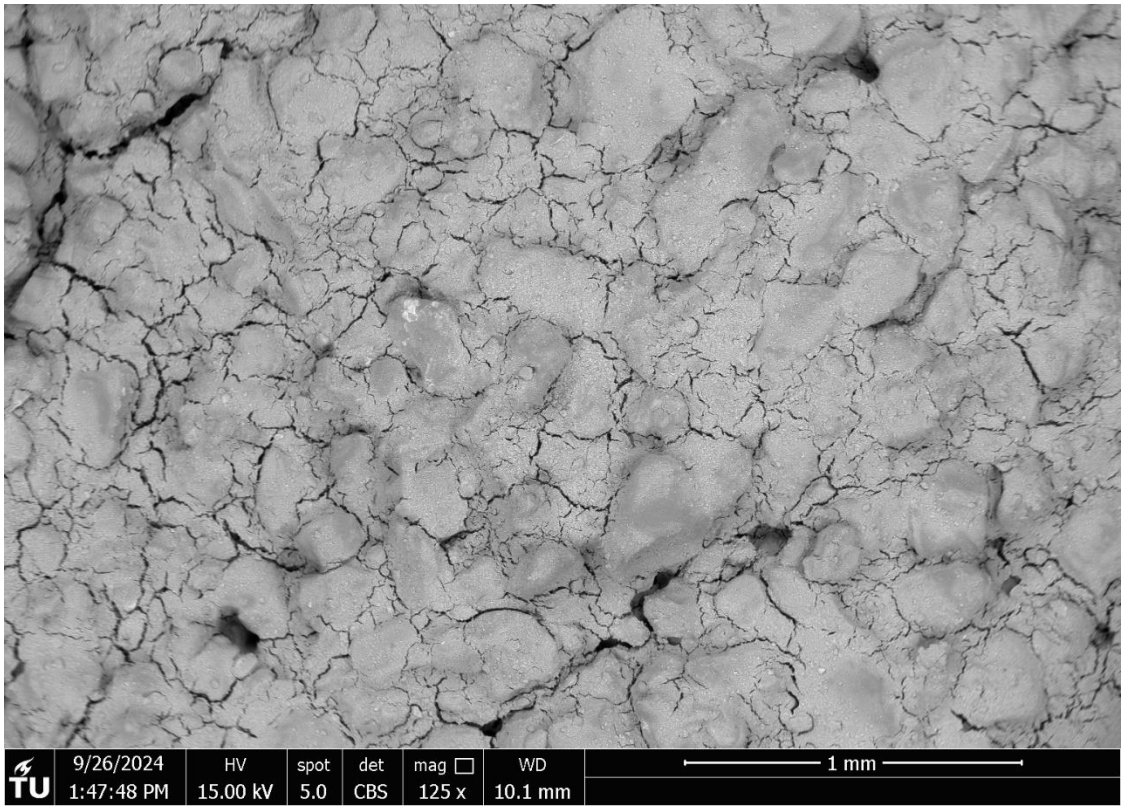
Leuven Sand: *Shear Zone Material from Cyclic DS Test on Rough Interface; Dried and Remixed; 250x Magnification*	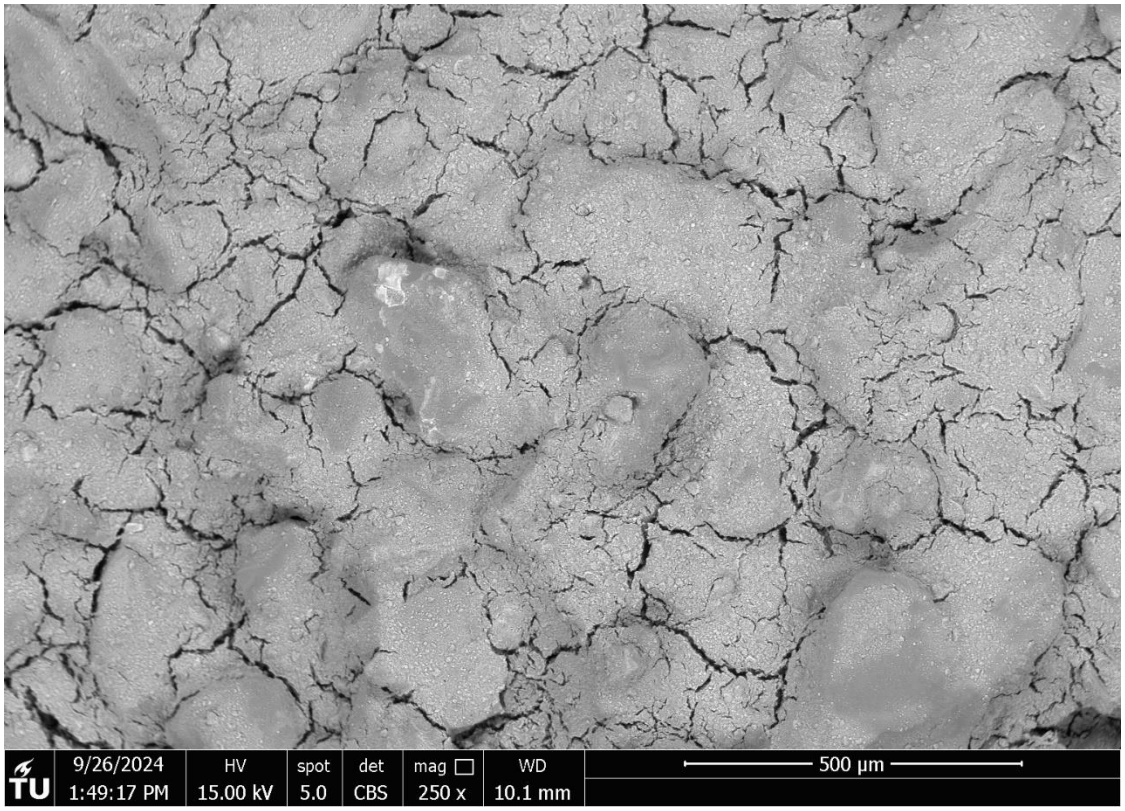

Image Description	*ESEM Image*
Leuven Sand: *Shear Zone Material from Cyclic DS Test on Rough Interface; Dried and Remixed; 500x Magnification*	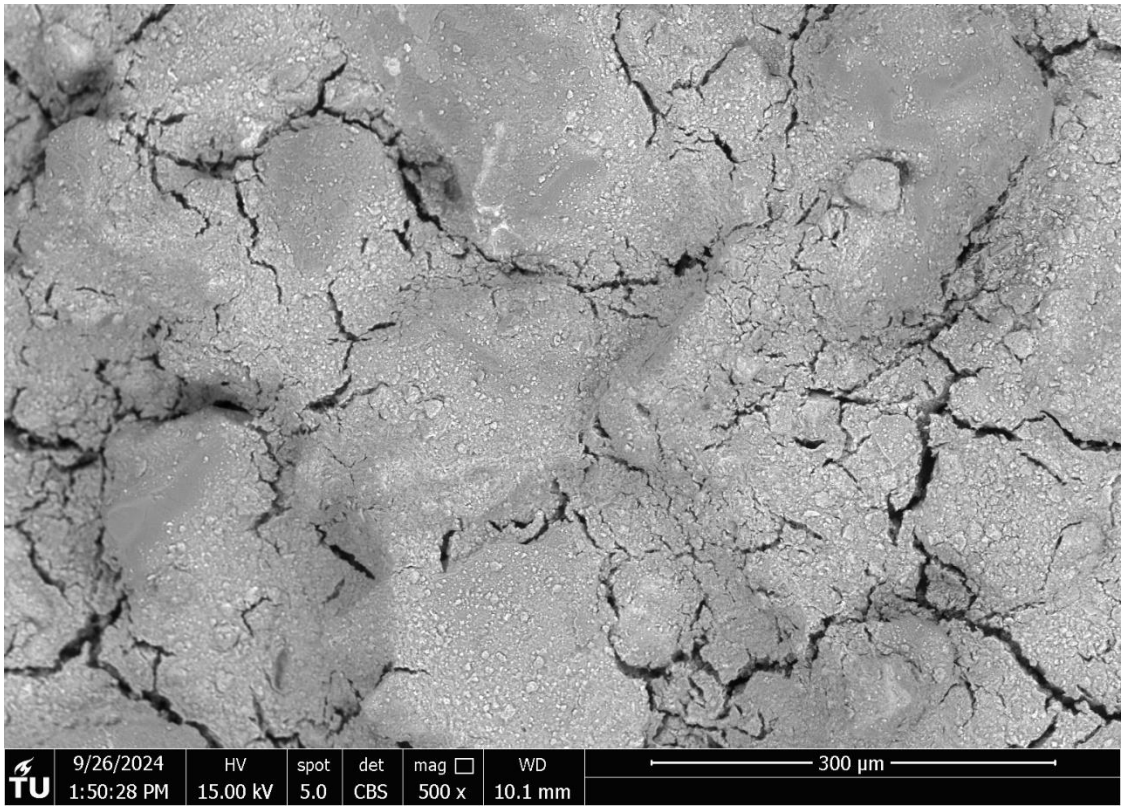
Leuven Sand: *Shear Zone Material from Cyclic DS Test on Rough Interface; Dried and Remixed; 1000x Magnification*	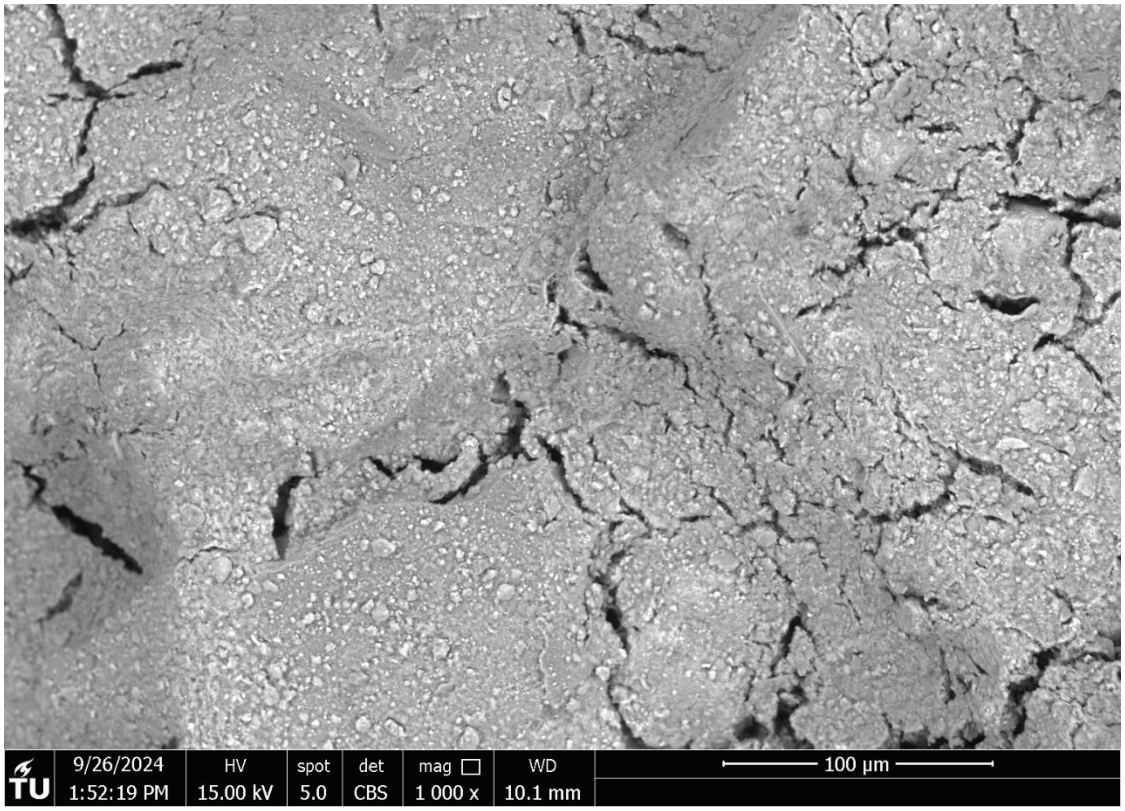

Image Description	*ESEM Image*
Leuven Sand: *4-hr Dispersion 425-µm Fraction from Atterberg Limit Test; Dried and Remixed; 250x Magnification*	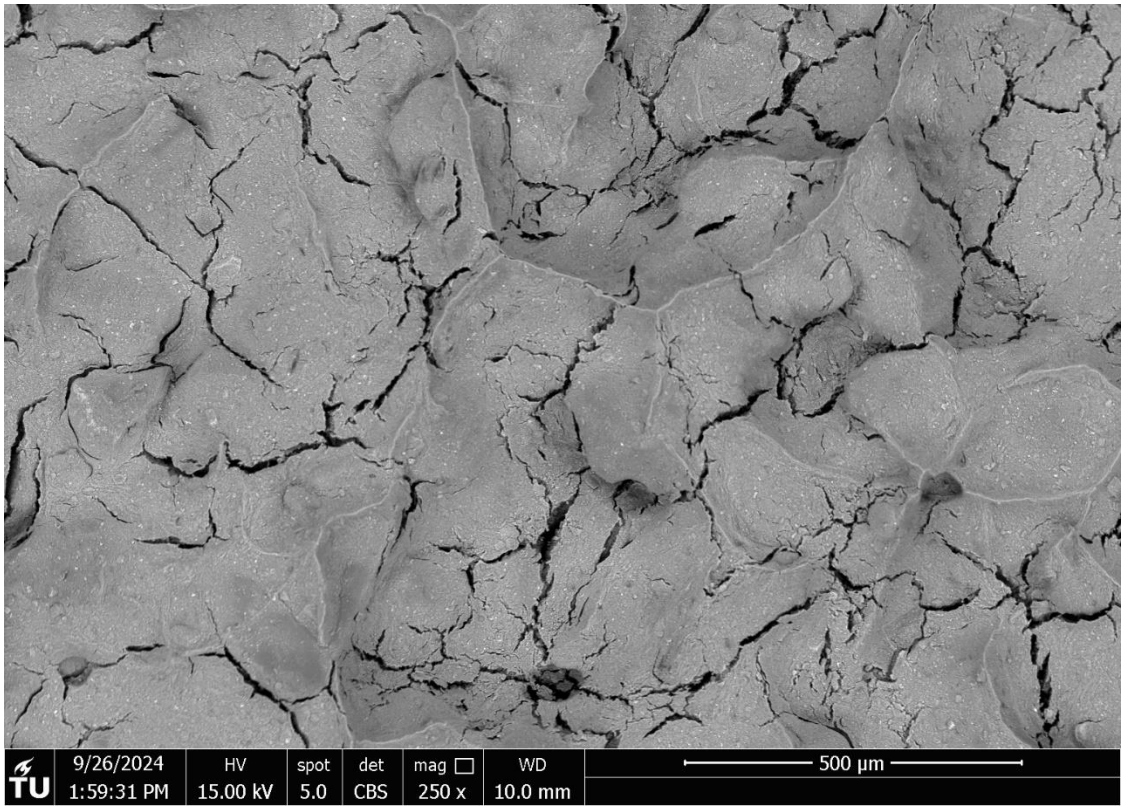
Leuven Sand: *4-hr Dispersion 425-µm Fraction from Atterberg Limit Test; Dried and Remixed; 500x Magnification*	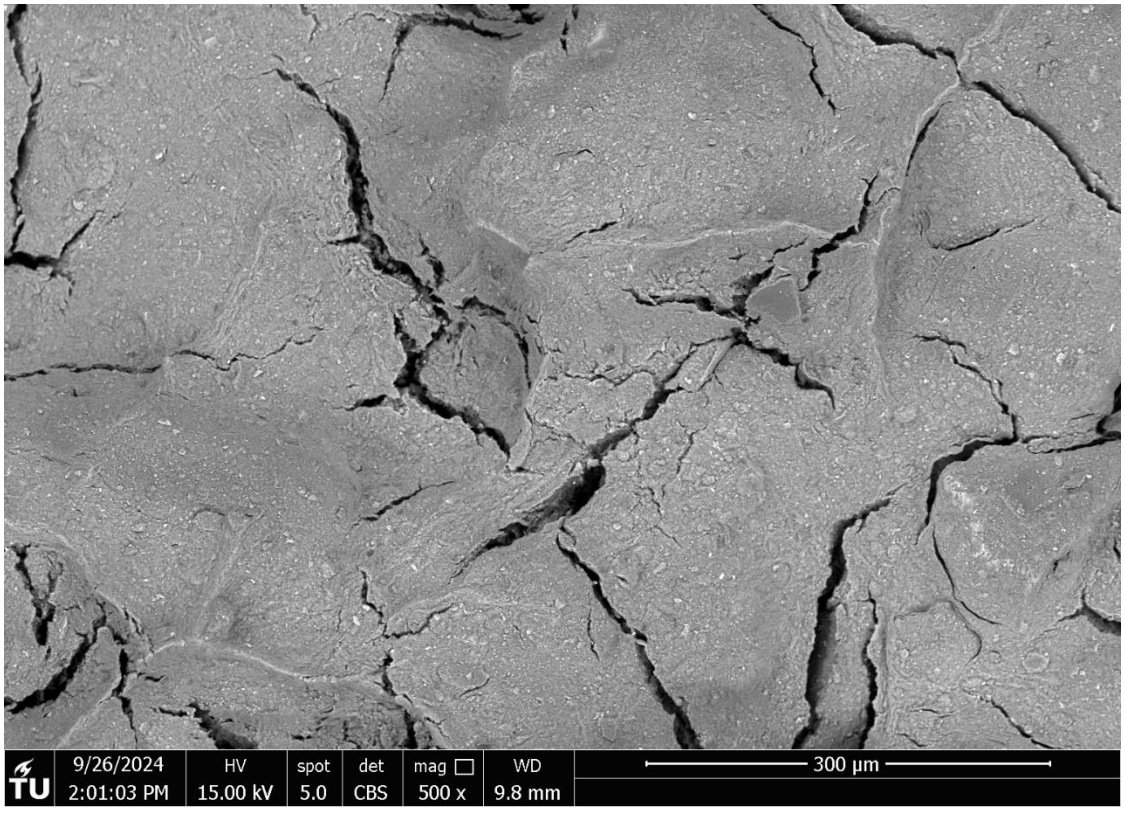

Image Description	*ESEM Image*
Antwerp Sand: *Top of Specimen from Cyclic DS Test on Rough Interface; Dried and Remixed; 125x Magnification*	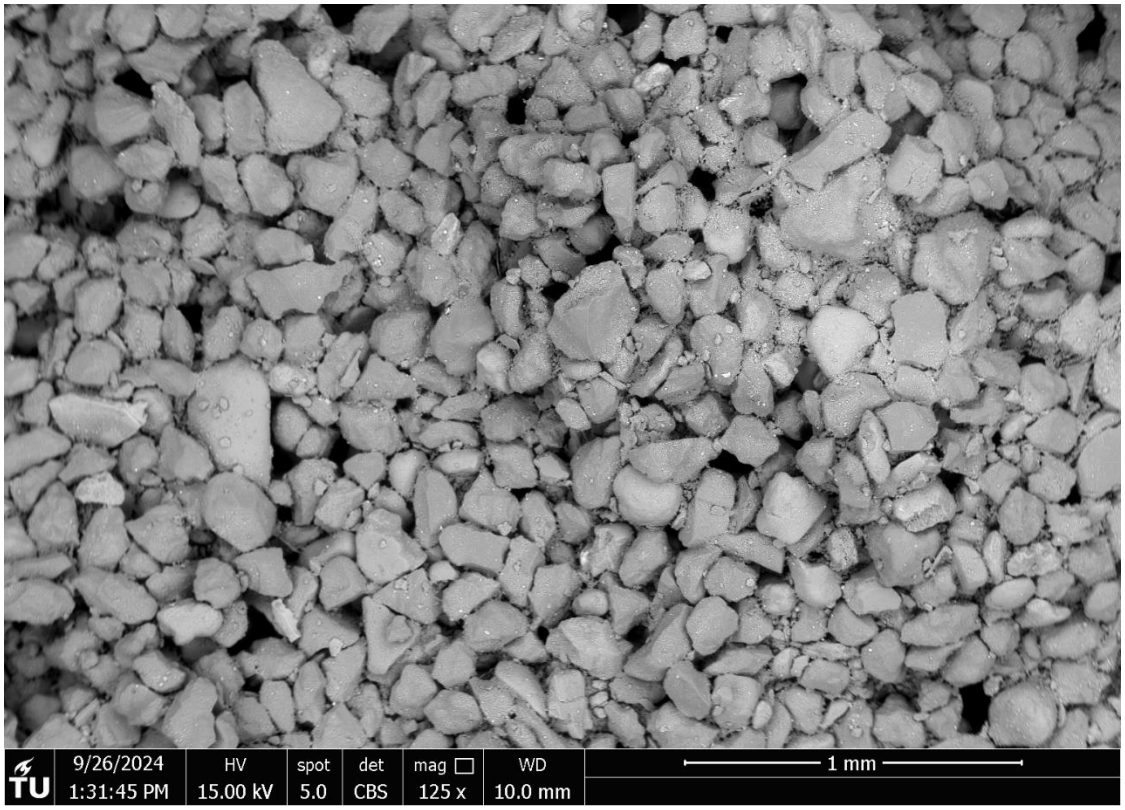
Antwerp Sand: *Top of Specimen from Cyclic DS Test on Rough Interface; Dried and Remixed; 250x Magnification*	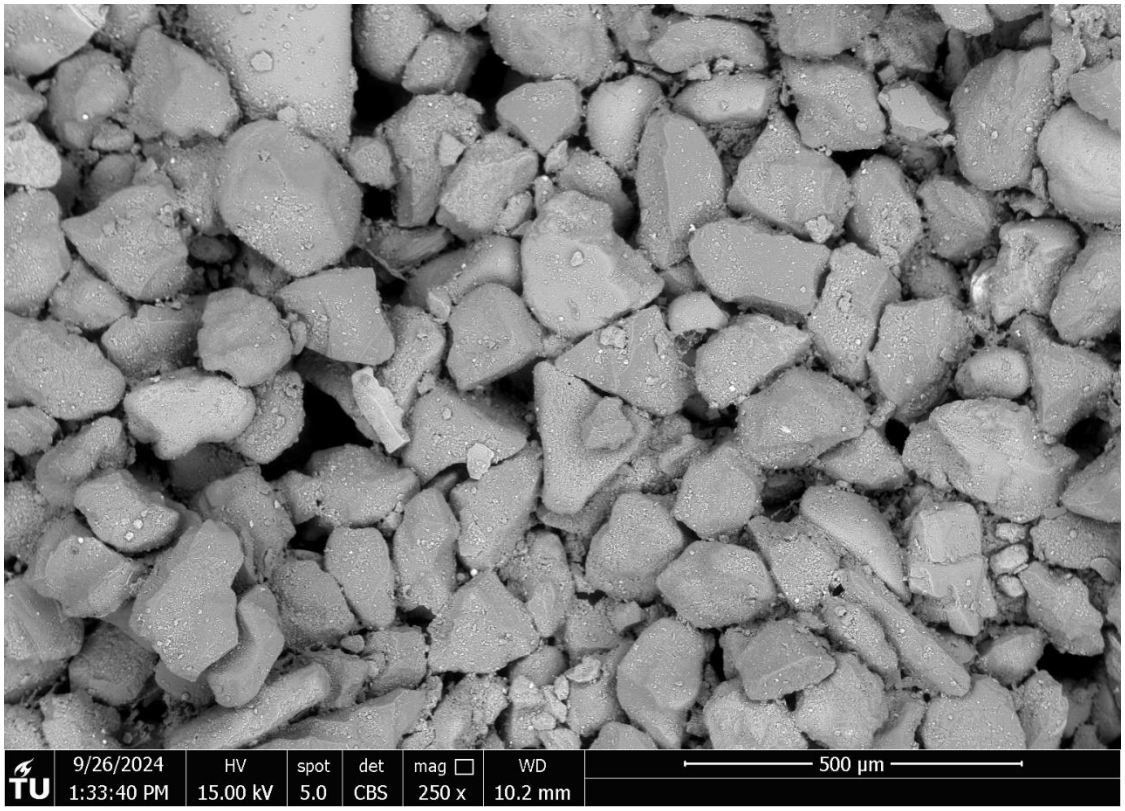

Image Description	*ESEM Image*
Antwerp Sand: *Top of Specimen from Cyclic DS Test on Rough Interface; Dried and Remixed; 500x Magnification*	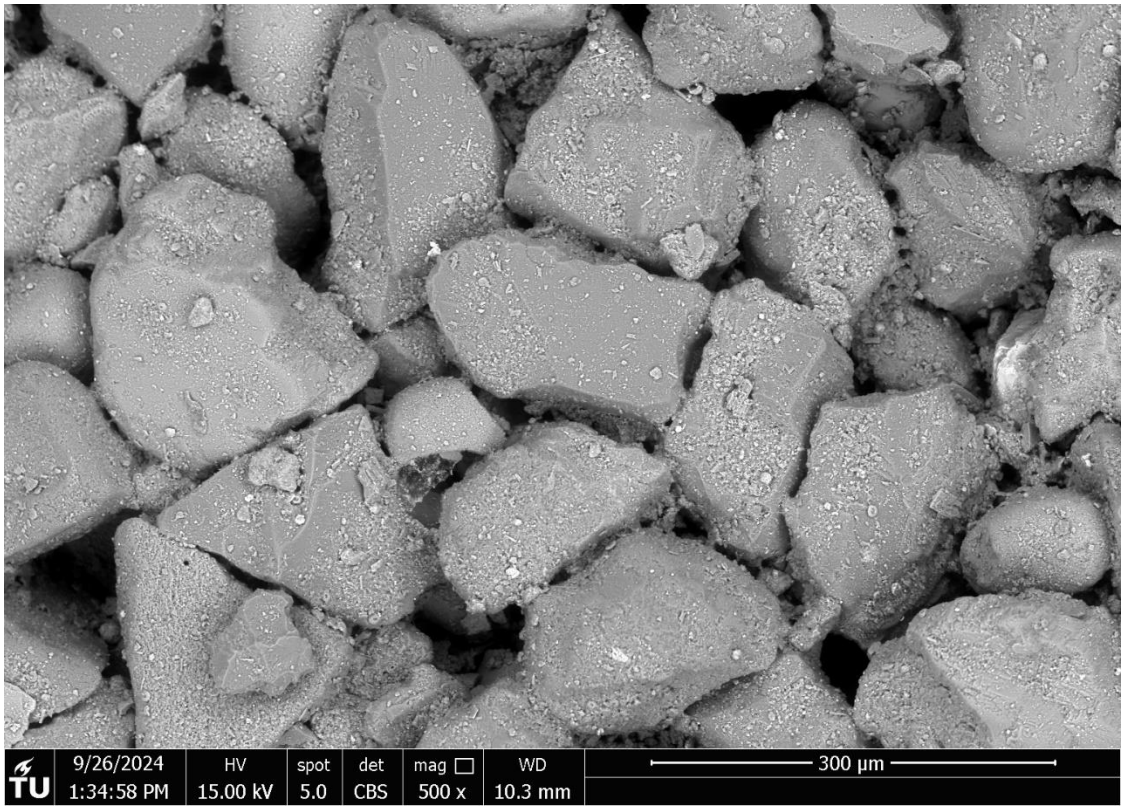
Antwerp Sand: *Shear Zone Material from Cyclic DS Test on Rough Interface; Dried and Remixed; 125x Magnification*	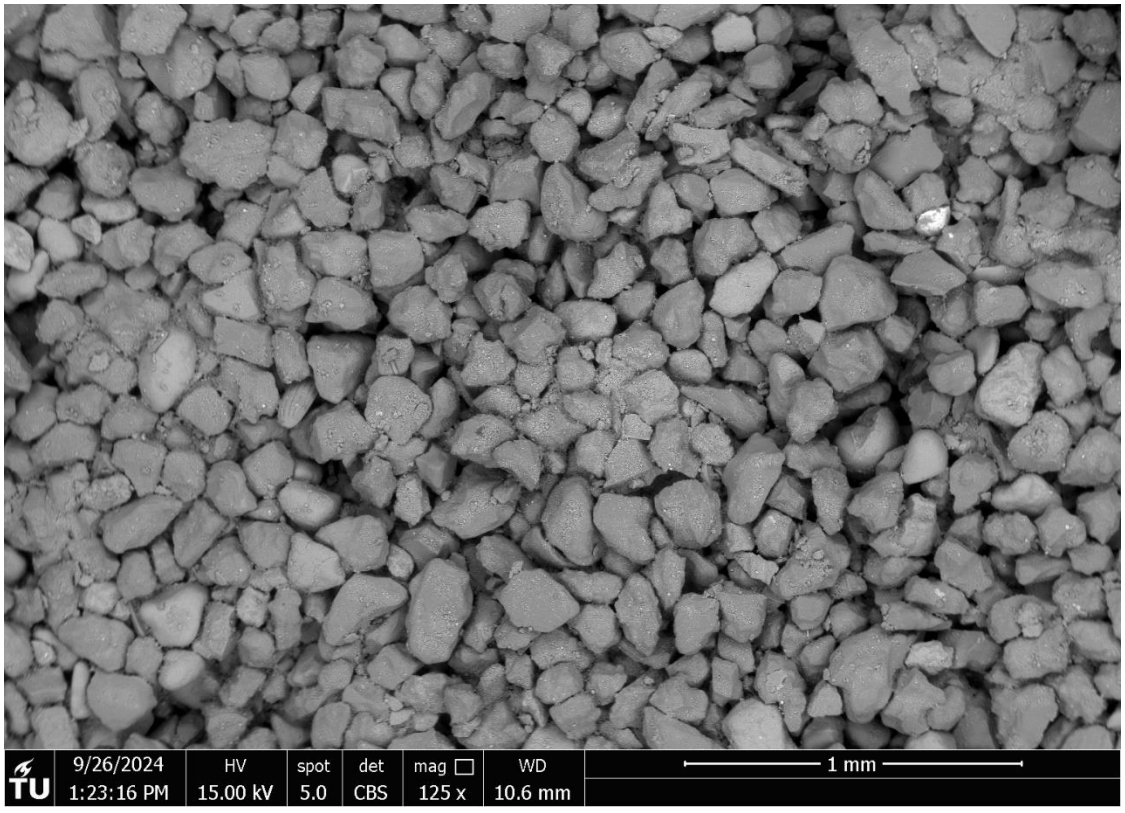

Image Description	*ESEM Image*
Antwerp Sand: *Shear Zone Material from Cyclic DS Test on Rough Interface; Dried and Remixed; 250x Magnification*	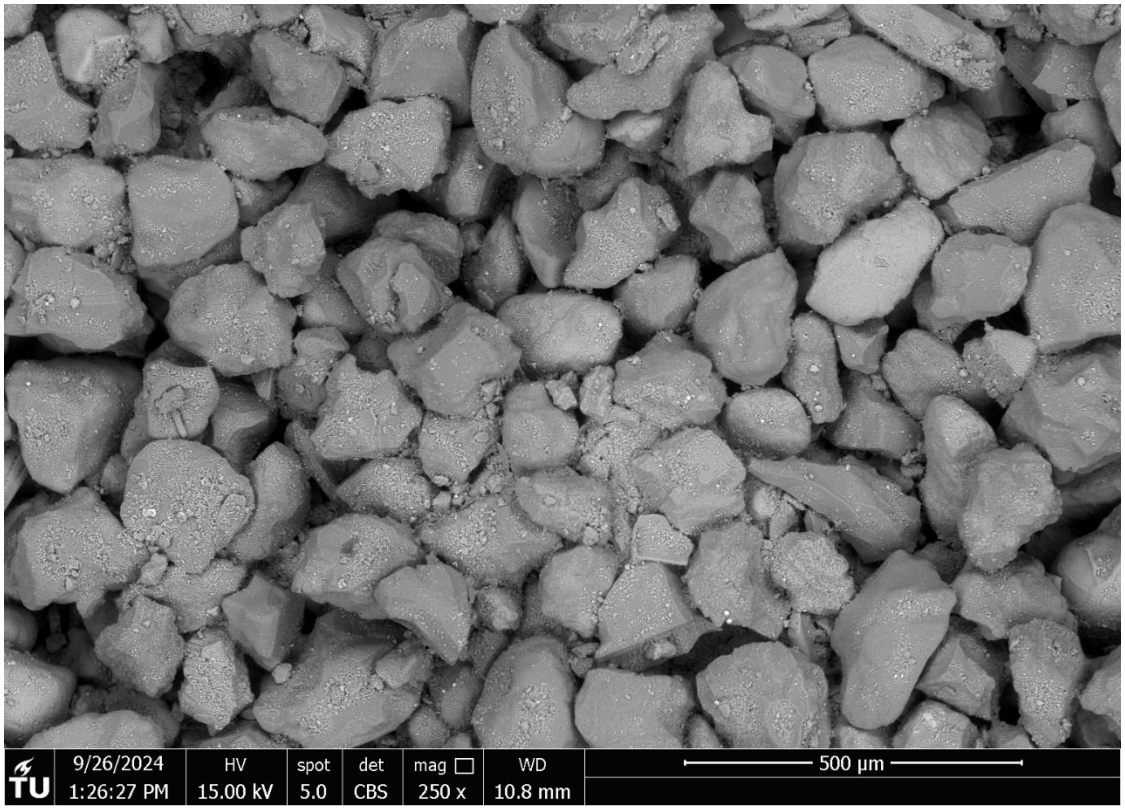
Antwerp Sand: *Shear Zone Material from Cyclic DS Test on Rough Interface; Dried and Remixed; 500x Magnification*	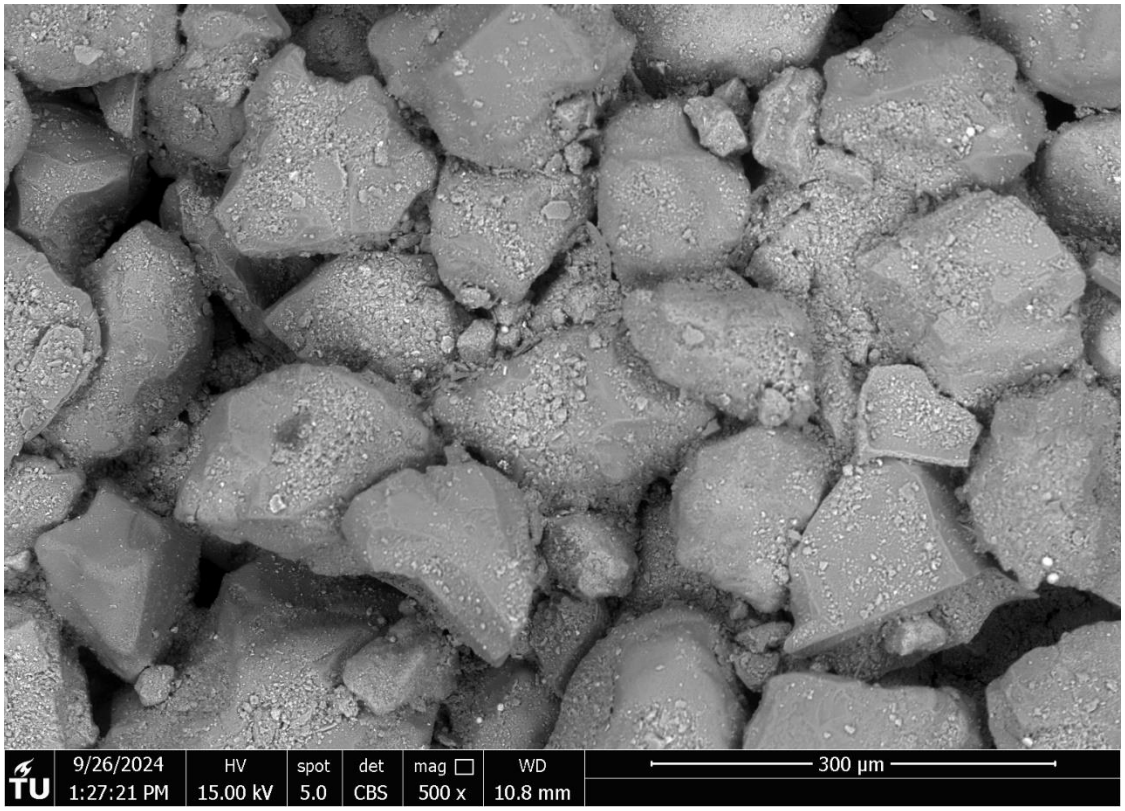

Image Description	*ESEM Image*
Antwerp Sand: *Shear Zone Material from Cyclic DS Test on Rough Interface; Dried and Remixed; 250x Magnification*